# DNA IN THE SPOTLIGHT:

## VISUALIZATION, QUANTIFICATION, AND MANIPULATION OF DNA WITH SMALL MOLECULE INTERCALATORS

Pauline Julika Kolbeck

Utrecht 2023

# DNA IN THE SPOTLIGHT:

## VISUALIZATION, QUANTIFICATION, AND MANIPULATION OF DNA WITH SMALL MOLECULE INTERCALATORS

### DNA IN DE KIJKER:

#### VISUALISATIE, KWANTIFICERING EN MANIPULATIE VAN DNA MET KLEINE MOLECULAIRE INTERCALATOREN

(met een samenvatting in het Nederlands)

PROEFSCHRIFT

ter verkrijging van de graad van doctor aan de
Universiteit Utrecht
op gezag van de
rector magnificus, prof. dr. H.R.B.M. Kummeling,
ingevolge het besluit van het college voor promoties
in het openbaar te verdedigen op
woensdag 6 december 2023 des middags te 12.15 uur

door

PAULINE JULIKA KOLBECK

geboren op 24 januari 1995
te Starnberg, Duitsland

*Für meine Familie.*

*L'essentiel est invisible pour les yeux.*

—— Antoine de Saint-Exupéry, Le Petit Prince (1943) ——

# A C K N O W L E D G E M E N T S

First of all, I would like to express my gratitude to my parents, my brother Benjamin and my sister Lea for all their support over the years.

Then, I would like to thank my doctoral supervisor Jan. Thank you for the freedom you have given me during my PhD, for the great supervision, for all your help, and for the stimulating atmosphere you created in the Lipfert Lab.

Special thanks to Willem for your continuous guidance and for your perceptive and astute criticism. And to Aidin Lak and Hermann Gaub for empowering and mentoring me, and for your passion for science. Thank you, Arthur, for proofreading my work, for your optimism and your spirit of encouragement.

And finally, yet importantly, thank you to all the great people I met during my PhD, current and former lab members, collaborators, and all other people who supported and inspired me. Each of them knows what I am thankful for:

| | | |
|---|---|---|
| Achim Löf | Franzi Kriegel | Miloš Tišma |
| Adina Hausch | Gerd Gemmecker | Moritz Weck |
| Aksana Svirydava | Gerhard Blab | Nick Hundt |
| Alex Urban | Gloria Müller | Nina Beier |
| Alfons van Blaaderen | Grega Posnjak | Patrick Kudella |
| Angelika Kardinal | Hester van der Putte | Philipp Nickels |
| Anna Baptist | Irina Martynenko | Philipp Walker |
| Annalena Salditt | Jérôme Mathé | Res Jöhr |
| Ann-Kathrin Wagner | Joachim Rädler | Sabine Hohenester |
| Annika Tölke | Jochen Müller | Samuel Stubhan |
| Anna Salvetti | Katy Erlich | Sebastian Konrad |
| Aron Venczel | Kelly Brouwer | Sha Li |
| Barbara Müller | Klaus Beckord | Simone Ezendam |
| Carl Gebauer | Laura Filion | Sophie Tschirpke |
| Carleen Kluger | Laura Krumm | Stefanie Pritzl |
| Carola Lampe | Lea Wassermann | Steffen Sedlak |
| Caroline Körösy | Leo Schendel | Susanne Hennig |
| Cecile Moucheron | Linda Brützel | Susi Kempter |
| Cees Dekker | Louis de Gaste | Sylvia Kreuzer |
| Cendrine Moskalenko | Lukas Milles | Thomas Zettel |
| Chris Sikeler | Magnus Bauer | Thorben Cordes |
| Christian Gebhardt | Margherita Gallano | Tim Liedl |
| Constantin Schöler | Marjolein de Jager | Tine Brouns |
| Damla Tetiker | Martin Lehmann | Tobi Forster |
| Dave van den Heuvel | Martin Benoit | Tom Nikolaus |
| Diana Pippig | Marvin Freitag | Wolfgang Ott |
| Dihia Benaoudia | Max Urban | Wout Frederickx |
| Elleke van Harten | Melanie Burkhard | Yi-Yun Lin |
| Ellis Durner | Michael Hafner | Zeger Debyser |
| Enrico Carlon | Michi Scheckenbach | and any others |
| Enrico Skoruppa | Mihir Dass | I may have overlooked. |
| Felix Müller | Mijke Heldens | Thank you! |

# CURRICULUM VITAE

## Pauline Kolbeck

## Personal profile

PhD candidate at the Department of Physics at the Universiteit Utrecht (UU), the Netherlands, and at the Department of Physics at Ludwig-Maximilians-Universität (LMU) Munich, Germany. Dedicated to biophysics, having more than four years of experience in biophysical and biochemical laboratory work, performing experiments, analyzing data, theoretical descriptions, and collaborations in the fields of nanotechnology, chemistry, biology, advanced theoretical modeling, and simulations at various levels. Interested in deciphering the statistical and thermodynamic properties of macromolecules using single molecule techniques such as magnetic tweezers and atomic force microscopy, and endavouring to explore potential applications for them.

## Education

**Ludwig-Maximilians-Universität**                               *Munich, Germany*
Master of Science in Physics                                      *Oct 2016 – Feb 2019*
· Graduated with distinction (grade 1.1, top 10%)
· Master thesis with Prof. Fabien Montel at ENS de Lyon, France, and Prof. Jan Lipfert at LMU München:
  *'Dynamics of translocation through thermally switchable nanopores and properties of the fluorescent dye SYBR Gold in interaction with DNA'*

**Ludwig-Maximilians-Universität**                               *Munich, Germany*
Bachelor of Science in Physics                                    *Oct 2013 – Jul 2016*
· Grade 1.8
· Bachelor thesis with Prof. Jan Lipfert: *'DNA branching and its effects on retroviral integration kinetics'*

**Gymnasium Penzberg**                                           *Penzberg, Germany*
Abitur                                                            *Sep 2005 – Jun 2013*
Grade 1.0, top 5%

## Research and professional experience

**Universiteit Utrecht**                                         *Utrecht, the Netherlands*
PhD candidate                                                     *Apr 2022 - present*
· Characterization of the mechanical and photophysical properties of the fluorescent dye SYBR Gold and its interactions with DNA
· Analysis of the binding properties of different Ruthenium dyes
· Single molecule and ensemble measurements of DNA mechanics and DNA-dye interactions
· Theoretical description and experimental data analyzing the topology dependence of small molecules binding to DNA

**Ludwig-Maximilians-Universität**                               *Munich, Germany*
PhD candidate                                                     *Mar 2019 - present*
· Investigation of phase transition in linear polymers in experiments and theory
· Visualization and modeling of retroviral integration at the single molecule level
· Development of a DNA origami-based *in situ* characterization tool for AFM imaging with optimized accuracy (now commercially available via gattaquant.com)
· Design of a novel temperature-controlled nanopore system for single-molecule gating (patented)
· Theoretical description and experimental approaches to study thermodynamic properties of DNA

**École normale supérieure de Lyon**                             *Lyon, France*
Student assistant in the laboratory of Prof. Fabien Montel        *Jan 2018 - Aug 2018*
Setup optimization and independent research

**Ludwig-Maximilians-Universität**                               *Munich, Germany*
Student assistant in the laboratory of Prof. Jan Lipfert         *Oct 2016 - Jul 2017*
Collaboration and independent research

**Patent law firm Beckord & Niedlich**                           *Holzkirchen, Germany*
Intern                                                            *Sep 2016*
Patent writing, research, customer meetings

**Ludwig-Maximilians-Universität**                               *Munich, Germany*
Tutor                                                            *Oct. 2015 – Jul 2016*
Preparation and execution of physics tutorials for undergraduate students in German

## Community service and leadership experience (selection)

**Coordination and realization of the student conference INASCON 2022**  *Munich, Germany*
Ludwig-Maximilians-Universität  *May 2021 – Sep 2022*
Participant management, fundraising, and planning of the scientific program

**Student Representative at the Center for Nano Science (CeNS)**  *Munich, Germany*
Ludwig-Maximilians-Universität  *Mar 2021 – Feb 2022*
• Representation of >300 students in front of the CeNS-Board
• Planning and implementation of research and information events for students

**Supervision of three Bachelor's (10 weeks) and three Master's (12 months) projects**  *Munich, Germany*
Ludwig-Maximilians-Universität  *Mar 2019 – Feb 2022*
Project development, supervision of project realization

**Organization and implementation of the Girls' Day**  *Munich, Germany*
Ludwig-Maximilians-Universität  *Apr 2019 – Apr 2021*
Planning and realization of science workshops for students (age 10-14)

**Language courses within the organization ItinérENS**  *Lyon, France*
École normale supérieure de Lyon  *May – Jul 2018*
Voluntary implementation and planning of language classes in French (A1 level)

**Volunteer work**  *Dunkerque, France*
Refugee Women's Centre  *Feb – Apr 2017*
Legal support, language support, project development

## Skills

| | |
|---|---|
| **Lab work** | Atomic force microscopy (AFM), magnetic tweezers (MT), basic optical setups, spectroscopy, gel electrophoresis and staining, PCR, molecular cloning, DNA origami, setup calibration |
| **Programming** | Data analysis and -visualization in MATLAB (experienced) and Python (basic skills) |
| **Miscellaneous** | LaTeX(Overleaf), Microsoft Office, Adobe Illustrator, Origin, Snapgene, SPIP, Gwyddion |
| **Soft Skills** | Analytical skills, problem-solving, data presentation, time management, innitiative, teamwork |
| **Languages** | German (native), English (C2), French (C1), Russian (B1) |

## Awards and fellowships (selection)

| | | |
|---|---|---|
| 2022-2023 | **"Zia: visble women in science"**, Fellowship of the ZEIT Verlag | *Hamburg, Germany* |
| Jul 2021 | **"CeNS travel award"**, Center for Nanoscience, LMU Munich | *Munich, Germany* |
| Feb 2019 | **"Best talk award"**, Physics Student Research Conference LMU Munich | *Munich, Germany* |
| Dec 2016 | **"LMU Forschungspreis für exzellente Studierende"**, for the Bachelor thesis | *Munich, Germany* |

## Conference participation (selection)

| | | |
|---|---|---|
| May 2023 | **SoftComp Annual Meeting**, Talk | *Ancona, Italy* |
| Sep 2022 | **INASCON – Energy materials for a sustainable future**, Part of organization team | *Munich, Germany* |
| May 2022 | **Cold Spring Harbor meeting on Retroviruses**, Talk | *Long Island, NY, US* |
| Sep 2021 | **CeNS/MCQST Workshop "Bridging the gap - nano meets quantum"**, Poster | *Munich, Germany* |
| Jun 2021 | **"DNA Mechanics: From base pairs to chromosomes" meeting**, Talk (online) | *Leuven, Belgium* |
| Feb 2020 | **Single-molecule biophysics meeting**, Poster | *Les Houches, France* |
| Sep 2019 | **CeNS/MCQST Workshop "Evolving Nano sciences"**, Poster | *Venice, Italy* |
| Jul 2018 | **"Nano fluidics in physics and biology" meeting**, Poster & organizational help | *Lyon, France* |

# PUBLICATIONS

## RESEARCH CONTRIBUTIONS THAT ARE PART OF THIS THESIS

[1]  P. J. Kolbeck, W. Vanderlinden, G. Gemmecker, C. Gebhardt, M. Lehmann, A. Lak, T. Nicolaus, T. Cordes, and J. Lipfert. „Molecular structure, DNA binding mode, photophysical properties and recommendations for use of SYBR Gold." In: *Nucleic Acids Research* 49.9 (2021), pp. 5143–5158. ISSN: 0305-1048. DOI: 10.1093/nar/gkab265.

[2]  W. Vanderlinden, P. J. Kolbeck, W. Frederickx, S. F. Konrad, T. Nicolaus, C. Lampe, A. S. Urban, C. Moucheron, and J. Lipfert. „Ru(TAP)32+ uses multivalent binding to accelerate and constrain photo-adduct formation on DNA." In: *Chem. Commun.* 55 (2019), pp. 8764–8767. DOI: 10.1039/C9CC02838B.

[3]  P. J. Kolbeck, M. Tišma, B. T. Analikwu, W. Vanderlinden, C. Dekker, and J. Lipfert. „Topology-dependent DNA binding." In: *bioRxiv* (2023), p. 2023.06.30.547266. DOI: 10.1101/2023.06.30.547266.

## OTHER RESEARCH CONTRIBUTIONS

[1]  W. Vanderlinden, T. Brouns, P. U. Walker, P. J. Kolbeck, L. F. Milles, W. Ott, P. C. Nickels, Z. Debyser, and J. Lipfert. „The free energy landscape of retroviral integration." In: *Nature Communications* 10.1 (2019), p. 4738. ISSN: 2041-1723. DOI: 10.1038/s41467-019-12649-w.

[2]  W. Vanderlinden, P. J. Kolbeck, F. Kriegel, P. U. Walker, and J. Lipfert. „A benchmark data set for the mechanical properties of double-stranded DNA and RNA under torsional constraint." In: *Data in Brief* 30 (2020), p. 105404. ISSN: 2352-3409. DOI: https://doi.org/10.1016/j.dib.2020.105404.

[3]  W. Vanderlinden, E. Skoruppa, P. J. Kolbeck, E. Carlon, and J. Lipfert. „DNA fluctuations reveal the size and dynamics of topological domains." In: *PNAS Nexus* 1.5 (2022). ISSN: 2752-6542. DOI: 10.1093/pnasnexus/pgac268.

[4] P. J. Kolbeck, M. Dass, I. V. Martynenko, R. J. A. van Dijk-Moes, K. J. H. Brouwer, A. van Blaaderen, W. Vanderlinden, T. Liedl, and J. Lipfert. „DNA Origami Fiducial for Accurate 3D Atomic Force Microscopy Imaging." In: *Nano Letters* 23.4 (2023). PMID: 36745573, pp. 1236–1243. DOI: 10.1021/acs.nanolett.2c04299.

[5] P. J. Kolbeck, D. Benaoudia, L. Chazot-Franguiadakis, G. Delecourt, J. Mathé, S. Li, R. Bonnet, P. Martin, J. Lipfert, A. Salvetti, et al. „Thermally Switchable Nanogate Based on Polymer Phase Transition." In: *Nano Letters* 23.11 (2023), pp. 4862–4869. ISSN: 1530-6984. DOI: 10.1021/acs.nanolett.3c00438.

[6] Y.-Y. Lin, T. Brouns, P. J. Kolbeck, W. Vanderlinden, and J. Lipfert. „High-yield ligation-free assembly of DNA constructs with nucleosome positioning sequence repeats for single-molecule manipulation assays." In: *Journal of Biological Chemistry* 299.7 (2023). ISSN: 0021-9258. DOI: 10.1016/j.jbc.2023.104874.

[7] A. Lak, Y. Wang, P. J. Kolbeck, C. Pauer, M. S. Chowdhury, M. Cassani, F. Ludwig, T. Viereck, F. Selbach, P. Tinnefeld, et al. „Cooperative dynamics of DNA grafted magnetic nanoparticles optimize magnetic biosensing and coupling to DNA origami." In: *bioRxiv* (2023), p. 2023.04.11.536349. DOI: 10.1101/2023.04.11.536349.

[8] P. J. Kolbeck, M. de Jager, M. Gallano, T. Brouns, S. F. Konrad, Z. Debyser, S. De Feyter, L. Fillion, J. Lipfert, and W. Vanderlinden. „HIV integrase compacts viral DNA into biphasic condensates." In preparation.

[9] P. J. Kolbeck, W. Vanderlinden, E. Skoruppa, M. Segers, J. Boltersdorf, M. Gallano, E. Carlon, and J. Lipfert. „A critical point for DNA at low forces." In preparation.

[10] P. J. Kolbeck, W. Vanderlinden, H. Chhabra, A. Aksimentiev, and J. Lipfert. „ Exploring the limits of AFM-based nano-mechanical property mapping using DNA origami." In preparation.

[11] D. Tetiker, E. Skoruppa, P. J. Kolbeck, W. Vanderlinden, and J. Lipfert. „Decimating the DNA persistence length." In preparation.

[12] J. Mathé, S. Li, P. J. Kolbeck, F. Montel, D. Benaoudia, P. Guégan, V. Bennevault, C. Huin, and J.-C. Lacroix. „Filtration of biomolecules using nanoporous membranes functionalized by eletrografted polymers mimicking the nuclear pore." In: *European patent, EP2022057121W* (2022). European patent, EP2022057121W.

Moleculair and celbiologisch onderzoek zijn niet meer denkbaar zonder fluoroforen voor het kleuren van nucleinezuren. Recent werd een breed spectrum aan fluoroforen ontwikkeld, die fluoresceren bij nucleinezuur binding. Deze unieke eigenschappen worden in biologisch onderzoek aangewend voor het kleuren van nucleinezuren na in vitro scheiding in gelen, in enkel molecuul experimenten, of in de (levende) cel door middel van fluorescentie beeldvorming.

Om een optimale beeldvorming te garanderen, is het van groot belang om de parameters van de binding te kennen. In deze thesis rapporteer ik drie onderzoeksprojecten waarin de moleculaire bindingsmechanismen tussen verschillende kleurstoffen en DNA worden onderzocht, en hoe de binding de fotofysica and fotochemie van de kleurstoffen beinvloedt.

In het eerste deel beschrijf ik in detail het commercieel beschikbare fluorofoor SYBR Gold. Ik introduceer de chemische structuurformule van SYBR Gold en bepalen de structurele aspecten van de bindingsplaats in DNA. Door combinatie van enkel molecuul methodes en bulk fluorescentie metingen, kwantificeer ik de thermodynamische parameters van het systeem, en toon ik aan dat binding door intercalatie aan de basis ligt van de de enorme stijging in de kwantumefficientie van fluorescentie.

Het tweede project focust op de interacties tussen het rutheniumcomplex $Ru(TAP)_3^{2+}$ [TAP = 1,3,5,8-tetraazafenantreen] en DNA. Met verschillende enkel-molecuul technieken toon ik aan dat $Ru(TAP)_3^{2+}$ kan binden aan DNA met een sterke bindingsmodus via intercalatie, en een zwakke bindingsmodus die vermoedelijk gebeurd op basis van waterstofbrug vorming. Door combinatie van beide interacties kan $Ru(TAP)_3^{2+}$ twee DNA segmenten met elkaar op niet-covalente manier verbinden. Door middel van bulk fotofysische en fotochemische experimenten demonstreer ik hoe multivalente binding de fotochemie van covalente adductvorming kan versnellen.

In het derde deel van deze thesis onderzoek ik DNA-ligand binding in een topologisch gesloten systeem. Experimenteel onderzoek is gebaseerd op de intercalatoren ethidium bromide, SYBR Gold, Sytox orange, en trimethylpsoraleen. Ik introduceer een theoretisch model dat de experimentele data accuraat beschrijft, en dat toelaat om verschillende densiteiten van DNA supercoiling kwantitatief te bestuderen, zowel *in vitro* als *in vivo*.

# ABSTRACT

Fluorophores for staining nucleic acids have become an essential part of molecular and cell biology research. Recently, a wide range of DNA- and RNA-binding fluorophores has been developed for staining nucleic acids after *in vitro* separation in gels, in single molecule experiments, and in (living) cells for fluorescence imaging. For optimal staining, it is crucial to know the binding parameters. Here, I present three research projects investigating the molecular binding mechanisms between different dyes and DNA, how binding affects the photophysics and photochemistry of the dyes, and in turn the structural and mechanical properties of DNA.

In the first part, I review the fluorescent dye SYBR Gold. I present its chemical structure and determine structural aspects of DNA binding. Using a combination of single molecule methods and bulk fluorescence measurements, I quantify the binding of SYBR Gold to DNA and show that SYBR Gold binds in an intercalative binding mode, which leads to a tremendous increase in fluorescence quantum efficiency.

The second part focuses on the interactions between the ruthenium complex $Ru(TAP)_3^{2+}$ [TAP = 1,3,5,8-tetraazaphenanthrene] and DNA. Using several single-molecule techniques, I show that $Ru(TAP)_3^{2+}$ can bind to DNA with a strong binding mode via intercalation, and a weak binding mode that presumably occurs based on hydrogen bond formation. By combining both interactions, $Ru(TAP)_3^{2+}$ can bind two DNA segments together in a non-covalent manner. Through bulk photophysical and photochemical experiments, I demonstrate how multivalent binding can accelerate the photochemistry of covalent adduct formation.

In the third part of this thesis, I investigate DNA-ligand binding in a topologically closed system. The experimental investigation is based on the intercalators ethidium bromide, SYBR Gold, SYTOX Orange and trimethylpsoralene. In addition, I introduce a theoretical model that accurately describes the experimental data and allows the quantitative study of different DNA supercoiling densities both *in vitro* and *in vivo*.

# CONTENTS

# LIST OF FIGURES

# ABBREVIATIONS

| | |
|---|---|
| 1D | one-dimensional |
| 2D | two-dimensional |
| 3D | three-dimensional |
| AFM | atomic force microscope |
| DNA | deoxyribonucleic acid |
| dsDNA | double-stranded DNA |
| FJC | freely-jointed chain |
| MT | magnetic tweezers |
| NMR | nuclear magnetic resonance |
| PCR | polymerase chain reaction |
| RNA | ribonucleic acid |
| ssDNA | single-stranded DNA |
| WLC | worm-like chain |

# PREFACE

## 1.1 DNA - THE MOLECULE OF LIFE

Throughout the kingdoms of life the genetic code, which contains all the information necessary for metabolism, development, growth and reproduction, is stored in the form of deoxyribonucleic acid (DNA) [1]. This makes DNA the central biomolecule of life.

### 1.1.1 *Early history of DNA*

The history of DNA research can be traced back to the 1800s when scientists first identified the chemical components of nucleic acids. In that time, the first important scientific discoveries about cells and heredity took place. Although farmers had previously explored concepts of genetics - without knowing it - through selective breeding of plants and animals, they had done so neither systematically nor in writing [2]. In the early 1800s, the French zoologist Jean-Baptiste de Lamarck methodically explored heredity and found that life evolves and adapts based on environmental conditions [2, 3]. However, it was not until the mid-1800s that the English botanist Charles Darwin understood the significance of these discoveries and took up Lamarck's ideas. Darwin published his groundbreaking discoveries in 1859 in his book *On the Origin of Species* [2, 4, 5], that he himself begins extremely modestly:

> When on board H.M.S. Beagle, as naturalist, I was much struck with certain facts in the distribution of the inhabitants of South America, and in the geological relations of the present to the past inhabitants of that continent. These facts seemed to me to throw some light on the origin of species (that mystery of mysteries, as it has been called by one of our greatest philosophers. On my return home, it occurred

>to me, in 1837, that something might perhaps be made out
>on this question by patiently accumulating and reflecting on
>all sorts of facts which could possibly have any bearing on
>it. After five years' work I allowed myself to speculate on the
>subject, and drew up some short notes [4].

Around the same time, the Augustinian monk Gregor Mendel discovered in his research on pea plants that some traits are inherited in definite and predictable patterns. In addition, he could show that certain traits are dominant whereas others are recessive. Here, dominant refers to the visible trait, and recessive refers to the one, which is not visible morphologically since a dominant trait effectively overrules a recessive trait. His findings contributed significantly to the understanding of inheritance patterns and lay the groundwork for understanding how our traits can be influenced by genes passed down from previous generations [2].

Together, these discoveries have had an immense impact on our current views of heredity, evolution, life, and ultimately DNA. And moreover, they have paved the way for further discoveries in the field of DNA. One of the most important early figures in the study of DNA was Friedrich Miescher, a Swiss doctor and biochemist. In 1869, Miescher conducted experiments on the chemical composition of leukocytes in the laboratory of Felix Hoppe-Seyler at the University of Tübingen. In the process, Miescher noticed a precipitate of an unknown substance that would later turn out to be DNA. Since he had isolated it from the cell nuclei, he gave the substance the name *nuclein*, a name that still survives in the present-day name deoxyribonucleic acid. In later work, Miescher could show that *nuclein* is a characteristic component of all cell nuclei [6–8]. Subsequently, the German physiologist Albrecht Kossel, another scientist in Hoppe-Seyler's laboratory, studied the new substance *nuclein* more closely and was able to identify in 1891 that it consisted of four bases and sugar molecules [9, 10]. A further important step was taken by the German botanist Eduard Zacharias, who showed that *nuclein* is an integral part of chromosomes. With this discovery, he could show that the histological concept of chromatin and the chemical substance *nuclein* are intertwined. However, the scientific majority opinion remained until far into the 20th century that not the *nuclein*, but the more complex

proteins (consisting of 20 different amino acids) must be the carriers of the genetic information [7, 8].

### 1.1.2  *Genes, chromosomes, and transposons*

In the early 20th century, the term *gene* was coined for the first time by the Danish botanist Wilhelm Johannsen to describe an unknown cellular factor, which (partially) determines the characteristics of an organism. Johannsen also introduced the terminology still in use today of *genotype* for traits originating from genes and *phenotype* for visible traits [11, 12]. Shortly thereafter, the American biologist Thomas Hunt Morgan discovered that genes are discrete units that make up chromosomes and explained the role that the chromosome plays in heredity. For this enormous progress in the field, he received the Nobel Prize in Physiology or Medicine in 1933 [13–15]. A few years later, in the end of the first half of the 20th century, the American geneticist Barbara McClintock used maize plants to investigate the structure of chromosomes and how genes can migrate to different locations in the genome. She discovered spontaneously occurring breaks of chromosome 9 at a specific location (dissociator) in the maize plant and that the dissociator can change its position on the chromosome. This was the first time someone had discovered a transposon - or a *jumping gene* as McClintock called it - one of the most important causes of spontaneous mutations. Transposons can cause unstable mutations by jumping to sites on the chromosome that contain, for example, a gene for the production of a pigment, rendering the affected pigment gene non-functional. The result is speckled maize kernels. "For her discovery of mobile genetic elements" she received the Nobel Prize in Physiology or Medicine in 1983 [16–19].

### 1.1.3  *The discovery of the DNA double-helix and the beginning of molecular biology*

In 1944, in the famous so-called Avery-MacLeod-McCarty experiment, the American geneticists Oswald Avery, Colin MacLeod, and Maclyn McCarty were able to show that DNA is the substance that causes

bacterial transformation [20]. Shortly thereafter, in 1952, the American chemist Alfred Hershey and the American geneticist Martha Chase could show in experiments with viruses that the genetic information is stored in the DNA [21]. The experiment known as the Hershey-Chase experiment provided independent confirmation of the result already obtained in 1944 in the Avery-MacLeod-McCarty experiment. Together these discoveries definitively disproved the assumption that proteins carry the genetic information, and proved that DNA is indeed the carrier of genetic information [7].

One year later, in 1953, a major breakthrough in DNA research took place with the discovery of the DNA double-helix. Based on the x-ray diffraction data of the British chemists Rosalind Franklin and Raymond Gosling [22, 23], the American biologist James Watson and the English physicist (and later also molecular biologist) Francis Crick published the complementary double-helical three-dimensional (3D) structure for nucleic acids in 1953 [24, 25]. They could show that for DNA, form is function: the molecule can make exact copies of itself as well as carry genetic instructions. This laid the foundation for molecular genetics and dominates contemporary thinking about these molecules, as Francis Crick writes in his book "From Gene to Protein: Information Transfer in Normal and Abnormal Cells" in 1979:

> The double helix is indeed a remarkable molecule. Modern man is perhaps 50,000 years old, civilization has existed for scarcely 10,000 years and the United States for only just over 200 years; but DNA and RNA have been around for at least several billion years. All that time the double helix has been there, and active, and yet we are the first creatures on Earth to become aware of its existence [26].

The discovery of the double-helical structure of DNA revolutionized the field of molecular biology and opened up new areas of research, like DNA analysis and sequencing. Gaining insight into biological processes at the molecular level has opened new doors in all life sciences, changing, for example, how we research and understand diseases, and ultimately how we explore treatments and cures for them.

In the following years, researchers developed new ways to study the behavior of DNA, including how it is replicated, how it encodes genetic information, and how it interacts with proteins. One important discovery of this time was the role of DNA in controlling gene expression. It was found that specific sequences of DNA could code for different proteins, and that these proteins could control specific cellular processes. The essential idea is that DNA contains all necessary genetic information, which can then be translated to make the proteins needed by the cell. This is a two-step process: In the first step, the information in the DNA is transferred to an ribonucleic acid (RNA) molecule, also called messenger RNA (mRNA), by a process called transcription. During transcription, the DNA of a gene serves as a template for complementary base pairing, and the enzyme RNA polymerase II catalyzes the formation of a pre-mRNA molecule, which is then processed into a mature mRNA. The resulting mRNA is a single-stranded copy of the gene that is subsequently translated into a protein. Because of its significance, this process is also called the central dogma of molecular biology. For this breakthrough discovery, the American biochemists Robert W. Holley, Har Gobind Khorana, and Marshall W. Nirenberg jointly received the Nobel Prize in Physiology or Medicine in 1968 "for their interpretation of the genetic code and its function in protein synthesis" [27–30]. The role of nucleic acids in the central dogma will be discussed in more detail in Section 2.1.

### 1.1.4  *The DNA sequencing revolution: a selection of highlights*

A wide range of sciences, including archaeology, anthropology, genetics, biotechnology, molecular biology and forensics, rely on determining the order of nucleic acid residues in biological samples, also called DNA sequencing. Since the 1970s, a quiet but remarkable revolution has been underway in many disciplines, and DNA sequencing techniques are fostering new discoveries that are rewriting the conceptual underpinnings of many fields [31–33]. DNA sequencing was pioneered by the British biochemist Frederick Sanger who first described in 1975 "a rapid method for determining sequences in DNA by primed synthesis with DNA polymerase" [34]. This sequencing technique is based on a DNA polymerase (an enzyme that catalyzes the synthesis of DNA from nucleotides, the

basic building blocks of DNA) and radiolabelled (labelled by replacing specific atoms by their radioactive isotopes in order to track them) nucleotides. Using this method, Sanger was the first to sequence an entire DNA-based genome, the 5,386 nucleotides of the single-stranded bacteriophage ΦX174. However, the technique was still very labour-intensive and time-consuming. In 1977, just two years later, Sanger and his colleagues introduced a more sophisticated "dideoxy chain termination method" for sequencing DNA molecules, also known as the "Sanger method". In this method, four different dideoxynucleotide triphosphates are used in combination with a polymerase as 3'-end chain terminators to produce different DNA fragments. These DNA fragments could subsequently be

fractionated by electrophoresis (to differentiate different fragment sizes) and visualised by autoradiography (a photographic method used to detect radioactive materials). This was a major breakthrough because it made it possible to sequence long stretches of DNA quickly and accurately [35]. "For his contributions concerning the determination of base sequences in nucleic acids", Sanger received the Nobel Prize[1] in Chemistry only three years later, in 1980 [37].

In 1990, another important development in the field of DNA sequencing took place with the start of the so-called 'Human Genome Project' [38]. This extensive international and collaborative project aimed to map the entire human genome, i. e., the complete set of DNA instructions for building and maintaining a human being. While the human genome project did not produce a perfectly complete genome sequence, it accounted for 92% of the human genome and less than 400 gaps when terminated in 2003. In 2022, the Telomere-to-Telomere (T2T) Consortium announced that it had closed the remaining gaps and produced the first truly complete human genome sequence. The human genome project is seen as a major scientific success, as it provided fundamental information about the human blueprint that has since accelerated the study of human biology and improved medical practice [39]. As part of the Human Genome Project, Sanger sequencing (in a mass-produced form) was used to sequence relatively small fragments of human DNA, which were then

---

1 Frederick Sanger is one of the few people to have won two Nobel Prizes. Prior to his Nobel Prize for DNA sequencing in 1980, he had already received the Nobel Prize in Chemistry in 1958 "for his work on the structure of proteins, especially that of insulin" [36].

used to assemble larger fragments of DNA and, ultimately, whole chromosomes. However, a number of improvements in the processes and reagents used in the sequencing reaction have made sequencing faster and more accurate than it was in the 1970s. An important aspect has also been the development of a technique called polymerase chain reaction (PCR). This biochemical method allows the rapid and inexpensive amplification of DNA *in vitro*. It was developed in 1983 by the American biochemist Kary Mullis and is now a ubiquitous biomolecular technique. PCR is based on thermal cycling and a DNA polymerase that can synthesise a new DNA strand complementary to the template strand. This makes it possible to amplify a single copy (or a few) of a DNA fragment over several orders of magnitude [40–42].

*For the development of PCR, Kary Mullis received the Nobel Prize in Chemistry in 1993.*

Over the years, innovations in sequencing protocols, molecular biology, and automation (these new techniques were then called "second- and third-generation" sequencing methods) have increased the technological capabilities of sequencing while reducing its cost, allowing DNA hundreds of base pairs in length to be read in massively parallel fashion. These increases in throughput and dramatic reductions in cost are make sequencing today a ubiquitous tool in DNA research and opens the door to personalised genome-based medicine [33]. At the same time, developments in DNA sequencing also raise new and very important issues such as bioethics, public health, and safety. In particular, the question of DNA detection is one that is closely related to the issue of DNA sequencing. While much of the early work (e. g., the Hershey-Chase experiment (Section 1.1.3), which showed that DNA is the genetic material, and also Sanger sequencing) used radioactivity (especially the radioactive isotope Phosphorus-32 ($^{32}$P)), more recently there has been a shift towards detection by fluorophores, and especially towards intercalating dyes (Figure 1). Fluorescent labelling has several advantages over radiolabelling, such as reducing the safety hazards associated with radioactivity (and the consequent problems of waste handling and disposal) and providing a labelled molecule that does not decay, while still ensuring the sensitivity required for many procedures. Additionally, fluorescent dyes can be detected in real time with high resolution and even several different dyes can be monitored in one experiment [43, 44].
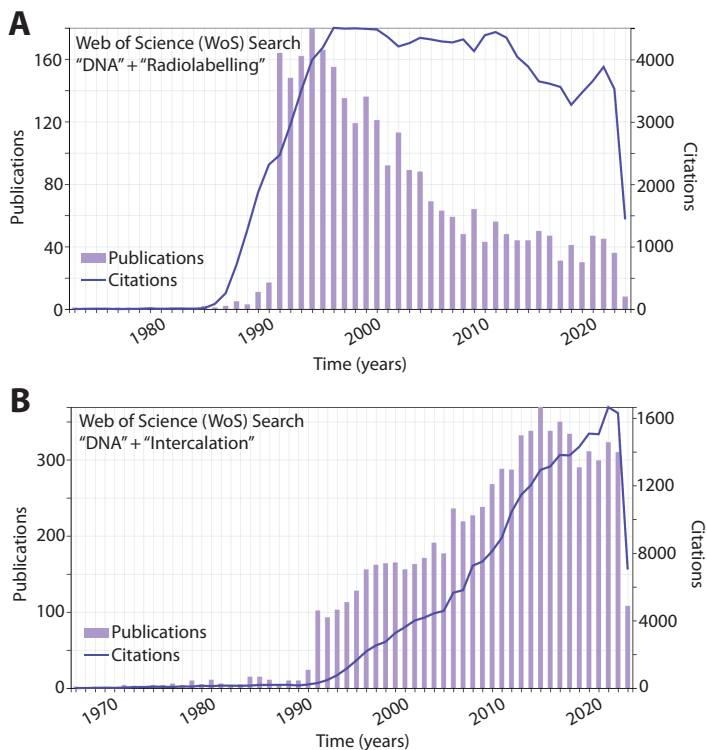
Figure 1: Relevance of DNA radiolabelling versus DNA intercalation for visual-
ization illustrated by a Web of Science (WoS) serach for publications
and citations including A) "DNA" and "Radiolabelling" and B) "DNA"
and "Intercalation". Courtesy: Web of Science.

As technology continues to improve, more exciting developments in
the field of DNA research are still to come. Thanks to advances in
genome sequencing technology, it is now possible to compare DNA from
people alive today with DNA from ancient skeletons, giving us a unique
snapshot of life many thousands of years ago. Furthermore, entirely new
sequences of DNA can be created, which opens the field to developing
customized biological systems that can perform specific tasks, such as
energy production or environmental cleanup.

## 1.2   SCIENTIFIC SCOPE OF THIS THESIS

In this thesis, I will study the visualization, quantification, and manipulation of DNA with small-molecule intercalators. I will shed light on the interaction between small DNA-binding molecules, in particular, fluorescent dyes for staining DNA. To understand the interplay between DNA and small DNA-binding molecules at the molecular level, precise and accurate measurements are required. In this work, I establish new experimental methods and theoretical concepts that significantly improve state-of-the-art approaches for in-depth studies of small molecule-DNA interactions for applications in research and DNA analysis methods.

This thesis is structured in the following way: In Chapter 2, I will give an overview over the structural, chemical, and mechanical properties of the DNA molecule, global conformations of DNA including DNA models and DNA topology, as well as the theoretical basics of DNA-ligand interactions. In Chapter 3, I will present DNA analysis methods and experimental techniques using intercalating dyes in greater detail - for single-molecule measurements as well as for ensemble measurements. In Chapter 4, I will introduce a series of experiments that quantify the characteristics of the widely used yet poorly characterized fluorescent DNA stain SYBR Gold. Using single-molecule force-extension and rotation experiments, I show how SYBR Gold changes the mechanical properties of DNA. Complementary to this, I apply spectroscopic methods to characterize SYBR Gold DNA interaction and to give guidelines for optimal use of this frequently employed fluorescent dye. The work presented in Chapter 5 introduces another type of small DNA-binding molecules, ruthenium complexes. By applying different single-molecule approaches, I will demonstrate DNA binding mode heterogeneity and evaluate how multivalent binding governs the photochemistry of ruthenium complexes. In the third and last result chapter, Chapter 6, I will study the interplay of DNA topology on the binding of intercalating molecules to DNA. The focus lies here on the well-known DNA stains ethidium bromide, SYBR Gold, trimethylpsoralen, and SYTOX Orange, which are known to intercalate between adjacent DNA base pairs. Lastly, in Chapter 7, I will summarize the findings of this thesis and give a short outlook to future perspectives and ideas for follow-up projects to my work.

# BACKGROUND

## 2.1 PROPERTIES OF DNA

The discovery of the double-helical structure of DNA in 1953 was a major breakthrough for molecular biology and other related fields. Nevertheless, in the middle of the 20th century there were still scientists who doubted that the DNA was really the genetic material because its chemistry seemed just too simple. DNA is merely two long polymer chains consisting
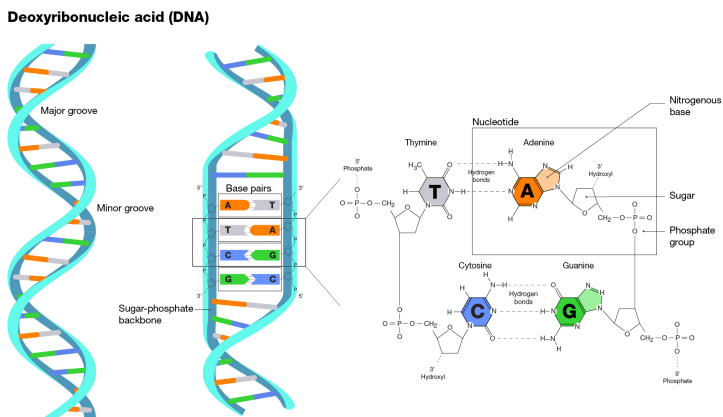
Figure 2: The chemical structure of nucleotides and DNA. The DNA double-helix is built up from two antiparallel polynucleotide chains, intertwined with each other like a spiral staircase. One nucleotide consists of a sugar group, a phosphate group, and one of the for nitrogenous bases, also called nucleobases. The sugar and phosphate groups (in alternating order) form the DNA backbone. The nucleobases are located on the inside of the helix and pair via so-called Watson-Crick base pairing: A (adenine) pairs only with T (thymine), and G (guanine) pairs only with C (cytosine). The nucleotides then join together to form the DNA double helix, with hydrogen bonds between two complementary bases. Taken from Ref. [46]. Courtesy: National Human Genome Research Institute.

of only four types of chemically similar nucleotide subunits, which are linked covalently into a polynucleotide chain (Figure 2). The two chains, also called DNA strands, are held together by hydrogen bonds between the base segments of the nucleotides. Each nucleotide consists of a pentose, a sugar with five carbon atoms, to which one or more phosphate groups and a nitrogenous base (nucleobase) are connected.

In the case of DNA, the nucleotide sugar is a deoxyribose, which is attached to a single phosphate group (therefore also the name deoxyribonucleic acid). There are four possible nucleotide bases (Figure 2A), adenine (A), thymine (T), cytosine (C), and guanine (G). The nucleotides are covalently linked by their sugars and phosphates to form the so-called DNA backbone consisting of alternating sugar and phosphate groups (Figure 2C).

The way that the nucleotide subunits are strung together gives a DNA strand a chemical polarity. The phosphate group of one nucleotide binds to the deoxyribose ring of the adjacent via an asymmetric phosphodiester bond, which gives the chain directionality. The terminal of one DNA strand ends with a hydroxyl group at the 3' carbon (3' end), whereas the other ends with a phosphate group at the 5' carbon (5' end). For example, enzymes are sensitive to this directionality, their default direction is in most cases from the 5'-end to the 3'-end [47].

DNA can occur in single-stranded form (single-stranded DNA (ssDNA)), i. e.only one DNA strand, or in double-stranded form (double-stranded DNA (dsDNA)), so two complementary DNA strands. Complementarity of the bases is a unique property of dsDNA, which is also known as Watson-Crick base pairing. One of the four possible nucleic bases binds exclusively to one of the other three: A only to T and C only to G. So, two ssDNA molecules with an inversely complementary sequence can join together such that the antiparallel strands together form a double helix (dsDNA). The bases hereby form stable hydrogen bonds with their respective partners, two between A and T and three between G and C. This structural complementarity gives DNA determination because it allows to form an exact copy of one nucleotide sequence. The cell makes use of this for example during replication, but also biomolecular techniques like PCR or DNA origami rely on this complementarity of

DNA bases. Other nucleic acids exhibit similar but slightly different forms of base pairing. In addition, there are also other forms of base pairing such as Hoogsteen base pairing, for example, which is also physiological and can lead to locally and globally different DNA structures [48, 49].

The chemical and structural properties of the two DNA strands lead to the three-dimensional structure of the DNA double helix. Both polynucleotide chains are held together by hydrogen bonds between the bases of the different strands. Therefore, all the bases are on the inside of the double helix whereas the sugar-phosphate backbones are on the outside (Figure 2B). There is always a larger two-ring base, called a purine, paired with a one-ring base, a pyrimidine (Figure 2A). This base pairing allows the base pairs to be packed in the most energetically favourable arrangement inside the double helix. Thus, each base pair has a similar width such that the sugar-phosphate backbones are equally spaced along the DNA molecule. To optimise the efficiency of base pair packing, the two backbones twist around each other to form a double helix, completing one full turn every 10.5 to 10.75 base pairs [47]. In addition, the aromatic rings of the nucleotides align, meaning that they are arranged almost perpendicular to the helical axis. Thus, $\pi$ orbitals of the aromatic ring of one base overlap with the $\pi$ orbitals of the aromatic ring of the next base. This so-called stacking is the main contribution to the stability of the DNA double helix- even more than base pairing [50].

The form that the DNA double helix takes under physiological conditions, in aqueous, neutral to basic solutions is referred to as the B-form of dsDNA or in short B-DNA. It is a right-handed helix with a helix period of $\sim$ 10.5 - 10.75 base pairs per turn (which corresponds to $\sim$ 3.5 nm). Its outer diameter is about 2 nm and the vertical distance between two adjacent base pairs is 0.34 nm [51–53]. B-DNA has one larger groove (called major groove) and a smaller one (called the minor groove) (Figure 2). The two different sized grooves form due to the angle, at which the nucleotides of the base pairs connect in the plane perpendicular to the helix axis. There are other forms of dsDNA but these are almost solely adopted under extreme conditions of salt or pH and/or under very high forces and/or torques [54].

The four-letter genetic code of DNA is divided into sections (genes) that give it biological significance as a carrier of information about the sequence of cellular amino acids in proteins. However, in order to carry out this function as an information carrier, DNA must be able to do more than just replicate itself. It must also be able to express this information by allowing the information to guide the synthesis of proteins in the cell. Proteins are essential for the proper functioning of the cell, performing important tasks such as cellular regulation, signal reception and transduction, cell shape and structure, internal organization, product manufacturing, waste disposal, and routine maintenance. This
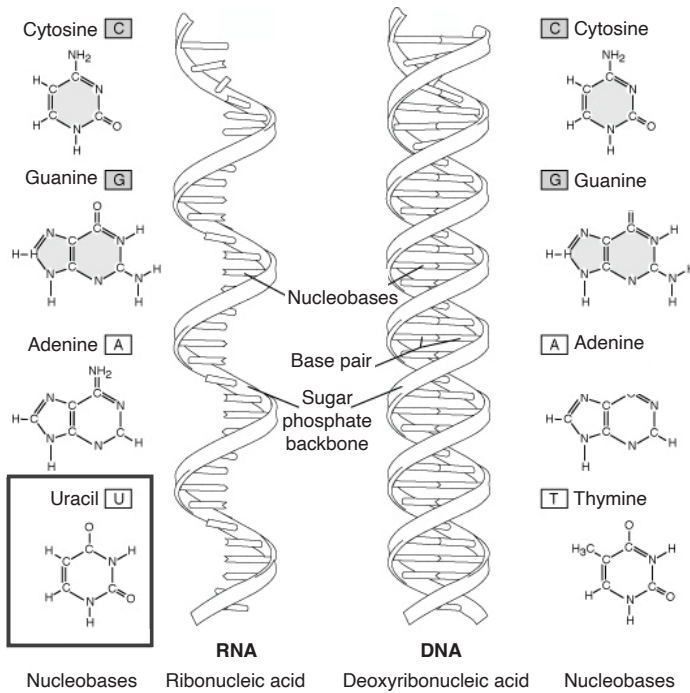


Figure 3: Structural differences between the nucleic acids DNA and RNA. DNA is double-stranded, whereas RNA is single-stranded. The nucleobase thymine (T) in DNA is replaced with uracil (U) in RNA. It should be noted that the single-stranded helix is shown as an illustration here; in solution, single-stranded RNA will typically adopt complex secondary structures. Figure taken from Ref. [55]. Courtesy: National Human Genome Research Institute.

expression occurs through a mechanism common to all living organisms and leads primarily to the production of two other important classes of biological polymers: RNA and proteins. During this process, first a template polymerisation called transcription takes place. In this step, segments of the DNA sequence are used as templates for the synthesis of shorter molecules of the closely related polymer RNA. Later, in the more elaborate process of translation, several of these RNA molecules lead the synthesis of polymers of a completely different chemical class - proteins.

RNA is the second major class of nucleic acids after DNA (Figure 3). In contrast to DNA, the basic structure of RNA consists of ribose instead of deoxyribose. In addition, RNA has the base uracil (U) instead of the base thyme (T), but the two bases differ only minimally and both pair with adenine (A). A third, essential difference between DNA and RNA is the structural form: DNA can occur in single- and double-stranded form, whereas RNA is in general single-stranded. Nevertheless, it should be noted at this point that RNA can have local double-stranded regions via base pairing interaction types other than Watson-Crick base pairing, such as wobble pairs. These secondary structures of RNA based on self-folding occur commonly and are extremely important for its functionality. In the course of transcription, the RNA monomers are strung together and selected for polymerisation on a DNA template strand, similar to how DNA monomers are selected during replication. The result is a polymer molecule with a nucleotide sequence that accurately reproduces part of the cellular genetic information, even though it is written in a slightly different alphabet - it consists of RNA monomers instead of DNA monomers. The information contained in this so-called messenger RNA (mRNA) is then used to synthesise proteins through a process called translation. So, the genome contains all information required for the production of cell proteins, yet it does not control protein synthesis itself, but uses RNA as an intermediate. Thus, in order to produce a specific protein, the nucleotide sequence of the corresponding segment within the cellular DNA is first copied into RNA. This in turn is used as a template for protein synthesis.

Francis Crick, one of the discoverers of the double helix form of DNA, referred to the relationship between an DNA sequence and a protein sequence as the "two great polymer languages" of cells. The finding that the DNA sequence of the cell directly determines the amino acid sequence of the proteins of the same cell was an tremendous success and important step in the development of the field of molecular biology [56]. This relationship forms the basis of the so-called central dogma of molecular biology (already briefly mentioned in Section 1.1.3), first formulated by Crick in 1958:

> The Central Dogma. This states that once "information" has passed into protein it cannot get out again. In more detail, the transfer of information from nucleic acid to nucleic acid, or from nucleic acid to protein may be possible, but transfer from protein to protein, or from protein to nucleic acid is impossible. Information means here the precise determination of sequence, either of bases in the nucleic acid or of amino acid residues in the protein [57].

So, the physiological flow of genetic information in cells hence runs from DNA to RNA to protein. Despite the universality of the central dogma of molecular biology, there are significant differences among organisms in the way information flows from DNA to protein. Moreover, in the meantime it has been found out that RNA possesses many roles beyond the central dogma, for example it can also store genetic information (e. g., in RNA viruses), exhibit enzymatic properties (called ribozymes, the most prominent example being the ribosome, the macromolecular cellular complex where proteins are produced, and whose central catalytic region is made out of ribosomal RNA), and silence specific genes (RNA interference) [47].

### 2.1.1  *Physical and chemical properties of DNA*

The four-letter alphabet in which DNA is written represents a crucial aspect of DNA for the storage of genetic information. Nevertheless, its physical properties are also of great importance: for example, the genome must be physically stored and accessible for genomic processes.

### 2.1.1.1  *Mechanical properties of DNA*

The biological functions of DNA depend on the elastic properties of the molecule. These special attributes include high thermal stability, high negative charge density, and strong resistance to bending as well as twisting and they can be altered by local and global interactions. Nonetheless, it was not until the end of the 20th century that more attention was paid to these properties of DNA. During the early 1990s, new techniques were developed that facilitated the first quantitative studies of individual DNA molecules to gain insight into their mechanical properties [58–62].

In 1992, Steven Smith performed measurements on a single DNA molecule in the laboratory of the Peruvian-American biophysicist Carlos Bustamante at the University of Oregon to investigate the relationship between stretching forces and lengthening of dsDNA (Figure 4A). To perform
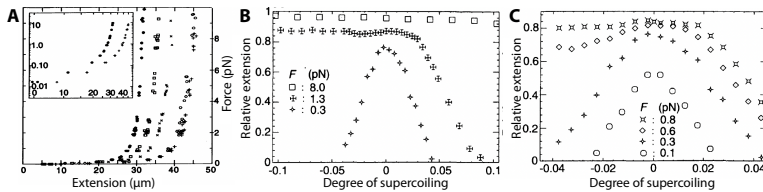


Figure 4: A) Force-extension curves of dsDNA in 5 mM $Na_2HPO_4$ in the presence of various concentrations of the DNA stain ethidium bromide (increasing concentration from 0.03 µg / mL to 2 µg / mL from left to right). The intrinsic elastic properties of DNA are not changed by the dye-DNA interaction, the molecules are simply lengthened, apparent by the shift in the asymptotic value of the contour length of the DNA. Figure taken from Ref. [58]. B) Relative DNA extension versus degree of supercoiling a at various forces: $F = 8$ pN, 1.3 pN, and 0.3 pN. C) Same as in panel B for $F = 0.8$ PN, 0.6 pN, 0.3 pN, and 0.1 pN. At low forces, the curves are symmetric, indicating that there is no difference between over- or underwinding of the DNA. In contrast, at higher forces, a transition to an extended state takes place - first at negative degree of supercoiling ($> 0.45$ pN), then at positive degree of supercoiling ($> 3$ pN). Figure taken from Ref. [61].

these experiments, the Bustamante lab chemically attached single lambda phage DNA molecules ($\lambda$-DNA) by one end to a glass surface and by the other end to a paramagnetic bead. This setup then allows to exert forces and torques on the DNA molecule [58]. Two years later, Bustamante

demonstrated that the experimental data are in line with theoretical predictions that were made in the context of the elastic rod model, indicating that DNA can be approximated as a monodisperse polymer [59].

Another two years later, in 1996, Smith *et al.* carried out further single-molecule experiments designed to investigate the elastic response of single dsDNA and ssDNA molecules to exerted forces of tens of pN, so much higher than in the previous experiments. As a result, they discovered the overstretching transition in DNA at high forces. This phenomenon describes a transition between completely stretched DNA to an overstretched DNA conformation upon a further increase in applied force. Interestingly, in this overstretched DNA conformation, the average distance between adjacent base pairs was about 1.6 times greater than in standard B-DNA [60].

Also in 1996, Terence Strick from the group of the French biophysicist Vincent Croquette at the ENS in Paris conducted the first experiments to investigate the elastic behaviour of single under- and overwound DNA molecules (Figure 4B,C). With these studies, they were able to decipher the molecular mechanisms behind the elastic response of a single DNA molecule over a broad range of experimental conditions. For example, it was possible to measure one of the essential parameters for the bending stiffness of DNA, namely the persistence length. This parameter is defined as the length over which the directional correlation of the segments in the polymer chain has decreased to $1/e$ ($\sim 37\%$). Using the single-molecule measurements of the 1990s, this length could be determined to be almost exactly 50 nm (in a 15 µM NaCl solution, i. e.at low salt concentration).

### 2.1.1.2  *Optical properties of DNA*

Over the years, spectrophotometric measurements have been developed to determine the purity and quantity of nucleic acid samples. The four nucleobases (A, T, C and G) exhibit absorption maxima at a wavelength of $\lambda = 260$ nm. The total absorbance of a DNA molecule can then be calculated as the sum of the absorbances of the individual nucleotides, plus the contribution of the interactions of the nucleotides.

To distinguish unbound nucleotides from ssDNA or dsDNA by spectrophotometry, the effect of hypochromism can be exploited: The absorbance of dsDNA decreases by up to 25% compared to the absorbance of ssDNA and by up to 40% compared to the absorbance of the single nucleotides. Thus, a single DNA strand absorbs less than the sum of its nucleotides and one dsDNA strand absorbs less than the two ssDNA strands.

The optical properties of DNA can be exploited to quantify DNA amounts and determine their purity, which is an important pre-analytical step for further investigations. The two most commonly used methods are UV-Vis and fluorescence spectroscopy. In UV-vis spectrophotometry, the absorbance of the sample is measured. The advantages of this technique are that it is quick and easy to perform. Fluorescence techniques for the quantification of DNA, on the other hand, offer the advantage of higher accuracy and greater sensitivity at low concentrations. However, since DNA molecules emit almost no absorbed radiation, these techniques require further steps like additional treatment of the samples with fluorescent stains [63–65].

*Spectrophotometric techniques will be discussed at length in Section 3.2.2.*

### 2.1.1.3  *Polyelectrolyte properties of DNA*

Each nucleotide of a DNA molecule carries a net negative charge as a result of the presence of the negatively charged phosphate group. Due to this high linear charge density, the DNA molecule acts as a strong polyelectrolyte (charged polymer). This leads to a loosely associated *cloud* of positively charged ions from the solution surrounding the nucleic acid polyelectrolyte, which is referred to as an ion atmosphere. Because of electrostatic interactions between the negatively charged DNA molecule and the ion atmosphere around it, a number of important properties of DNA are highly dependent on the salt concentration of the surrounding medium. Thus, ions play an important role, for example, in the structure, folding, and functioning of the DNA as well as in the interactions of DNA with RNA or proteins. Unfortunately, the complex mobile, fluctuating and transient nature of the ion atmosphere makes it very difficult to visualise and to experimentally decompose. Therefore, theoretical models

*A detailed description of DNA-ion interactions is given in Ref. [66], which is also the main reference for this section.*

are often relied upon to describe the ionic atmosphere of nucleic acids [66].

The polyelectrolyte properties of DNA have important consequences for the behavior of DNA in biological systems. For example, the charge density of DNA can affect its interactions with proteins and other molecules in the cell, as well as its ability to condense and form higher-order structures such as chromosomes. Also, the polyelectrolyte properties can be exploited in laboratory methods, the key application being gel electrophoresis, a technique used to separate and analyze polyectrolytes like DNA (fragments) or proteins based on their size and charge. Overall, the polyelectrolyte behavior of DNA is a fundamental aspect of its biological function and has important implications for a wide range of applications in biotechnology and medicine.

The American physicist Gerald Manning was a pioneer in studying the polyelectrolyte properties of DNA in the 1970s. He developed theoretical models to describe the interaction of DNA with counterions (ions with an opposite charge to DNA, so positively charged), and demonstrated that the behavior of DNA in solution could be strongly affected by changes in the ionic strength of the solution. His so-called counterion condensation theory describes the behavior of charged macromolecules, such as DNA, in a solution in which ions are present. According to this theory, the counterions are attracted to the surface of the DNA backbone, where they form a condensed layer, shielding the charges on the DNA from other ions in the solution. This shielding effect reduces the electrostatic repulsion of the DNA strands and allows the DNA to stay close together, leading to more bent conformations. The degree of counterion condensation depends on the concentration and charge density of the macromolecule and the ions in solution [66–70].

Already in the beginning of the 20th century, the French physicist Louis Gouy (1910) and the British physicist David Chapman (1913) laid the theoretical basis for our current understanding of polyelectrolyte behavior. By equating the chemical potential and the force acting on small adjacent volumes in an ionic solution between two plates at a different voltage, they developed the Poisson-Boltzmann equation, which allows to calculate the electrostatic potential around charged macromolecules in solution [71,

72]. The Poisson-Boltzmann theory is named after the French physicist and mathematician Siméon Poisson and the Austrian physicist Ludwig Boltzmann. It describes the interaction of mobile ions with fixed charges in solution [66, 73].

The solvent surrounding the charged molecule is treated as a continuous medium with a dielectric constant $\epsilon(\vec{r})$. In this scenario, mobile ions of charge $z_i$ interact with a fixed charge density $\rho^{fix}$ adding up to a mean potential of all ions, which is determined by their Boltzmann factor. The index $i$ enumerates all ion types with their respective charge present in the solution. Using a mean-field approximation, the resulting differential equation for the electrostatic potential $\Phi(\vec{r})$, also called Poisson-Boltzmann equation, can then be written as:

$$\vec{\nabla}(\epsilon(\vec{r})\vec{\nabla}\Phi(\vec{r})) = -4\pi\rho^{fix}(\vec{r}) - \lambda(\vec{r}) \cdot 4\pi \sum_i c_i^\infty z_i e \cdot \exp\left(\frac{-z_i e\Phi(\vec{r})}{k_B T}\right)$$

(1)

with $e$ the elementary charge, $k_B$ the Boltzmann constant, and $T$ the absolute temperature. The term $\lambda(\vec{r})$ describes the accessibility, so essentially the areas in space accessible ($\lambda$=1) or inaccessible ($\lambda = 0$; i.e.inside the polyelectrolyte) to ions. The term $c_i^\infty$ is the bulk concentration of the ion species $i$, i.e., the concentration far away from the charged macromolecule [66, 73].

If one assumes that the ionic strength of the solution is sufficiently low such that the ions behave as if they were completely dissociated from each other, the Poisson-Boltzmann equation (Equation 1) can be simplified resulting in the Debye-Hückel approximation [74]. This theory was developed in 1923 by the Dutch physicist and theoretical chemist Peter Debye[1] together with his habilitand and assistant, the German physicist and chemist Erich Hückel. It makes use of the concept of screening of the electrostatic interactions between two charges in the presence of all other ions in the solution. Thus, all ions can be treated as a continuum [76].

---

[1] Peter Debye received his doctorate from the LMU Munich, where he worked from 1906 to 1910. In 1912, he became a professor at the University of Utrecht. In 1936, he received the Nobel Prize in Chemistry "for his contributions to the study of molecular structure" [75].

As a simplification of the Poisson-Boltzmann equation for dilute electrolyte solutions, the Debye-Hückel approximation Debye and Hückel is mostly based on simpler expressions for the following two quantities:

$$I = \frac{1}{2} \sum_i c_i z_i^2 \tag{2}$$

and

$$\kappa = \sqrt{\frac{2 \cdot N_A \cdot e^2 \cdot I}{\epsilon \cdot k_B T}} \tag{3}$$

where $I$ is the ionic strength, $c_i$ the concentration of different ion species in solution, $\epsilon = \epsilon_0 \epsilon_r$ the permittivity of the solvent, and $N_A$ the Avogadro constant. With this, they could derive the activity coefficient $f$ of the ionic species $i$:

$$\ln(f_i) = -\frac{z_i^2 \cdot e^2}{8 \cdot \pi \cdot \epsilon \cdot k_B T} \cdot \frac{\kappa}{1 + \kappa r_i} \tag{4}$$

with $r_i$ the radius of the ionic species $i$. The characteristic length scale for which the electrostatic interactions are screened is called Debye length $\lambda_D$ and is defined as:

$$\lambda_D \equiv \kappa^{-1} = \sqrt{\frac{\epsilon \cdot k_B T}{2 \sum_i (z_i e)^2 c_i^\infty}} \tag{5}$$

The Debye length is a key parameter in describing the behavior of polyelectrolytes. It is defined as the distance over which the concentration of counterions decreases to 1/e of its bulk value. The Debye length is an important factor in determining the strength of the electrostatic interactions between charged macromolecules in solution. Depending on the ionic conditions, it varies from about $\sim 0.3$ nm in strong ionic solutions (e. g., $\sim 1$ M NaCl) to $\sim 1$ µm in distilled water.

## 2.2 GLOBAL DNA CONFORMATION

In recent years, a variety of different and complementary approaches has been developed to model DNA conformations on a global as well as on a local scale. Concurrently, new kinetic approaches and other equilibrium studies have refined the modelling of DNA. Together, they provide new physical and biological insights into fundamental functional processes of DNA [77].

### 2.2.1  *DNA models*

DNA is not only the storage medium of genetic information, but can also be considered a bio-polymer. As such, it serves as a model system for an ideal macromolecular coil due to its monodispersity as well as its large variability in molecular length. Under physiological ionic conditions and temperatures, the DNA axis takes many different conformations in solution, which is a characteristic feature of polymer chains. The conformational properties of DNA can be described by using different models.

#### 2.2.1.1  *The freely-jointed chain model*

By definition, polymers consist of repeating subunits (monomers) that are linked together to form a polymer chain. Such a polymer chain is called ideal if there is no correlation between the polymer monomers, which are separated by large distances along the chain. This also excludes interactions caused by conformations in space, so that the polymer can cross itself in an ideal chain, i.e.there is also no self-avoidance.

The simplest model for an ideal polymer chain is the freely-jointed chain (FJC) model. A polymer in this model is defined as a chain of $n$ rigid and inextensible segments of length $b$, the so-called Kuhn length (named after the Swiss chemist and physicist Hans Kuhn), where the orientations of the individual segments are completely uncorrelated to each other. The segments are connected by perfectly flexible hinges or joints, they do not interact and can even pass through each other (no
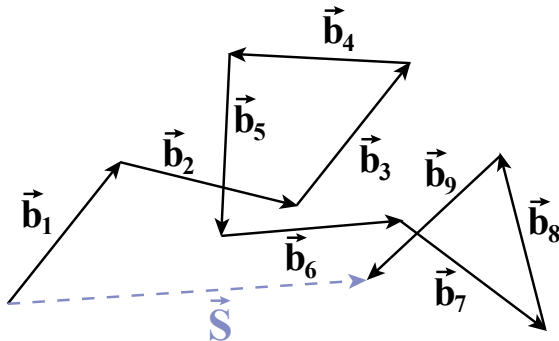
Figure 5: Freely-jointed chain model. Vector representation of a random walk of nine steps ($\vec{b}_1$ to $\vec{b}_9$). The trajectory vectors are depicted as solid line arrows; the total displacement, $\vec{S}$, is represented by a dashed line arrow.

self-avoidance). The total DNA length, also referred to as the DNA contour length $L_C$, is then given by $L_C = n \cdot b$ [54].

Mathematically, a polymer in the FJC-model can be described by a random walk[2], in other words a walker that takes each step in a random direction (all directions have equal probability), independent of its previous step, and where each step is of the same length $b$ [78]. The total displacement of the walker after $n$ steps, $\vec{S}$, can be calculated by taking the sum of all (vectorial) steps $\vec{b}_i$ (Figure 5):

$$\vec{S} = \sum_{i=1}^{n} \vec{b}_i \tag{6}$$

Since at any point in time a step forward is just as likely as a step backwards, the expected average end position must be back at the starting position. So, the average value of $\vec{S}$ over all possible walks with $n$ steps, $\langle \vec{S} \rangle$, is zero. Interestingly, however, the average distance of the walker from the starting point after $n$ steps (regardless of the direction)

---

2 The analogy between a random walk and a filamentary polymer was first described in 1934 by the Swiss chemist Werner Kuhn in reference [78] (in German). Werner Kuhn was also the doctoral supervisor of Hans Kuhn (not related though), after whom the Kuhn length is named.

is not equal to zero. This value can be described as the root mean square end-to-end distance $S_0 = \sqrt{\langle S^2 \rangle}$:

$$S_0 = \sqrt{\langle S^2 \rangle} = \sqrt{\left\langle \left( \sum_{i=1}^{n} b_i \right)^2 \right\rangle} = \sqrt{\sum_{i=1}^{n} \langle b_i^2 \rangle} = \sqrt{\underbrace{b^2 + b^2 + ... + b^2}_{n \ times}} =$$

$$= \sqrt{nb^2} = \sqrt{n}b \tag{7}$$

Another possibility to describe the spatial extent of a polymer chain is the term of radius of gyration $R_g$. In general, the radius of gyration is defined as the distance from the centre of mass of a body where the entire mass could be concentrated without changing the rotational moment of inertia about an axis through the centre of mass. The radius of gyration and the root mean square end-to-end distance are related via:

$$R_g^2 = \frac{1}{2N^2} \sum_{i,j} (\vec{b_i} - \vec{b_j})^2 = \frac{S_0^2}{\sqrt{6}} = b\sqrt{\frac{N}{6}} \tag{8}$$

### 2.2.1.2  *The worm-like chain model*

Taken together, the FJC model provides a simple and, to a first approximation, reasonably precise description for biomolecules like DNA. It retains important polymer properties and allows the calculation and interpretation of several critical parameters. Nevertheless, the description of an ideal polymer based on random motion on a regular lattice does not directly relate to the fundamental laws of statistical physics, especially not as a continuous description [79].

To overcome these limitations, a continuous and semi-flexible DNA model must be applied. This model is known as the worm-like chain (WLC) model, or - in the discrete form - as the Kratky-Porod model named after the Austrian physicists Otto Kratky and Günther Porod [80]. The polymer has a resistance to bending, which can be described by a bending energy $E$, which penalizes deformations:

$$E = -\kappa_b \sum_{s=2}^{N} \vec{t}(s) \cdot \vec{t}(s+1) = -\kappa_b \sum_{s=2}^{N} \cos(\theta(s)) \tag{9}$$

with $\vec{t}(s)$ the tangent vector in $s$ with unit length to describe the local bending at position $s$ in the polymer, and $\kappa_b$ the bending modulus. As the energy only couples neighboring vectors, the partition function $Z$ can be factorized into a product of single junction contributions $Z = Z_1^N$ with

$$Z_1 = \int_0^\pi \sin(\theta) \, \exp\left(\frac{\kappa_b \cdot \cos(\theta)}{k_B T}\right) \, d\theta = \frac{2 \, \sinh\left(\frac{\kappa_b}{k_B T}\right)}{\frac{\kappa_b}{k_B T}} \tag{10}$$

From this result, the correlation function of the orientation $\langle\cos(\theta)\rangle$ can then be determined as

$$\langle\cos(\theta(s))\rangle = \frac{\partial \ln(Z_1)}{\partial(\frac{\kappa_b}{k_B T})} = \frac{1}{\tanh(\frac{\kappa_b}{k_B T})} - \frac{\kappa_b}{k_B T} \tag{11}$$

By expanding this equation to the lowest non-vanishing order, it follows that

$$\langle\cos(\theta(s))\rangle \approx 1 - \frac{k_B T}{\kappa_b} \tag{12}$$

Next, by decomposing the tangent vector $\vec{t}(s)$ in its parallel and orthogonal components, it can be shown that

$$\vec{t}(s+1) = \vec{t}(s)\cos(\theta(s)) + \vec{t}(s)^{ortho}\sin(\theta(s)) \tag{13}$$

From this, it follows that

$$\langle\vec{t}(s) \cdot \vec{t}(s+i)\rangle = (\langle\cos(\theta)\rangle)^i \tag{14}$$

Combining Equations 12 and 14 then yields

$$\langle\vec{t}(s) \cdot \vec{t}(s+i)\rangle \approx \exp\left(-\frac{i \cdot k_B T}{\kappa_b}\right) = \exp\left(-\frac{i \cdot b}{L_P}\right) \tag{15}$$

with $L_P \equiv \frac{b \cdot \kappa_b}{k_B T}$ the persistence length of DNA, which is a measure for its bending stiffness. It is defined as the distance over which the directional correlation of the segments in the DNA chain is lost.

The WLC model exhibits also a continuous form. In this model (Figure 6), the polymer's trajectory varies continuously and smoothly through space (as opposed to the jagged contours of the more flexible FJC) [54,
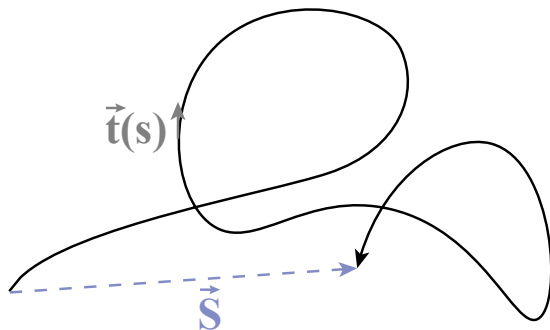
Figure 6: Continous WLC model: the polymer chain is represented as a continuous flexible isotropic rod. The tangent vector $\vec{t}(s)$ gives the local bending at a position $s$ of the polymer.

64]. The continuous position in the polymer can be expressed by the coordinate along the polymer $s$. To describe the local bending at position $s$ in the polymer, $\vec{t}(s)$ is again defined as the tangent vector in $s$ with unit length. The end-to-end vector $\vec{S}$ for a polymer of length $L_C$ is then given by

$$\vec{S} = \int_0^{L_C} \vec{t}(s)ds \tag{16}$$

The mean square end-to-end distance $\langle S^2 \rangle$ can then be calculated as

$$\langle S^2 \rangle = \langle \vec{S} \cdot \vec{S} \rangle = \left\langle \int_0^{L_C} \vec{t}(s)ds \cdot \int_0^{L_C} \vec{t}(s')ds' \right\rangle =$$

$$= \int_0^{L_C} ds \int_0^{L_C} ds' \langle \vec{t}(s) \cdot \vec{t}(s') \rangle = \int_0^{L_C} ds \int_0^{L_C} ds' e^{-\frac{|s-s'|}{L_P}} =$$

$$= 2 \cdot L_P \cdot L_C \cdot \left( 1 - \frac{L_P}{L_C} \left( 1 - e^{-\frac{L_C}{L_P}} \right) \right) \tag{17}$$

For the case of a very long chain, $L_C \to \infty$ and $\langle S^2 \rangle \approx 2 L_C L_P$. Since for the FJC model $\langle S^2 \rangle = n \cdot b^2$, it follows that $b_{Kuhn} = 2 \cdot L_P$. So for the semi-flexible chain model, the Kuhn length is defined as twice the persistence length $L_P$ [81–83].

### 2.2.1.3  *Force-extension behavior of linear polymers*

As an extension to describing the behavior of DNA, linear polymer models can also be applied to describe the response of DNA to an external stretching force [84]. As described in the previous Section 2.2.1.1, the polymer in the FJC-model is described by a chain of $n$ non-extensible and rigid segments of length $b$ held together by flexible hinges. The segments do not interact with each other and can even cross each other. The behaviour of the polymer in the absence of a force ($F = 0$) can then be described by random walk and the mean extension $\langle z \rangle = 0$. Applying an external force stretches the polymer to an extension $z > 0$. In x- and y-direction there is still random alignment of the segments possible as the force is only exerted in z-direction, consequently $\langle x \rangle = \langle y \rangle = 0$.

The extension of the polymer chain in z-direction is only possible with the energy associated with this force, as the polymer otherwise resists the stretching, as it is entropically less favourable to bring the polymer into a stretched state (fewer possible configurations). In a spherical coordinate system, the energy attributable to the external force is the sum of all segments from the projection of the segment length on the z-axis times the external force:

$$E = \sum_{i=1}^{n} E_i = -F \cdot b \sum_{i=1}^{n} \cos(\theta_i) \tag{18}$$

with $\theta$ being the angle with the z-axis. In order to calculate the average expansion in z, $\langle z \rangle$, the probability of a given configuration in the system must first be determined. This can be represented by means of its normalised Boltzmann factor:

$$P_j = \frac{\exp\left(-E_j/k_B T\right)}{\sum_j \exp\left(-E_j/k_B T\right)} = Z^{-1} \exp\left(-E_j/k_B T\right) \tag{19}$$

with the Boltzmann factor of state $j$, $\exp(-E_j/k_B T)$, and the partition function, $Z = \sum_j \exp(-E_j/k_B T)$ . Here, the sum runs over all possible states of the system $j$ (for a system with continuous values, the sum can be replaced by an integral).

The canonical average of $z$, $\langle z \rangle$, is then calculated by averaging its value in states $j$ weighted by the probability of the state $j$.

$$\langle z \rangle = \sum_j z_j P_j = Z^{-1} \sum_j z_j \exp\left(-E_j / k_B T\right) \tag{20}$$

As already employed for Equation 18, the extension along the z-axis is given as a function of the angle $\theta$, namely as the sum of all segments from the projection of the segment length on the z-axis:

$$z(\theta) = \sum_{i=1}^{n} b \cdot \cos(\theta_i) \tag{21}$$

For a system that takes on continuous values, the sum can be replaced by an integral

$$\langle z \rangle = Z^{-1} \int_0^{2\pi} d\phi_1 \int_0^{\pi} d\sin(\theta_1)\, d\theta_1 \, ...$$

$$... \int_0^{2\pi} d\phi_N \int_0^{\pi} d\sin(\theta_N)\, d\theta_N \left(\sum_{i=1}^{N} b\cos(\theta_i)\right) \exp\left(-\frac{E(\phi,\theta)}{k_B T}\right) \tag{22}$$

With $\phi$ and $\theta$ the polar and azimuthal angle of the spherical coordinate system. By introducing the expression for the energy of the system from Equation 18, this can be rewritten as:

$$\langle z \rangle = Z^{-1} \int_0^{2\pi} d\phi_1 \int_0^{\pi} d\sin(\theta_1)\, d\theta_1 \, ...$$

$$... \int_0^{2\pi} d\phi_N \int_0^{\pi} d\sin(\theta_N)\, d\theta_N \left(\sum_{i=1}^{N} b\cos(\theta_i)\right) \exp\left(\frac{F \cdot b \sum_i \cos(\theta_i)}{k_B T}\right) \tag{23}$$

The last expression can be rewritten as a derivative of the logarithm of the partition function. With this, Equation 23 simplifies to

$$\langle z \rangle = k_B T \frac{\partial}{\partial F} \ln(Z) \tag{24}$$

with the partition function

$$Z = \int_0^{2\pi} d\phi_1 \int_0^{\pi} d\sin(\theta_1)d\theta_1 ... \int_0^{2\pi} d\phi_N \int_0^{\pi} d\sin(\theta_N)d\theta_N \exp\left(\frac{F \cdot b \sum_i \cos(\theta_i)}{k_B T}\right) \tag{25}$$

Since the partition function $Z$ is a product of $N$ identical and independent factors, it follows that

$$Z = \left(\int_0^{2\pi} d\phi \int_0^{\pi} d\sin(\theta)d\theta \exp\left(\frac{F \cdot b \cos(\theta)}{k_B T}\right)\right)^N \tag{26}$$

and with this

$$\langle z \rangle = k_B T \frac{\partial}{\partial F} \ln\left(\left(\int_0^{2\pi} d\phi \int_0^{\pi} d\sin(\theta)d\theta \exp\left(\frac{F \cdot b \cos(\theta)}{k_B T}\right)\right)^N\right) \tag{27}$$

By applying basic logarithm rules, this can be rewritten as

$$\langle z \rangle = N \cdot k_B T \frac{\partial}{\partial F} \ln\left(\int_0^{2\pi} d\phi \int_0^{\pi} d\sin(\theta)d\theta \exp\left(\frac{F \cdot b \cos(\theta)}{k_B T}\right)\right) \tag{28}$$

Using the variable substitutions $x = \cos(\theta)$ and $dx = \sin(\theta)d\theta$, the integral can be simplified as

$$\langle z \rangle = N \cdot k_B T \frac{\partial}{\partial F} \ln\left(\int_0^{2\pi} d\phi \int_{-1}^{+1} dx \, \exp\left(\frac{F \cdot b \cdot x}{k_B T}\right)\right) \tag{29}$$

and then, in the next step, be resolved as:

$$\langle z \rangle = N \cdot k_B T \frac{\partial}{\partial F} \ln\left(2\pi \frac{k_B T}{F \cdot b}\left(\exp\left(\frac{F \cdot b}{k_B T}\right) - \exp\left(-\frac{F \cdot b}{k_B T}\right)\right)\right) \tag{30}$$

By performing the force derivative, this expression can be written as:

$$\langle z \rangle = N \cdot k_B T \cdot F\left(-\frac{1}{F^2} + \frac{b}{F \cdot k_B T} \frac{\left(\exp\left(\frac{F \cdot b}{k_B T}\right) + \exp\left(-\frac{F \cdot b}{k_B T}\right)\right)}{\left(\exp\left(\frac{F \cdot b}{k_B T}\right) - \exp\left(-\frac{F \cdot b}{k_B T}\right)\right)}\right) \tag{31}$$

Using the trigonometric identity

$$\coth(x) = \frac{\exp(x) + \exp(-x)}{\exp(x) - \exp(-x)} \tag{32}$$

Equation 31 simplifies to

$$\langle z \rangle = N \cdot k_B T \left( -\frac{1}{F} + \frac{b}{k_B T} \coth \left( \frac{F \cdot b}{k_B T} \right) \right) \tag{33}$$

which can be rewritten as

$$\langle z \rangle = N \cdot b \left( \coth \left( \frac{F \cdot b}{k_B T} \right) - \frac{k_B T}{F \cdot b} \right) \tag{34}$$

Thus, Equation 34 indicates that the polymer can be significantly lengthened by exerting relatively low forces. However, if the extension approaches the contour length of the chain, higher and higher forces are required to extend the polymer further (Figure 7).

This theoretical approach can be used to interpret experimental DNA force-extension data and to quantitatively compare between single-molecule experiments and different polymer theories. The first force-extension measurements on dsDNA, performed by Bustamante *et al.* in the early 1990s [59] - introduced already in Section 2.1.1.1 - showed that even the simple FJC polymer model fits the data qualitatively, yet the fit shows systematic deviations, especially at intermediate forces. The more sophisticated WLC model achieves a better approximation to real nucleic acid molecules (Figure 7) [64, 85, 86]. Comparing these single-molecule force-extension experiments to theoretical models provides the opportunity to fit the persistence length of DNA. Using the WLC model, the persistence length of dsDNA could be accurately determined for different environmental conditions (sequence, salt, temperature, etc.) [54, 59].

### 2.2.1.4   *Excluded volume effects*

One aspect that has not been considered in this section so far is the so-called excluded volume effect. Until this point, interactions between monomers with each other and with the surrounding solvent have been neglected. But while the trajectory of a random walk can occupy the same
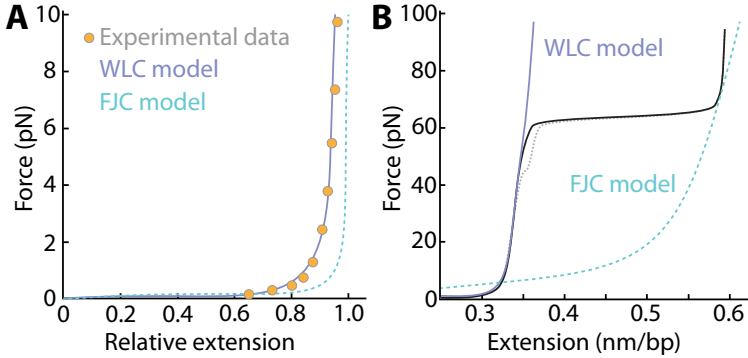
Figure 7: DNA force-extension measurements. A) dsDNA elongation as a function of stretching force for low forces (up to 10 pN): comparison between experiment and theoretical model. The experimental data are taken from Smith *et al.*, Ref. [58]. The FJC model (turquoise dashed line) gives the right trend, but only the WLC model (solid violet line) describes the behavior of the dsDNA well. B) dsDNA elongation as a function of stretching force for high forces (up to 100 pN): stretch data for a typical λ-DNA molecule are depicted as a solid black line (relaxation data are depicted as a dotted gray line). Close to approaching its contour length, the dsDNA molecule undergoes a force-induced melting transition to ssDNA. The WLC model (solid violet line) describes the dsDNA well, whereas the FJC model describes the ssDNA (turquoise dashed line) only approximately.

coordinates several times, two segments of a polymer cannot coincide in space.

In 1934, Werner Kuhn first described this concept and shortly afterwards the American chemist Paul Flory applied the excluded volume effect to polymer theory. The strength of this effect evidently depends on the length of the polymer chain and on the 'quality' of the solvent: if the chain is in a good solvent, the monomers will favor being in contact with the solvent than with other monomers of the chain. As a result of this, the inside of the chain moves outwards to surround the monomers with solvent. Consequently, the presence of the solvent increases the volume occupied by the polymer and the entropy of the system is reduced because more positions become inaccessible to the monomers since they are either already occupied by another monomer or by the solvent [54, 81]. Through the combination of these two contributions to the free energy

of the polymer, Flory showed that the polymer has an intermediate size configuration and the radius of gyration then becomes

$$R_g \propto N^{\frac{3}{5}} \tag{35}$$

with the Flory exponent $\nu = \frac{3}{5}$ in 3D space. So the extent of the excluded volume effect depends on the polymer length, and especially for long polymer chains the effect is not negligible.

### 2.2.2  *DNA topology*

In 1963, a decade after the discovery of the DNA double helix, American biochemists Roger Weil and Jerome Vinograd discovered that polyomavirus DNA exists in a closed circular form and that this form is typical for bacterial DNA and cytoplasmal DNA of eukaryotic cells of animals. By finding that the DNA axis can be coiled, they unraveled a fundamental tertiary structural feature of DNA. The resulting coiled DNA coil structure is called supercoiled DNA. There is positively or negatively supercoiled DNA, which refers to a DNA molecule whose double helix has undergone an additional twist in the same direction as the original helix or in the opposite direction. For a DNA molecule, in order to be supercoilable, it needs to be closed circular. Per definition, closed-circular DNA is a circular molecule of dsDNA without a nick in either of the two strands. The supercoiled DNA molecule minimizes its elastic energy by forming superhelical structures also called DNA plectonemes, loops of helices twisted together. Importantly, the mechanical resistance to torsional deformations (twisting) requires the continuity of both DNA strands (Figure 8).

The peculiarity of closed circular molecules is that their topological state cannot be changed by a conformational rearrangement that does not involve a break in at least one DNA strand; they can only be deformed geometrically by, for example, bending or stretching. The topology of polymers generally refers to the interlinking or entanglement properties, which are invariant under uniform geometric deformations. This topological constraint is the basis for the unique intriguing properties of circular DNA molecules. Breaking (or cutting) one of the strands
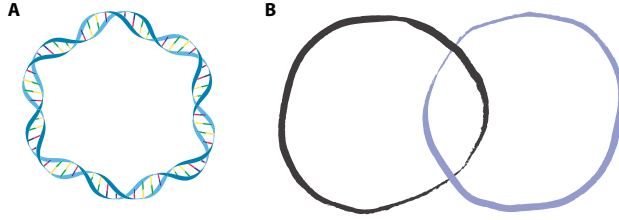
Figure 8: DNA topology. A) In a closed-circular DNA molecule each single strand of the dsDNA double helix is covalently closed, forming a circular double-stranded molecule. B) Two closed circles linked together once. Thus, $Lk = 1$.

transforms the supercoiled DNA into an open circular DNA molecule, while a closely spaced break in both strands results in a linear DNA molecule [64, 86–89].

Topological ideas were first applied to the study of closed-circular DNA properties by the American mathematician F. Brock Fuller in 1971, when he adapted the results of band theory to the analysis of DNA properties [90]. Very descriptively, he compared the DNA supercoiling to the twisting of a rubber tube representing the DNA double helix: If the ends are twisted relative to each other and then closed to a circle (with a connecting piece) to remove external constraints, the result is a coiled axis of the rubber tube (Figure 8B). DNA supercoiling can be achieved in a similar way by introducing changes in helical twist when the DNA is topologically constrained [90].

The conserved quantity following from this topological constraint is called the linking number, $Lk$, a topological invariant that describes the entanglement or linking of that describes the linking of two (or more) closed curves in 3D space. The concept of the $Lk$ can also be applied to DNA, however importantly, this property only exists in closed-circular DNA as it only makes sense in this context [91]. Quantitatively, the standard linking number of a molecule $Lk_0$ can be calculated as the number of base pairs in the molecule $N$ divided by the number of base pairs per helix turn $\gamma$:

$$Lk_0 = \frac{N}{\gamma} \tag{36}$$

It should be noted that $Lk_0$ is not a topological invariant, since it can be changed, for example, by the addition of salt. Introducing supercoils into a DNA molecule then increases or decreases the number of enclosed helical turns and consequently changes the value of the global linking number $Lk$, so

$$Lk = Lk_0 + \Delta Lk \tag{37}$$

So, $Lk$ can vary from the expected helical turns based on normal dsDNA turns (i.e., over- and undercoiling). Since DNA is right-handed, an
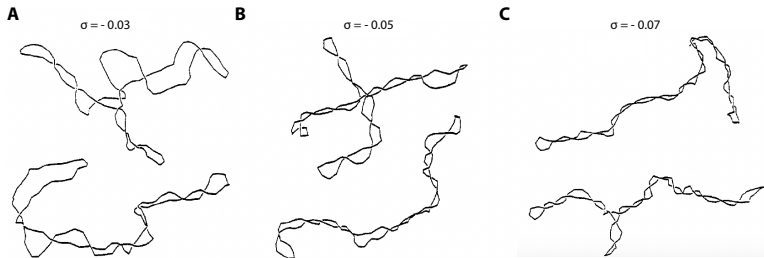


Figure 9: Results of computer simulations of supercoiled DNA molecules for different values of superhelical density $\sigma$. Data from Klenin *et al.* (Ref. [92]). Figure taken from Ref. [64].

overcoiling corresponds to a right-hand twist, while an undercoiling corresponds to a left-hand twist [93]. Thus, $\Delta Lk$ is a measure for supercoiling. Often, $Lk$ is normalized by $Lk_0$ to a supercoiling density $\sigma$ to obtain a contour length independent variable:

$$\sigma = \frac{\Delta Lk}{Lk_0} \tag{38}$$

Examples for DNA molecules generated via Monte Carlo simulations at different $\sigma$ are shown in Figure 9.

$Lk$ can be decomposed into a local and a non-local crossing contributions, the local being DNA twist, $Tw$, and non-local, or global, the DNA writhe, $Wr$. $Tw$ is a measure of the coiling of the two DNA strands around each other (or more precisely, around the DNA double helix axis). $Wr$ describes the coiling of the helix axis in space [64, 86, 94]. All three characteristics are interrelated by the so-called White's theorem named

after the American physicist James White who first formulated this equation in 1969 [95]:

$$Lk = Tw + Wr \tag{39}$$

It should be noted that $Lk$ is a topological property, while $Wr$ and $Tw$ are geometric and change their value when the molecule is distorted.

## 2.3 DNA-LIGAND INTERACTIONS

DNA interactions with ligands such as RNA or proteins are the basis for a variety of indispensable cellular processes and are essential for the proper functioning of DNA storage, replication, transcription, and repair, as well as the regulation of gene expression. Ligands can interact with DNA either specifically or non-specifically. In non-specific interactions, the order of the nucleotides has no role in the binding interactions. An example of such interactions are ion-DNA interactions. In contrast, DNA-binding proteins often slide along the DNA to locate a specific binding sequence. A subgroup of proteins are able to interact with dsDNA as well as ssDNA, like DNA polymerases, which bind both forms of DNA with high affinity at different binding sites on the replication fork [85, 96]. Small molecules that bind to DNA can interfere with these intracellular processes in an invasive yet reversible manner and therefore form the basis for a wide range of applications such as drug development for complex diseases including genetic diseases, autoimmune diseases and cancer [97–101]. One such approach is chemical genomics, which uses small molecules to probe gene function and identify potential drug targets. The characterization of the protein tubulin as a "colchicine-binding protein" was an early example of the powerful capabilities of chemical genetics; impressively, this discovery occurred more than ten years before the sequencing of the tubulin gene [101, 102].

### 2.3.1 *Quantitative description of ligand-DNA binding*

Fine-tuning such interactions requires a detailed understanding of the binding mechanisms. Characterization of the dynamic and equilibrium aspects of DNA-ligand complex formation may allow optimization of DNA binding for specific functions [103].

In the simplest model describing ligand binding with DNA, the bound ligands do not interact with each other. The equation for the binding of a ligand $L$ to a polynucleotide site $S$ can then be written as follows:

$$L + S \rightleftharpoons LS \tag{40}$$
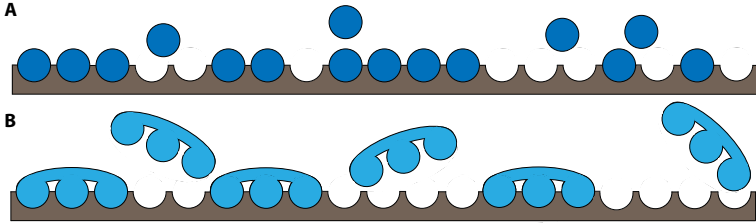
Figure 10: DNA binding models for non-specific binding of ligands. The polynucleotide units are shown in gray, the ligands in blue. A) Simple model with one ligand $L$ occupying one polynucleotide site $S$. Every unoccupied site is available for ligand binding. B) Sophisticated model with one ligand $L$ occupying more than one polynucleotide site $S$. Therefore, some units are unoccupied but nevertheless unavailable for binding, for example the two unoccupied units on the left side of the diagram between two bound ligands.

where $LS$ corresponds to a ligand bound to the binding site. As indicated by the double-arrow, this equation describes the equilibrium of the ligand-binding site system. The change in the concentration of bound ligands, $[LS]$, can be described as the loss in product concentration $[LS]$ and the gain in the reagent concentrations $[L]$ and $[S]$. At equilibrium, the equilibrium association constant of the reaction $K$ is then defined as [42, 45, 54]:

$$K = \frac{[LS]}{[L][S]} \tag{41}$$

This simple model can be extended to account for the fact that the site occupied by one ligand becomes inaccessible to other ligand molecules (Figure 10A) or that one ligand occupies even more than a single binding site and that the bound ligands can interact with each other (Figure 10B). It is assumed that all binding sites are equal and that each bound ligand occupies $n$ consecutive base pairs or nucleotides [54]. The latter scenario is for example needed to describe the binding of a ligand to DNA and it is more complicated because the number of accessible binding sites depends not only on the number of ligands bound but also on their specific positions [54]. This model was fist described by Zasedatelev *et al.* in 1971 [104] and three years later in a more elaborate way by McGhee and von Hippel and is therefore also known as McGhee-von

Hippel model [105]. For their analysis they introduced the fraction of occupied nucleotide units $\nu$, which can be written as

$$\nu = \frac{[LS]}{C_S} \tag{42}$$

with $C_S$ being the total concentration of the nucleotide units.

For the case of non-interacting ligands occupying $n$ polynucleotide units McGhee and von Hippel obtained the following fraction of occupied nucleotide units:

$$\nu = [L] \cdot K (1 - n\nu) \left( \frac{1 - n\nu}{1 - (n - 1)\nu} \right)^{-1} \tag{43}$$

When taking into account the interaction between the bound ligands (cooperativity), the equation describing the binding becomes much more complex. To this end, the binding constant for a ligand molecule that forms a contact with one already bound molecule is defined as $K\omega$ with $\omega$ being the cooperativity parameter. With this, the fraction of occupied nucleotide units can then be written as:

$$\nu = [L] \cdot K (1 - n\nu) \left( \frac{(2\omega + 1)(1 - n\nu) + \nu - R}{2(\omega - 1)(1 - n\nu)} \right)^{n-1} \left( \frac{1 - (n + 1)\nu + R}{2(1 - n\nu)} \right)^2 \tag{44}$$

with

$$R = \sqrt{(1 - (n + 1)\nu)^2 + 4\omega\nu(1 - n\nu)} \tag{45}$$

The model can be further extended by, for example, considering a dependence of binding affinity or the DNA sequence [54, 105], but these extensions are not discussed further here.

### 2.3.2 Small-molecule DNA interaction

Small molecules can bind to DNA in different ways. The ligands can, for example, bind covalently to DNA, interact due to their electrical charge or their ability to establish non-electrostatic interactions with the DNA backbone or bases. Non-covalent DNA binding modes include binding in

the major or minor grooves of DNA and intercalation, which describes
the insertion of ligands between the base pairs of DNA (Figure 11).
Intercalators bind DNA by inserting their flat aromatic rings between
adjacent DNA base pairs, simultaneously lengthening and unwinding the
DNA helix [85, 99, 103, 106–113]. Intercalators and intercalative binding
will be topic of all three result chapters, Chapter 4, 5, and 6.
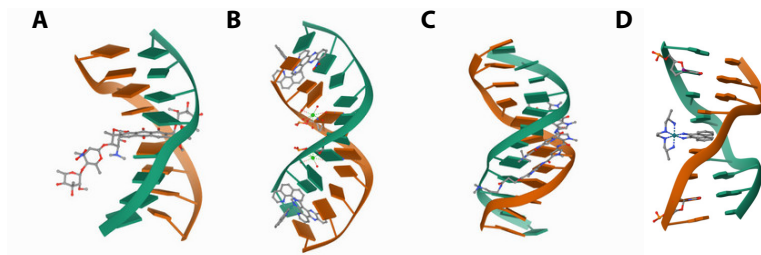


Figure 11: Examples for ligand-DNA binding. A) nuclear magnetic resonance
(NMR) solution structure of the Anthracycline Respinomycin D in-
tercalation complex with a dsDNA molecule (AGACGTCT)2 (NDB
ID: 1N37). B) Structure of [Ru(phen)2(10-NO2-DPPZ)]2+ bound
to the DNA sequence D(TCGGCGCCGA) (NDB ID: 6RSO), partly
intercalated. C) Polyamide-DNA complex (minor groove binding)
NMR structure (NDB ID: 6GZ7). D) Intercalation and major groove
recognition in the crystal structure of RH[ME2TRIEN]PHI bound
to 5'-G(5IU)TGCAAC-3' (NDB ID: UD0005). Courtesy: Nucleic
Acid Data Base [114, 115].

A specific type of small molecules, which is widely used in (bio-)chemistry
and molecular biology are fluorescent markers, which can bind nucleic
acids. These compounds are often used to probe DNA structure in
drug–DNA and protein–DNA interactions. One example is ethidium, a
DNA intercalator with applications for example in gel electrophoresis
(as already briefly mentioned in Section 2.1.1.2) [116, 117]. In aqueous
solution, ethidium is balanced by a $Br^-$ counterion, therefore it is also
referred to as ethidium bromide.

But small molecules that can interoperate with nucleic acids are also of
high relevance for biology, medicine, and related fields. One application
being small molecules interacting with RNA (SMIRNAs). Targeting small
molecules with RNA represents a new approach in drug engineering. The
broad range of folded RNA structures provides an immense reservoir of

targets to which small molecules can bind, thus opening up the possibility of influencing human biology, for example by recognizing disease-relevant RNA structures [118, 119].

One example for a well-studied small DNA-binding molecule with medical application is daunorubicin (daunomycin), a glycoside belonging to the group of anthracyclines with antibiotic and cytostatic activity. It is used as a cytostatic agent in combination chemotherapy of acute leukemias [120–122]. Daunorubicin interacts with DNA in form of intercalatoin. This blocks transcription of DNA to synthesize RNA or replication of DNA during cell division, also mediated by inhibition of the protein topoisomerase II, which relaxes DNA. Similarly, targeting DNA repair with specifically designed and synthetically produced small-molecule inhibitors is an emerging strategy for cancer therapy. In this approach, small molecule inhibitors are used to block DNA repair in cancer cells with high efficiency, resulting in cell death, and therefore represents a promising new cancer therapy [123]. Hence, small nucleic acid binding molecules are of great importance for a broad spectrum of applications ranging from molecular biology to pharmaceutical and medical applications in cancer therapy and beyond.

Another application of small-molecule DNA binding is real-time quantitative PCR (qPCR), a technique combining standard PCR with real-time fluorescence read out so that the products generated during each cycle of the PCR process can detected and quantified. Over the past years, qPCR has become the state-of-the-art technology for rapid, inexpensive, and reliable quantification of nucleic acids [124, 125]. Two general methods are available for amplification detection by fluorescence signal. The first approach uses a so-called 'TaqMan' probe, which is a fluorogenic, non-extendable probe with a fluorescent reporter dye at the 5'-end and a quencher dye at the 3'-end, which can anneal to a specific target sequence in the DNA. Cleavage of the probe by the polymerase (usually Taq polymerase, therefore also the name 'TaqMan') during the PCR results in a change in fluorescence intensity [124]. Alternatively, DNA intercalating dyes can be used to detect amplification via a fluorescence signal. These dyes exhibit increased fluorescence intensity when intercalated into DNA. As the fluorescence signal is dependent on the amount

of DNA present in the reaction, the recorded fluorescence allows direct detection and quantification of the success of the PCR [124, 126]. With this, real-time qPCR technology has revolutionised the field of molecular diagnostics, allowing a shift towards high-throughput and automated molecular procedures.

# 3

## EXPERIMENTAL METHODS

Fluorescence approaches have become a very powerful and widely used approach to visualize and quantify biological structures, and to understand biological processes at the cellular level. Yet, in many research areas, especially in biology, medicine and related fields, it is of great importance to visualize and study objects in the nanometer range. However, this is limited by the diffraction limit of light in microscopy. For example, in a sample containing fluorophoric molecules at the nanometer scale, it can be difficult to distinguish two fluorophores that are very close to each other. The minimum distance between two fluorophores so that they can still be detected as two light sources is determined by the Abbé limit, a lower limit on the resolvable distance $d$ formulated by the German physicist Ernst Abbé in 1873:

$$d = \frac{\lambda}{2n \cdot sin(\alpha)} \tag{46}$$

Thus, this distance $d$ is not infinitely small, but is limited by the wavelength of the observing light $\lambda$, the refractive index $n$, and the aperture angle of the objective $\alpha$. Since microscopes have technical limits and the refractive index for gases is typically close to 1, $d$ can be estimated to be at least $\lambda/2$. The spectral range visible to the human eye is about 400 - 800 nm, so for classical optical microscopy $d$ is larger than 200 nm. Nevertheless, in order to study biomolecules at the nanoscale, a number of biophysical and biochemical techniques exists that can be used to circumvent the Abbé boundary. In the following, I will discuss some of these techniques. For biophysical research, micromanipulation of single cells and molecules is becoming increasingly important, as overall biochemical analyses can provide very reliable qualitative and also quantitative descriptions, but can only inadequately describe phenomena at the molecular level. Only single-molecule measurements can fully explore the

kinetics, mechanics and variation of structure, function and interactions to provide a complete physiological picture [127].

A potential strategy for single-molecule measurements is to use electric and magnetic fields to manipulate particles. The beginnings of the first attempts to study individual biological systems date back more than 70 years. Already in 1950, Francis Crick, who should only three years later discover the double-helical structure of DNA (see beginning of this thesis, Section 1.1.3) together with the American biologist Arthur Hughes, investigated the viscoelastic properties of the cytoplasm of a cell using magnetic micromanipulation. They were able to pull, push, and rotate magnetic particles into the cytoplasm of cells using magnetic forces [127, 128]. 20 years later, in 1970, the American physicist Arthur Ashkin[1] achieved a major breakthrough in the field by developing his so-called "levitation traps" by using the intense electromagnetic fields of highly focused lasers to precisely position latex particles [129, 130]. Today, this technique is known as optical tweezers. A major advantage of these optical trapping techniques (which have been extensively refined over the years) is that they do not require contact and can thus measure or manipulate the behaviour of a single-molecule under stretching or torsional forces without interference of surface effects. As further advantages, practical aspects such as lower cost (compared to other force spectroscopy measurement devices), ease of implementation, and biocompatibility can be mentioned, which make optical tweezers an elementary method for manipulating and measuring individual biological molecules and their interactions [127].

In contrast, one of the major disadvantages of these trapping techniques is that the object to be observed must have an electric contrast to the surrounding medium in order to experience a force in an optical field. Since the molecule of interest often lacks favourable intrinsic properties, it is necessary to attach a particle or label to the molecule to improve contrast in order to image it or to exert a force or torque on it. Another challenge of conducting single-molecule measurements on biological structures using optical tweezers is that for many biological processes not only nm-scale spatial but also ms-scale temporal resolution is needed. To accomplish this, the technical parts of the measurement instruments

---

1 Arthur Ashkin was awarded the Nobel prize in Physics 2018 "for the optical tweezers and their application to biological systems" [129].

have been extensively developed over the years [131–133]. Today, optical tweezers reach ms.scale temporal resolution. Also, they can exert forces in the range of 0.1 to 200 pN, which makes them a well-suited approach for single-molecule biophysics [127].

## 3.1    SINGLE-MOLECULE MAGNETIC TWEEZERS

An alternative single-molecule trapping method is magnetic tweezers (MT). Here biomolecules or even cells can be manipulated by magnetic forces acting on superparamagnetic particles instead of optical manipulation. MTs offer several advantages over other force spectroscopy
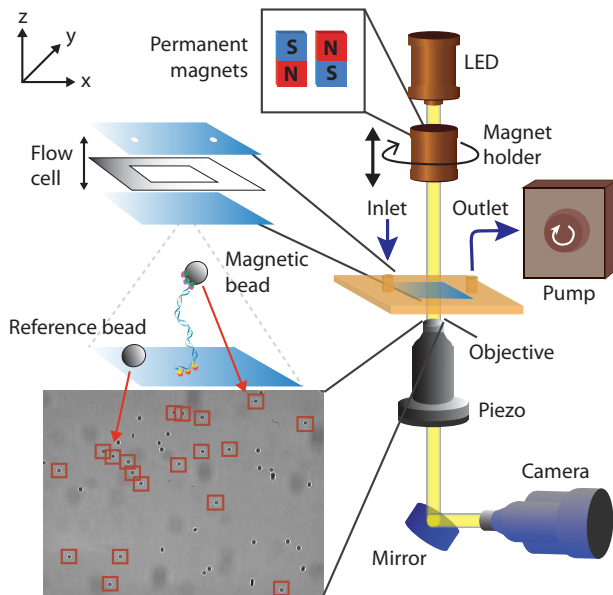


Figure 12: Schematic representation of a single-molecule MT setup [134–137]. The measurement chamber (the so-called flow cell) is assembled from two glass slides (light blue on the right) separated by a layer of parafilm (light gray). The flow cell, which is connected to a pump for fluid exchange, is then fixed in place using a flow cell holder (light brown color) and mounted on a stage, which allows direct contact with the objective (with an oil film in between). The objective is placed on a piezoelectric stage to enable control over the focal plane. A light-emitting diode (LED) is used to illuminate the sample. The outgoing light beam is deflected by a mirror into a charge-coupled device (CCD) camera connected to a computer to track the positions of the beads. The magnet holder including a pair of permanent magnets is located on top of the flow cell. The z-position and rotation about the vertical axis of the magnet holder are controlled by motors.

techniques such as optical tweezers and are therefore particularly well

suited for certain measurements. For example, they do not suffer from the problems of sample heating and photodamage that are a critical point in optical tweezers. In addition, they have the advantage of being easier to multiplex, e. g., forces can be applied to several molecules simultaneously. Furthermore, magnetic manipulation is highly selective for the magnetic beads used as probes and is generally insensitive to sample and microscope chamber preparation. And additionally, extremely low forces ($< 0.1$ pN) can be achieved with MTs, and forces can also be kept very constant over long periods of time [138]. The beginnings of this technique, developed by the laboratories of Bustamante and Croquette, have already been described in the previous chapter in Section 2.1.1 [58–61, 127]. Since then, MTs have become a high-performance tool for precise, high-resolution measurements under the influence of external forces and torques. As such, they enable real-time observation of biological processes at the molecular level. With this, quantitative determination of mechanical parameters, conformational transitions, dynamics and interactions of nucleic acids is made possible [134–136, 139, 140].

In MT experiments, the molecule of interest (for example a DNA molecule) is tethered between a surface and a superparamagnetic bead. This setup facilitates to apply precisely calibrated forces between $\lesssim 0.05$ pN and $\sim$ 100 pN via an external magnetic field. The bead position can be tracked accurately by a CCD camera with a detection frequency of about 50 - 1000 Hz (and even faster [141]) with a resolution along the z-axis of $< 1$ nm [131–133, 140]. After the beginnings in the 1990s (described in Section 2.1.1.1) [61], the various elements of the MT setup have evolved considerably [131–133, 142]. However, the underlying measurement concept has remained the same: As a prerequisite, the molecule of interest (for simplicity, we consider here a dsDNA molecule, but it is also possible to attach ssDNA, RNA, proteins, etc.) is tethered between the glass surface of the flow cell and a paramagnetic bead. In order to achieve this, the DNA molecule is designed to have several nucleotides tagged with digoxigenin (DIG) at one end. To bind the the DNA to the surface of the flow cell, the latter is coated with an anti-DIG antibody. A similar mechanism is used on the other side of the DNA, only with biotin labels on the DNA and streptavidin coating on the surface of the magnetic beads. With a pair of small permanent magnets mounted above the flow

cell, magnetic fields and thus magnetic forces can be exerted on the paramagnetic beads, which in turn allows micro-manipulation of the molecule of interest. By moving the magnet pair closer to the flow cell, the magnetic force on the beads increases and the tethered molecule experiences a stretching force. Furthermore, by rotating the magnet pair, it is also possible to exert torques and thus twist the DNA molecule, since both ends of the DNA molecule are held in torsion [131, 140].

An inverted microscope and monochromatic illumination are used to track the diffraction pattern of each individual bead using video microscopy. This allows to precisely determine the x, y, and z positions of the micrometer-sized magnetic beads in real time [61, 131, 135, 136, 139]. At a constant applied force, the magnetic bead fluctuates around its equilibrium position due to Brownian motion. The fluctuations are governed by the applied force and the flexibility of the tethered DNA. This relationship can be used to calculate the stretching force acting on the molecule, if the location of the bead and its fluctuations transverse to the stretching direction are know, since these fluctuations $\langle \delta x^2 \rangle$ are related to the stiffness $k_x$ by the equipartition theorem:

*The equipartition theorem relates the temperature of a system to its mean energies.*

$$\frac{F}{l} = k_x = \frac{k_B T}{\langle \delta x^2 \rangle} \tag{47}$$

with $k_B$ the Boltzmann constant, $T$ the temperature, and $l$ the extension of the DNA molecule determined by the position of the magnetic bead [139]. This approach has its drawbacks, for example due to the finite acquisition frequency of the CCD camera, artifacts in variance measurements due to camera blurring and the introduction of aliasing. To overcome these limitations, te Velthuis *et al.* have proposed an approach to deconvolve camera effects to allow reliable force calibration of MT experiments. To determine the underlying correct variance from the measured (incorrect) variance, the measured power spectrum is iteratively corrected and the integral of the spectrum fitted until the fitting error reaches the desired value [139, 143].

## 3.2 ENSEMBLE MEASUREMENTS

In contrast to single-molecule experiments, in measurements made on large ensembles or a bulk collection of molecules the individual behavior of molecules cannot be distinguished. But, to get the average characteristics of the system, the laws of thermodynamics can be applied. While there is the drawback that ensemble measurements do not provide information about the system at the single-molecule level, on the other hand, this type of measurement also has advantages over single-molecule measurements, such as the ability to measure far more than millions of molecules simultaneously and the ability to simply average out outliers.

Well-known examples of ensemble measurements are UV-Vis spectroscopy or fluorescence spectroscopy. These techniques allow measuring DNA-specific absorption of light or dye-specific light absorption and emission. Another commonly used technique that uses the fluorescence signal from dyes bound to DNA as an indication of DNA is gel electrophoresis (which will be discussed in the next paragraph). These are just a few selected examples; overall, the toolboxes of biochemistry and biospectroscopy offer a wide variety of experimental techniques.

### 3.2.1 *Electrophoresis*

A simple technique to study DNA is gel electrophoresis (Figure 13). Introduced in the 1970s, it has revolutionized the field of molecular biology and is nowadays routinely used to visualize, separate, and purify nucleic acids and proteins [64, 144].

In brief, gel electrophoresis works by applying an electric field to a gel matrix containing DNA samples, causing the negatively charged DNA molecules to migrate toward the positive electrode. The rate and direction of migration depend on the size and charge of the DNA fragments, thus allowing to separate and identify different components of a mixture. For (long) DNA molecules, the gel matrix used to contain the samples and provide size barriers is usually agarose[2] [47], a linear polysaccharide

---

2 For the separation of proteins, short DNA duplexes and ssDNA fragments, poly-acrylamide is commonly used as medium instead.
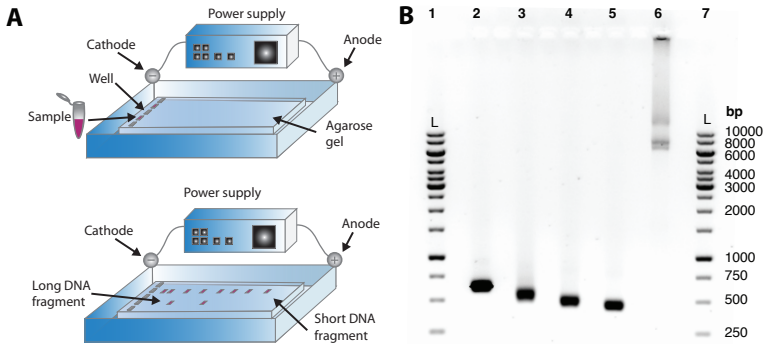
Figure 13: Gel electrophoresis. A) Schematic of an agarose gel electrophoresis chamber. The DNA samples are introduced into wells in the agarose gel placed in an electrophoresis chamber filled with buffer. When applying an electric field, the negatively charged DNA molecules move through the gel from the cathode to the anode with different velocities depending on their size. B) Visualization result of an agarose gel with different DNA species and amounts. As a size reference, a commercial DNA sample with known bands in the gel, a so-called ladder (L), is loaded on the two outer lanes of the gel. Panel B is taken from Ref. [138].

that has the ability to cross-link. Therefore, the porosity of the resulting gel can be controlled by the concentration of agarose. The sorting of molecules is based on a combination of molecular characteristics such as size, hydrodynamic radius, net charge, and surface charge density. Most commonly though, DNA is separated by length. The electrophoretic mobility $\mu$ is related to the length of the DNA fragment $l$ by

$$\mu \propto l^{-1} \tag{48}$$

Also DNA molecules belonging to different topological classes move in a gel at different speeds, albeit for a different reason than linear DNA. Here, the mobility is governed by the $Lk$ value, or more precisely by the absolute value of the writhe of the molecule. Because of the different 3D forms, supercoiled DNA moves faster through the agarose gel than linear DNA, which itself is faster than open circular DNA [64, 145].

To separate the samples, the agarose gel is placed in an electrophoresis chamber filled with an aqueous buffer solution, the samples are loaded

into pre-shaped wells in the gel, and an electric field is applied. The negatively charged DNA molecules migrate through the gel towards the anode - at different velocities depending on their length and topological form.

To visualize the DNA, the samples are mixed with a buffer containing a fluorescent dye prior to loading them in the gel wells ('pre-staining') or alternatively, the entire gel is stained in a solution containing a fluorescent dye after running the gel ('post-staining'). The latter is commonly used when working with different DNA topologies since DNA-binding dyes can have an effect on the DNA twist. Thereafter, the gel is imaged using a visualization system specialized for gels [54].

### 3.2.2   *UV/Vis Spectroscopy*

Another bulk measurement to analyze samples containing nucleic acids is UV/Vis spectroscopy. In this spectroscopy method, a sample is illuminated with electromagnetic rays of different wavelengths in the ultraviolet (UV) and visible (Vis) regions. Depending on the substance, the light in the UV or visible range is partially absorbed by the sample. The remaining light, i.e., transmitted light, is detected by a suitable detector as a function of wavelength. The detector then generates the unique UV/Vis spectrum of the sample (also called absorption spectrum). UV/Vis spectroscopy can be used to determine the molar concentration of nucleic acids in solution (see Chapter 2 for more information on the optical properties of DNA). DNA bases absorb UV radiation around 260 nm [64, 146]. Therefore, the concentration of DNA in solution can be derived by measuring the absorbance $A$ at 260 nm of a sample by applying Lambert-Beer's law:

$$A = \log \left( \frac{I_0}{I} \right) = \epsilon \cdot l \cdot c \tag{49}$$

with $I_0$ the intensity of incident light, $I$ the intensity of transmitted light, $\epsilon$ the wavelength-dependent molar extinction coefficient of the molecule of interest, $l$ the length of the light path through the sample, and $c$ the molar concentration. The molar extinction coefficient $\epsilon$ at 260 nm for long sequences of dsDNA with an AT/GC ratio of $\sim 50\%$ is approximately 50

$(\mu g/mL)^{-1}$ cm$^{-1}$. For shorter DNA or AT/GC ratios $\neq 50\%$, $\epsilon$ needs to be calculated explicitly, because the absorbance of the four different nucleobases varies [147, 148].

# 4

# INVESTIGATION OF DNA-DYE INTERACTIONS IN MOLECULAR DETAIL EXEMPLIFIED BY THE INTERCALATOR SYBR GOLD

## 4.1 DNA VISUALIZATION AND FLUORESCENT DNA STAINS

Advances in technology have led to numerous applications of DNA analysis in fields such as medicine, forensics, and genetics. Nucleic acid stains are one example of the growing number of applications of DNA analysis. These fluorescent dyes bind to nucleic acids such as DNA or RNA with dramatically increasing fluorescence signal intensity upon binding and thus enable detection and quantification of nucleic acids, oligo-nucleotides, PCR products, and related molecules. They find wide application in fluorescence microscopy, flow cytometry, and other analytical techniques to visualize and quantify nucleic acids in cells and tissues.

Recently, various nucleic acid-binding dyes have been developed for sensitive detection of dsDNA, ssDNA, and oligonucleotides in gels and solution. These dyes are used to directly visualize DNA in gels, tissues, or cells, making them useful for diagnostic and research purposes. There are several types of nucleic acid stains that are commonly used in research and diagnostic applications. One of the most popular DNA stains is DAPI (4',6-diamidino-2-phenylindole), which binds strongly to the minor groove of double-stranded DNA [149–151]. DAPI emits blue fluorescence upon binding to DNA and is often used to visualize nuclear DNA in fixed cells and tissues. Another commonly used nucleic acid stain is ethidium bromide. This stain intercalates between the base pairs of DNA and fluoresces orange-red upon binding. Ethidium bromide is used extensively to detect DNA in agarose gel electrophoresis, where it is used to visualize and quantify the size and concentration of DNA fragments. However, it is a potent mutagen and is not used in living cells.

## 4.2 CYANINE DYES

For ultra sensitive nucleic acid detection in a wide range of applications, various cyanine dyes have been developed as fluorescent stains, labels, or probes for sensitive detection of dsDNA, ssDNA, and oligo nucleotides in gels and in solution. Cyanine dyes allow rapid and reliable quantitative fluorescent staining due to their ability to form fluorescent complexes with nucleic acids [152]. Common examples for cyanine dyes are Cy3, Cy5, TO, TO-PRO-1, TOTO, YOYO, FUN-1, Thiazole Orange, SYTOX Orange, SYTOX Green I, SYBR Green II, Pico Green, SYBR Green, and SYBR Gold (a few examples are shown in Figure 14). These stains have different affinities for RNA and DNA and vary in their excitation and emission spectra, allowing them to be used in a broad spectrum of applications. Upon binding to nucleic acids, cyanine dyes show astonish-



| Dye | R1 | R2 |
| --- | --- | --- |
| TO | $CH_3$ | H |
| TO-PRO-1 | $(CH_2)_3N^+(CH_3)_3$ | H |
| FUN-1 | Phenyl | Cl |
| SYBR Green | Phenyl | |
| Pico Green | Phenyl | |
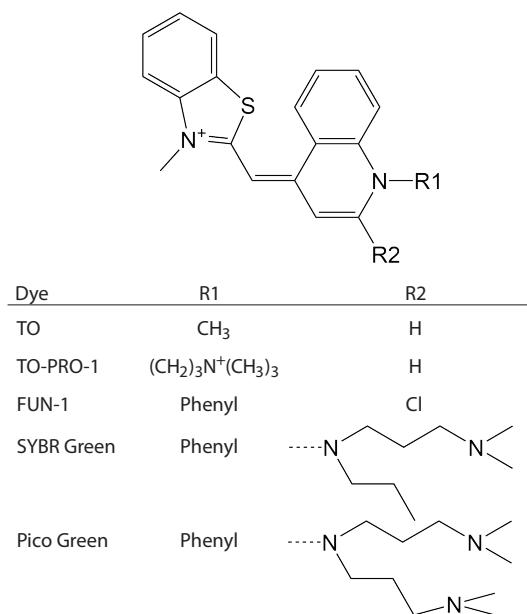
Figure 14: Chemical structures of five different monomeric cyanine dyes based on the same core structure and only varying side chains R1 and R2. Data taken from Ref. [153].

ing strong enhancements of fluorescence emission. This behavior makes them an excellent choice for detecting nucleic acids by luminescence imaging or even inside cells by fluorescence microscopy. The highest fluorescence response (> 1000-fold enhancement upon intercalation between nucleobases) was observed for the fluorescent stain SYBR Gold upon binding to dsDNA, making it an outstanding tool for gel electrophoresis or for example qPCR real-time measurements to detect even very small (changes of) amounts of DNA [152, 154].

The first cyanine compound was already synthesized in 1856. Since then, a large number of different cyanine dyes has been developed and nowadays, they are widely applied in biotechnology [152, 155]. Classical cyanine dyes are cationic molecules consisting of two terminal nitrogen-containing heterocyclic subunits linked by a polymethine bridge containing an odd number of carbons (Figure 15). Thereby, one nitrogen subunit is a quaternary ammonium group that serves as an electron acceptor (antiauxochrome), and the nitrogen subunit on the other side is a tertiary amino group that acts as an electron donor (auxochrome). This allows resonance delocalization of a positive charge between the two nitrogens. Both groups have a relatively strong bathochromic effect, meaning that the degree of electron delocalization is high. This is the reason why cyanine dyes absorb light already in the visible range even with relatively small $\pi$-electron systems.
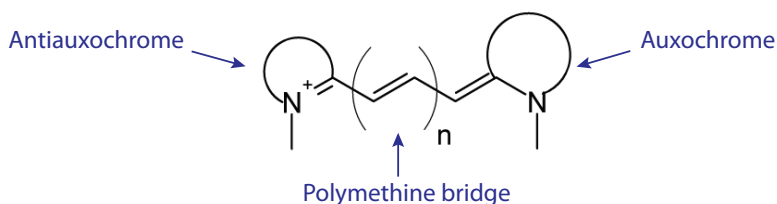


Figure 15: General structure of cyanine dyes consisting of a conjugated system (polymethine bridge) between two nitrogen-containing heterocyclic subunits that serve as electron donor (auxochrome) and electron acceptor (antiauxochrome).

Even though the name 'cyanine' originally goes back to the ancient greek word $\kappa \nu \alpha \nu o \varsigma$, which describes a greenish-blue shade, the cyanine

family of dyes covers the electromagnetic spectrum from the ultra-violet ($< 380$ nm) to the a near-infrared region ($> 700$ nm). The position of the absorption maximum depends mostly on the number of methine groups in the polyene chain. For example, monomethine ($n = 1$) and trimethine ($n = 3$) cyanines generally exhibit their absorption maxima in the visible region. Adding additional vinylene moieties ($CH = CH$) to the polymethine bridge leads to a bathochromic shift (red shift) of about 100 nm each [156]. Cyanine dyes exhibit narrow absorption bands and high extinction coefficients, up to 20 0000 $M^{-1}cm^{-1}$. They are only weakly fluorescent in solution but their fluorescence efficiency greatly increases when binding to nucleic acids or proteins because the fluorophore becomes more rigid [155].

The work presented in the following, features an in depth study of the fluorescent dye SYBR Gold, which also belongs to the synthetic cyanine dyes. I will present its chemical structure, which was determined using NMR and mass spectrometry. In addition, I will investigate the binding to DNA and demonstrate that SYBR Gold binds DNA in an intercalative way meaning that it is inserted in between two adjacent base pairs. This binding mode is known to lengthen and unwind the DNA, which I will also show for SYBR Gold. Furthermore, I will show similarities and differences to the closely related synthetic cyanine dye SYBR Green I. Additionally, I will analyze the photophysical properties of SYBR Gold: its fluorescence enhancement by DNA intercalation scales linearly at low dye concentrations whereas dynamic self-quenching limits the linear fluorescence response at high SYBR Gold concentrations. Fluorescence lifetime measurements show that dynamic quenching at high SYBR Gold concentrations decreases the fluorescent signal. By combining the collected information about the fluorescent DNA stain SYBR Gold, I will give recommendations for optimal application for quantitative DNA analysis using SYBR Gold staining.

# Molecular structure, DNA binding mode, photophysical properties and recommendations for use of SYBR Gold

By

Pauline J. Kolbeck[1], Willem Vanderlinden[1,*], Gerd Gemmecker[2], Christian Gebhardt[3], Martin Lehmann[4], Aidin Lak[1], Thomas Nicolaus[1], Thorben Cordes[3], and Jan Lipfert[1,*]

[1] Department of Physics and Center for NanoScience, LMU Munich, Amalienstrasse 54, 80799 Munich, Germany
[2] Bavarian NMR Center (BNMRZ), Department of Chemistry, Technical University of Munich, Garching, Germany
[3] Physical and Synthetic Biology, Faculty of Biology, LMU Munich, Planegg-Martinsried, Germany
[4] Plant Molecular Biology, Faculty of Biology, LMU Munich, Planegg-Martinsried, Germany
* Corresponding authors

published in

My contribution to this publication was performing spectroscopy and single-molecule magnetic tweezers measurements, analyzing the resulting data, and co-writing the manuscript with input from all authors.

### 4.3.1 *Abstract*

SYBR Gold is a commonly used and particularly bright fluorescent DNA stain, however, its chemical structure is unknown and its binding mode to DNA remains controversial. Here, we solve the structure of SYBR Gold by NMR and mass spectrometry to be 2-(4-[diethyl(methyl)ammonio]methylphenyl)-6-methoxy-1-methyl-4-[(2Z)-3-methyl-1,3-benzoxazol-2-ylidene]methylquinolin-1-ium and determine its extinction coefficient. We quantitate SYBR Gold binding to DNA using two complementary approaches. First, we use single-molecule MT to determine the effects of SYBR Gold binding on DNA length and twist. The MT assay reveals systematic lengthening and unwinding of DNA by 19.1° ± 0.7° per molecule upon binding, consistent with intercalation, similar to the related dye SYBR Green I. We complement the MT data with a spectroscopic characterization of SYBR Gold fluorescence. The data are well described by a global binding model for dye concentrations ≤ 2.5 µM, with parameters that quantitatively agree with the MT results. The fluorescence increases linearly with the number of intercalated SYBR Gold molecules up to dye concentrations of ∼ 2.5 µM, where quenching and inner filter effects become relevant. In summary, we provide a mechanistic understanding of DNA-SYBR Gold interactions and present practical guidelines for optimal DNA detection and quantitative DNA sensing applications using SYBR Gold.

### 4.3.2 *Introduction*

The interaction of DNA with ligands is fundamental for many cellular processes as well as biotechnological applications. In particular, fluorescent dyes are routinely used to label DNA for visualization and quantification in a wide variety of assays ranging from imaging of cells to analysis and quantification of gel bands or PCR products. SYBR Gold is a popular stain with very high sensitivity owing to the > 1000-fold increase in fluorescence quantum yield on binding to DNA [158, 159]. Despite its widespread use, its structure is unknown and there is disagreement whether SYBR Gold binds in an intercalative [159, 160] or in a minor-groove binding mode [161–163].

In general, the binding mode of DNA dyes impacts how binding depends on environmental conditions, DNA chain topology, or sequence context. Conversely, small-molecule binding to DNA can alter its structure and mechanical properties. Specifically, intercalation lengthens and unwinds the DNA helix [117, 164], and the changes upon intercalation into DNA have been investigated at the single-molecule level using optical tweezers [160, 165–177], atomic force microscope (AFM) force spectroscopy [110, 111], and MT [116, 178–180]. In contrast, minor groove binding has only much smaller effects, if any, on DNA length and winding angle[116].

Detection of DNA e. g.after separation by gel electrophoresis requires labeling and staining for visualization and quantitation. The extent of DNA binding depends both on DNA and dye concentration, as with any equilibrium binding reaction. We need to quantitatively understand the binding properties of SYBR Gold to DNA in order to determine conditions for high signal-to-noise detection and to obtain a linear relationship between the amount of DNA and fluorescence intensity, which is desirable for quantitation.

We first solved the molecular structure of SYBR Gold by NMR and mass spectrometry, which allows us to determine the charge, molecular weight, and molecular extinction coefficient. To determine the binding mode of SYBR Gold to DNA and to investigate the fluorescence response under varying DNA and SYBR Gold concentrations, we combined single-molecule micromanipulation experiments with a range of fluorescence measurements. We present a binding model that describes both the single-molecule manipulation and bulk fluorescence data quantitatively. Binding parameters, i. e., the binding constant (dissociation constant) $K_d$ and the binding site size n, were determined independently from both single-molecule manipulation and fluorescence experiments and were found to quantitatively agree. The close agreement between binding parameters determined from micro-manipulation and fluorescence strongly suggests that intercalation is the sole binding mode of SYBR Gold that enhances fluorescence upon DNA binding. In addition, we performed single-molecule binding measurements for the closely related compound SYBR Green I, which we find to intercalate with binding parameters very similar to SYBR Gold.

For SYBR Gold, we observe a reduction of fluorescence intensity at SYBR Gold concentrations $> 2.5$ µM (for typical experimental path lengths $\sim 5$ - $10$ mm) and distinguish quenching mechanisms by fluorescence lifetime measurements. Based on our experimental results, we present practical guidelines for optimal DNA detection and quantitative DNA sensing applications using SYBR Gold.

### 4.3.3  *Results*

To investigate the binding mode of SYBR Gold to DNA and to quantitatively monitor the resulting changes in DNA properties and fluorescence increase upon SYBR Gold binding, we use different, complementary techniques. First, we determined the molecular structure of SYBR Gold and its extinction coefficient to calibrate the concentration of the stock solution. Then, in a first series of experiments, we use MT micromanipulation to monitor binding and examine the effects of SYBR Gold and of the related dye SYBR Green I on the structural and mechanical properties of DNA under controlled stretching forces and degrees of supercoiling. In a second set of experiments, we monitor SYBR Gold fluorescence in the presence of various concentrations of dye and DNA via fluorescence spectroscopy.
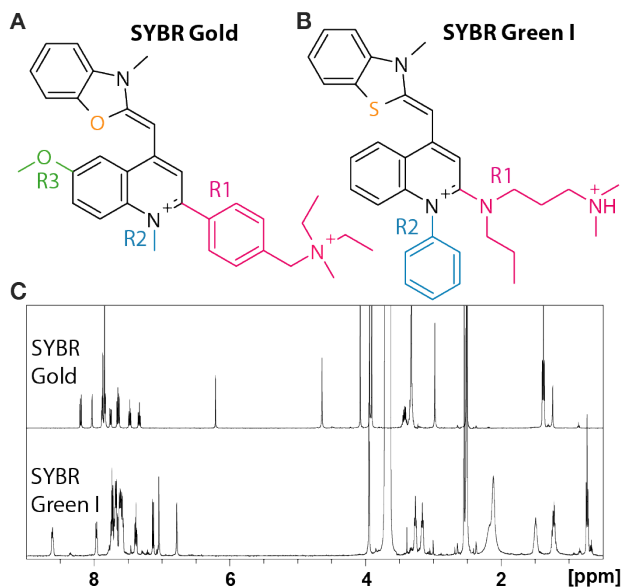
Figure 16: SYBR Gold structure and ^{1}H NMR spectra. (A) The structure of SYBR Gold as determined by NMR studies and mass spectrometry. For clarity, the side chains are shown in color and named R1, R2, R3. (B) The structure of SYBR Green I from [153]. The protonation state of the side chain R1 is for aqueous solution near neutral pH. (C) ^{1}H NMR spectra of SYBR Gold and SYBR Green I recorded in DMSO-d6.

#### 4.3.3.1 *SYBR Gold structure determination*

Using NMR analysis and mass spectrometry, we determined the molecular structure of SYBR Gold to be 2-(4-[diethyl(methyl)ammonio]methylphenyl)-6-methoxy-1-methyl-4-[(2Z)-3-methyl-1,3-benzoxazol-2-ylidene]methylquinolin-1-ium (Figure 16A). The structure assignment used one-dimensional (1D) ^{1}H and ^{13}C spectra (Figure 16C and Figure 24) as well as several sets of two-dimensional (2D) correlation spectra (See "Structure determination" in Materials and Methods (Section 4.3.9) and Supplementary Table 2). The main population in the mass spectrum is at m/z = 247.6, in excellent agreement with the prediction from the structure of m/z = 247.5 and charge +2, corresponding to a molecular mass of SYBR Gold of 495.2 Da (Figure 26). Minor populations are found at m/z = 408.2 and around 480 and very likely correspond to fragments of the molecule with z = +1 after dissociation of one or several methyl groups at the side chain amine. The SYBR Gold core structure consists of benzoxazole and quinoline heterocycles connected by a monomethine group.

It is identical to the core of SYBR Green II and similar to the core structures of SYBR Green I, Pico Green, and SYBR Safe, which feature a benzothiazole instead of the benzoxazole [153] (Figure 16B). In addition to O vs. S in the core, the main differences between the SYBR family dyes are in the side chain substitutions of the quinolone moiety (labeled R1-R3 in Figure 16A,B). SYBR Gold has a charge of +2 in aqueous solution around neutral pH as well as in DMSO, in contrast to SYBR Green I, which is divalent in aqueous solution, but monovalent in DMSO.

### 4.3.3.2  *SYBR Gold and SYBR Green I lengthen the DNA contour*

To determine the binding mode and influence on DNA structure of SYBR Gold and SYBR Green I we performed MT experiments at varying concentrations using a custom-built multiplexed MT setup (Figure 17A and Materials and Methods (Section 4.3.9)). To assess to what extent SYBR Gold or SYBR Green I binding lengthens the DNA contour, we first performed DNA stretching experiments in the presence of increasing concentrations of dye on torsionally relaxed (nicked) DNA. We focused on the force regime below 5 pN for our force–extension measurements: in this regime the DNA extension is well described by the WLC model of entropic stretching elasticity [59] and we can neglect enthalpic contributions to stretching and the force-dependence of intercalative binding [160, 171, 181]. In the absence of dye the response of DNA to force shows the characteristic response of entropic stretching elasticity (Figure 17B, dark blue circles). A fit to the WLC model [182] (Figure 17B, dark blue line) yields a contour length $L_C = (2.5 \pm 0.1)$ µm (mean and standard deviation from ten independent measurements), in close agreement with the expected crystallographic length of 2.6 µm expected for a 7.9 kbp DNA.

We then examined the force-extension response of torsionally unconstrained DNA at increasing concentrations of SYBR Gold (Figure 17B, curves from blue to red) and SYBR Green I (Figure 27A, curves from blue to red). Fitting the WLC model to the force-extension data demonstrates that the contour length of the molecule systematically increases with increasing dye concentration: compared to the contour length of bare DNA, the contour length of DNA in the presence of $\sim$ 10 µM SYBR Gold or SYBR Green I is increased by a factor of 1.7. A contour length increase upon binding by $\sim$ 1.7-fold is in line with previous force spectroscopy measurements on SYBR Gold [160] and indicative of an intercalative binding mode [116, 165, 171].

An increase of the contour length by $\sim$ 1.7 fold is very unlikely to result from minor or major groove binding and is similar to the length increase in the DNA overstretching transition at much higher forces, which both have been suggested to be limited by the dihedral sugar angle in the DNA backbone [175]. The increase in the contour length follows a binding curve behavior and saturates at concentrations $\geq$ 2.5 µM (Figure 17C and Figure 27C). To
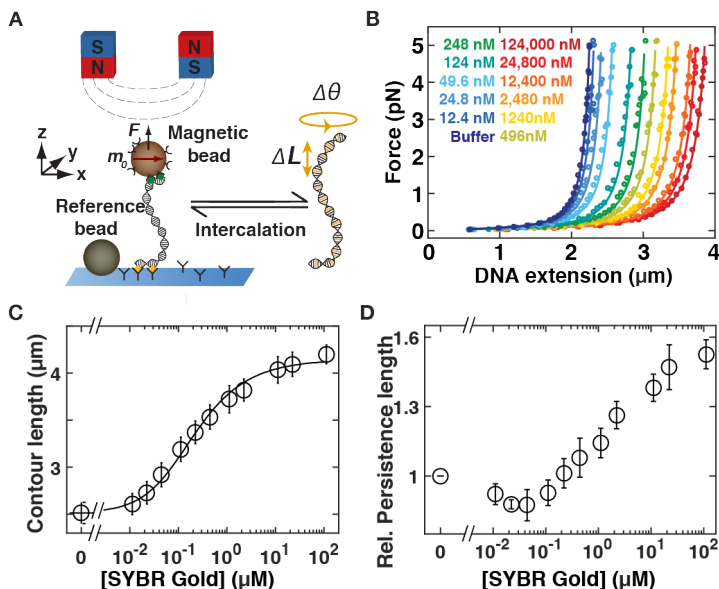
Figure 17: Effects of SYBR Gold on the force-extension behavior of DNA. (A) Schematic of MT. DNA molecules are tethered between a surface and magnetic beads in a flow cell. Permanent magnets above the flow cell enable the application of stretching forces and torques, respectively. Upon intercalation, the DNA molecules lengthen and change their equilibrium twist. (B) Force-extension curves for 7.9 kbp DNA in the presence of increasing concentrations of SYBR Gold (increasing concentrations from blue to red indicated in the Figure legend). Symbols are raw data, lines are fits of the WLC model. A systematic increase the DNA extension with increasing SYBR Gold concentration is apparent. (C) DNA contour length determined from fits of the WLC model as a function of SYBR Gold concentration. The black line is a fit to the McGhee–von Hippel model (reduced $\chi^2 = 0.18$; see main text for details), with a dissociation constant $K_d = (2.73 \pm 0.26) \times 10^{-7}$M and a binding site size $n = 1.67 \pm 0.04$. (D) DNA bending persistence length from WLC fits measured as a function of the dye concentration, normalized to the bending persistence length measured for bare DNA, indicating that the persistence length increases with increasing amount of SYBR Gold. Data points and error bars in panels C and D are the mean and standard deviation from at least ten independent measurements. In panel B one typical experiment is shown for clarity.

quantitatively determine binding parameters from the mechanical response of DNA, we employ the McGhee-von Hippel model (Equation 52 in Materials and Methods (Section 4.3.9)) [105]. The fractional number of bound dye molecules

is computed from the fitted contour length $L_C$ (c) at a given concentration $c$ by Equation 53. We use a value for the length increase per dye molecule bound of $\Delta z = 0.34$ nm, typical for intercalation [106, 116, 160, 171].

Fitting the McGhee-von Hippel model to the contour length data determined from our force-extension measurements, we find the dissociation constant $K_d$ = $(2.73 \pm 0.26) \times 10^{-7}$M and a binding site size $n = 1.67 \pm 0.04$ for SYBR Gold and very similar values of $K_d = (3.33 \pm 0.7) \times 10^{-7}$M and $n = 1.77 \pm 0.06$ for SYBR Green I. Errors are obtained from a "bootstrapping" procedure [183] by generating 1000 synthetic data sets from the experimental data and computing the standard deviation over repeated McGhee-von Hippel fits. The value of the binding site size $n$ can be interpreted as SYBR Gold or SYBR Green I intercalation at saturation occurring slightly more than at every other base pair [184], similar to other monointercalators with similar structures [116, 160, 171, 185].

In addition to an increase in DNA contour length upon SYBR Gold binding, the effective bending rigidity is also changing (Figure 2D). We found $L_P = (38 \pm 4)$ nm in the absence of dye. This value is in agreement though slightly lower than reported data for DNA persistence length in PBS [116]. With increasing SYBR Gold concentration, the persistence length initially stays constant or decreases very slightly up to a concentration of $\sim 0.16$ µM and then significantly increases at higher dye concentrations (Figure 2D). In comparison to the persistence length of bare DNA, the persistence length of DNA in the presence of $\sim 10$ µM SYBR Gold increases by a factor of 1.55.

In contrast, for SYBR Green I we observe no systematic change in $L_P$ (Figure 27D). Previous studies of intercalators have reported both decreases in effective bending stiffness, e. g.for ethidium bromide, PicoGreen, or a Ru(II) metallo-intercalator [116, 185, 186], but also constant or increasing stiffness, e. g.for the bis-intercalators YOYO and TOTO [179, 187, 188]. We speculate that the observed increase of $L_P$ upon SYBR Gold binding might be due to steric interactions of the bulky phenyl group in the side chain at position R1, which is missing in the otherwise similar dyes PicoGreen and SYBR Green I.

### 4.3.3.3  *SYBR Gold and SYBR Green I untwist DNA*

Force-extension measurements of torsionally unconstrained DNA in the presence of different concentrations strongly suggest that SYBR Gold and SYBR Green I both bind DNA in an intercalative binding mode. To further investigate their binding to DNA, we probe the effects of varying concentrations of dye on DNA twist using rotationally constrained DNA molecules [116]. We control the DNA linking number $Lk$ by rotation of the magnets and monitor DNA extension as a function of applied magnet turns at a low constant force F = 0.5 pN (Figure 18A).
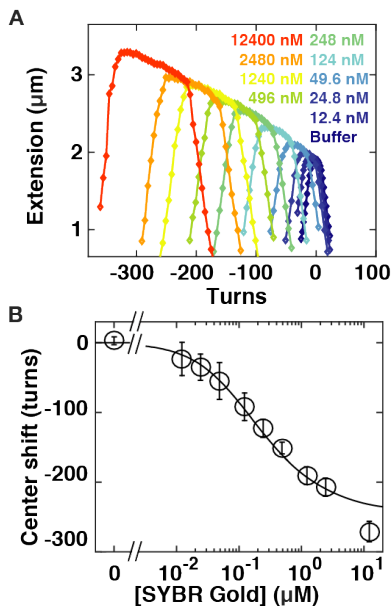
Figure 18: Effects of SYBR Gold on DNA twist. (A) Rotation-extension curves for 7.9 kbp DNA at F = 0.5 pN in the presence of increasing concentrations of SYBR Gold. The SYBR Gold concentrations are (from blue to red) 0, 12.4, 24.8, 49.6, 124, 248, 392, 1240, 2480, 12,400 nM. With increasing concentrations of SYBR Gold the rotation curves shift to negative turns; the DNA length at the center of the curves increases; and the rotation-extension curves broaden. (B) Quantification of the shift in the center position of the rotation-extension curves as a function of the SYBR Gold concentration. The center positions were determined from fitting slopes in the positive and negative plectonemic regime and by computing the intersection of the two slopes. The black line is a fit of the McGhee–von Hippel model (reduced $\chi^2 = 2.9$; see main text for details), with the dissociation constant $K_d$ and binding site size $n$ set to the values determined from the force extension data (Figure 17) and the unwinding angle per SYBR Gold intercalation determined from the fit to be $\Delta\theta = (19.1 \pm 0.7)^\circ$. Data points and error bars in panel B are the mean and standard deviation from at least 14 independent measurements. In panel A one typical experiment is shown for clarity.

In the absence of dye, we observe the characteristic response of bare DNA (Figure 18A, dark blue data): Initially the change in turns ($\Delta Lk$) leads to elastic twist deformations of DNA that minimally affect the tether extension. Subsequently, the DNA buckles to form plectonemic supercoils. In the plectonemic regime, a further increase of $\Delta Lk$ results in a linear reduction of its end-to-end

extension. For measurements at low forces (here F = 0.5 pN), the response of the DNA is symmetric about $Lk_0$ (i. e. zero applied turns, corresponding to a torsionally relaxed molecule): if we introduce positive or negative turns the DNA forms positive or negative plectonemic supercoils, respectively. Throughout, we use the number of applied turns where the DNA tether is torsionally relaxed in the absence of added SYBR Gold, i. e. $Lk = Lk_0$, as a reference.

The point corresponding to $Lk = Lk_0$ was determined as the midpoint of the symmetric rotation curve (Figure 28A). Addition of increasing concentration of SYBR Gold or SYBR Green I leads to dramatic changes in the shape and position of the extension vs. applied turns curves (Figure 18A and Figure 27B, increasing dye concentration from blue to red). There are four effects that become increasingly pronounced with increasing dye concentration: i) an overall increase of the DNA tether length, ii) a shift of the centers of the curves towards negative turns, iii) a broadening of the curves, i. e. an extension of the pre-buckling regime, and iv) a negative slope of extension vs. turns in the pre-buckling regime. In the following, we will discuss each of these observations:

(i) The increase in the extension with increasing SYBR Gold or SYBR Green I concentration is readily understood from the force-extension measurements discussed in the previous section. The center of the rotation-extension curves corresponds to torsionally relaxed DNA for which a systematic length increase with increasing SYBR Gold concentration by up to $\sim 1.7$-fold at saturating dye concentrations was observed in the force-extension measurements (Figure 17C).

(ii) The shift in center position of the rotation-extension curves with increasing dye concentration compared to bare DNA is indicative of DNA unwinding upon binding, which is again consistent with intercalation. We can understand the shift following the addition of SYBR Gold or SYBR Green I by considering that our DNA molecules are torsionally constrained ($Lk$ is a topological constant). If dye binding causes a change in the DNA $Tw$, compensatory changes in $Wr$ must occur, which, in turn, result in a reduction of the DNA end-to-end extension due to the formation of plectonemes. We quantified the shift in the extension curves by linearly fitting the extension vs. applied turns response in the plectonemic regime for both positive and negative plectonemes and determine the center of the curve as the intersection of the two slopes. Plotting the shift in the rotation curve centers as a function of the SYBR Gold concentration (Figure 18B), we again obtain a binding curve behavior. We fit the center shifts by $\Delta Tw([dye]) = \gamma \cdot N_{bp} \cdot \Delta\theta$, where we use $\gamma$ as computed from the force extension measurements (Figure 17C). The change in DNA twist per binding event $\Delta\theta$ is treated as a fitting parameter. The resulting fit (Figure 18B, solid line, and Figure 27E) gives $\Delta\theta = (19.1 \pm 0.7)°$ for SYBR Gold and $\Delta\theta = (19.3 \pm 1.3)°$ for SYBR Green I. The errors were computed as the standard deviation over fits to 1000 synthetic bootstrap data sets. The

fitted values for $\Delta\theta$ are comparable to values found for other intercalators using magnetic tweezers manipulation, for example $(27.3 \pm 1)°$ for ethidium bromide [116, 189] or $(21 \pm 14)°$ for Pico Green [185] (Supplementary Table 6). The very similar values for $\Delta\theta$ measured for SYBR Gold and SYBR Green I suggest that the side chains R1-R3 (Figure 16A,B), where SYBR Gold and SYBR Green I differ, do not significantly contribute to the intercalation geometry. In contrast, the phenanthridine moiety of ethidium appears to lead to greater unwinding of the DNA helix compared SYBR Gold or SYBR Green I. The slopes in the plectonemic regime at F = 0.5 pN are the same, within experimental error, for positive and negative supercoils and also do not change, within error, with increasing concentrations of SYBR Gold or SYBR Green I (Figure 28B and 27F).

(iii) and (iv) Broadening of the rotation curves and a slope in the pre-buckling regime for SYBR Gold and SYBR Green I (Figure 18A, Figure 28C for SYBR Gold, and Figure 27B, Figure 27G for SYBR Green I) are similar to what has been observed for other intercalators, notably ethidium bromide [116, 189], PicoGreen [185], and the bis-intercalator YOYO-1 [180]. The two effects can be understood from the properties of the DNA tethers and how they are changed upon SYBR Gold intercalation. Fundamentally, a molecule buckles if the energy required to form a plectoneme becomes less than the twist energy stored in the chain induced by adding turns to the molecule. For naked DNA in the pre-buckling regime, the torque builds up as $\Gamma = (k_B T \cdot \frac{C}{L_C}) \cdot 2\pi \cdot \Delta Lk$, where $k_B$ is the Boltzmann constant, $T$ the absolute temperature, and $C$ the torsional persistence length. Buckling occurs once the built-up torque reaches the critical torque for buckling $\Gamma_{buck}$, which increases with increasing bending persistence length, approximately [190, 191] as $\Gamma_{buck} \approx (k_B T \cdot L_P F)^{\frac{1}{2}}$. Part of the broadening of the rotation curves can, therefore, likely be explained by changes in the mechanical properties of DNA in the presence of SYBR Gold. The observed increase in bending persistence length (Figure 2D) will tend to increase the number of turns required for buckling (yet only by $1.61/2 \approx 1.25$-fold); similarly, a decrease in the torsional persistence length, as has been observed for ethidium bromide upon intercalation [192], would increase the number of turns required for buckling and broaden the curves [116].

However, in addition to changing mechanical properties in the presence of intercalation, torque-dependent intercalation will also contribute to the broadening of the rotation curves. The extension is maximal not at the center of the rotation-extension curve, as is the case for bare DNA, but at negative turns just before buckling, due to the overall slope in the pre-buckling regime. The dependence of tether extension on the number of applied turns at a given force and SYBR Gold or SYBR Green I concentration suggests that the application of a negative torque increases binding, whereas the application of a positive torque hinders it, which is to be expected from Le Chatelier's principle as intercalation unwinds the DNA helix.

We note that the slopes of the plateaus in the pre-buckling regime corresponded roughly to the slope of the curve connecting the center position of the rotation-extension curves, similar to what has been observed for ethidium bromide [189]. The center positions of the rotation-extension curves are given by the coupling between DNA elongation and untwisting upon intercalation. The observation that the slope in the pre-buckling plateaus matches the slope of the line connecting the rotation curve centers suggests that upon twisting dye-bound DNA, the applied turns are predominantly absorbed by torque-induced intercalation, again suggesting an important role of torque-dependent binding, due to the unwinding of the helix upon intercalation. In conclusion, the results of our DNA micromanipulation experiments reveal that SYBR Gold and SYBR Green I binding to DNA systematically lengthens, by up to $\sim 1.7$-fold, and unwinds DNA, by $(19.1 \pm 0.7)°$ and $(19.3 \pm 1.3)°$, respectively, per binding event, strongly suggesting intercalative binding for both dyes.

### 4.3.3.4  *SYBR Gold fluorescence enhancement by DNA intercalation*

To relate the SYBR Gold binding behavior revealed by the MT measurements to SYBR Gold fluorescence, we first determined absorption, excitation, and emission spectra (Figure 25A,B) of the dye in the presence of DNA. The absorption spectra show a systematic increase of absorbance with SYBR Gold concentration, at fixed DNA concentration, with a peak around 490 nm (Figure 25A) and a second absorption band below 300 nm, consistent with previous measurements [158, 159]. The position of the main visible absorbance peak shifts to shorter wavelength with increasing SYBR Gold concentrations at constant DNA concentration (Figure 19A). The position of the peak is well described by a model (Figure 19A, solid line) that assumes fixed absorbance peak wavelengths $\lambda_{max,free}$ and $\lambda_{max,bound}$ for free and bound SYBR Gold, respectively, and a linear superposition of the form

$$\lambda_{max}(c_{total}, c_{DNA}) = \frac{c_{free}}{c_{total}} \cdot \lambda_{max,free} + \frac{c_{bound}}{c_{total}} \cdot \lambda_{max,bound} \qquad (50)$$

The free and bound SYBR Gold concentrations are computed from the finite concentration McGhee-von Hippel model (Equation 57), using the $K_d$ and $n$ values determined from the MT force-extension measurements (Figure 17). The absorbance peak wavelengths are determined from a fit as $\lambda_{max,free} = 486$ nm and $\lambda_{max,bound} = 494$ nm, very close to the previously reported values of 487 nm and 495 nm or 496 nm for free and bound SYBR Gold, respectively [158, 159] and in excellent agreement with the position of the maximum of 486 nm determined in the absence of DNA (Figure 23). The absorbance increases linearly with increasing SYBR Gold concentration (Figure 25C), which suggests that absorption does not depend on the dye being intercalated or in free solution (since the DNA concentration is fixed for the data set in Figure 25C). The slope of the linear dependence agrees well with the value for $\epsilon_{486nm}$ used in
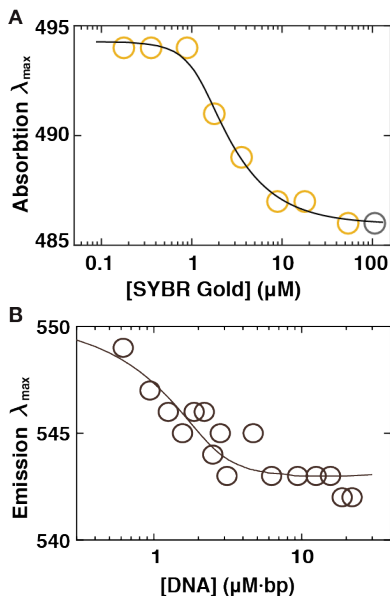
Figure 19: Shifts in SYBR Gold absorbance and emission spectra. (A) Position of the absorbance maxima of the SYBR Gold absorbance spectra (Figure 25A) as a function of the SYBR Gold concentration (circles). The peak of the spectrum at the highest concentration is noisy, as the dynamic range of the instrument is approached, thus the point from this spectrum is included but greyed out. The solid line is a fit to the finite concentration McGhee-von Hippel model with the wavelengths for maximum absorbance of free $\lambda_{max,free}$ and intercalated $\lambda_{max,bound}$ SYBR Gold as the only fitting parameter (see main text and Equation 50). From the fit we find $\lambda_{max,free}$ = 486 nm and $\lambda_{max,intercalated}$ = 494 nm. (B) Position of the emission maxima at constant SYBR Gold concentration (2.5 µM) and varying DNA concentrations. The data are well described by the model in Equation 50, with binding parameters $K_d$ and $n$ fixed to the values determined from the MT measurements (analogous to panel A). From the fit we find for $\lambda_{max,free}$ = 550 nm and $\lambda_{max,bound}$ = 543 nm for emission.

the concentration determination using a different instrument (Figure 25C and Methods (Section 4.3.9)), which represents a consistency check.

The excitation and emission spectra exhibit single peaks in the range probed (Figure 25B). While the position of the excitation peak at 496 nm does not shift significantly upon binding (Figure 25D), we observe a systematic shift for the emission peak (Figure 19B). The emission data are well described by the model that was fit to the absorbance data (Equation 50), using again

the finite concentration McGhee-von Hippel model with $K_d$ and $n$ fixed to the values determined from the MT measurements and fitting $\lambda_{max,free}$ and $\lambda_{max,bound}$ for emission. We find $\lambda_{max,free} = 550$ nm and $\lambda_{max,free} = 543$ nm for emission, similar to, but slightly higher than the values reported previously [158, 159]. The difference is likely within experimental error and we note that the magnitude of the shift is very similar to what was previously reported. The fact that the shifts in the absorbance and emission spectra follow the same binding curve as determine from mechanical manipulation in the MT strongly suggests that intercalation is the relevant binding mode for fluorescence, which is fully consistent with the molecular mechanism proposed for the fluorescence enhancement of unsymmetric cyanine dyes by impeding twisting about the monomethine bridge [193].

SYBR Gold is structurally related to SYBR Green I (Figure 16B) and thus to the family of unsymmetric cyanine dyes based on the thiazole orange (TO) chromophore. TO is composed of a benzothiazole and quinoline heterocycle coupled via a monomethine bridge (Figure 16A). Compared to TO, SYBR Gold has additional residues at position R1 and R3 and a benzoxazole moiety instead of a benzothiazole (Figure 16A) [193]. The atom replacement in the core and varying substituents on the quinoline heterocycles impact the observed spectroscopic features and thus account for differences observed in comparison to other members of the family. It is, however, evident that the fluorogenic character of the dyes by nucleic acid intercalation is based on a similar photophysical mechanism [193–195]. This mechanism is well described for TO (and its derivatives) where the fluorescence quantum yield is controlled by the competition of two pathways for excited state deactiviation: (i) non-radiative internal conversion via *cis / trans* isomerization around the central double bond and (ii) the radiative fluorescence transition. In aqueous solution, TO and all related derivatives are virtually non-fluorescent [195] since photoisomerization (i) is fully dominating the excited state deactivation. In more viscous solution, e. g., in glycerol, or upon interaction with nucleobases, photoisomerization, which requires a torsional motion around the monomethine bridge, becomes less efficient, giving rise to stronger fluorescence and longer excited state lifetimes.

The spectroscopic parameters we determined here for SYBR Gold are consistent with those of TO-based cyanine dyes including TO, Pico Green, and SYBR Green I [159]. In general DNA complexation of the dyes to nucleic results in: (i) increased wavelength of the absorbance maximum, (ii) decreased wavelength of the emission maximum and overall narrower absorbance/emission bands, (iii) up to 1000-fold increase in fluorescence quantum yield and (iv) strongly increased excited state lifetimes (see below).

A clear difference between SYBR Gold and the other dyes of the same family is the much larger Stokes shift ($\sim 50$ nm for SYBR Gold vs. $\sim 20$ nm for the other dyes). The larger Stokes shift for SYBR Gold might in part be explained by the

methoxy-substituent at position R3 (Figure 16A), by energetic stabilization of the fluorescent excited state via resonance effects. Similar findings were reported for (hemi)thioindigo photoswitches, where both the energetic position of the excited state minimum and its lifetime scaled with chemical substitutions at either sides of the chromophore [196–198]. Alternatively, the formation of twisted-internal charge transfer states (TICT) [199, 200] might account for variations of the Stokes shift, e.g., via varying R1 and R2 residues in SYBR Gold and SYBR Green I. Also the rotational freedom of the side chains R1-R3 in SYBR Gold and SYBR Green I in the electronic ground-state might have contributed towards spectral broadening of the free dye, which becomes restricted upon DNA intercalation [159]. We hypothesize that the exchange of the benzothiazole moiety in SYBR Green I to benzoxazole in SYBR Gold has a relative minor impact on the fluorogenic character of the two dyes. This idea is supported by spectroscopic studies of indigoid photoswitches, where an exchange of nitrogen to sulfur in the hemiindigo-moeity preserved the overall photophysical and photochemical character of the photoswitches [201, 202].

### 4.3.3.5 *Fluorescence intensity scales linearly with SYBR Gold intercalation at concentrations below 2500 nM*

To further correlate our findings from DNA micromanipulation with SYBR Gold fluorescence and to determine guidelines for optimal quantification of DNA by SYBR Gold staining, we performed a series of experiments probing the interaction of SYBR Gold with DNA by monitoring bulk fluorescence intensity values. We measured fluorescence intensities as a function of DNA and SYBR Gold concentration using three different techniques: a plate reader, a qPCR cycler with fluorescence intensity readout, and gel electrophoresis (Methods (Section 4.3.9), Figure 20A-C, and Figure 29).

The absorbance spectra showed that for concentrations $\leq 2.5$ µM SYBR Gold, the absorbance is $\leq 0.1$ (Figure 25), such that inner filter effects (i.e. absorption of the excitation intensity and/or absorption of emitted photons before detection in the measurement cell) could be neglected [203] for our measurement geometries. Fluorescence intensities recorded for a range of DNA and SYBR Gold concentrations $\leq 2.5$ µM increase with increasing DNA concentration for fixed dye concentration (data sets with different color codes in Figure 20D-F) and conversely also increased with increasing dye for fixed DNA concentration. The results obtained from the plate reader, the qPCR cycler, and gel electrophoresis are very similar (compare Figure 20D-F). The fluorescence data from the three measurement modalities were well described by the finite concentration McGhee-von Hippel model, Equation 59, with $K_d$, $n$, and $\alpha$ as fitting parameters. We find good agreement between the fitted binding parameters for the three different fluorescence measurement modalities and also between the values obtained from single-molecule MT measurements of DNA mechanics and
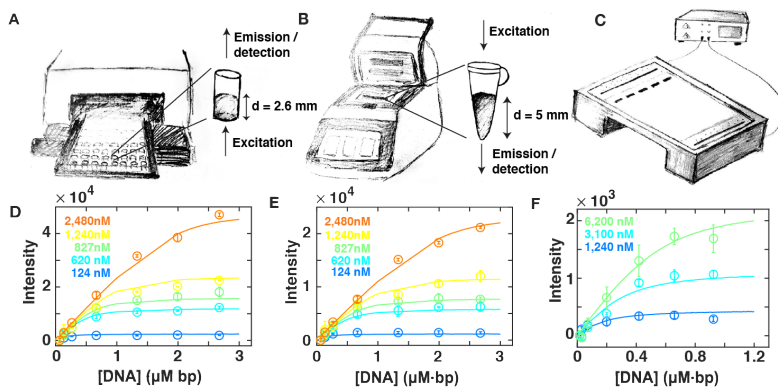
Figure 20: Fluorescence as a function of DNA and SYBR Gold concentrations below 2.5 µM dye. (A) Schematic of the 96-well plate reader setup: the SYBR Gold-DNA solution is inserted into the wells of the plate. The sample is excited from the bottom and the fluorescence intensity is measured from the top. The pathlength of the setup is d = (2.6 ± 0.05) mm. (B) Schematic of the qPCR cycler setup: the SYBR Gold-DNA solution is inserted into PCR tubes that are then placed in the thermal cycler. The sample is excited from the top and the fluorescence intensity is measured from the bottom. The pathlength of the setup is d = (5.0 ± 0.05) mm. (C) Schematic of the gel electrophoresis setup; the gel is stained with SYBR Gold after running. (D) Fluorescence intensities recorded using a plate reader and torsionally unstrained DNA (pBR322). The circles and error bars are the mean and standard deviation from at least two independent measurements. The solid line is the best fit of the finite concentration McGhee-von Hippel model (see Materials and Methods (Section 4.3.9.9) and Table 1). The SYBR Gold concentrations are (from blue to orange) 124, 620, 827, 1240, 2480 nM. (E) Fluorescence intensities recorded using a qPCR cycler. Same conditions and same fitting as for the plate reader data shown in (D). (F) Fluorescence intensities recorded using gel electrophoresis. Same fitting as for the plate reader data shown in (D). The SYBR Gold concentrations indicated in the legend text are of the staining solution. The actual concentrations in the gel are lower, by approximately 10-fold, as determined from fitting a global dilution factor (see Materials and Methods, Section 4.3.9.7).

from the fluorescence intensities (Table 1). The close agreement between the binding parameters from mechanical manipulation and from fluorescence again strongly suggests that intercalation is the only binding mode of SYBR Gold to DNA that contributes to the fluorescence signal. In addition, the data suggest that the fluorescence intensity is linear in the number of intercalated SYBR Gold molecules, over a broad range of DNA dye molecules per DNA base pair,

|  | Dissociation const. $K_d$ (µM) | Binding site size $n$ | Fluorescence int. scale $\alpha$ |
|---|---|---|---|
| Magnetic tweezers force-extension data | $0.273 \pm 0.026$ | $1.67 \pm 0.04$ | N.A. |
| Plate reader fluorescence | 0.139 | 1.46 | $4.28 \times 10^{10}$ |
| qPCR cycler fluorescence | 0.155 | 1.45 | $2.21 \times 10^{10}$ |
| Gel electrophoresis | 0.191 | 1.57 | $7.59 \times 10^{9}$ |

Table 1: McGhee-von Hippel model binding parameters determined from different data sets

which in turn rules out significant effects on fluorescence from proximity of SYBR Gold molecules in the helix, e. g. through static quenching effects.

### 4.3.3.6 *Dynamic self-quenching limits the linear fluorescence response at high SYBR Gold concentrations*

From bulk fluorescence intensity measurements at SYBR Gold concentrations > 2.5 µM, fluorescence increases with increasing SYBR Gold concentration were lower than expected (Figure 30). In a first step we used the available absorbance data (Figure 25) to correct for the inner filter effect using the formula [203]

$$I_{corr} = I_{obs} \cdot 10^{\frac{(A_{ex} + A_{em})}{2}} \tag{51}$$

where $I_{corr}$ and $I_{obs}$ are the corrected and observed fluorescence intensity and $A_{ex}$ and $A_{em}$ the path-length (indicated in Figure 20) corrected absorbance values. Correcting for the inner filter effect increases the fluorescence values significantly in this concentration regime (Figure 30, red circles). Nonetheless, even the corrected fluorescence values are still below the intensities observed at lower dye concentration and much below the values predicted by the finite concentration McGhee-von Hippel model using the parameters determined from the fits to the lower concentration data (Figure 30, solid lines). This suggests that some form of self-quenching occurs. The observed quenching above 2.5 µM SYBR Gold is unlikely due to dye-dye interactions intercalated in the DNA helix, which have been described previously for other dyes [204], as the quenching is similar for different DNA concentration, which correspond to different loading densities in the DNA helix at a given dye concentration. In particular, we do not observe significant quenching at SYBR Gold concentrations < 2.5 µM even under conditions with a very high packing density of dye in the DNA helix (Figure 20D,E).
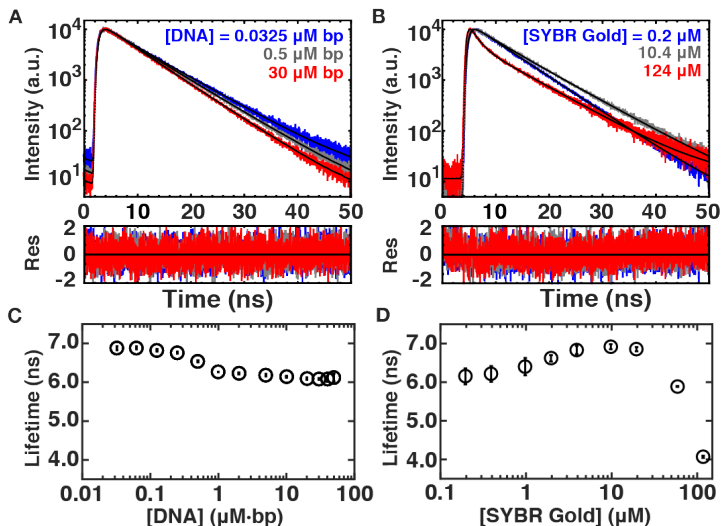
Figure 21: Fluorescence lifetime measurements. (A) Fluorescence lifetime measurements for 0.0325 (blue), 0.5 (grey) and 30 (red) µM · base pair DNA at a SYBR Gold concentration of 2.5 µM. The data are fit by a single exponential decay. (B) Fluorescence lifetime measurements for 0.2 µM (blue), 10.4 µM (gray) and 124 µM (red) SYBR Gold in the presence of a constant DNA concentration of 2 µM · bp DNA. At high dye concentrations, the data show a clearly bi-exponential decay, therefore, we fit the data by a two-exponential model (Materials and Methods, Section 4.3.9.8. (C) Fluorescence lifetimes as a function of DNA concentration determined from single-exponential fits as in (A). (D) Amplitude weighted fluorescence lifetime as a function of SYBR Gold concentration from measurements at 2 µM · bp DNA determined from two exponential fits (Materials and Methods, Section 4.3.9.8).

### 4.3.3.7 *Fluorescence lifetime measurements reveal dynamic quenching at high SYBR Gold concentrations*

To better understand the mechanism of self-quenching, we determined fluorescence lifetimes of SYBR Gold by time-correlated single photon counting. In a first set of experiments we varied the DNA concentration at a constant SYBR Gold concentration of 2.5 µM. In the absence of DNA, SYBR Gold shows a time-correlated single photon counting histogram that cannot be distinguished from the instrumental response function of our system. DNA binding results in a single exponential fluorescence decay (Figure 21A,C) with a lifetime in range of ∼ 6.5 ns. This lifetime value is similar, but slightly larger than the values reported previously [159]. The difference might be due to variations in

data analysis (tail fitting vs. reconvolution fitting) and experimental conditions (DNA sample and buffer).

At constant SYBR Gold concentration of 2.5 µM, lifetimes vary from $\sim 6.9$ ns at high loading ratios $> 1:2$ to $\sim 6.1$ ns at lower loading density of dye in the DNA helix ($< 1:10$). This is consistent with the absence of dynamic quenching between SYBR Gold molecules along the DNA helix, since this would likely lead to a reduction in the lifetime with increasing packing density (i.e., lower DNA concentration), while we experimentally observe an increase (Figure 21C). The slightly longer lifetime at high loading densities is consistent with a stabilization of the excited state and with the observed red shift in the emission (Figure 19B), possibly caused by the stiffening of the helix at high packing densities (Figure 17D).

In a second set of measurements we varied the SYBR Gold concentration while keeping the DNA concentration constant at 2 µM · bp (Figure 21B,D). For SYBR Gold concentrations $\leq 10$ µM, fluorescence decays are well described by single exponential fits, and the fitted lifetimes slightly increase up to $\sim 6.9$ ns with increasing SYBR Gold concentration (Figure 21B). However, at SYBR Gold concentrations $> 10$ µM, the lifetimes are no longer well-described by a single exponential fit. Instead, we see an additional faster decaying component appearing (Figure 21B). For consistency, we fitted the entire data set with a two-component model, with two exponential decays (described in detail in the Methods Section 4.3.9). For simplicity, we report an amplitude weighted overall decay constant in Figure 21D and the individual decay times and amplitudes in Figure 31.

The observation of a reduction in lifetime, together with a reduction in fluorescence intensity (Figure 30), for SYBR Gold concentrations $> 2.5$ µM at constant DNA concentration suggests a dynamic self-quenching mechanism. Since the data disfavor a self-quenching by intercalated dyes in the DNA helix, a more likely scenario is a dynamic quenching mechanism involving non-intercalated SYBR Gold. A quenching mechanism from free SYBR Gold in solution would imply for our data at the highest SYBR Gold concentration with a quenching decay time constant of $\sim 1$ ns (Figure 31) and a free dye concentrations of $\sim 100$ µM an apparent bimolecular quenching constant of ($\sim 1$ ns · 100 µM$^{-1} \approx 10^{13} M^{-1} s^{-1}$, which is roughly three orders of magnitude larger than diffusion controlled on-rates [203]. The most likely explanation of dynamic quenching of the intercalated SYBR Gold is that quenching occurs from SYBR Gold molecules kept in close proximity to the DNA helix, possibly due to electrostatic interactions, favoured by the fact that SYBR Gold carries two positive charges (Figure 16A) and DNA is highly negatively charged [66]. Charge interactions or, possibly, a combination of charge interactions and other association modes of SYBR Gold with the DNA helix will increase the local effective concentration

of SYBR Gold around DNA and could, therefore, facilitate dynamic quenching [203].

### 4.3.3.8   *Recommendations for quantitation of DNA using SYBR Gold staining*

Our single-molecule MT and fluorescence spectroscopy assays provide a comprehensive view of DNA-SYBR Gold interactions. This knowledge enables us to provide practical guidelines for optimal DNA detection and quantitative DNA sensing applications using SYBR Gold. For quantitative assays, it is desirable to have a linear relationship between fluorescence intensity and DNA concentration. The optimal SYBR Gold concentration to ensure a linear relation between DNA concentration (up to DNA concentrations of $\sim$ 2 µM · bp or $\sim$ 1.3 ng/µL) and fluorescence intensity as well as an optimal sensitivity for DNA detection is at 2.5 µM ($\approx$ 1:5000 dilution of the stock solution). This value for the optimal SYBR Gold concentration is 2x larger than the manufacturer's recommendation of 1:10000-fold dilution. Reliable detection is possible with lower dye concentrations, however, with a reduced range for a linear fluorescence-DNA concentration response (Figure 22A). So if linearity and high signal are important, using high dye concentrations is desirable. However, at very high dye concentration (SYBR Gold concentrations > 2.5 µM) quenching and inner filter effects become relevant for typical measurement setups and need to be corrected for to get accurate and quantitative results (Figure 22A,B). For many measurements, it is likely beneficial to avoid inner filter and quenching effects by keeping the SYBR Gold concentration $\leq$ 2.5 µM. In addition, we note that that the fluorescence intensity depends, in general, on both the dye and DNA concentration. Reporting concentrations as "dye per base pair" –as is frequently done for DNA stains– is problematic, since a large range of intensities correspond to the same dye per base pair ratio (Figure 22C,D) and since the connection between dye to base pair ratio and fluorescence intensity is many-to-one. Therefore, we advise to report both DNA and dye concentrations explicitly.

### 4.3.4   *Conclusions*

We have solved the structure of SYBR Gold by NMR spectroscopy and mass spectrometry and employed single-molecule MT that provide rotational control in addition to control of the stretching forces to probe the binding properties of SYBR Gold to DNA. The single-molecule MT assay reveals systematic lengthening (up to 1.7 times the DNA contour length in the absence of dye) and unwinding of DNA ($(19.1 \pm 0.7)°$ per SYBR Gold bound) upon SYBR Gold binding. The mechanical signature strongly suggests intercalation, with an unwinding angle at the low end of the range of previously investigated
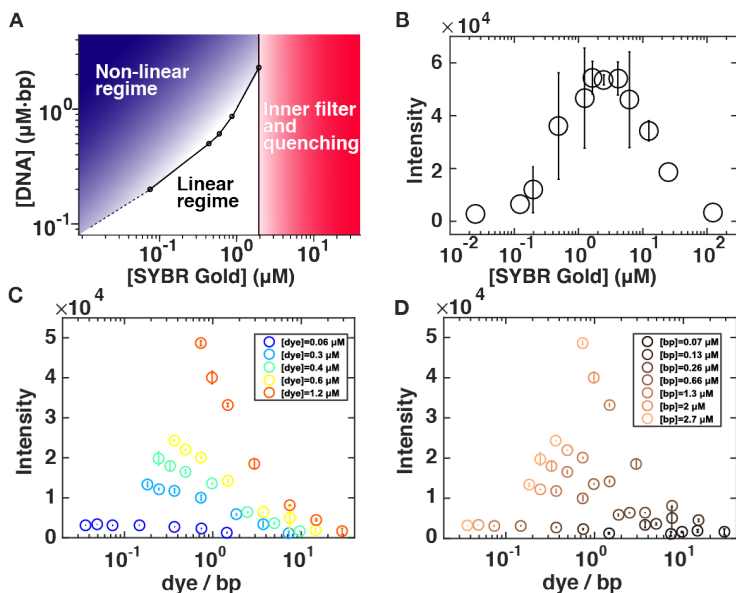
Figure 22: Recommendations for DNA quantitation by SYBR Gold fluorescence. (A) Phase diagram depicting different regimes of DNA detection by SYBR Gold fluorescence, as a function of SYBR Gold and DNA concentrations. (B) Fluorescence intensity recorded using a qPCR cycler at constant DNA concentration ($\lambda$-DNA, 2.7 µM · bp) at varying SYBR Gold concentrations. The data points are the mean values of two independent experiments including their standard deviations or stem from just one experiment. (C) Fluorescence intensity recorded using a plate reader as a function of the dye per base ratio. The circles and error bars are the mean and standard deviation from at least two independent measurements. The SYBR Gold concentrations are (from blue to orange) 0.124, 0.62, 0.83, 1.24, 2.48 µM. These are the same data as in Figure 21D plotted as a function of dyes per base pair. (D) Fluorescence intensity recorded using a plate reader as a function of the dye per base ratio. The circles and error bars are the mean and standard deviation from at least two independent measurements. The DNA base pair concentrations are (from dark to light brown) 0.07, 0.13, 0.26, 0.66, 1.3, 2, 2.7 µM.

intercalators. Fitting the McGhee-von Hippel model to the MT data, we find a binding constant $K_d = (2.73 \pm 0.26) \times 10^{-7}$M and binding site size of $n = 1.67 \pm 0.04$. These findings are in good agreement with the parameters from fluorescence intensity experiments for dye concentrations of up to $\sim 2.5$ µM suggesting that the intercalative binding mode is responsible for the observed fluorescence.

Additionally, we find that for SYBR Gold concentrations $> 2.5$ µM, fluorescence quenching and inner filter effects become relevant. While we see no evidence for quenching between dyes intercalated in the helix, our data provide clear evidence for dynamic quenching from dyes in a loosely bound (likely at least partially driven by electrostatics) „cloud" around the DNA. Overall, we found that while SYBR Gold is advantageous due to its high quantum yield and brightness, it has a relatively narrow range of concentrations that strike a balance between avoiding inner filter effects and quenching, while staining DNA with a linear fluorescence to DNA concentration relationship. In summary, our work shows how using complementary techniques can provide a highly quantitative and comprehensive view of DNA-small molecule interactions and we anticipate our approach to be broadly applicable to other DNA binding agents.

### 4.3.5   *Acknowledgements*

### 4.3.6   *Funding*

### 4.3.7   *Conflicts of Interest*

The authors declare no competing interests.

### 4.3.8   *Data Availability statement*

Data are available upon request.

### 4.3.9  *Materials and Methods*

#### 4.3.9.1  *Chemicals and Concentration Determination*

SYBR Gold and SYBR Green I were purchased as "0.5 mL 10,000x concentrate in DMSO" from Invitrogen. For SYBR Green I, we determined the absorbance at 495 nm of the stock solution to be $585 \pm 35$ (the error is from the uncertainty of the fit to data from a serial dilution) and used the published [205] molecular extinction coefficient $\epsilon_{495nm} = 58000$ $M^{-1}$ $cm^{-1}$ to determine the stock concentration to be $(10.1 \pm 0.6)$ mM. For SYBR Gold, no molecular extinction coefficient had been reported and the concentration of the stock solution is not specified by the vendor. We therefore determined the concentration and molecular extinction coefficient by lyophilizing the stock solution (2d at 0.04 mbar) and weighing the dried sample. We determined the mass of the lyophilized stock to be $(3.5 \pm 0.4)$ mg (with a 10% uncertainty from sample handling).

The mass of the SYBR Gold cation was determined to be 495.2 Da by mass spectrometry, see the next section. Assuming further 2 chloride ions as the relevant anions [153, 201], we find a concentration of the stock solution of $12.4 \pm 1.2$ mM. From a serial dilution, we determined the absorbance of the lyophilized stock at 486 nm to be $703 \pm 10$ (Figure 23), which gives a molar extinction coefficient for SYBR Gold of $\epsilon_{486nm} = 57000$ $M^{-1}$ $cm^{-1}$. We found that the concentrations determined from absorbance measurements vary significantly (by $\sim 50\%$ greater than our measurement uncertainty) for different SYBR Gold stocks supplied by the same vendor (Figure 23 and Supplementary Table 2). We, therefore, determined the concentrations for each stock solution used in the experiments separately from absorbance measurements (Figure 23).

#### 4.3.9.2  *Structure Determination*

We revealed the molecular structure of SYBR Gold using a combination of NMR and mass spectrometry. All NMR spectra were acquired at 298 K on different NMR spectrometers (Bruker Avance III, with 500 / 600 / 800 / 950 MHz $^1$H frequency, mostly equipped with helium-cooled cryoprobes; Bruker Daltonik, Germany). Besides 1D $^1$H and $^{13}$C spectra (Figure 16 and Figure 24), sets of 2D spectra were acquired to enable the assignment and structure elucidation (2D DQF-COSY, 2D TOCSY, 2D long-range COSY, 2D NOESY, $^1$H,$^{13}$C-DEPT, $^1$H,$^{13}$C–HSQC, $^1$H,$^{13}$C–HMBC, $^1$H,$^{15}$N–HSQC, $^1$H,$^{15}$N–HMBC); sample impurities were identified from DOSY experiments. Starting from the characteristic signal of the cyanine bridge (position 2a', singlet at ca. 6.2 ppm $^1$H / 7.4 ppm $^{13}$C shift), the whole benzo-X-azole / quinoline scaffold could be assigned from DQF-COSY and $^1$H,$^{13}$C –HMBC correlations.

A comparison of the shifts of positions 2a', 3a', 7a', 3a'-CH$_3$ and $^{15}$N3' (Supplementary Table 3 - 5) with the values for SYBR Safe, Thiazole Orange

[206] and SYBR Green I (X = S) on one hand, and SYBR Green II and the simulated data for SYBR Gold (X = O) on the other hand [207] unambiguously showed that SYBR Gold must have a benzo-oxazole moiety in its scaffold (which is also in agreement with the MS data). Position and identity of the O-CH$_3$ substituent at position 6 of the quinoline moiety were derived from the DQF-COSY and $^1$H,$^{13}$C–HMBC correlations in this part and the characteristic $^1$H and $^{13}$C shifts of the methyl signals. The structure of the "tail" sidechain (R1) was established from $^1$H,$^{13}$C–HMBC correlations between the quinolone moiety and the signals of the 1,4 disubstituted phenyl ring in the tail. The quaternary nitrogen could be identified by $^1$H,$^{15}$N–HMBC correlations between $^{15}$N$\zeta$ and the $^1$H signals of the surrounding positions $\epsilon$, $\theta$ and N$\zeta$–CH$_3$. After establishing the structure of SYBR Gold, additional long range-COSY and NOESY correlations were studied to see if they would confirm the structure. All correlations found in the experimental NMR spectra were in full agreement with the proposed structure of SYBR Gold. An assignment of the observed NMR peaks is presented in Supplementary Table 3 - 5.

Fluorophore standards were run on an ultra-high-performance liquid chromatographic (UHPLC) system coupled to a Bruker timsTOF MS (Bruker Daltonik, Bremen, Germany). Five microliter were injected and separated using a C8 reversed phase column (Ultra C8, 3 µm, 2.1 × 100 nm, Restek GmbH, Bad Homburg, Germany) with 300 µL flow per minute at 60 °C. Solvents were water (A) and a mixture (70/30 v/v) of acetonitrile and isopropanol (B), both containing 1% ammonium acetate and 0.1% acetic acid. The gradient started with 1 min at 55% B followed by a ramp to 99% B within 14 min. This was kept constant for 7 min and returned to 55% B with additional 4 min of re-equilibration.

Mass spectra were acquired by otofControl 4.0 in negative MSMS mode from 100-1300 m/z mass range. The most important parameters are set as followed: capillary voltage 4000 V, nebulizer pressure 1.8 bar, nitrogen dry gas 8 L/min at 200 °C, collision energy 70 eV, Collision RD 800 Vpp (volt peak to peak). The evaluation was performed by Data Analysis 4.5 provided by Bruker (Bruker Daltonik, Germany).

### 4.3.9.3  *DNA constructs*

For MT measurements, we use a 7.9 kbp DNA construct, prepared as described previously [116]. The construct is generated by ligating handles ($\sim$ 600 base pair) with either multiple biotin or multiple digoxigenin moieties fragments to an unmodified central DNA segment 7.9 kbp in length. Fluorescence intensity measurements of SYBR Gold are recorded in the presence of linear pBR322 plasmid DNA (NEB), which is produced by restriction of supercoiled circular pBR322 using restriction enzyme EcoRV (NEB) according to the protocol provided by the manufacturer. Completion of the linearization reaction was

validated by agarose gel electrophoresis. Absorption, excitation and emission spectra of SYBR Gold are recorded in the presence of lambda phage DNA (NEB) due to large cuvette volumes needed, which was dialyzed against 1x phosphate buffered saline (PBS, consisting of 10 mM phosphate buffer, pH 7.4, with 137 mM NaCl and 2.7 mM KCl; Sigma-Aldrich, USA) prior to use.

### 4.3.9.4 *Magnetic tweezers setup*

Experiments on DNA are performed on a home-built MT setup described previously [135]. Two magnets ($5 \times 5 \times 5$ mm$^3$; W-05-N50-G, Supermagnete) are placed in a vertical configuration [135, 208] on a motorized arm with a translational motor (M-126.PD2 motor with C-863.11-Mercury controller, Physik Instrumente) as well as a rotational motor (C-150.PD motor with C-863.11-Mercury controller, Physik Instrumente) to control the magnets' rotation and z-position. The flow cell outlet is connected to a pump (ISM832C, Ismatec) for fluid handling. The setup is controlled using a Lab-VIEW software (National Instruments) described by Cnossen *et al.* [132].

Flow cells are built from two coverslips ($24 \times 60$ mm, Carl Roth, Germany). The bottom coverslip was first functionalized using (3-Glycidoxypropyl)trimethoxysilane (abcr GmbH, Germany) and consecutively incubated with 50 µL of a 5000x diluted stock solution of polystyrene beads (Polysciences, USA) in ethanol (Carl Roth, Germany) to serve as reference beads for drift correction. The top coverslip has two openings with a radius of 1 mm for liquid exchange in the flow channel. The bottom and the top coverslip are glued together by a single layer of melted Parafilm (Carl Roth, Germany), precut to form a $\sim 50$ µL channel connecting the inlet and the outlet opening of the flow cell. After the flow cell assembly, one flow cell volume of 100 µg/mL anti-digoxigenin (Roche, Switzerland) in 1x PBS is introduced, and incubated overnight (at least 12h). Subsequently, the flow cell is rinsed with 1 mL of 1x PBS and then passivated using a commercial passivation mix (BlockAid Blocking Solution, Thermo-scientific) for 1 h to minimize non-specific interactions. Unbound material is removed from the flow cell by flushing with 1 mL of 1x PBS.

As magnetic beads we use 1 µm diameter MyOne beads (Life Technologies, USA). The DNA construct is attached to the streptavidin coated beads by incubating 0.5 µL of picomolar DNA stock solution and 2 µL beads in 250 µL PBS for 5 min. Then, the bead-coupled DNA constructs are introduced into the flow cell to bind to the flow cell surface via multiple digoxigenin:anti-digoxigenin bonds.

### 4.3.9.5 *Magnetic tweezers measurements*

Prior to the experiments, DNA tethered beads are screened for the presence of multiple DNA tethers and torsional constraint by measuring their response to

force and torque. To find out whether a magnetic bead is bound by more than one DNA tether to the surface, we introduce negative turns under high tension (F = 5 pN). In the case of a single double-stranded DNA tether, high tension prevents the formation of plectonemes at negative linking differences due to DNA melting and consequently, no change in height is observed. In contrast, if a bead is attached via two or more double-stranded DNA molecules, the molecules form braids when the bead is rotated causing a decrease in tether extension. Beads bound by multiple tethers are discarded from further analysis. To evaluate the presence of single strand breaks, positive linking differences are introduced at low force (F = 0.4 pN). Overwinding of torsionally constrained DNA leads to the formation of plectonemes, which decrease the tether extension, whereas in nicked DNA tethers, no linking difference can be induced, and the extension remains constant on magnet rotation.

For force-extension analysis, we exclusively examine torsionally unconstrained (nicked) DNA tethers. At first, we calibrate the magnet distance-to-force relation for each bead by recording the transverse fluctuations of the beads at different magnet separations for times approximately 100-fold larger than the characteristic time of the system at the corresponding force, and analyze the power spectral density of the transverse fluctuations to quantify the force at each magnet position [139, 143]. The force-extension relation was then fitted using the WLC model [182] to extract the contour length and bending persistence length of the DNA.

To determine the force-extension behavior in the presence of different concentrations of dye, we introduce 200 µL ($\sim$ 5 cell volumes) of the lowest dye dilution and measure the tether extension at 25 magnet positions corresponding to forces in the range 0.04 pN to 5 pN. The measurements are repeated for different dye concentrations in increasing order. After each concentration change, we wait for several minutes to allow for equilibration. We use the previously calibrated force for each bead to construct force-extension curves that are fit using the WLC model to provide the contour length and persistence length as a function of concentration.

Rotation curve measurements on torsionally constrained DNA tethers start by introducing 200 µL of 1x PBS in the flow cell using the peristaltic pump, at a flow rate of $\sim$ 300 µL/min. While flushing, the magnets are positioned close to the flow cell to establish a force of 6.5 pN. The pulling force helps to prevent the magnetic beads from getting stuck on the surface, and, importantly, the field constrains the free rotation of the bead [209] during flushing, which is a requirement for determining the absolute shifts in DNA twist upon binding. During the actual measurement, the force is kept constant at 0.5 pN. While monitoring the DNA extension, we turn the magnet from negative to positive turns or from positive to negative turns. Then, we introduce 200 µL ($\sim$ 5 cell volumes) of the lowest dye concentration, wait for several minutes to

allow for equilibration, and record another rotation curve measurement at F = 0.5 pN. The experimental procedure is repeated for all dye concentrations in increasing order. Processing of the MT data was carried out using custom-written MATLAB routines.

### 4.3.9.6   *Absorption, excitation, and emission spectra*

Emission spectra on excitation at 495 nm were recorded in PBS in the wavelength range 505 nm - 700 nm and excitation spectra for emission at 537 nm were recorded in the wavelength range 400 nm - 550 nm, employing a commercial spectrofluorometer and a 1 cm path-length cuvette (Fluoromax Plus; Horiba). While keeping the SYBR Gold concentration constant at 2.5 µM, the DNA concentration in the cuvette was stepwise decreased by replacing a fraction of the DNA solution with the same volume of a buffered solution containing 2.5 µM SYBR Gold. In addition, reference measurements at the same SYBR Gold concentration in the absence of DNA and with only PBS buffer were carried out. Absorbance was recorded using an EvolutionTM 201/220 UV-Vis-spectrophotometer in a 1 cm path-length cuvette (ThermoFisher Scientific).

### 4.3.9.7   *Fluorescence intensity measurements*

Linearized pBR322 plasmid DNA at varying concentrations was pipetted (25 µL) into a well of the well plate reader (Tecan Infinite M1000 PRO; Well plate: corning black polystyrene 384 well microplate with a flat bottom, Sigma-Aldrich, catalogue number: CLS3821). The fluorescence was read out from the bottom of the wells, with the excitation and emission bandwidth set to 5 nm, the gain to 100, the flash frequency to 400 Hz, and the integration time to 20 µs. We choose the excitation and emission wavelengths to be 495 nm and 537 nm (excitation and emission maxima for SYBR Gold, as provided by Invitrogen). For control measurements, lambda phage DNA (NEB) at a constant concentration of 3.5 ng/µL and varying SYBR Gold concentration were used and performed otherwise identically.

For the qPCR cycler (CFX96 Touch Real-Time PCR Detection System, Bio Rad) fluorescence read-out experiments, again linearized pBR322 DNA was used and dilution series were filled into low-profile PCR tubes (Bio Rad, product ID: TLS-0851), which were closed with flat, optical, ultra-clear caps (Bio Rad, product ID: TCS-0803). We used the channel with absorption and emission wavelengths of 494 nm and 518 nm, respectively, which are the closest match to those of SYBR Gold (495 nm and 537 nm, respectively) and read out the fluorescence intensities at 24 °C from the top.

For the gel electrophoresis we added Gel Loading Dye Purple (6x) (NEB) to pBR322 DNA. We used 1%-agarose (Carl Roth) gels and TAE buffer (40 mM

Tris, 20 mM acetic acid, and 1 mM EDTA, pH 8.6). The gels were run for 120 min at 75 V. Afterwards the gel was removed from the gel box and placed for 20 min in 100 mL of 1.24, 3.1, or 6.2 µM SYBR Gold in TAE buffer, respectively, for staining. Subsequently, the gel was de-stained in TAE buffer for 15 min at room temperature. The gels were then visualized using a Gel Doc XR+ System (Biorad).

### 4.3.9.8 *Fluorescence lifetime measurements*

Fluorescence lifetime measurements were carried out on a homebuilt apparatus for time-correlated single-photon counting (TCSPC). Pulsed excitation was at 485 nm (PicoQuant LDH–D–C–485, controller: PicoQuant PDL 828 "Sepia II", 20 or 13.33 MHz laser repetition rate) to excite the sample cuvette. A lambda-half waveplate (Laser Components ACWP-450-650-10-2-R30 AR/AR, Ø1") and a linear polarizer (Edmund Optics POLARIZER 25.4 mm DIA UNMTD) were used to rotate and adjust the excitation polarization to vertically polarized light. Light emitted by the sample after excitation was filtered for polarization with a second linear polarizer (Edmund Optics ULTRA BB WIREGRID POL 25RND MTD) under magic angle condition (54.7°) with respect to the vertical axis. The emission polarizer was mounted inside a 3D custom-printed chassis housing with automated rotation mount (Thorlabs CRM1/M, Reichelt GRABIT SERVO), which was controlled by a processing unit (Arduino Mega 2560) for automated rotation of the emission polarizer. A lens (Thorlabs AC254-110-A) was used for higher collection efficiencies in combination with filters (AHF 488 long pass filter BLP01-488-R-25 and notch filter ZET488NF) for removal of scattered laser light before the avalanche photodiode used for detection (Excelitas SPCM-AQRH-34). Data were recorded by a TCSPC unit (PicoQuant HydraHarp 400, 16 ps TCSPC time resolution) with a commercial control and evaluation software provided by the supplier (PicoQuant SymPho Time 64). Further details are as described [210].

We diluted lambda phage DNA (NEB), dialyzed overnight against PBS, and SYBR Gold to the specified dye concentrations (0.062 to 124 µM) and analyzed the sample in a $10 \times 2$ mm$^2$ cuvette (Perkin Elmer UV/VIS Spectroscopy Cell B0631122) for 5 min for each condition. The excitation laser power was 1.5 or 15 µW in order to operate in an optimal range with the photon detection rates between 20 and 80 kHz. Additionally, we measured the instrument response function (IRF) by replacement of the cuvette with a silver mirror to direct the laser beam directly onto the APD chip, which gave the best IRF quality (scattering based approaches with e. g., Ludox suspension resulted in lower quality IRF).

For the fluorescence lifetime evaluation, we used the n-exponential reconvolution fit that is implemented in the measurement software SymPho Time 64. The optimization uses a maximum likelihood estimator, where the fluorescence

signal $I(t)$ is described as the convolution of the IRF $IRF(t - t_{off})$ with a triple exponential decay [203]:

$$I(t) = IRF(t - t_{off}) \cdot \left( A_{mm} \, e^{-\frac{t}{\tau_{mm}}} + A_{long} \, e^{-\frac{t}{\tau_{long}}} + A_{short} \, e^{-\frac{t}{\tau_{short}}} \right) + bkg \tag{52}$$

In this formula, the first exponential component $A_{mm} \, e^{-\frac{t}{\tau_{mm}}}$ accounts for a small mismatch between measured IRF (with a mirror) and the "real" IRF in the cuvette measurements. This mismatch was compensated by including a fast decay component in the fitting procedure, with a fixed decay time $\tau_{mm} = 50$ ps, which is 1-2 orders of magnitude faster than the lifetime components of the fluorophore. The fluorophore lifetime was described with two exponential decays with lifetimes $\tau_{long}$ and $\tau_{short}$, accounting for a fast component, which becomes relevant at high dye concentrations, in addition to the dominant slow lifetime. The reported lifetimes in the main text are amplitude-weighted averages $\tau_{dec} = \frac{A_{long} \cdot \tau_{long} + A_{short} \cdot \tau_{short}}{A_{short} \cdot \tau_{short}}$ of the two lifetime components $\tau_{long}$ and $\tau_{short}$. The errors for $\tau_{dec}$ are derived from the fit uncertainty of all parameter based on standard error propagation rules for non-independent combined quantities.

### 4.3.9.9 *Binding models: McGhee-von Hippel model and DNA concentration effects*

In order to describe the binding of SYBR Gold and SYBR Green I to double-stranded DNA in our single-molecule tweezers assays, where the DNA concentration is very low and, therefore, the free and total ligand concentrations approximately equal, we used the McGhee-von Hippel model of ligand-substrate binding [105] for the fractional number of molecules bound per base pair, $\gamma$:

$$\gamma = \frac{c_{free}}{K_d} \cdot \frac{(1 - n \cdot \gamma)^n}{(1 - n \cdot \gamma + \gamma)^{n-1}} \tag{53}$$

where $c_{free}$ ($\approx c_{total}$ under these conditions) is the free ligand concentration, $K_d$ is the binding (dissociation) constant (in M) and $n$ is the binding site size (in base pair). $\gamma$ was determined from the DNA contour length change with increasing ligand concentration determined in stretching experiments on rotationally unconstrained DNA as

$$\gamma = \frac{L_C(c_{free}) - L_C(0)}{\Delta z \cdot N_{bp}} \tag{54}$$

where $L_C(c_{free})$ is the DNA contour length at a certain ligand concentration, $\Delta z$ is the increase in DNA contour length per ligand bound, and $N_{bp}$ is the number of base pairs of the DNA ($N_{bp} = 7922$ for our DNA constructs). We used a fixed value for the DNA contour length increase per dye binding event

$\Delta z = 0.34$ nm, as was suggested previously for intercalators [106, 116, 160, 171].

From bulk experiments using a plate reader, qPCR cycler, or a gel imager we determined the fluorescence intensity I as a function of DNA concentration $c_{DNA}$ and dye concentrations $c_{total}$. For bulk measurements, the assumption that $c_{free} \approx c_{total}$ often does not hold, as the free ligand concentration is on the order of the bound ligand concentration and both the finite dye and DNA concentrations need to be taken into account. Therefore, we rewrote Equation 53 in terms of $c_{total}$, which is experimentally known, by expressing the total ligand concentration as the sum of free ligand concentration and bound ligand concentration:

$$c_{total} = c_{free} + c_{bound} \tag{55}$$

We define

$$\gamma = \frac{c_{bound}}{c_{DNA}} \tag{56}$$

with $c_{DNA}$ being the total DNA concentration which is also experimentally known. Subsequently, we combined Equations 55 and 56 and inserted them into Equation 53 to obtain:

$$\frac{c_{bound}}{c_{DNA}} = \frac{c_{total} - c_{bound}}{K_d} \cdot \frac{(1 - n \cdot \frac{c_{bound}}{c_{DNA}})^n}{(1 - n \cdot \frac{c_{bound}}{c_{DNA}} + \frac{c_{bound}}{c_{DNA}})^{n-1}} \tag{57}$$

We call Equation 57 the McGhee-von Hippel model for finite DNA concentrations. To fit our fluorescence intensity data with the McGhee-von Hippel model for finite DNA concentrations, we assume that the fluorescence intensity is proportional to the concentration of bound SYBR Gold molecules

$$I = \frac{1}{\alpha} \cdot c_{bound} \tag{58}$$

where $\alpha$ is a proportionality constant that we treated as a fitting parameter. For SYBR Gold the fluorescence intensity increases by more than a factor of 1000 upon binding to dsDNA [158, 159] and experimentally we found that measurements in absence of DNA give much lower fluorescence intensity than measurements even at low DNA concentrations (Figure 25, therefore, we neglected fluorescence contributions from the free dye. We substituted the concentration of bound dye molecules $c_{bound}$ in Equation 57 by $\alpha \cdot I$ to obtain the final Equation that can be fit to the fluorescence intensity data:

$$\frac{\alpha \cdot I}{c_{DNA}} = \frac{c_{total} - \alpha \cdot I}{K_d} \cdot \frac{(1 - n \cdot \frac{\alpha \cdot I}{c_{DNA}})^n}{(1 - n \cdot \frac{\alpha \cdot I}{c_{DNA}} + \frac{\alpha \cdot I}{c_{DNA}})^{n-1}} \tag{59}$$

In Equation 59, the total ligand concentration $c_{total}$ as well as the total DNA concentration $c_{DNA}$ are experimentally known, the fluorescence intensity $I$ is measured, and the dissociation constant $K_d$, the binding site size $n$, and the

proportionality factor $\alpha$ are fitting parameters. For the gel imaging data, we need to take into account that the concentration in the staining solution is not equal to the final concentration in the gel, due to dilution by the gel volume, incomplete penetration of the dye into the gel, and the final de-staining step. We, therefore, rescale the SYBR Gold concentrations for all gel data with a single global dilution factor, which we determine to be $\approx 0.1$.

4.3.10  *Supplementary Tables and Figures*

| Stock | LOT number | Extrapolated absorbance at 495 nm measured via UV-Vis |
|-------|------------|-------------------------------------------------------|
| 1     | 2068280    | $496 \pm 5$                                           |
| 2     | 2098432    | $431 \pm 6$                                           |
| 3     | 2174893    | $640 \pm 8$                                           |
| 4     | 2174893    | $703 \pm 10$                                          |

Table 2: Absorbance values for different SYBR Gold stocks.

| | SYBR Safe* | Thiazole Orange* | SYBR Green-I | SYBR Green-II | SYBR Gold (DMSO) | SYBR Gold (CD3OD) | SYBR Gold (simul.) |
|---|---|---|---|---|---|---|---|
| **Quinoline** | | | | | | | |
| 1-CH2(H)$\alpha$ | 4.57 | | | | | | |
| | 55.40 | | | | | | |
| 1-CH2$\beta$ | 1.89 | | | | | | |
| | 22.10 | | | | | | |
| 1-CH3$\gamma$ | 0.96 | | | | | | |
| | 10.60 | | | | | | |
| N1 | | | 153.0 | 160.3 | 149.0 | 122.0 | |
| N1-CH3 | | 4.17 | | | 3.94 | 4.02 | 3.95 |
| | | 42.30 | | | 40.40 | 39.00 | 37.30 |
| 2 | 8.64 | 8.61 | | | | | |
| | 144.40 | 145.00 | 158.50 | 158.10 | 152.00 | 151.70 | 152.00 |
| 3 | 7.39 | 7.36 | 7.04 | 8.00 | 7.85 | 8.04 | 7.98 |
| | 107.70 | 107.70 | 102.80 | 106.20 | 112.00 | 112.10 | 119.20 |
| 4 | 148.50 | 148.50 | 149.10 | 148.40 | 148.50 | 149.20 | 130.80 |
| 4a | | | | | | | |
| | 124.20 | 123.90 | 122.00 | 121.70 | 124.90 | 125.00 | 126.00 |
| 5 | 8.81 | 8.80 | 8.61 | 8.76 | 8.02 | 7.94 | 7.54 |
| | 125.70 | 125.40 | 125.50 | 126.10 | 106.80 | 105.30 | 106.40 |
| 6 | 7.76 | 7.78 | 7.58 | 7.65 | | | |
| | 126.70 | 126.80 | 126.10 | 126.40 | 158.30 | 158.50 | 156.50 |
| 6-OCH3 | | | | | 4.08 | 4.12 | 4.00 |
| | | | | | 56.80 | 55.30 | 55.50 |
| 7 | 7.99 | 8.02 | 7.67 | 7.74 | 7.75 | 7.72 | 6.93 |
| | 133.20 | 133.10 | 133.00 | 133.60 | 123.60 | 123.60 | 123.80 |
| 8 | 8.17 | 8.05 | 7.13 | 6.83 | 8.19 | 8.14 | 7.34 |
| | 118.10 | 118.20 | 119.00 | 118.70 | 121.40 | 120.00 | 128.70 |
| 8a | 137.00 | 137.90 | 140.70 | 141.20 | 134.80 | 134.70 | 143.50 |

Table 3: NMR shifts assignment Table for SYBR dyes: quinoline. Boxed areas mark chemical shifts with large differences between benzo-thiazoles and benzooxazoles, with good agreement between measured and simulated data for SYBR Gold (for $^{15}$N3 no simulation is available; for position 2a' the simulation fails completely for both the $^{1}$H and $^{13}$C shifts). The naming of the atoms can be taken from Figure 24. *taken from Ref. [206].

| | SYBR Safe* | Thiazole Orange* | SYBR Green-I | SYBR Green-II | SYBR Gold (DMSO) | SYBR Gold (CD3OD) | SYBR Gold (simul.) |
|---|---|---|---|---|---|---|---|
| **Benzo-X-azole** | X = S | X = S | X = S | X = O | X = O | X = O | X = O |
| 2' | 160.00 | 159.70 | 158.90 | 162.10 | 161.80 | 161.90 | 161.40 |
| 2a' | 6.94 | 6.93 | 6.78 | 6.33 | 6.21 | 6.17 | 8.06 |
| | 88.00 | 87.80 | 87.20 | 73.90 | 74.10 | 73.10 | 113.70 |
| N3' | | | 140.0 | 127.9 | 126.5 | 112.7 | |
| 3'-CH3 | 4.03 | 4.01 | 3.95 | 3.93 | 3.91 | 3.90 | 3.93 |
| | 33.70 | 33.70 | 33.90 | 31.10 | 31.10 | 29.40 | 37.80 |
| 3a' | 140.40 | 140.40 | 141.20 | 131.80 | 131.90 | 131.40 | 132.60 |
| 4' | 7.80 | 7.77 | 7.70 | 7.69 | 7.63 | 7.53 | 7.82 |
| | 112.90 | 112.80 | 112.90 | 111.30 | 111.10 | 109.80 | 110.90 |
| 5' | 7.63 | 7.61 | 7.59 | 7.52 | 7.47 | 7.48 | 7.13 |
| | 128.10 | 128.00 | 128.70 | 126.50 | 126.40 | 125.90 | 126.10 |
| 6' | 7.43 | 7.41 | 7.39 | 7.44 | 7.33 | 7.35 | 7.10 |
| | 124.40 | 124.30 | 124.60 | 124.90 | 124.50 | 124.00 | 122.50 |
| 7' | 8.06 | 8.04 | 7.97 | 7.80 | 7.65 | 7.59 | 6.89 |
| | 122.80 | 122.80 | 123.20 | 111.40 | 111.20 | 110.30 | 110.40 |
| 7a' | 123.80 | 123.70 | 123.80 | 146.50 | 146.40 | 146.50 | 147.60 |

Table 4: NMR shifts assignment Table for SYBR dyes: benzo-X-azole. Boxed areas mark chemical shifts with large differences between benzo-thiazoles and benzooxazoles, with good agreement between measured and simulated data for SYBR Gold (for [15]N3 no simulation is available; for position 2a' the simulation fails completely for both the ^{1}H and ^{13}C shifts). The naming of the atoms can be taken from Figure 24. *taken from Ref. [206].

| | SYBR Safe* | Thiazole Orange* | SYBR Green-I | SYBR Green-II | SYBR Gold (DMSO) | SYBR Gold (CD3OD) | SYBR Gold (simul.) |
|---|---|---|---|---|---|---|---|
| **Tail (R1)** | | | | | | | |
| $\alpha$ | | | N:84.2 | | 137.10 | 137.50 | 136.70 |
| $\beta/\beta'$ | | | 3.26/3.16 | 3.49 | 7.88 | 7.89 | 7.89 |
| | | | 50.4/54.8 | 31.8 | 130.10 | 129.80 | 128.50 |
| $\gamma/\gamma'$ | | | 1.49/1.23 | 2.71 | 7.84 | 7.91 | 7.36 |
| | | | 24.7/20.3 | 56.8 | 134.10 | 133.60 | 127.80 |
| $\delta/\delta'$ | | | 2.19/0.73 | | | | |
| | | | 56.3/11.5 | N:26.2 | 130.50 | 129.85 | 130.50 |
| $N\delta$-CH3 | | | | 2.20 | | | |
| | | | | 45.3 | | | |
| $\epsilon$ | | | | | 4.64 | 4.72 | 4.39 |
| | | | N:23.7 | | 63.50 | 63.80 | 65.30 |
| $N\epsilon$-CH3 | | | 2.12 | | | | |
| | | | 45.2 | | | | |
| $N\zeta$ | | | | | 61.4 | 87.5 | |
| $N\zeta$-CH3 | | | | | 2.97 | 3.10 | 2.86 |
| | | | | | 46.70 | 46.10 | 48.20 |
| $\eta$ | | | | | 3.33/3.43 | 3.49/3.56 | 3.15 |
| | | | | | 55.80 | 55.90 | 54.30 |
| $\theta$ | | | | | 1.38 | 1.53 | 1.34 |
| | | | | | 8.90 | 6.90 | 8.40 |

Table 5: NMR shifts assignment Table for SYBR dyes: tail (R1). Boxed areas mark chemical shifts with large differences between benzo-thiazoles and benzooxazoles, with good agreement between measured and simulated data for SYBR Gold (for [15]N3 no simulation is available; for position 2a' the simulation fails completely for both the ^{1}H and ^{13}C shifts). The naming of the atoms can be taken from Figure 24. *taken from Ref. [206].

|                       | Dissociation const. $K_d$ (µM) | Binding site size $n$ (bp) | Unwinding angle $\theta$ (°) |
|-----------------------|--------------------------------|----------------------------|------------------------------|
| SYBR Gold*            | $0.216 \pm 0.021$              | $1.67 \pm 0.04$            | $19.1 \pm 0.7$               |
| SYBR Green I*         | $0.203 \pm 0.037$              | $1.77 \pm 0.06$            | $19.3 \pm 1.3$               |
| Pico Green[+]         | $0.943 \pm 0.050$              | $2.32 \pm 0.21$            | $21 \pm 14$                  |

Table 6: McGhee-von Hippel model binding parameters for different SYBR dyes determined by single-molecule magnetic tweezers experiments. * this work, [+] Ref. [185].
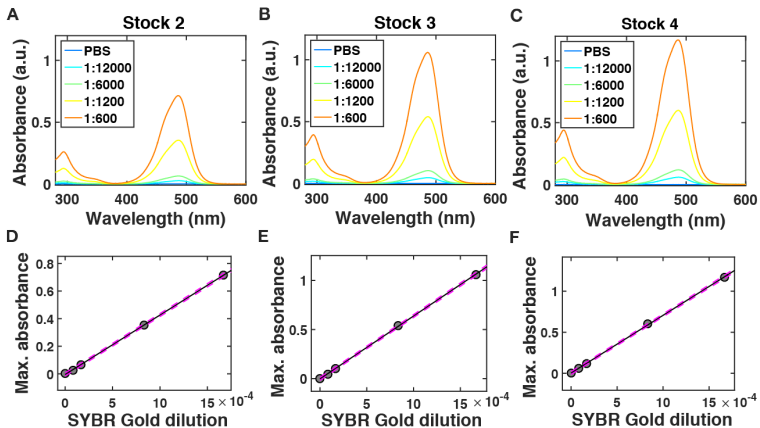


Figure 23: Absorbance of different SYBR Gold stocks. A-C) Absorbance spectra for varying SYBR Gold dilutions (from blue to orange: PBS, 1:12000, 1:6000, 1:1200, 1:600) for three different SYBR Gold stocks purchased from Invritrogen (LOT numbers 2098432, 2174893, 2174893). Spectra shown are recorded in the absence of DNA. The maximum absorbance is at a wavelength of 486 nm. D-F) Value of the absorbance maxima of the SYBR Gold absorbance spectra as a function of the SYBR Gold concentration. The circles are the experimental data, the solid line is a linear fit; extrapolation of the linear fit yields the value for the undiluted SYBR Gold which is found to be $413 \pm 6$, $640 \pm 8$, $703 \pm 10$ (Table 2).
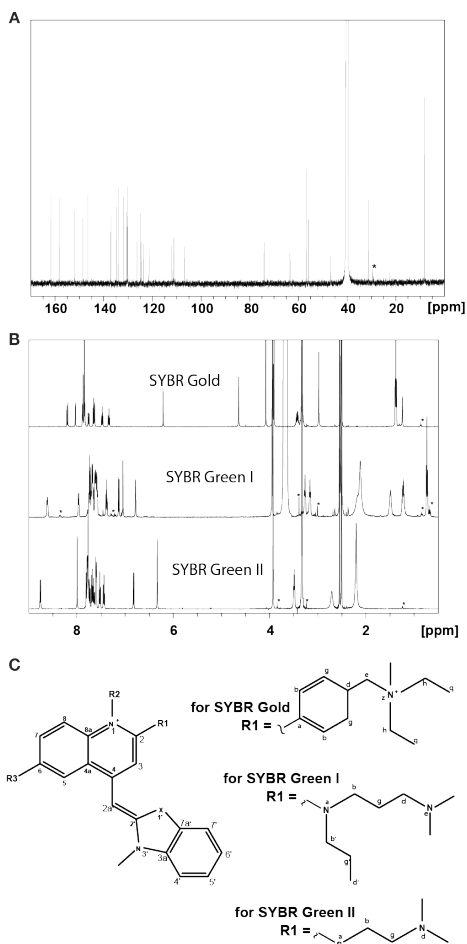
Figure 24: SYBR Gold NMR spectra. A) 1D $^{13}$C NMR spectrum of SYBR Gold in DMSO-d6, AV III 500 MHz (cryo). The peak highlighted with a star is a contamination. B) 1D $^1$H spectra of SYBR Gold, SYBR Green I, and SYBR Green II in DMSO-d6 (298 K, MHz; SYBR Gold and SYBR Green II 1 scan, SYBR Green I 16 scans). Impurities identified by DOSY experiments are marked with an asterix *. C) The core structure of the SYBR family of dyes and the side chain R2 for SYBR Gold, SYBR Green I, and SYBR Green II. For clarity, we labelled all atoms and the side chains R1, R2, R3. The same nomenclature is used in the NMR shifts assignment Table for SYBR dyes (Table 3 - 5).
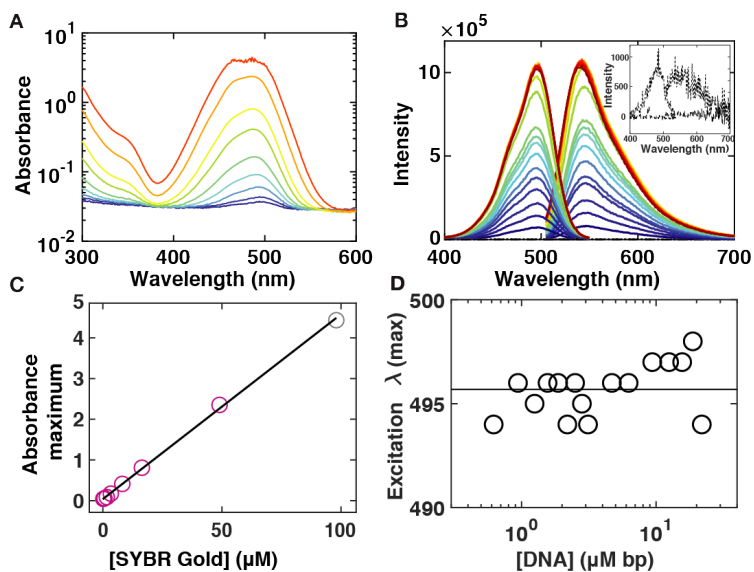
Figure 25: SYBR Gold absorbance, excitation, and emission spectra. A) Absorbance spectra for varying SYBR Gold concentrations (from blue to red: 0.16, 0.33, 0.82, 1.6, 3.3, 8.2, 16, 49, 98 µM) in the presence of 2 µM · bp DNA (Lambda-DNA (NEB)). The peak of the spectrum at the highest concentration is noisy, as the dynamic range of the instrument is approached. Points from this spectrum are included below in panel C (as well as Figure 19A in the main text) but greyed out. B) SYBR Gold excitation and emission spectra at constant SYBR Gold concentration (2.5 µM) and varying DNA concentration (from blue to red: 0.9, 1.3, 1.6, 1.9, 2.2, 2.8, 3.1, 4.7, 6.3, 9.4, 12.5, 15.6, 18.8, 21.9, 25.0, 28.1, 31.3 µM · bp, dotted line: SYBR Gold only, dashed line: PBS only. The inset shows PBS only and SYBR Gold only spectra on a different scale for clarity. C) Value of the absorbance maxima of the SYBR Gold absorbance spectra as a function of the SYBR Gold concentration. The circles are the experimental data, the solid line is a linear fit (R = 0.9997); extrapolation of the linear fit yields the value for the undiluted SYBR Gold which is found to be $435 \pm 6$ and implies a concentration of the undiluted SYBR Gold of $(9.8 \pm 0.1)$ mM. This is significantly different from the stock concentration we determined for other SYBR Gold stocks (Figure 23)D) Position of the excitation maxima at constant SYBR Gold concentration (2 µM) and varying DNA concentrations. No significant shift is observed for the excitation maxima. The line is simply the mean of the data points at all concentrations, which is 495.7 nm $\pm$ 1.25 nm (mean $\pm$ std).
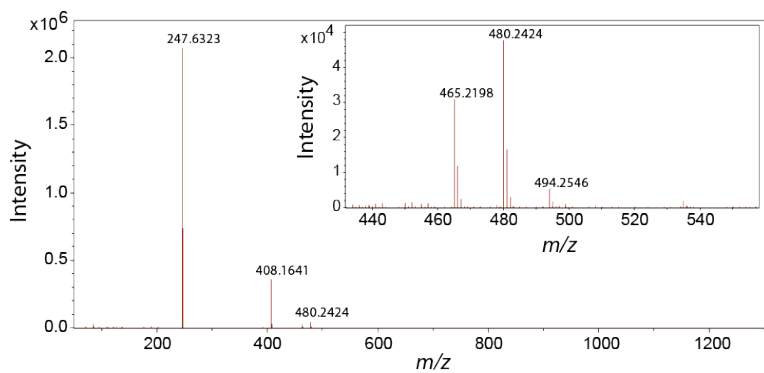
Figure 26: Mass spectrometry analysis of SYBR Gold. The main population is at m/z = 247.6. Minor populations are found at m/z of 408.2 and around 480. The inset has a zoom into the region around m/z = 480.
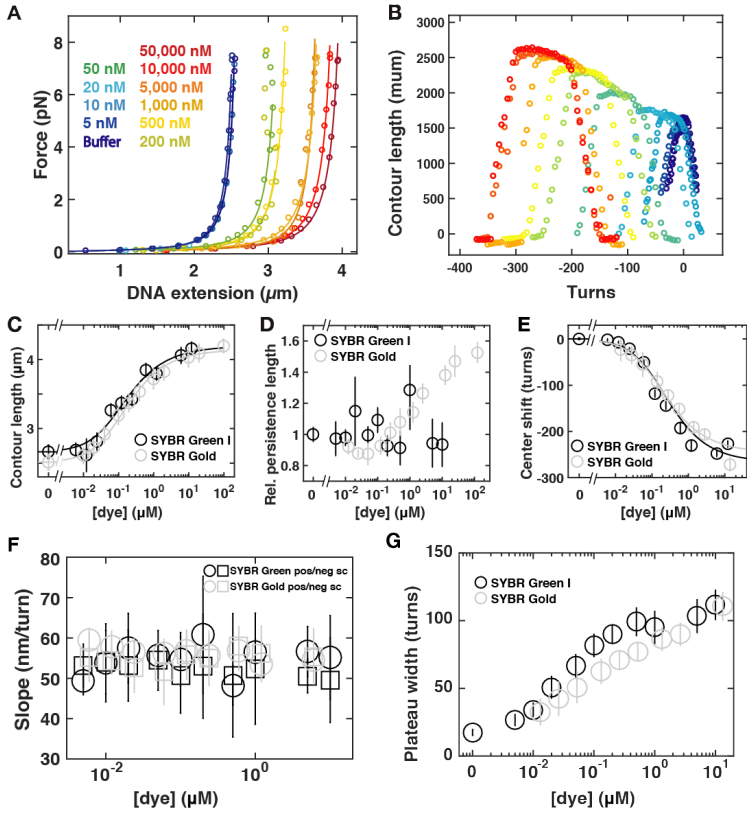
Figure 27: (Caption next page.)

Figure 27: (Previous page.) Effects of SYBR Green I on DNA force-extension behaviour, twist and torque. A) Force-extension curves for 7.9-kb DNA in the presence of increasing concentrations of SYBR Green (increasing concentrations from blue to red indicated in the Figure legend). Symbols are raw data, lines are fits of the WLC model. A systematic increase the DNA extension with increasing SYBR Gold concentration is apparent. B) Rotation-extension curves for 7.9 kb DNA at F = 0.5 pN in the presence of increasing concentrations of SYBR Green. The SYBR Green concentrations are (from blue to red) 0, 5, 10, 20, 50, 100, 200, 500, 1000, 5000 1000, 50000 nM. With increasing concentrations of SYBR Gold the rotation curves shift to negative turns; the DNA length at the center of the curves increases; and the rotation-extension curves broaden. C) DNA contour length determined from fits of the WLC model as a function of SYBR Green concentration. The black line is a fit to the McGhee–von Hippel model (reduced $\chi^2 = 0.75$), with a dissociation constant $K_d = 0.20 \pm 0.04$ µM and a binding site size $n = 1.77 \pm 0.06$. We show the corresponding data for SYBR Gold in grey as a comparison (Figure 17C). D) DNA bending persistence length from WLC fits measured as a function of the dye concentration, indicating that the persistence length stays constant with increasing dye concentration. We show the corresponding data for SYBR Gold in grey as a comparison (Figure 17D). E) Quantification of the shift in the center position of the rotation-extension curves as a function of the SYBR Green concentration. The center positions were determined from fitting slopes in the positive and negative plectonemic regime and by computing the intersection of the two slopes. The black line is a fit of the McGhee-von Hippel model (reduced $\chi^2 = 5.5$), with the dissociation constant $K_d$ and binding site size $n$ set to the values determined from the force extension data (Panel A) and the unwinding angle per SYBR Gold intercalation determined from the fit to be $\Delta\theta = 19.3° \pm 1.3$. We show the corresponding data for SYBR Gold in grey as a comparison (Figure 18B). F) Extension vs. turn slopes in the plectonemic regime (determined as indicated by the red lines in Figure 28A) as a function of SYBR Green concentration for positive (circles) and negative (squares) plectonemic supercoils. We show the corresponding data for SYBR Gold in grey as a comparison (Figure 28B). G) Width of the pre-buckling regime (in turns) vs. SYBR Green concentration. In grey we show the corresponding data for SYBR Gold in grey as a comparison (Figure 28C). In panel A and B one typical experiment is shown for clarity. Data points and error bars for SYBR Green in the panels C to G are the mean and standard deviation from at least 24 independent measurements.
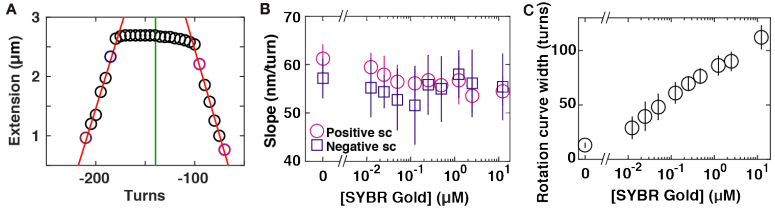
Figure 28: SYBR Gold rotation curve analysis. A) Example of a rotation-extension curve and analysis of center positions and slopes. Data are for 7.9 kb DNA at F = 0.5 pN in the presence of 496 nM SYBR Gold (circles). The center positions are determined from fitting slopes in the positive and negative plectonemic regime (red lines) and by computing the intersection of the two slopes (indicated by the green line). B) Extension vs. turn slopes in the plectonemic regime (determined as indicated by the red lines in panel A) as a function of SYBR Gold concentration for positive (red circles) and negative (blue squares) plectonemic supercoils. C) Width of the pre-buckling regime (in turns) vs. SYBR Gold concentration. Data points and error bars in panel B and C are the mean and standard deviation from at least 14 independent measurements. In panel A one typical experiment is shown for clarity.
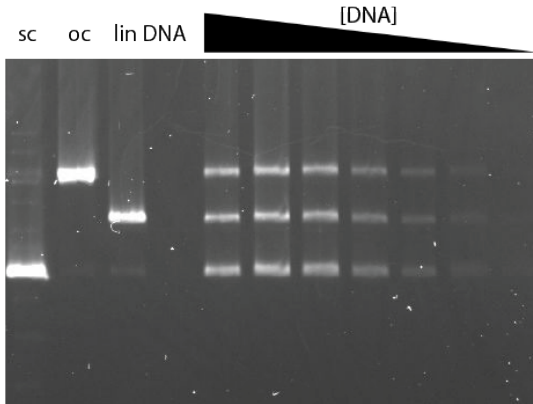
Figure 29: Gel electrophoresis of PBR322 plasmid DNA and visualization by SYBR Gold fluorescence. Lanes from left to right: supercoiled DNA, open circular DNA, linear DNA, empty lane, and equimolar mixtures of supercoiled, open-circular, and linear DNA with decreasing amounts of DNA: 30 ng, 21.4 ng, 13.6 ng, 6.5 ng, 2.3 ng, 1.0 ng, 0.5 ng. The gel was stained after electrophoretic separation with 3.1 µM SYBR Gold in TAE buffer (see Materials and Methods, Section 4.3.9.7).
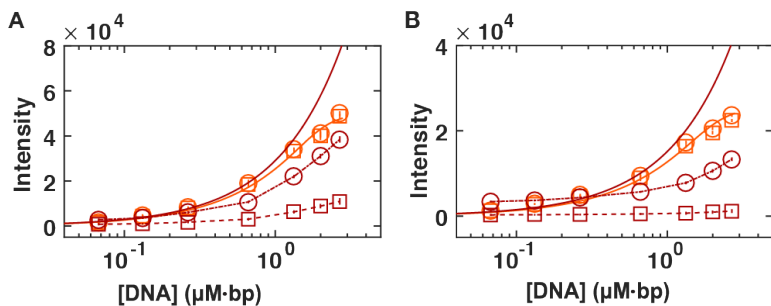
Figure 30: SYBR Gold fluorescence at high dye concentrations. A) Fluorescence intensity recorded using a plate reader for torsionally unstrained DNA (pBR322). The orange circles and line are for [SYBR Gold] = 2.5 µM and identical to the data shown in Figure 19C, included as a reference. Red squares are raw data for [SYBR Gold] = 124 µM. Red circles are the same data corrected for the inner filter effect using Equation 51 and the path-lengths indicated in Figure 20. Dashed and dot-dashed lines are included as guides to the eye. The solid red line is the prediction for [SYBR Gold] = 124 µM using the finite concentration McGhee-von Hippel model and the parameters from Figure 19C. B) Fluorescence intensities recorded using a qPCR cycler. Same symbols, conditions, and fitting procedure as for the plate reader data shown in panel A.
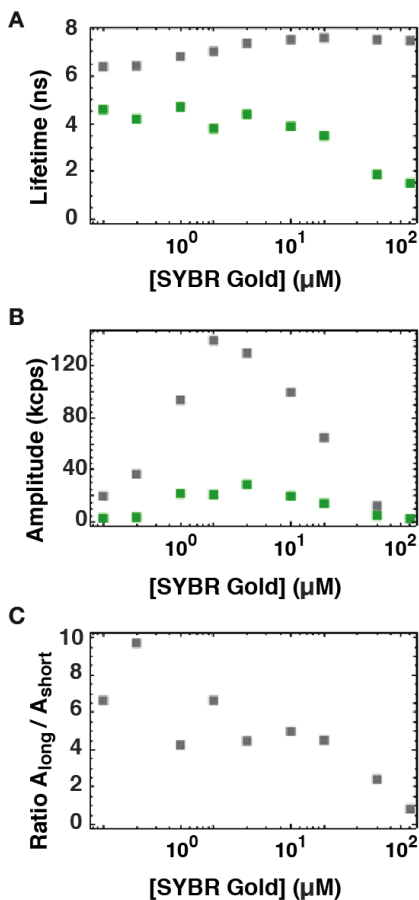
Figure 31: Fluorescence lifetime measurements. A) Fluorescent lifetimes as a function of SYBR Gold concentration at a constant concentration of 2 μM · bp DNA determined from bi-exponential fits. These are the same data as shown in Figure 21B and D. The fit gives a shorter lifetime (green, ∼ 2-4 ns) that decreases strongly with increasing SYBR Gold concentration and a longer lifetime (gray, ∼ 6-7 ns) that slightly increases with increasing SYBR Gold concentration. B) Amplitudes of the two fluorescence lifetimes vs. SYBR Gold concentration; longer lifetime in green, shorter lifetime in grey. C) Ratio of the two amplitudes of the fluorescence lifetimes vs. SYBR Gold concentration. Up to concentrations of ∼ 10 μM SYBR Gold, the long lifetime dominates the fit, with the short lifetime contributing < 25% of the total amplitude. At higher concentration, both amplitudes decrease as the total intensity strongly decreases, but the shorter lifetime – which we attribute to dynamic quenching from SYBR Gold molecules close to the DNA – becomes more important and roughly equal in magnitude to the long component.

5

# EFFECTS OF DNA BINDING ON THE
# PHOTOCHEMISTRY OF RUTHENIUM-TRIS-TAP

Over the last years, ruthenium complexes have become promising anticancer drug candidates with selective antimetastatic properties and low systemic toxicity. Ruthenium compounds appear to penetrate tumor cells as well as bind effectively to DNA. Therefore, it is extremely important, especially for medicinal chemistry applications, to investigate the DNA binding modes of different Ru(II) and Ru(III) complexes in order to specify and optimize possible applications as anticancer agents [211, 212].

## 5.1 RU(II)-POLYPYRIDYL COMPLEXES

Polypyridine complexes are coordination complexes that contain polypyridine ligands (Figure 32). Pyridine also known as azine or azabenzole, is a heteroaromatic, i.e. a heterocyclic compound with aromatic properties (Figure 32a). Polypyridines are multidentate ligands (that means they can donate (multiple)
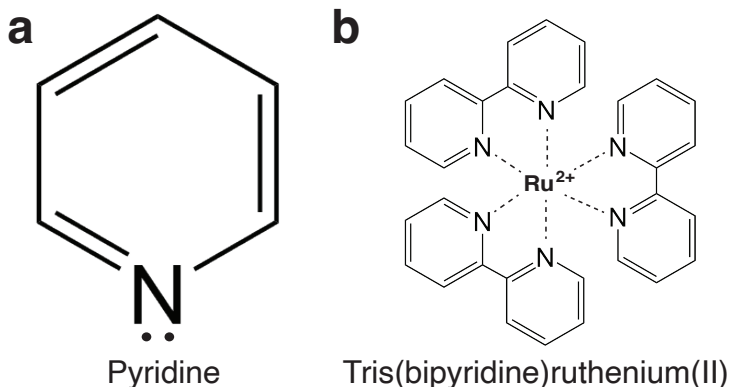


Figure 32: a) Chemical structure of a pyridine, a six membered heterocycle with an electronegative heteroatom (nitrogen), which makes it π-deficient. b) Chemical structure of an exemplary polypyridine complex: Tris(bipyridine)ruthenium(II).

electron pairs to a metal atom), which impart characteristic properties to the metal complexes they form. Some of these complexes have the property to strongly absorb light via a process called metal-ligand charge transfer (MLCT), which will be discussed in greater detail in the following section (Section 5.2). The properties of these complexes are tunable by making changes in substituents, for example, electron donation, electron withdrawal, and $\pi$-conjugating groups on the polypyridine moiety. Also the MLCT absorption band can be shifted, and the emission wavelength and duration can be changed [213].

Polypyridyl complexes can interact with DNA in different ways. Since, in contrast to the negatively charged phosphate backbone of the DNA double helix, polypyridyl complexes are positively charged, they interact electrostatically. In addition, the complex may adsorb selectively within the grooves of dsDNA, depending on its size, shape, hydrophobicity and hydrophilicity etc. Moreover, for complexes that also contain a planar ligand with an extended aromaticity, this aromatic ring can also be partially trapped between two base pairs, while the other two ligands are directed to the outside of the double helix. In this constellation, the complex is called "partially intercalated" [214].

Complexes with the metal Ruthenium in the center and with polypyridine ligands are among the most popular metal complexes due to their luminescence and photocatalytic properties, offering a wide range of applications in the fields of photophysics and photochemistry, e. g., in lighting, sensing, solar cells, and photoredox catalysis. As a result of the great interest generated by these complexes, Ruthenium polypyridyl complexes have also formed the basis for the development of concepts and methods in inorganic photochemistry. Since they are involved in various photochemical processes, this has also led to the development of experimental techniques and conceptual models that have applications in a variety of areas of inorganic photochemistry [215, 216].

## 5.2 METAL-TO-LIGAND CHARGE TRANSFER (MLCT)

Ruthenium(II) polypyridyl complexes can form excited charge transfer states on visible light absorption. This charge transfer makes these complexes useful for numerous applications. Charge transfer (CT) complexes are electron donor-acceptor complexes that change to a charge-separated state upon light absorption. Through radiative and non-radiative transitions, the CT complex subsequently returns to the ground state. CT complexes are often complexes with a metallic center. If the charge transfer is from metal (e. g.Ru) to ligand (e. g.pyridine), the transition is called metal to ligand charge transfer (MLCT; Figure 33). The metal acts as electron donor and the ligand as electron acceptor. The transition occurs from occupied d orbitals of the metal to empty $\pi^*$ orbitals (antibonding $\pi$-orbitals) of the ligand [217, 218].
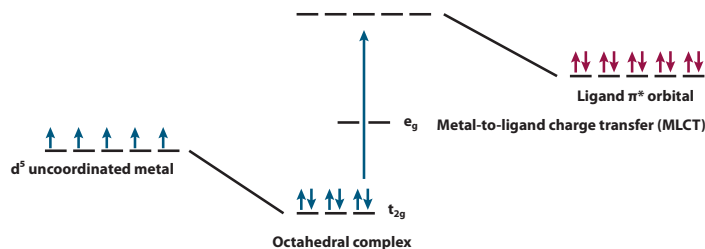
Figure 33: Schematic depiction of metal-to-ligand charge transfer (MLCT) in a d5 octahedral complex.

In the following work, I will demonstrate DNA binding mode heterogeneity of $Ru(TAP)_3^{2+}$ (TAP= 1,4,5,8-tetraazaphenanthrene) and evaluate how multivalent binding governs the complex's photochemistry. Single-molecule MT and AFM measurements indicate that $Ru(TAP)_3^{2+}$ binds to DNA in an intercalative binding mode that occasionally forms kinks, suggesting helical extension and unwinding. Furthermore, there is clear evidence of binding-induced loop formation in our measurements. These results imply multivalent binding to DNA, suggesting that $Ru(TAP)_3^{2+}$ can interact through (at least) two interfaces simultaneously. In contrast, $Ru(phen)_3^{2+}$ (phen = 1,10-phenanthroline) does not form DNA synapses to the extent observed for $Ru(TAP)_3^{2+}$, despite the higher affinity for intercalation. This infers that loop formation is mediated in part by the N1 and N8 atoms of TAP, possibly via hydrogen bonds. With spectrometric measurements it is demonstrated that the luminescence quenching follows the same concentration dependence as the lengthening observed in MT. This implies that intercalative DNA binding governs quenching of the [3]MLCT state. In addition, the spectroscopic data show that photoadduct formation is faster for long DNA than for short DNA, in contrast to what was found for luminescence quenching. The lower yield and better defined photoadducts might be due to the geometric constraints imposed by binding to long DNA. This work will help to get a better understanding of how ground-state DNA-binding affects the photochemistry of $Ru(TAP)_3^{2+}$, which may potentially contribute to innovative medicines, particularly in the area of phototherapeutic applications in cancer treatment as several ruthenium-based compounds have been shown to possess interesting biological properties that point in this direction [214, 219–221].

# Ru(TAP)$_3^{2+}$ uses multivalent binding to accelerate and constrain photoadduct formation on DNA

By

Willem Vanderlinden[*,1,2], Pauline J. Kolbeck[1], Wout Frederickx[2], Sebastian F. Konrad[1], Carola Lampe[1], Alexander Urban[1], Cécile Moucheron[3], and Jan Lipfert[1]

[1] Department of Physics, Nanosystems Initiative Munich, and Center for NanoScience, LMU Munich, Amalienstrasse 54, 80799 Munich, Germany
[2] Department of Chemistry, Division of Molecular Imaging and Photonics, KU Leuven-University of Leuven, Celestijnenlaan 200F, B-3001 Leuven, Belgium
[3] Department of Chemistry, Laboratory of Organic Chemistry and Photochemistry, Université Libre de Bruxelles, Avenue Franklin D. Roosevelt 50, 1050 Brussels, Belgium
[*] Corresponding author

published in

*ChemComm* (2019), Vol. 55, No. 60, 8661–8886

My contribution to this publication was performing single-molecule magnetic tweezers measurements as well as spectroscopic measurements and analyzing the resulting data.

### 5.3.1  *Abstract*

Ru(II)-complexes with polyazaaromatic ligands can undergo direct electron transfer with guanine nucleobases on blue light excitation that results in DNA lesions with phototherapeutic potential. Here we use single-molecule approaches to demonstrate DNA binding mode heterogeneity and evaluate how multivalent binding governs the photochemistry of $[\text{Ru(TAP)}_3]^{2+}$ (TAP = 1,4,5,8-tetraazaphenanthrene).

### 5.3.2  *Introduction*

Ru(II)-polypyridyl complexes carry three bidentate ligands that can be designed to tune the DNA-binding and electronic properties of the complex [221, 222]. Complexes bearing DNA-intercalating moieties can exhibit light-switching properties in the presence of DNA [223, 224] and targeted ligand design has enabled selective detection of mismatches and abasic sites in DNA duplexes [225, 226]. Further, $\pi$-deficient ligands such as polyazaaromatic TAP (1,4,5,8-tetraazapenanthrene) convey highly oxidizing properties to the complex in the triplet metal-to-ligand charge transfer ($^3$MLCT) excited state: on excitation, the homoleptic complex $\text{Ru(TAP)}_3^{2+}$ (Figure 34) can extract an electron from guanine nucleobases [214]. The oxidized guanine either undergoes a back-electron transfer with the reduced complex or results in DNA-lesions. While the formation of single-strand DNA breaks is easily detected via topological conversions of supercoiled DNA targets, recombination of the oxidized guanine with the reduced complex to form covalent photoadducts [227] is the dominant pathway. Recent work has demonstrated targeted photo-induced DNA damage by Ru-TAP complexes in live cells [228], suggesting that this class of compounds could be used in phototherapeutic applications. To design Ru-TAP complexes for therapeutic applications, it is essential to understand how ground-state DNA-binding affects the photochemistry of $\text{Ru(TAP)}_3^{2+}$ with DNA. However, the binding mode of $\text{Ru(TAP)}_3^{2+}$ and the related $\text{Ru(phen)}_3^{2+}$ (phen = 1,10-phenanthroline; Figure 34) to DNA is controversial, with evidence for (hydrogen bond-mediated [229]) groove-binding as well as binding through intercalation [230] or semi-intercalation, i. e.partial insertion between adjacent base pairs [231–234]. Here, we use single-molecule approaches to unravel the binding modes of racemic $\text{Ru(TAP)}_3^{2+}$ and show how they affect the photochemistry with DNA.

### 5.3.3  *Results*

Previously, single-molecule manipulation assays have revealed the binding modes of small molecules interacting with DNA [116, 168, 171, 176, 179]. Here we use MT to quantify the ground-state binding of racemic $\text{Ru(TAP)}_3^{2+}$ and
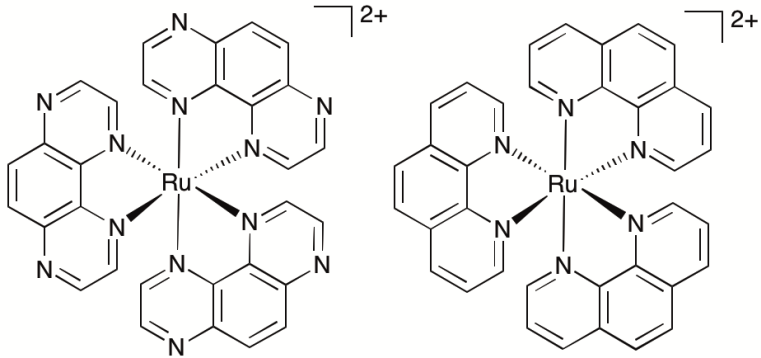
Figure 34: Chemical structures of $Ru(TAP)_3^{2+}$ (left) and $Ru(phen)_3^{2+}$ (right).

$Ru(phen)_3^{2+}$ to DNA in 10 mM phosphate buffer (Figure 35A). In MT, DNA molecules (7.95 kbp; crystallographic length 2.7 µm) were attached at one end to the bottom surface of a flow cell and at the other end to a paramagnetic bead. Using permanent magnets, we can controllably exert stretching forces and torques [61] on the DNA molecules. First, we performed force-extension measurements on nicked DNA tethers to evaluate the changes in DNA extension and elasticity on titration with racemic $Ru(TAP)_3^{2+}$ (Figure 35B). By fitting the WLC model [182], we determined the DNA contour length $L_C$ and bending persistence length $L_P$. In the absence of $Ru(TAP)_3^{2+}$ we find $L_C = 2.68 \pm 0.03$ µm and $L_P = 45 \pm 3$ nm, in excellent agreement with the crystallographic length of B-form DNA and with previous measurements of $L_P$, respectively [135]. On addition of low to intermediate concentrations ($[Ru(TAP)_3^{2+}] \leq 10$ µM), $L_C$ increases gradually, while $L_P$ decreases (Figure 35C,D). The increase of $L_C$ is consistent with intercalative binding, and can be used to calculate the fractional occupancy $\gamma$ of intercalated $Ru(TAP)_3^{2+}$ via $\gamma = (L_C(C) - L_C(0))/(\Delta l \cdot N)$ with $L_C(0)$ the contour length in the absence of $Ru(TAP)_3^{2+}$, $\Delta l$ the contour length increment per intercalation event, and $n$ the number of base pairs (7.95 kbp) [171]. Assuming $\Delta l = 0.34$ nm, we fit the $Ru(TAP)_3^{2+}$ data to the McGhee-von Hippel model [105]:

$$\gamma(c) = \frac{[Ru(TAP)_3^{2+}]}{K_d} \cdot \frac{(1 - n\gamma)^n}{(1 - n\gamma + \gamma)^{n-1}} \tag{60}$$

and obtain the dissociation constant $K_d = 19.7 \pm 4$ µM and binding site size n = 2.7 ± 0.4 (Figure 35C). While lengthening of the DNA contour is consistent with an intercalative binding mode, linear dichroism experiments [232] and crystallographic data [235] have suggested semi-intercalation, i.e. partial insertion of a TAP ligand between subsequent base pairs. Co-crystal structures of DNA and TAP-containing (but heteroleptic) Ru(II)-complexes further feature

a sharp kink (with bend angle $\theta = 51°$) in the DNA at the semi-intercalation binding pocket of the complex [234]. We tested whether the dependency of the effective bending persistence length $L_{P,eff}$ on $[Ru(TAP)_3^{2+}]$ can be described by the model of Popov *et al.* [236] that features a line density $\kappa$ of rigid bends with bend angle $\theta$:

$$L_{P,eff} = \frac{L_{P,0}}{1 + \kappa \cdot L_{P,0}(1 - \cos(\theta))} \tag{61}$$

Fixing $K_d = 19.7$ μM and $n = 2.7$ (determined from the contour length increase), we obtain a kink angle $\theta = 11°$ (Figure 35D), far below the value suggested by crystallography [234]. Conversely, fixing $\theta = 51°$, we obtain a best fit with a kink frequency that is $\approx$ 10-fold smaller than the fractional occupancy of intercalated $Ru(TAP)_3^{2+}$ $\gamma$. Thus, our data are inconsistent with the view that TAP predominantly interacts with DNA via semi-intercalation that results in severe DNA kinking.

We note that at $[Ru(TAP)_3^{2+}] > 10$ μM the WLC model does not provide a good fit to the force-extension data and that the DNA length decreases with increasing concentration, suggesting effects of $Ru(TAP)_3^{2+}$ binding beyond intercalation. In contrast, the force-extension behaviour of DNA interacting with racemic $Ru(phen)_3^{2+}$ is accurately described by the WLC model over the entire concentration range tested (0 - 100 μM) and we find $K_d = 4.9 \pm 1$ μM, n = $4.0 \pm 0.2$ fitting the McGhee-von Hippel equation (Equation 60 and Figure 35C). Similar to $Ru(TAP)_3^{2+}$, $Ru(phen)_3^{2+}$-binding decreases the DNA bending persistence length $L_{P,eff}$, and fitting the Popov model [236] yields a kink density $\kappa = 0.12 \times \gamma$ (for $\theta = 51°$) (Figure 35D).

To obtain additional insights in the binding of $Ru(TAP)_3^{2+}$ with DNA, we use the capability of MT to control the DNA linking number $Lk$ in torsionally constrained DNA by rotating the external magnets. At low force (F = 0.3 pN) magnet rotation leads to a symmetrical response of the molecular extension for both under- and over-winding of bare DNA, due to the formation of plectonemic supercoils [61] (Figure 35E). Titration with $Ru(TAP)_3^{2+}$ induces a shift of the midpoints of the rotation curves to more negative linking differences $\Delta Lk$, in line with DNA unwinding upon $Ru(TAP)_3^{2+}$ intercalation [116] (Figure 35E). Using $K_d$ and n from the force-extension data (Figure 35B,C), we determined the unwinding angle $\phi = 16 \pm 4°$ per intercalation event from the dependence of $\Delta Lk$ on $c(Ru(TAP)_3^{2+})$ (Figure 35F). Notably, at $[Ru(TAP)_3^{2+}] > 10$ μM the extension of the rotation curves rapidly decreases with increasing concentration, in contrast to the behaviour for classical intercalation, but in agreement with the observations from force-extension experiments. Notably, at these higher concentrations, the rotation curves become more erratic and feature sudden extension jumps.

In contrast, rotation curves with increasing concentrations of $Ru(phen)_3^{2+}$ follow the behaviour of a classical intercalator (Figure 38). Analysis of the shift in $\Delta Lk$

yields an unwinding angle $\phi = 26.3 \pm 2°$ for Ru(phen)$_3^{2+}$ (Figure 35E,F), in reasonable agreement with the results of a topoisomerase assay [237]. Together, our data indicate that Ru(phen)$_3^{2+}$ is a stronger intercalator than Ru(TAP)$_3^{2+}$, in agreement with a previous report [238]. We note that for Ru(phen)$_3^{2+}$ only at high [Ru(phen)$_3^{2+}$] = 100 μM, and in few cases ($\sim$ 10% of all beads), the maximal extension in rotation curves is reduced with respect to the expected values, in contrast to the anomalous behaviour observed for Ru(TAP)$_3^{2+}$.

To dynamically probe the anomalous behaviour at [Ru(TAP)$_3^{2+}$] > 10 μM we subjected nicked DNA tethers to rotation in the MT (Figure 39A). At low concentrations (< 10 μM), tether extension remains unaffected on magnet rotation, as expected for a torsionally unconstrained DNA. However, at [Ru(TAP)$_3^{2+}$] > 10 μM, the DNA extension occasionally decreases on magnet rotation until sudden extension jumps restore the original z-position. We interpret this result as the consequence of topological shielding of the nicking site via transient DNA looping by binding to multiple sites that bridge the nick. To further test the hypothesis of DNA looping by Ru(TAP)$_3^{2+}$ we performed force-jump experiments wherein the DNA is first kept at a low force (0.1 pN) and then suddenly subjected to a high force (6 pN). In the presence of [Ru(TAP)$_3^{2+}$] > 10 μM, our data demonstrate step-wise extension increments on application of high force, in line with forced dissociation of Ru(TAP)$_3^{2+}$-mediated loops (Figure 39B). Consistent with our observations of classical intercalation (Figure 35), no signatures for Ru(phen)$_3^{2+}$-mediated loop formation were observed from force-jump experiments or rotation of nicked DNA.

To directly visualize the bending or kinking behaviour at short length scales, we performed AFM imaging. Linear DNA fragments (486 bp) were incubated with Ru(TAP)$_3^{2+}$ under dimmed light conditions and subsequently deposited onto poly-L-lysine coated mica (Methods, section 5.3.7). We analysed the AFM images by tracing the DNA contour [83] with a step length $l = 5$ nm. Under the conditions used, we find that at the molecular length scale DNA adopts conformations corresponding to kinetic trapping on surface adsorption, as observed previously [235]. Yet, at short length scales ($l = 5$ nm) the bend angle distribution implies local chain equilibration that enables quantitative evaluation of DNA bending or kinking (if any) on incubation with Ru(TAP)$_3^{2+}$. The bend angle distributions of DNA molecules incubated with varying amounts of Ru(TAP)$_3^{2+}$ are, to first approximation, well described by a single folded Gaussian (Figure 36B) with a variance $\langle \theta^2 \rangle$ that relates to the DNA persistence length as $\langle \theta^2 \rangle = l/L_P$. Based on this analysis, we only find a weak dependence of $L_P$ on [Ru(TAP)$_3^{2+}$]. On average $L_P = 58 \pm 3$ nm in agreement with previous AFM analyses of DNA bending behaviour [83]. However, the fit residuals feature a peak at angles of 40-50°, in a concentration-dependent fashion. The integrated peak accounts only for $\approx 1.5\%$ of the total angle distribution at the highest concentrations tested in good agreement with our MT analysis that suggests infrequent kinks induced by Ru(TAP)$_3^{2+}$.

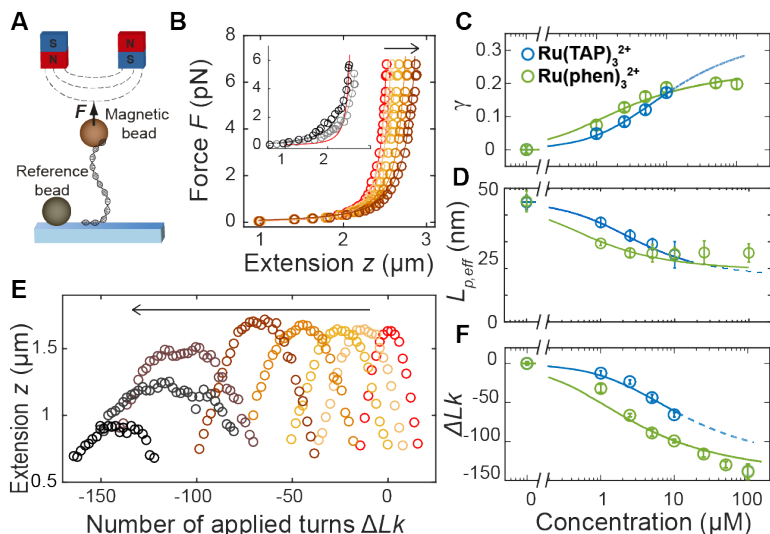Figure 35: Magnetic tweezers probe DNA structural changes on binding Ru(TAP)$_3^{2+}$ and Ru(phen)$_3^{2+}$. A) Schematic representation of DNA in MT. B) Force-extension analysis of DNA in the absence (red) and presence (brown gradient) of increasing concentrations (1-10 µM) of Ru(TAP)$_3^{2+}$. Inset: anomalous force-extension behaviour at high (50 and 100 µM) ligand concentration. Solid lines are WLC fits to the data. C) Fractional occupancy $\gamma$ as function of c(Ru(TAP)$_3^{2+}$) (blue) and c(Ru(phen)$_3^{2+}$) (green) and fits to the McGhee-von Hippel model with ($K_d = 19.7 \pm 4$ µM, n = 2.7 $\pm$ 0.4) and ($K_d = 4.9 \pm 1$ µM, n = 4.0 $\pm$ 0.2) for Ru(TAP)$_3^{2+}$ and Ru(phen)$_3^{2+}$ respectively. D) Effective bending persistence length as a function of c(Ru(TAP)$_3^{2+}$) (blue) and c(Ru(phen)$_3^{2+}$) (green) and fit to the Popov model. E) Rotation curves of DNA in the absence (red) and presence (brown gradient) of increasing concentrations (1-100 µM) of Ru(TAP)$_3^{2+}$. F) Shift of the centre position of rotation curves as a function of c(Ru(TAP)$_3^{2+}$) (blue) and c(Ru(phen)$_3^{2+}$) (green) . Solid lines are fits to the McGhee-von Hippel model taking ($K_d$,n) from the lengthening data. The fitted unwinding angles are $\phi = 16 \pm 4°$ for Ru(TAP)$_3^{2+}$ and $\phi = 26 \pm 2°$ for Ru(phen)$_3^{2+}$.

Taken together, our MT and AFM data suggest that Ru(TAP)$_3^{2+}$ binds to DNA in an intercalative binding mode that occasionally forms kinks and that infers helix lengthening and unwinding. In addition, we observe clear evidence for binding-induced loop formation that implies multivalent binding to DNA, which in turn suggests that Ru(TAP)$_3^{2+}$ can interact via (at least) two interfaces simultaneously. Interestingly, Ru(phen)$_3^{2+}$ does not form DNA synapses to the

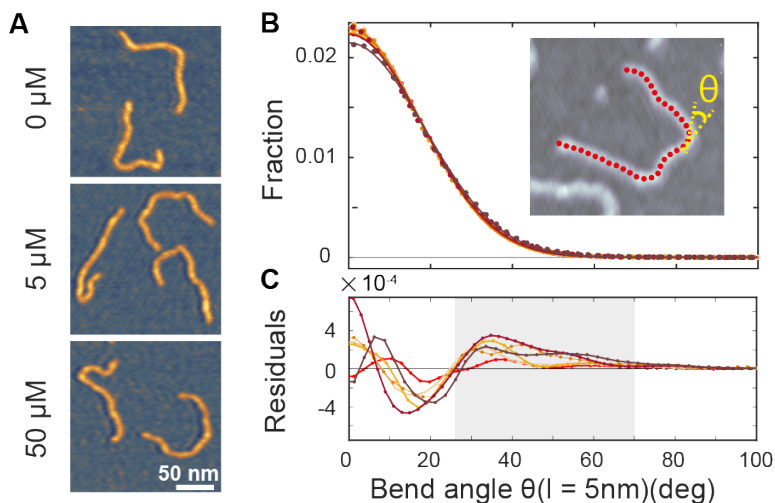Figure 36: AFM demonstrates Ru(TAP)$_3^{2+}$-mediated DNA kinking with low yield. A) AFM topographs of 486 base pair linear DNA molecules incubated with increasing concentrations of Ru(TAP)$_3^{2+}$. B) Bend angle distributions (Kernel density estimate with band width 4°) of DNA generated by automated tracing of the chain contours with a step length $l = 5$ nm. For each condition $\approx 10000$ angles are recorded. Solid lines are fits to a folded Gaussian. Colour code is the same as in Figure 35C. Residuals of the folded Gaussian fits in (B) depicting a concentration-dependent increase of bend angles in the range of 30 deg $< \theta <$ 70 deg (grey area).

extent observed for Ru(TAP)$_3^{2+}$, despite the higher affinity for intercalation, suggesting that loop formation is mediated in part by the N1 and N8 atoms of TAP, potentially via hydrogen bonding [229].

To address how multivalent binding by Ru(TAP)$_3^{2+}$ might impact excited state processes, we carried out spectroscopic measurements with either short (32 base pair; 50% GC; expected to behave as a rigid rod) or long (48501 base pair; 49% GC; that will adopt a random coil conformation, which increases the local concentration of DNA segments) DNA to modulate the contact probability that would lead to Ru(TAP)$_3^{2+}$-mediated synapse formation. First we tested whether DNA length affects luminescence by recording spectra upon titrating Ru(TAP)$_3^{2+}$ (5 µM) with the different DNA substrates. Luminescence quenching was evaluated for both DNA substrates in the same concentration range ([base pair] $= 0 - 250$ µM) and found to be approximately independent of DNA length (Figure 37A,B). The quenching as a function of [base pair] is well-described by the McGhee-von Hippel binding model with (K$_d$,n) from the force-extension
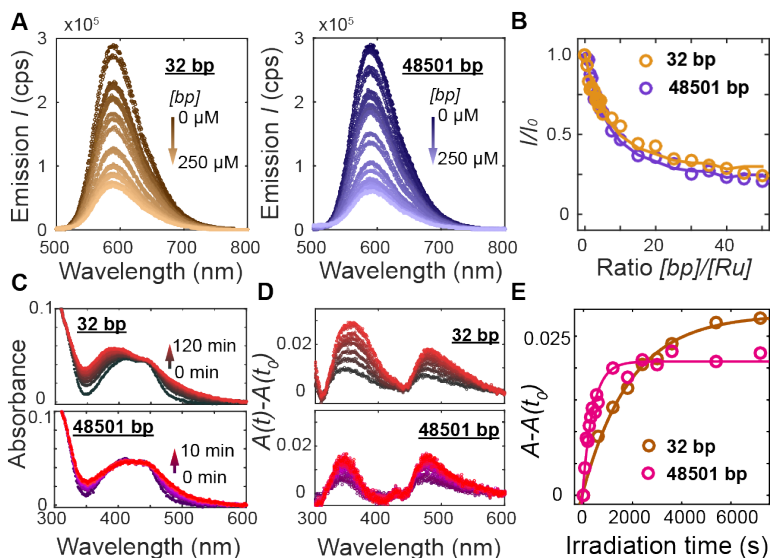
Figure 37: DNA length-dependence of excited state processes in Ru(TAP)$_3^{2+}$.
A) Photoluminescence ($\lambda_{excitation}$ = 436 nm) of Ru(TAP)$_3^{2+}$ (5 µM) on titration with DNA. Left: Titration with 32 base pair DNA ([bp] = 0 – 250 µM; brown gradient). Right: Titration with 48501 base pair DNA ([bp] = 0 – 250 µM; violet gradient). B) Normalized luminescence intensity ($\lambda_{emission}$ = 590 nm) as a function of base pair – to – Ru$^{2+}$ concentration ratio. Solid lines are fits to the McGhee-von Hippel equation (equation 60), using K$_d$ and n obtained from MT data and a variable plateau value that accounts for unproductive binding. C) Absorbance spectra of Ru(TAP)$_3^{2+}$ (5 µM) in the presence of DNA ([bp] = 100 µM) after irradiation at 465 nm for different irradiation times. Top: absorbance spectra on irradiation in the presence of 32 base pair DNA. Bottom: spectra obtained on irradiation in the presence of 48501 base pair DNA. D) Difference absorption spectra for different irradiation times with respect to absorbance prior to irradiation (t = t$_0$). E) Difference absorption at 350 nm as a function of irradiation time in mixtures containing 5 µM Ru(TAP)$_3^{2+}$ and either 32 base pair or 48501 base pair DNA ([bp] = 100 µM). Solid lines are fits to first-order kinetics, with reaction lifetimes $\tau$ = 33 ± 7 min and $\tau$ = 7 ± 2 min for photoadduct formation on 32 base pair and 48.5 kbp DNA, respectively.

data and including an offset that takes into account non-productive binding at AT-sequences. The luminescence quenching follows the same concentration dependence as the lengthening observed in MT, which strongly suggests that intercalative binding governs quenching of the $^3$MLCT state.

To probe the effect of local DNA concentration on photoadduct formation, we recorded the changes in absorption at the MLCT bands on irradiation of $\text{Ru(TAP)}_3^{2+}$ (5 µM) at 465 nm, in the presence of either 32 base pair or 48.5 kbp-long DNA ([base pair] = 100 µM; Figure 37C,D). Formation of covalent adducts leads to the appearance of an absorption peak at $\approx$ 350 nm whereas non-covalent adducts resulting from ligand-exchange with a nucleobase increase the absorption at $\approx$ 500 nm [239]. We find that photoadduct formation is faster for the long than for the short DNA (with first order reaction times of $\tau = 7 \pm 2$ min and $\tau = 33 \pm 7$ min, respectively; Figure 37E), but achieves a lower final yield. In addition, the peak at 350 nm is much narrower for the long DNA construct as compared the short variant (Figure 37D), implying a smaller range of photoadduct species. The spectroscopic data suggest that photoadduct formation, in contrast to luminescence quenching, is faster on long than on short DNA. The lower yield and better-defined photoadducts suggest that binding to long DNA imposes geometrical constraints that prevent the formation of a broad range of products.

### 5.3.4    *Conclusions*

In conclusion, our work reconciles previous -apparently contradicting- reports on the DNA-binding modes of $\text{Ru(TAP)}_3^{2+}$. Racemic $\text{Ru(TAP)}_3^{2+}$ and $\text{Ru(phen)}_3^{2+}$ can interact with DNA via (semi-)intercalation that occasionally occurs in a kinked state, consistent with a combination of the differential effects observed for enantiopure complexes [230–234]. $\text{Ru(TAP)}_3^{2+}$ additionally can mediate DNA looping, presumably via combined (semi-)intercalation and hydrogen-bonding [229]. This multivalent binding might explain the differential yield of photoadduct formation on short versus long DNA. The dependence of photoadduct formation on local DNA concentration is important towards applications of Ru-TAP complexes *in vivo*.

### 5.3.5    *Acknowledgements and Funding*

### 5.3.6    *Conflicts of Interest*

There are no conflicts to declare.

### 5.3.7  *Materials and Methods*

#### 5.3.7.1  *DNA substrates*

For the MT measurements a 7.9-kbp DNA construct, prepared as described previously [116], was used. In brief, PCR-generated DNA fragments ($\sim$ 600 bp) labeled with multiple biotin or digoxigenin groups were ligated to the DNA, to bind magnetic beads and the flow cell surface, respectively. Linear DNA fragments (486 base pair) used for AFM imaging were obtained by PCR amplification of a synthetic DNA fragment (gBlock fragment; Integrated DNA Technologies). PCR products were purified from primers, proteins and salts using a PCR Cleanup kit (QIAquick PCR Purification Kit – Qiagen) and resuspended in 10 mM phosphate buffer. To test the effect of DNA length on the spectroscopic properties of Ru(TAP)$_3^{2+}$, we used phage lambda DNA (NEB; N3011L) that was dialyzed overnight against 10 mM phosphate buffer to remove the EDTA used for storage. In addition we tested a 32 base pair double stranded fragment that was obtained by annealing the complementary oligodeoxynucleotides 5' ACG TCA GTC AGC ATC AGA GTT TTC CCG TGA AG 3' and 5' CTT CAC GGG AAA ACT CTG ATG CTG ACT GAC GT 3'.

#### 5.3.7.2  *Ruthenium complexes*

Racemic Ru(TAP)$_3$Cl$_2$ was synthesized following published methods [240]. The powder was dissolved in 10 mM phosphate buffer and the concentration was measured using the extinction coefficient $\epsilon_{437nm} = 13000$ M$^{-1}$cm$^{-1}$). Racemic Ru(Phen)$_3$Cl$_2$ was obtained commercially (Sigma-Aldrich; 904767). The powder was dissolved in 10 mM phosphate buffer and the concentration was assessed spectroscopically using the extinction at 445 nm ($\epsilon_{445nm} = 19000$ M$^{-1}$cm$^{-1}$).

#### 5.3.7.3  *Buffers*

All experiments were performed in 10 mM phosphate buffer, pH = 7.0.

#### 5.3.7.4  *Atomic force microscopy imaging*

Samples were prepared by incubating 486 base pair linear DNA (1 ng/µL) and Ru(TAP)$_3^{2+}$ at different concentrations in phosphate buffer (pH = 7.0), for 10 min. After incubation, 20 µL of the sample was drop-casted on poly-L-lysine (0.01 % w/v) coated muscovite mica (West Chester, USA). After 30 s, the substrates were gently rinsed using 20 mL of milliQ water and dried using a gentle stream of filtered N2 gas. AFM imaging was performed on a commercial Multimode AFM, equipped with a Nanoscope III controller and a

type E scanner. Images were recorded in amplitude modulation mode under ambient conditions and using silicon cantilevers (Nanoworld; type SSS-NCH; resonance frequency $\approx$ 300 kHz; typical end-radius 2 nm). Scans of 1 µm$^2$ were recorded at 4 Hz line frequency, with optimized feedback parameters and at 512 $\times$ 512 pixels. For image processing, Scanning Probe Image Processor (SPIP v6.4; Image Metrology) was employed. Image processing involved background correction using global fitting with a third-order polynomial, and line-by-line correction through the histogram alignment routine. Data analysis involved tracing of the DNA contours with a step-length l = 5 nm using the algorithm by Wiggins *et al.* [83]

### 5.3.7.5  *Magnetic tweezers*

We used a custom-built MT setup, described previously [134, 241], with a pair of 5 $\times$ 5 $\times$ 5 mm$^3$ permanent magnets (W-05-N50-G, Supermagnete, Switzerland) oriented in vertical configuration [208] and with a gap size of 1 mm. A DC-Motor (M-126.PD2, PI, Germany) controlled the distance between the flow cell and magnets, and another DC-Motor (C-150.PD, PI, Germany) was used to rotate the magnets. A 40x oil immersion objective (UPLFLN 40x, Olympus, Japan) was used to image the beads onto a CMOS sensor camera (12M Falcon2, Teledyne Dalsa, Canada) with a field of view of 400 $\times$ 300 µm$^2$. Images were recorded at 58 Hz and transferred to a frame grabber (PCIe 1433, NI, USA). A custom-written tracking software analyzed the images to yield the (x,y,z) coordinates of all beads in real time [132]. A LED (69647, Lumitronix LED Technik GmbH, Germany) was used to illuminate the sample. For tracking the z-position of the beads, look-up tables (LUT) were generated to relate the defocused pattern of the bead to its height [242]. The LUT was generated by moving the objective using a piezo stage (Pifoc P-726.1CD, PI, Germany).

Flow cells were built from two glass coverslips (24 $\times$ 60 mm, Carl Roth, Germany). To attach the DNA to the flow cell, the bottom coverslip was first modified with (3-Glycidoxypropyl)trimethoxysilane (abcr GmbH, Germany). Afterwards, 75 µL of 5000x diluted stock solution of polystyrene beads (Polysciences, USA) in ethanol (Carl Roth, Germany) was dropcasted on the silanized slides, dried in a closed container, and baked at 80 °C for 1 min, to serve as reference beads. A laser cutter was used to produce openings with a radius of 1 mm in the top coverslip, to enable liquid exchange. The two coverslips were glued together by a single layer of melted Parafilm (Carl Roth, Germany), comprising a $\sim$ 50 µL channel connecting the inlet and outlet opening of the flow cell. Following flow cell assembly, 100 µg/ml anti-digoxigenin (Roche, Switzerland) in 1x PBS was introduced and incubated for 2 h. To reduce non-specific interactions, the flow cell was flushed with 800 µL of 25 mg/ml bovine serum albumin (Carl Roth, Germany), incubated for 1 h and rinsed with 1 ml of 1x PBS.

For all measurements, we used 1.0 μm diameter MyOne magnetic beads (Life Technologies, USA). The DNA construct was attached to streptavidin coated beads by incubating 0.5 μL of picomolar DNA stock solution and 2 μL MyOne beads in 250 μL 1x PBS (Sigma-Aldrich, USA) for 5 min. Subsequently, the bead-coupled DNA solution was introduced in the flow cell for 5 min to allow formation of digoxigenin-anti-digoxigenin bonds. Subsequently, the flow cell was rinsed with 2 ml of 1x PBS to flush out unbound beads. Next, the magnet was mounted, which constrains the rotation and applies an upward force on the beads.

After installing the magnets, selected beads were tested for the presence of multiple tethers, and torsional constraint, by measuring their response to forces and torques. The presence of multiple tethers was assessed by rotating the magnet to introduce negative supercoiling under high tension (F ≥ 5 pN.) In the case of a single DNA tether, high tension impedes the formation of plectonemes at negative linking differences. As a result, no height change is observed. In contrast, in case of multiple tethers are attached to a bead, introduction of negative supercoiling results in braiding, decreasing the z-extension of the bead. Beads bound by multiple tethers are discarded from further analysis. To assess whether DNA tethers were torsionally constrained, positive linking differences are introduced at low force (0.4 pN). In torsionally constrained DNA tethers, this results in plectoneme formation, thereby decreasing the z-extension. In nicked DNA tethers, no linking difference can be introduced and the z-extension remains constant on rotation of the magnet.

Following bead selection and testing, the buffer in the flow cell was exchanged for a 10 mM phosphate buffer (pH = 7.0) using a peristaltic pump (flow rate ∼ 150 μL · min$^{-1}$). For force-extension analysis, we exclusively focus on torsionally unconstrained (nicked) tethers and calibrate the magnet distance-to-force relation for each bead by recording the transverse fluctuations of the beads at different magnet separations for times approximately 10-fold larger than the characteristic time of the system at the corresponding force, and analyze the power spectral density of the fluctuations to quantify the force at each magnet position [139, 143].

The force (F) -extension (z) relation was subsequently fitted using an approximation of the WLC model [182] to extract the contour length and bending persistence length of the DNA. Next, we record the force-extension behavior after flushing approximately 5 cell volumes of 10 mM PB buffer supplemented with 1-100 μM of either Ru(TAP)$_3^{2+}$ or Ru(Phen)$_3^{2+}$. In the presence of Ru-complex, we record magnet distance vs. tether extension (z) curves, and use the previously calibrated force for each bead to construct force vs. extension curves, which are fitted using the WLC model to give the contour length and persistence length as a function of complex concentration. For the construction of rotation curves, we focused on torsionally constrained DNA tethers and

used the external magnets to introduce supercoiling at a tension F = 0.3 pN. Both clockwise and counterclockwise rotation of the magnets (with respect to the relaxed state) results in a symmetrical decrease of the extension due to plectonemic supercoil formation.

We use the intersection of the extrapolated linear regimes of the rotation curves [116, 137] to define the midpoint of the rotation and to quantify the rotation offset as a function of added Ru(II)-complex with respect to midpoint of rotation curves obtained in the absence of added complex. Data analysis of MT data was performed using MATLAB (Mathworks). All quoted error bars are standard deviations obtained from multiple observations. Fitting uncertainties are 95% confidence intervals.

### 5.3.7.6 *DNA-induced luminescence quenching*

To study $Ru(TAP)_3^{2+}$ luminescence quenching by addition of DNA, we mixed either phage lambda DNA (NEB; dialyzed overnight against PB buffer) or a 32 base pair double stranded fragment (obtained by annealing the complementary oligodeoxynucleotides 5' ACG TCA GTC AGC ATC AGA GTT TTC CCG TGA AG 3' and 5' CTT CAC GGG AAA ACT CTG ATG CTG ACT GAC GT 3') and $Ru(TAP)_3^{2+}$ at final concentrations $c_{DNA} = 165$ ng/mL and $c_{Ru} = 5$ µM. Emission spectra on excitation at 436 nm were recorded in the wavelength range 500-800 nm, employing a commercial spectrofluorometer (Fluoromax Plus; Horiba). The DNA concentration in the cuvette was stepwise decreased by replacing a fraction of the DNA solution with the same volume of a solution containing 5 µM $Ru(TAP)_3^{2+}$ in 10 mM phosphate buffer. The spectra were background corrected and further analyzed using MATLAB (Mathworks).

### 5.3.7.7 *DNA photoreaction*

To study photoadduct formation of $Ru(TAP)_3^{2+}$ with DNA, we employed solutions containing 65 ng of DNA (either dialyzed phage lambda, or the annealed 32 base pair oligo; see above) and 5 mM $Ru(TAP)_3^{2+}$ in 10 mM phosphate buffer (pH = 7.0) in a final volume of 1 mL. The reactions were carried out in a quartz cuvette under irradiation of 465 nm light (Lumitronix) while being continuously stirred. After defined irradiation times, the absorbance of the solution was recorded in the range of $280 - 600$ nm using an Evolution$^{TM}$ 201/220 UV-Vis-Spektrophotometer (ThermoFisher Scientific).

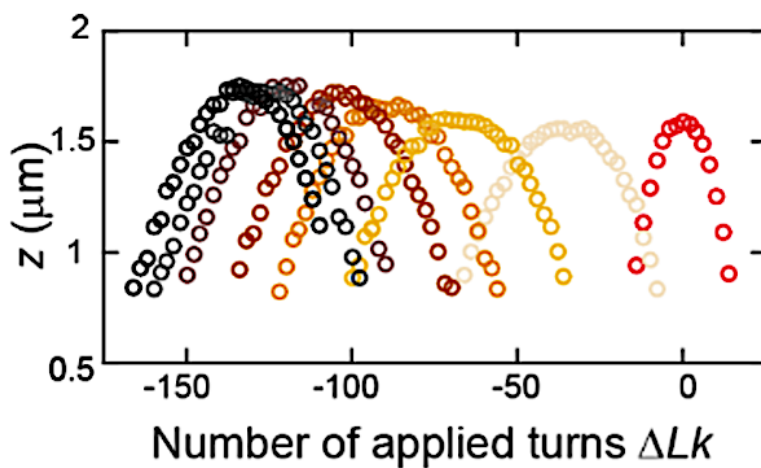### 5.3.8 *Supplementary Figures*



Figure 38: DNA unwinding by $Ru(Phen)_3^{2+}$. Rotation curves of DNA in the absence (red) and presence (brown gradient; see Figure 34 in section 5.3.3) of increasing concentrations (1-100 µM) of $Ru(TAP)_3^{2+}$.
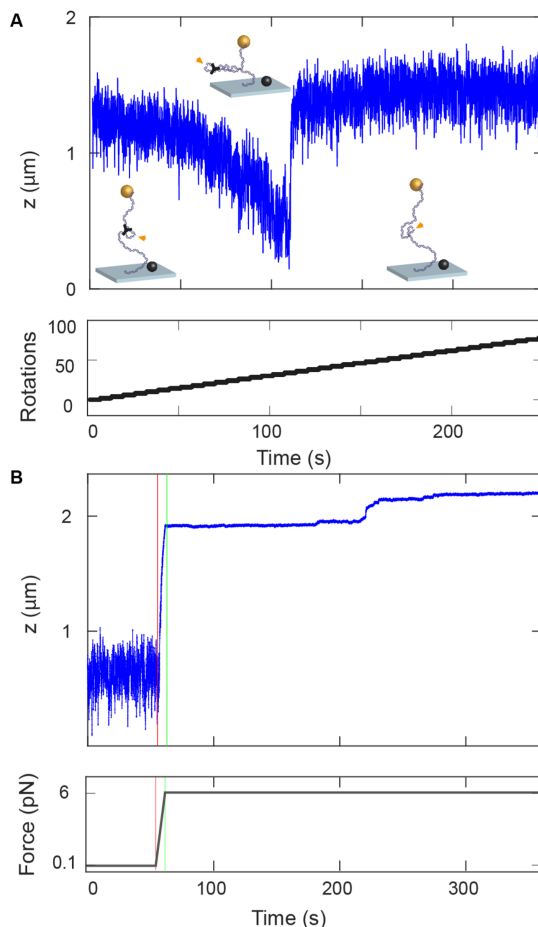
Figure 39: Evidence for $\text{Ru(TAP)}_3^{2+}$-mediated DNA looping. A. Rotation of a nicked DNA tether in the presence of 50 µM $\text{Ru(TAP)}_3^{2+}$ at F = 0.3 pN depicting extension decrease due to supercoiling, followed by a sudden extension jump to the relaxed state. Insets are schematic drawings (not to scale) demonstrating how multivalent binding by a single $\text{Ru(TAP)}_3^{2+}$ complex could shield the nick (orange arrow), thereby enabling introducing plectonemic supercoils that reduce the bead height. Dissociation (or partial dissociation) of the complex releases the topological constraint and removes the plectonemic supercoils by swivelling of the DNA at the nicking site, thereby restoring the extended state of the DNA. B. Force-jump experiment wherein DNA in the presence of 50 µM $\text{Ru(TAP)}_3^{2+}$ is first subjected to low tension (F = 0.1 pN) followed by a sudden increment in force (F = 6 pN). Note the discrete extension increments at high force.

# TOPOLOGY-DEPENDENT DNA BINDING

As discussed and demonstrated in the previous two chapters for various examples, fluorescent dyes are used in a wide range of biochemical and biotechnological procedures to stain and visualize DNA. Although the binding mechanisms for some dyes are known, the effects of DNA binding are often not well understood. As introduced in Section 2.3, the non-covalent interactions between DNA and ligands are complex and depend on the nature of the ligand. One feature of small DNA-binding ligands is that they have different modes of binding to DNA. These different modes of binding can be distinguished experimentally by the fact that they have different effects on DNA structure and mechanics, such as changes in molecular elongation or linking number, as shown for SYBR Gold in Chapter 4 and Ru(TAP)$_3^{2+}$ in Chapter 5. These changes in extension and linking number per binding protein can be characterized if the relationship between force, torque, extension, and linking number can be determined at a range of dye concentrations [110, 116, 243, 244].

## 6.1 DNA BINDING MODES

Small molecules can interact with dsDNA noncovalently by means of three main interaction types: major groove binding, minor groove binding, and intercalation (Figure 40) [110, 244–246]. As the names already suggest, major groove binding small molecules (Figure 40A) bind to the major groove of DNA and minor groove binding small molecules (Figure 40B) bind to its minor groove. The third binding mode is intercalation where the small molecule lodges between two adjacent base pairs of the dsDNA.

In DNA intercalation complexes, there are several factors that determine the binding of a small molecule between DNA base pairs. The electrostatic potential in the intercalation plane can be calculated using an accurate multipolar distributed electrostatic ab initio model for a range of intercalation sites. For chromophores with predominantly positive electrostatic potentials, there is a significant electrostatic contribution to the binding energy, which, however, varies greatly depending on the sequence and to some extent on the twist angle. Electrostatic forces play an important role in positioning and stabilizing intercalative binding in sterically constrained positions. Sequence selectivity of intercalator binding to DNA and the resulting twist angle are determined by a complex mix of factors, with electrostatics being only one component. Nevertheless, most intercalators do not exhibit strong sequence selectivity [247–249].
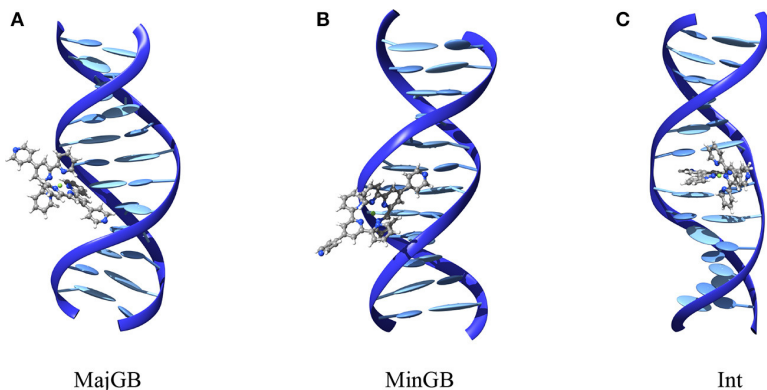
Figure 40: Different interaction modes of small molecules binding to DNA: A) major groove binding (MajGB), B) minor groove binding (MinGB), C) intercalation (Int). Structures are extracted from MD simulations. Figure taken from Ref. [245].

Another major question of intercalative binding is how the chemical nature of the small DNA-binding molecule affects the binding energy for its intercalation between two base pairs and what forces act between the small molecule and the bases. The stability of the stacked DNA base pairs originates in the electron correlation. Therefore, the electrostatic interactions between a given intercalator and the base pairs depend on how the charge distribution of the intercalator compares to the potential generated by the base pairs as well as the actual binding energy [248]. In addition, most intercalators have non-intercalating side-chains that can even bind to DNA grooves, and also steric effects can directly influence intercalation, and thus affect electrostatic energy.

## 6.2 LE CHATELIER'S PRINCIPLE

As discussed in detail for the intercalator SYBR Gold in Chapter 4, intercalative binding to DNA affects the DNA structure, i. e., it lengthens and unwinds the DNA helix [116, 157]. However, these ligand-induced conformational changes also affect ligand binding, so that there is generally an interaction between strain-dependent binding and binding-induced conformational changes.

In 1884, the French chemist Henri Louis Le Chatelier formulated general statements on the laws of chemical equilibrium [250], which should later be known as 'Le Chaterlier's principle':

> Any system in stable chemical equilibrium that is subject to an external cause that tends to vary either its temperature or its condensation (pressure, concentration, number of molecules per

unit volume), in total or only in some of its parts, can experience only those internal modifications that would bring about a change in temperature or condensation of opposite sign to the one that would result from the external cause if only those modifications were produced [250].

In other words, when a chemical system in equilibrium is subjected to a constraint (change in temperature etc.), it responds in such a way that the effect of the constraint is minimal. The newly established equilibrium then counteracts the applied change.

The concept of Le Chatelier's principle can be transferred to the binding of small molecules to DNA. Having a defined DNA topology, e. g.in closed-circular DNA, imposes a global constraint on the interplay between strain-dependent binding and binding-induced conformational changes. This suggests a torque-dependent binding constant

$$K = K_0 \cdot \exp\left(-\frac{\tau \cdot \theta}{k_B T}\right) \tag{62}$$

with $K_0$ the torque-independent binding constant, $\tau$ the torque, $\theta$ the unwinding angle per dye, and $k_B T$ the thermal energy. Indeed, in single-molecule studies with the intercalating dye ethidium bromide, torque-dependent binding of dyes to DNA has been observed. Overwinding or positive torque hinders binding while underwinding or negative torque promotes binding [116].

In the following publication, I will investigate the binding of DNA ligands under a global topological constraint both experimentally and theoretically. In the experiments, I will focus on the routinely used intercalators ethidium bromide, SYBR Gold, SYTOX Orange, and trimethylpsoralin. I will investigate intercalative binding to DNA by these fluorescent dyes that enable direct visualization and quantification of DNA binding via fluorescence detection and imaging. In addition, I will present a theoretical model for DNA ligand binding in a topologically closed system that accurately describes the experimental data and allows the quantitative study of different densities of DNA supercoiling both *in vitro* and *in vivo*. The model provides the opportunity to elucidate the complex interaction between topology and affinity of the ligand. Here I will show that binding depends on the initial topology and affinity of the intercalator. Interestingly, global topological constraint can increase or decrease binding, depending on concentration and binding regime. In particular, binding of DNA intercalators above their $K_d$ value is almost independent of topology. With this knowledge, recommendations can be made for the optimal use of intercalative dyes to visualize DNA under a global topological constraint. Taken together, a thorough understanding of DNA-ligand interactions is possible through the combination of theoretical modelling and several complementary

experimental techniques. The approach presented in the following should also be applicable to other DNA binders and provide reliable and unbiased detection and quantification of the different topological states of DNA. In addition, the results provide a basis for the quantitative study of complex *in vivo* processes. DNA topology plays a critical role for DNA interactions, which has important implications for the regulation of genomic information and needs to be taken into account in biochemical and biophysical assays.

# Topology-dependent DNA binding

By

Pauline J. Kolbeck[1,2,+], Miloš Tišma[3,+], Brian T. Analikwu[3], Willem Vanderlinden[1,2], Cees Dekker[3,*], and Jan Lipfert[1,2,*]

[1] Department of Physics and Center for NanoScience, LMU Munich, Amalienstrasse 54, 80799 Munich, Germany
[2] Soft Condensed Matter and Biophysics, Department of Physics and Debye Institute for Nanomaterials Science, Utrecht University, Princetonplein 1, 3584 CC Utrecht, The Netherlands
[3] Department of Bionanoscience, Kavli Institute of Nanoscience, Delft University of Technology, 2629HZ Delft, The Netherlands
[+] Both authors contributed equally to this work.
[*] Corresponding author

Submitted.

---

My contribution to this work was performing single-molecule magnetic tweezers measurements as well as spectroscopic and gel electrophoretic measurements, analyzing the resulting data, and co-writing the manuscript with input from all authors.

### 6.3.1  *Abstract*

DNA stores our genetic information and is ubiquitous in biological and biotechnological applications, where it interacts with binding partners ranging from small molecules to large macromolecular complexes. Binding is modulated by mechanical strains in the molecule and, in turn, can change the local DNA structure. Frequently, DNA occurs in closed topological forms where topology and supercoiling add a global constraint to the interplay of binding-induced deformations and strain-modulated binding. Here, we present a quantitative model of how the global constraints introduced by DNA topology modulate binding and create a complex interplay between topology and affinity. We focus on fluorescent intercalators, which unwind DNA and enable direct quantification via fluorescence detection. Using bulk measurements, we show that DNA supercoiling can increase or decrease intercalation relative to an open topology depending on ligand concentration and the initial topology. Our model quantitatively accounts for observations obtained using psoralen for UV-induced DNA crosslinking, which is frequently used to quantify supercoiling *in vivo*. Finally, we observe topology-dependent binding in a single-molecule assay, which provides direct access to binding kinetics and DNA supercoil dynamics. Our results have broad implications for the detection and quantification of DNA and for the modulation of DNA binding in cellular contexts.

### 6.3.2  *Introduction*

DNA is the carrier of genetic information in all cellular life. *In vivo*, dsDNA is often present in circular and, therefore, topological closed form. In particular, bacterial chromosomes and plasmids are circular DNA molecules, whose topology is tightly regulated *in vivo* [251–254]. In eukaryotes, DNA topology and supercoiling similarly play important roles in the context of a chromatinized genome, e. g., in the compaction and regulation of genetic information [255–259].

Both in its biological role and in many biotechnological applications, DNA interacts with a broad range of ligands, i. e., binding partners that range from small molecules to large proteins complexes. In particular, the detection and quantification of DNA often rely on staining with fluorescent small molecules that frequently bind in an intercalative binding mode [106, 117, 157, 164, 260, 261]. Ligand binding to DNA can, in general, locally alter the DNA structure and introduce strains away from the equilibrium B-form DNA conformation [262–266]. In turn, stretching forces and torsional strains have been shown to systematically affect binding equilibria [116, 171, 178, 267, 268]. Having a defined DNA topology, e. g., in a plasmid or other topological domains, imposes a global constraint on the interplay between strain-dependent binding and binding-induced conformational changes. However, it is not well understood

how this interplay affects binding in a typical experimental setting and how to quantitatively model binding equilibria under a global topological constraint.

Here we investigate DNA-ligand binding under a global topological constraint. We first develop a model of ligand binding to topologically closed DNA, which takes into account the conformational changes induced by the ligand, the influence of strains on binding equilibria, a physical model of plasmid mechanics, and the global constraint introduced by having a defined linking number due to the defined topology. We then experimentally probe interactions between small molecule intercalators and DNA of different, defined topologies. We focus on commonly used intercalators that are well-characterized by previous studies: Ethidium bromide (EtBr), SYBR Gold, and SYTOX Orange (Figure 47). EtBr is a very widely used stain for DNA visualization in gels and other applications [116, 164, 168, 171, 178, 189, 192, 269, 270]. SYBR Gold is a more recently developed DNA stain, which has very high quantum efficiency and brightness [157–160]. SYTOX Orange is frequently used to stain and supercoil DNA in single-molecule experiments [160, 181, 271–273]. Finally, we extend our analysis to the intercalator 4,5',8-trimethylpsoralen (TMP; also known as trioxsalen) that is used as a photo-crosslinking agent, both for phototherapy [274] and to detect supercoiling and chromatin structure *in vivo* [275–279].

We first perform experiments in bulk using topologically constrained plasmid DNA, i. e., circular DNA with both strands fully intact (referred to as the supercoiled species, "sc"; Figure 41A) and, for comparison, topologically open DNA that has been either nicked (open circular DNA, "oc"; Figure 41B) or linearized (linear DNA, "lin"; Figure 41C). Additionally, we use fluorescence detection to quantify the amount of binding, and demonstrate that intercalative binding to DNA is topology dependent, in quantitative agreement with our model. We then apply our model to a single-molecule DNA assay [271, 273], where DNA is supercoiled *in situ* by intercalation. We monitor the fluorescence change upon nicking of the DNA molecule, which induces an abrupt transition from a closed to an open topology, and we find excellent agreement with our model. The single-molecule assay enables us to observe the re-adjustment of the binding equilibrium upon change in topology in real time, which enables us to probe the dynamics of the process.

Our findings have direct practical applications since gel-based assays for the discrimination and detection of topoisomers are widely used to study the properties of circular DNA and of various enzymes that alter DNA topology, including topoisomerases, gyrase, reverse gyrase, and recombinases[280–282]. An unbiased quantification of the different topoisomers using fluorescence staining, which is increasingly used to replace radiolabelling due to the hazards associated with handling, storing, and disposing of radioactive materials, must take into account the observed topology dependencies. Using our findings, we

provide practical guidelines for unbiased detection of different topoisomers and discuss consequences of topology-dependent binding more broadly.

### 6.3.3    *Results*

#### 6.3.3.1    *Model for ligand binding under topological constraint*

Here we develop a model for ligand binding to plasmid (or otherwise topologically closed) DNA, where the topology imposes a global constraint (Figure 41D-F). Binding to plasmid DNA is different from a standard bimolecular binding equilibrium for several reasons that we take into account in our model. First, the linear structure of DNA imposes local constraints for ligand binding, if bound ligands occupy a binding size of $n$ bases (Figure 41D). Binding of ligands with binding site size $n$ can be modeled using the McGhee-von Hippel model [105, 116] in cases where the DNA concentration is much lower than the ligand concentration, such that the free and total ligand concentrations are approximately equal. For bulk measurements, however, the concentration of DNA bases can be similar to or even larger than the ligand concentration and needs to be considered. Therefore, we use an extension of the McGhee-von Hippel model that explicitly takes into account both the ligand ($c_{total}$) and DNA ($c_{DNA}$) concentration that was derived in Ref. [157]. The fractional binding $\gamma$ is given by

$$\gamma = \frac{c_{bound}}{c_{DNA}} = \frac{c_{total} - c_{bound}}{K_d} \cdot \frac{(1 - n \cdot \frac{c_{bound}}{c_{total}})^n}{(1 - n \cdot \frac{c_{bound}}{c_{DNA}} + \frac{c_{bound}}{c_{DNA}})^{n-1}} \tag{63}$$

Here $c_{bound}$ is the bound ligand concentration, $c_{free}$ is the free ligand concentration, $c_{total} = c_{free} + c_{bound}$ the total ligand concentration, $K_d$ is the dissociation constant (in M), and $n$ is the binding site size (in base pairs). Typical values of the binding site size for intercalators are $n \approx 2$, corresponding to binding every other base pair.

Intercalation affects the local geometry of the DNA helix, by locally unwinding and lengthening the helix [116, 164, 171, 261, 284, 285] (Figure 41E). Here we assume that each intercalation event locally lengthens the DNA by $\Delta z$ and unwinds it by $\Delta\theta$. Typical values for intercalators are in the range $\Delta z \approx 0.34$ nm and $\Delta\theta \approx 15° - 30°$. The fact that intercalation lengthens and unwinds the DNA helix suggests, by Le Chatelier's principle, that applying a stretching force or unwinding torque, respectively will increase intercalative binding. Conversely, overwinding the helix will hinder intercalation. We assume an Arrhenius-like exponential dependence of the binding constant [160, 171, 192, 286] on applied force $F$ and torque $\Gamma$:

$$K_d(F, \Gamma) = K_{d,0} \cdot \exp\left(\frac{\Gamma \cdot \Delta\theta}{k_B T}\right) \cdot \exp\left(-\frac{F \cdot \Delta z}{k_B T}\right) \tag{64}$$
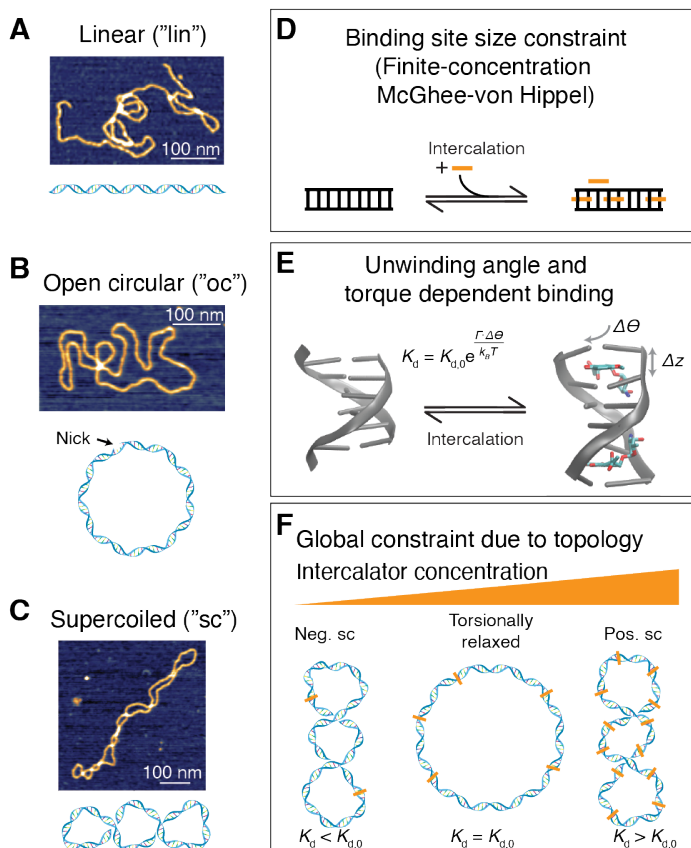
Figure 41: Overview of different topological conformations of plasmid DNA and outline of the binding model under global constraint. A) Schematic and an AFM height image of linear DNA. B) Schematic and an AFM height image of open circular DNA, i. e., of plasmid DNA that is nicked at a single site. C) Schematic and an AFM height image of a negatively supercoiled DNA plasmid. AFM images in panels A-C are of pBR322 plasmid DNA (4,361 bp; see Methods Section 6.3.8.1). D) Schematic of the McGhee-von Hippel binding model for ligand binding to DNA, whereby the binding site size modulates the binding equilibrium. E) Illustration of how intercalation into DNA lengthens and underwinds the B-form helix. Left: B-form DNA, rendered from PDB entry 4C64 [283]. Right: DNA in the presence of an intercalator, here daunomycin rendered from PDB entry 1D11 [252]. F) Schematic of how the global constraint due to topology leads to increased binding as long as the DNA is negatively supercoiled (left), but will decrease binding when the DNA is positively supercoiled (right), compared to the torsionally relaxed form (center). Intercalation, in turn, locally underwinds the DNA and, therefore, leads to an increase in $Wr$ with increasing intercalation.

Here $K_{d,0}$ is the dissociation constant for the relaxed molecule, i. e., in the absence of forces or torques, $k_B$ Boltzmann's constant and $T$ the absolute temperature. For plasmids in free solution, the force is zero (or at least small, specifically $F \ll \frac{k_B T}{\Delta z} \approx 10$ pN) and the second exponential factor in Equation 64 can be neglected. Values for $n$, $K_d$, $\Delta z$, and $\Delta \theta$ for selected dyes are summarized in Table 7.

| Quantity | EtBr [116] | SYBR Gold [157] | SYTOX Orange [160]+ | TMP [287, 288]* |
|---|---|---|---|---|
| Binding site size $n$ | 1.9 | 1.6 | 3.0 | 2 |
| Dissociation const. $K_d$ | $7.7 \cdot 10^{-6}$ M | $0.2 \cdot 10^{-6}$ M | $0.4 \cdot 10^{-6}$ M | $10^{-4}$ M |
| Elongation per dye $\Delta z$ | 0.34 nm | 0.34 nm | 0.30 nm | 0.34 nm |
| Untwisting per dye $\Delta \theta$ | 27° | 19.1° | 19.1° | 28° |

Table 7: Parameters of selected intercalators used in this work. [+]We used the values from Ref. [160] in 100 mM NaCl, close to the ionic strength used in this work. The value for $\Delta \theta$ is an estimate based on data for SYBR Gold. *Ref. [287] only determined the dissociation constant approximately. The binding site size and elongation per dye for TMP were assumed to assume the average values for intercalators indicated in the table.

For linear DNA or open circular DNA molecules, there is no torsional constraint, and the torque will be zero in equilibrium; consequently, binding will simply be determined by Equation 63. In contrast, for topologically closed plasmids, the topology imposes a global constraint. For a closed plasmid, the linking number $Lk$ is a topological invariant and partitions into twist $Tw$ and writhe $Wr$ by White's theorem [95]:

$$Lk = Tw + Wr \tag{65}$$

$Tw$ is a measure for the local winding of the helix and directly related to the torsional strain in the molecule. Conversely, $Wr$ corresponding the crossings of the double helical axis and in a plasmid is related to the number of plectonemic supercoils. We express the linking number balance relative to the torsionally relaxed dsDNA, for which we define $\Delta Lk = 0$, and where $\Delta Tw = Tw ⌣ Tw_0 = 0$, where $Tw_0$ is the natural twist of DNA, equal to the number of base pairs divided by the helical turn ($\approx 10.5$ bp per turn for bare DNA), and $\Delta Wr = Wr$, i. e. the torsionally relaxed conformation has $Wr = 0$.

Intercalation changes the intrinsic twist of the helix and, therefore, shifts the linking number difference at which the molecule is torsionally relaxed by

$N_{bound} \cdot \Delta\theta/360°$ where $N_{bound}$ is the number of dye molecules bound. For a given plasmid, the linking number difference relative to the torsionally relaxed state is, therefore, given by

$$\Delta Lk = \Delta Lk_0 + N_{bound} \cdot \Delta\theta/360° \qquad (66)$$

where $\Delta Lk_0$ is the linking number difference of the plasmid in the absence of intercalation. In general, excess linking number will partition into twist and writhe (Equation 65). For plasmids, it has been shown that the partitioning is independent of the magnitude [94] and sign [235] of the linking difference and is approximately 20% $Tw$ and 80% $Wr$. We assume that this partitioning between twist and writhe also holds in the presence of intercalators, such that

$$\Delta Tw = 0.2 \cdot \Delta Lk \qquad (67)$$

where $\Delta Lk$ is given by Equation 66. In order to compute the torsional strain for a given initial linking difference $\Delta Lk_0$ and given number of intercalated molecules $N_{bound}$, we convert the excess twist (Equation 67) to torque by taking into account the torsional stiffness of DNA:

$$\Gamma = \frac{C \cdot k_B T \cdot 2\pi}{L_C \cdot \Delta Tw} \qquad (68)$$

where $C$ is the torsional stiffness of DNA in nm and $L_C$ the contour length, which in turn depends on the number of molecules bound as $L_C = L_{C,0} + N_{bound} \cdot \Delta z$, where $L_{C,0}$ is the contour length in the absence of intercalation, $\approx 0.34$ nm per bp. The torsional stiffness of DNA has been measured using single-molecule methods [116, 135, 289], is independent of ionic strength [136], and reported values are in the range of $C \approx 100$ nm [116, 290, 291]. However, it is not well known whether or how $C$ is altered by intercalation. Previous measurements using DNA in free solution using EtBr [270, 292, 293] have found lower values of the torsional stiffness in the range $C \approx 50$ nm, which we take as a starting point for the EtBr data.

To determine the number of intercalated molecules per plasmid as a function of total ligand concentration $c_{total}$ and DNA concentration $c_{DNA}$ (typically expressed as the base pair concentration), we numerically solve the coupled Equations 63 to 68 using an iterative approach (Materials and Methods Section 6.3.8.8). The main output of the model is $N_{bound}$. Assuming a linear relationship between the number of intercalated molecules and the fluorescence intensity, which we have previously found to hold for a large range of dye concentrations [157], the observed fluorescence intensity $I$ is given by

$$I = \alpha \cdot c_{DNA} \cdot N_{bound} \qquad (69)$$

where $\alpha$ is a proportionality factor that depends on the quantum efficiency of the dye and the details of the experiments but is constant for a given intercalator and instrumental set up.

### 6.3.3.2  *DNA topology modulates intercalation*

Our model for intercalation into topologically closed DNA predicts that binding can be increased or decreased by the global constraint, relatively to a torsionally relaxed (or linearized) plasmid. Starting with a negatively supercoiled plasmid, which is the form typically found *in vivo*, intercalation at low ligand concentration is increased relatively to a topologically open DNA, due to the negative torsional strain in the molecule (Figure 41F). As more and more molecules intercalate, the negative linking difference is compensated until the plasmid becomes torsionally relaxed, at which point binding to the topologically closed and open forms is the same. Finally, as the intercalator concentration is increased further, the closed plasmid becomes overwound, and the positive torsional strain hinders further intercalation. Therefore, at high intercalator concentration, our model predicts binding of fewer molecules to the closed compared to the open plasmid (Figure 41F).

To experimentally test the prediction of our model, we used plasmid DNA in both topologically constrained, negatively supercoiled form and in open circular and linear topologies (Figure 41A-C; Materials and Methods Section 6.3.8). We prepared mixtures with equal amounts of the three different DNA topologies to facilitate direct comparison on a gel. We then separated the mixtures on a gel (Figure 42A), imaged the gel, and quantified the band intensities to monitor the amount of intercalation (Figure 49). While the open circle and linear topologies exhibit similar intensities, the topologically constrained species in comparison appears less bright on the gel for high EtBr concentrations (Figure 50A). In contrast, for the lowest EtBr concentration, the supercoiled species exhibits a higher intensity than the other two species (Figure 50B). We use our model to quantitatively account for the topology dependent intensities (Figure 42B,C). We find that for the experimental parameters used here, the number of intercalated molecules per plasmid is approximately independent of DNA concentration (Figure 42B). Consequently, the fluorescent intensity increases with DNA concentration (Figure 42C).

At the lowest EtBr concentration (Figure 42C, black lines and symbols), more molecules bind to the supercoiled species (Figure 42C, lines and symbols with red highlighting) as compared to open circular and linear, while at the highest concentration (Figure 42C, light brown lines and symbols) intercalation is reduced for supercoiled compared to the other species. At the intermediate EtBr concentration (Figure 42C, brown lines and symbols) the topologically open and closed species bind EtBr similarly. The differences in binding between the different topologies are a consequence of the negative torsional strain at the lowest EtBr concentration and the positive strain for the highest concentration (Figure 42D). Averaging over the different DNA concentrations, we can quantitatively compare the relative enhancement or reduction of interaction for the topologically closed species compared to the open circular and linear
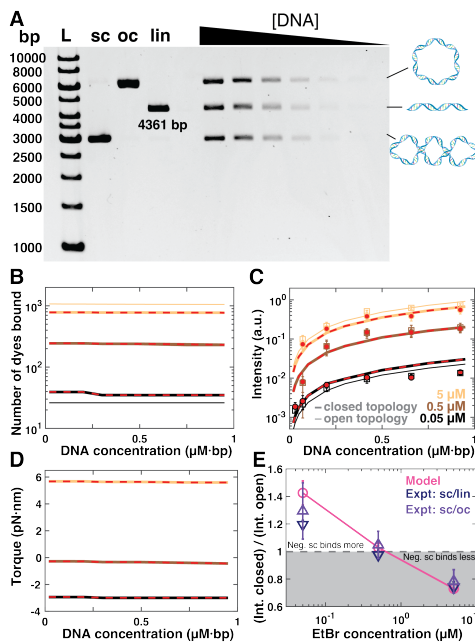
Figure 42: DNA topology dependent intercalation of ethidium bromide. A) Agarose gel stained with EtBr at a final concentration of 0.5 µM. Different DNA topologies are separated on the gel. L: DNA size ladders (1 kb gene ruler, Thermo Scientific, 5 µL). Lanes 2-4 are the stock solutions of negatively supercoiled DNA, linear DNA, and open circular DNA, respectively. Lanes 5-11 are equimolar mixtures of the three topologies, at different total DNA concentrations. B) Predicted number of intercalated molecules $N_{bound}$ as function of DNA concentration for pBR322 DNA (4361 bp). Different colors correspond to different EtBr concentrations: from dark to light 0.05, 0.5, and 5 µM. Thin lines are for topologically open DNA (linear and open circular); thick lines with red highlights are for topologically closed DNA (supercoiled, here with supercoiling density $\sigma$ = -5%, corresponding to $\Delta Lk_0$ = -20 turns). The number of molecules bound is approximately independent of DNA concentration under the conditions investigated, but clearly dependents on EtBr concentration and DNA topology. C) Experimentally determined fluorescence intensity for supercoiled DNA (circles with red highlight) and linear DNA (squares) as a function EtBr and DNA concentration. Symbols are the mean and std from at least two gels. Lines are predictions of our binding model (same color code as in panel B), with the scale factor $\alpha$ as the only fitting parameter (Equation 69). D) Predicted torque in the plasmid from our model, same color code as in panel B. E) Relative fluorescence intensity of a topologically closed DNA relative to the topologically open constructs. Data points are obtained by averaging the different DNA concentration at the same EtBr condition. Triangles are experimental data from at least two independent gels. Magenta symbols are the prediction of our model.

species (Figure 42E) and find excellent agreement between our model and the experimental data.

### 6.3.3.3 *Topology dependent binding depends on initial topology and intercalator affinity*

Having demonstrated that DNA topology can significantly alter DNA binding, we next use our quantitative model to explore how topology modulates intercalation. Starting with a negatively supercoiled plasmid ($\Delta Lk_0 < 0$) intercalation is increased at low intercalator concentrations and suppressed at high concentrations compared to an open topology (Figure 42E). A clear prediction of our model is that if the DNA is initially torsionally relaxed (or even positively supercoiled), intercalation should always be reduced for the closed topology compared to an open topology. We test this prediction experimentally by again preparing and separating DNA plasmids with different topologies, but now using a sample where the plasmid has been relaxed by topoisomerase treatment (Methods), such as that $\Delta Lk_0 \approx 0$ (Figure 43A). As predicted, we find that EtBr intercalation is reduced for the closed topology (Figure 43C and 51), in excellent agreement with our model. More broadly, the relative effect of DNA topology depends both in the initial linking number $\Delta Lk_0$ and on the intercalator concentration (Figure 43E).

Our model predicts that topology dependent binding is most pronounced at ligand concentration below the $K_d$ (Figure 43E, the $K_d$ value is indicated as a vertical line). At concentrations greater than the $K_d$, binding saturates and the modulation by the torsional strain the in the topologically closed plasmid is predicted to only lead to small or negligible changes in binding compared to the torsionally relaxed forms. To test this prediction, we carried out measurements using the intercalator SYBR Gold [157–159], which has a much lower $K_d$ (i.e. higher affinity) compared to EtBr (Table 7 and Figure 43B,D,F). Performing measurements with initially negatively supercoiled or relaxed plasmids at different SYBR Gold concentrations around and above its $K_d$, we find that indeed the topologically closed and open constructs bind similar amounts of SYBR Gold, in quantitative agreement with our model (Figure 43F). To show the broad range of applications, we used three different assays to obtain fluorescence intensity data for SYBR Gold, namely gel electrophoresis, a well plate reader, and a qPCR cycler (see Methods for details).

Importantly, the almost topology-independent binding of DNA intercalators above their $K_d$ is advantageous for assays that aim to quantitatively compare different DNA topologies, e.g., to monitor the products of integration or topoisomerization reactions [280, 294–296]. In particular, for SYBR Gold DNA staining is essentially unbiased by topology for dye concentrations in the range of 1 - 2 μM, which is the concentration range that we previously identified as
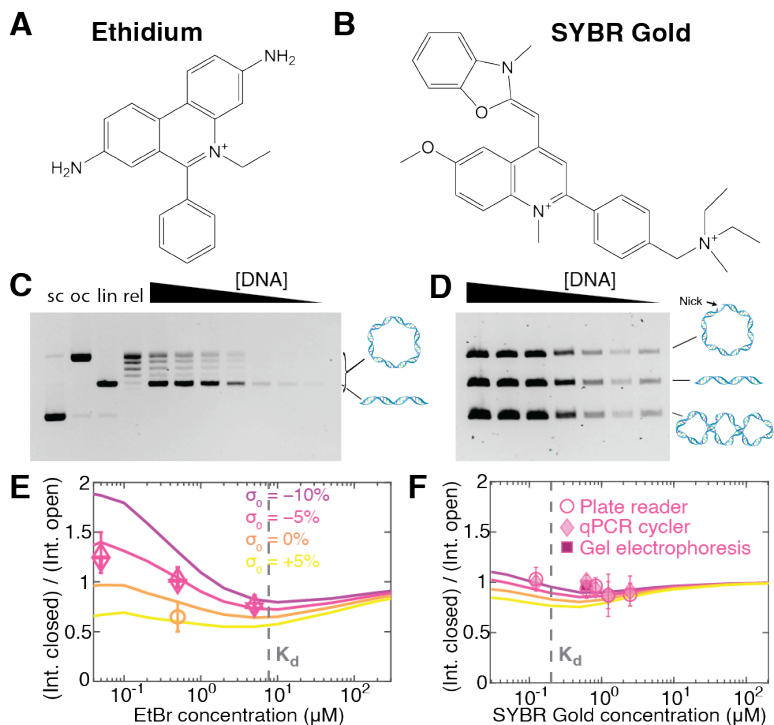
Figure 43: Molecular structure of the intercalator ethidium bromide; taken from Ref. [116]. B) Molecular structure of the intercalator SYBR Gold; taken from Ref. [157]. C) Agarose gel with linear ("lin") and topologically closed but initially torsionally relaxed DNA ("rel"), stained with EtBr at a final concentration of 0.5 µM. The linear DNA travels as a single band, while the relaxed DNA exhibits a topoisomer distribution. Lanes 5-11 are equimolar mixtures of the linear DNA and relaxed DNA. D) Agarose gel with equimolar mixtures of open circular DNA, linear DNA, and supercoiled DNA, stained with SYBR Gold at a final concentration of 0.6 µM. E) Relative binding to topologically closed DNA with different levels of initial supercoiling compared to topologically open constructs as a function of EtBr concentration. Colored lines are the predictions of our model. The vertical grey line indicates the $K_d$ of EtBr. Symbols are the data from Figure 42E; further analysis is shown in Figure 51. F) Same as in panel E for SYBR Gold. The data shown are from three different experimental modalities: fluorescent readout using a 96-well platereader, a qPCR cycler, and gel electrophoresis. Due to the much lower $K_d$ for SYBR Gold compared to EtBr, the binding is almost independent of topology for the SYBR Gold conditions investigated.

optimal for achieving a linear relationship between the fluorescence signal and the amount of DNA present [157].

#### 6.3.3.4  *Psoralen-based DNA crosslinking to quantify DNA supercoiling*

Intercalators of the psoralen family can crosslink DNA upon irradiation with UV light (Figure 44A). They have been widely used in phototherapy [274] and to detect chromatin structure and the degree of DNA supercoiling *in vivo* [275–279]. Often it is assumed that the amount of DNA crosslinking varies linearly with the supercoiling density $\sigma$ [217, 275]. Our model for intercalation under the global constraint induced by topology accurately captures the relative binding of the psoralen compound TMP to supercoiled DNA vs. nicked DNA, determined from a radioactivity assay using $^3$H-labeled TMP [279] (Figure 44B). Similarly, our model correctly predicts the degree of crosslinking induced by TMP for different supercoiling densities [275](Figure 44C and Figure 52A).

Importantly, the crosslinking conditions are chosen such that at most one crosslinking event per plasmid is induced, which means that only a small fraction of the intercalated TMP molecules reacts. For example, under the conditions of the data in Figure 44C, there are $> 10$ TMP molecules bound (Figure 52B), but $< 1$ on average react. However, the fact that the crosslinking signal is well approximated by our binding model using a proportionality constant analogous to Equation 69, suggests that crosslinking is directly proportional to binding. While TMP binding is at least approximately linear with supercoiling density in the range investigated in Figure 44B and C, we note that a linear relationship is only an approximation to the intrinsic exponential dependence on torque and its validity is limited to relatively small supercoiling densities (Figure 44D).

#### 6.3.3.5  *Single-molecule assay monitors topology dependent binding in real time*

To explore consequences of topology dependent binding at the single-molecule level, we investigated ligand binding to DNA under a topological constraint via single-molecule fluorescence imaging. In our assay, we attached DNA via multiple biotin-streptavidin bonds at each end to a surface (Figure 45A), ensuring that the molecule is topologically constrained. Adding the intercalator SYTOX Orange enables us both to induce supercoiling in the DNA and to visualize the molecules using fluorescence imaging [271, 273]. To systematically study the effect of topology, we performed two different types of experiments (Materials and Methods Section 6.3.8). In the first case, we prepared negatively supercoiled DNA by first staining with the intercalative dye SYTOX Orange at a high concentration (250 nM), then attaching the DNA to the surface to topologically constrain it, and subsequently imaging at a lower concentration (50 nM). Following the reduction of SYTOX Orange concentration, plectonemic
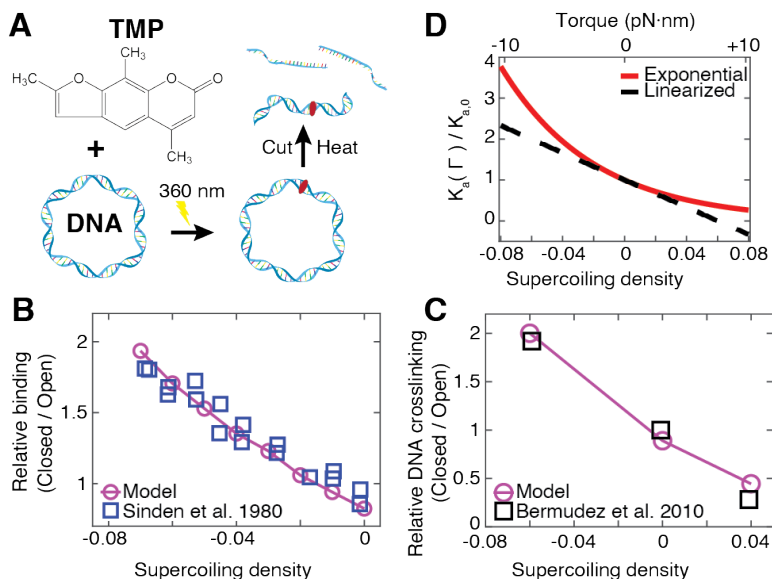
Figure 44: Topology-dependent DNA crosslinking by trimethylpsoralen. A) 4,5',8-trimethylpsoralen (TMP) intercalates into DNA and causes DNA crosslinking upon UV irradiation. DNA supercoiling-dependent crosslinking is widely used to probe DNA supercoiling and chromatin conformations *in vivo*. B) Binding of TMP to supercoiled DNA plasmids with different initial supercoiling densities relative to open circular DNA. Experimental binding data are from Ref. [279] and were determined using the radioactivity of ^{3}H-labeled TMP. C) Binding of TMP to supercoiled DNA plasmids. Experimental data are from Ref. [275] and were obtained by quantifying the amount of DNA crosslinking after irradiation. Experimental data are normalized to the data point at zero supercoiling density. The model in panels B and C uses the parameters in Table 7 and quantified binding to supercoiled relative to topologically open DNA. D) Dependence of the torque-dependent association constant (the inverse of the dissociation constant) on supercoiling density using Equations 64 - 68 (red solid line). The black dashed line shows the linearization of Equation 64, i. e., the approximation $\exp(-x) \approx 1 - x$ with $x = \Gamma \cdot \Delta\theta / k_B T$

supercoils are clearly visible as bright spots that diffuse along the length of the DNA molecules (Figure 45B,C and Supplementary Movie S1).

During continuous observation and laser exposure, DNA molecule will nick, likely due to radicals generated by photochemical processes [297, 298], which is usually an undesirable feature. However, here we use nicking upon illumination to our advantage since it enables us to observe both the supercoiled (closed) and later the nicked (open) topology of the same DNA molecule. Upon nicking, the fluorescence intensity suddenly decreases significantly (Figure 45D) and the bright spots indicative of plectonemic supercoils disappear (Figure 45B,C and Supplementary Movie S1). This is in line with our previous observations: The negative supercoiling helps intercalation, consequently, once the molecule nicks, less SYTOX Orange binds and the fluorescence intensity decreases.

For the second type of experiment, we prepared positively supercoiled DNA by attaching the DNA to the surface in the presence of a low SYTOX Orange concentration (25 nM; Figure 45E). We then increased the dye concentration (to 250 nM), but since positive supercoiling hinders intercalative binding to the DNA, the fluorescence intensity stays relatively low. Again, plectonemic supercoils appear as bright spots that diffusive along the DNA molecule (Figure 45F,G and Supplementary Movie S2). After the positively supercoiled molecule is nicked, we observe that the fluorescence intensity increases (Figure 45H). Importantly, our assay enables us to quantify the change in fluorescence intensity upon changes in topology by integrating the intensity over the entire molecule, before and after nicking (Figure 45D and H). We find a decrease in fluorescence intensity upon nicking for initially negatively supercoiled DNA of $1.35 \pm 0.18$ (mean $\pm$ std; ratio supercoiled/nicked) and an increase in fluorescence intensity upon nicking for initially positively supercoiled DNA of $0.75 \pm 0.09$ (mean $\pm$ std; ratio supercoiled/nicked) (Figure 45I).

To quantitatively model the changes in fluorescence upon nicking observed *in situ*, we used our model with the parameters reported by Biebricher *et al.* [160] for the binding site size $n$, elongation per dye $\Delta z$, and binding constant $K$ taken in 100 mM NaCl, which approximately corresponds to the ionic strength in our experiments (40 mM Tris-HCl, 2.5 mM MgCl$_2$, 65 mM KCl). The unwinding angle per intercalation event $\Delta\theta$ is not known for SYTOX Orange; we assume $\Delta\theta = 19.1°$, which is the value for SYBR Gold [157] since the dyes are relatively similar dyes and also generally values in the range of about $20°$ are typical [116, 157, 186].

Importantly, the model is applied here in two stages: We first compute the supercoiling density, relatively to relaxed, bare DNA and in the absence of intercalator, induced by attaching the DNA in the presence of 25 and 250 nM SYTOX Orange, which are $\sigma = 2.7\%$ and $\sigma = 9.7\%$, respectively. We then compute binding to DNA and re-adjustment of the supercoiling level at the new SYTOX Orange concentrations used for imaging (250 and 50 nM, for which we
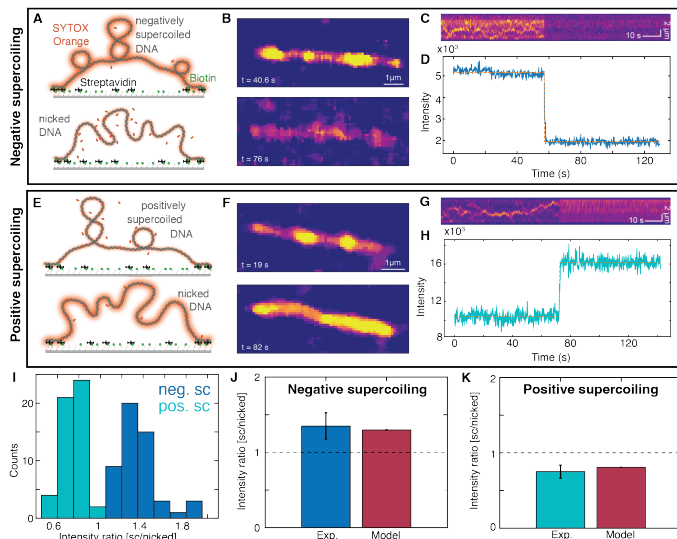
Figure 45: Single-molecule fluorescence assay to quantify topology dependent binding. A)-D): Negatively supercoiled DNA. A) Schematic representation of the experimental set up of the single-molecule fluorescence experiments. The SYTOX Orange-stained DNA is tethered at both its ends via multiple biotin-streptavidin bonds to the surface. Top: negatively supercoiled DNA; bottom: nicked DNA. B) Fluorescence image snapshots at 40.6 s when the DNA is still negatively supercoiled and at 76 s after the DNA was nicked. C) Kymograph of SYTOX Orange-stained DNA. When the DNA is nicked, the intensity decreases abruptly. D) Integrated fluorescence intensity of the kymograph shown in panel C. The dotted orange line is a fit of a two-state hidden Markov model to the data [299]. E)-H): Positively supercoiled DNA. E) Schematic representation of the experimental lineup as in panel A only now the DNA is positively supercoiled before the nicking. F) Fluorescence image snapshots at 19 s when the DNA is still positively supercoiled and at 82 s after the DNA was nicked. G) Kymograph of SYTOX Orange-stained DNA. When the DNA is nicked, the intensity increases abruptly. H) Fluorescence intensity of the kymograph shown in panel G. The dotted orange line is a fit (same as panel D) to the data. I) Intensity ratios before and after nicking for originally negatively supercoiled DNA (blue) and for for originally positively supercoiled DNA (turquoise). Averaging gives $1.35 \pm 0.18$ (N= 51, mean $\pm$ std; ratio sc/nicked) for originally negatively supercoiled DNA and $0.75 \pm 0.09$ (N= 51, mean $\pm$ std; ratio supercoiled/nicked) for originally positively supercoiled DNA. J) Comparison of the experimental intensity ratio to the value from theoretical modelling for for originally negatively supercoiled DNA. N= 51, K) Comparison of the experimental intensity ratio to the value from theoretical modelling for for originally positively supercoiled DNA. N= 51.

find $\sigma = +5.2\%$ and $\sigma = -3.9\%$), using the levels of supercoiling obtained in the first step as an input. For comparison, we compute binding to topologically open DNA, which enables us to calculate the changes in fluorescence upon nicking (Figure 45J,K). Here, we observe an excellent agreement between the predictions of our computed model and the experimentally observed changes in fluorescence intensity upon torsional relaxation in our single molecule experiments (Figure 45J,K).

### 6.3.3.6 *High-speed fluorescence tracking reveals binding dynamics*

To quantitatively study the dynamics of intercalation into DNA under topological constraint, we performed single-molecule fluorescence imaging at a 20 ms frame rate (Figure 46), ten times faster than the data shown in Figure 45. By fitting a simple kinetic model to the fluorescence intensity traces (Figure 46A,B and E,F) at the transition between supercoiled and nicked DNA, we are able to determine the on- and off-rate of SYTOX Orange. Our kinetic model for the total fluorescence intensity of the initially supercoiled molecules, reads as follows:

$$I(t) = I_{initial} \quad | \quad t < t_0$$
$$\&$$
$$= I_{initial} + (I_{final} - I_{initial}) \cdot (1 - \exp(-k \cdot (t - t_0))) \quad | \quad t > t_0 \qquad (70)$$

Where the initial intensity $I_{initial}$, the final intensity $I_{final}$, the rate $k$, and the time at which the intensity begins to change $t_0$ are fitting parameters.

For the DNA molecules that are negatively supercoiled prior to nicking, we find a reduction in fluorescence intensity with overall rate $k = (2.16 \pm 0.38)$ s$^{-1}$ (mean $\pm$ sem from 32 traces; Figure 46D), which is close to the off-rate extrapolated to zero force reported by Biebricher *et al.* of $(3.2 \pm 0.8)$ s$^{-1}$ using a single-molecule stretching assay [160]. Conversely, starting with positively supercoiled DNA prior to nicking, we find an increase in intensity with an overall rate $k = (1.92 \pm 0.26)$ s$^{-1}$ (mean $\pm$ sem from 22 traces; Figure 46H).

Assuming that this increase is due to binding with a simple bimolecular association rate, we find an on-rate of $(7.68 \pm 1.3) \cdot 10^6$ M$^{-1}$s$^{-1}$ (since the SYTOX Orange concentration is constant at 250 nM in this case), again in excellent agreement to the on-rate reported by Biebricher *et al.* of $(7.9 \pm 2.6) \cdot 10^6$ M$^{-1}$s$^{-1}$. The very good agreement of our fitted overall rates with previously published on- and off-rates for SYTOX Orange suggests that binding and dissociation of the dyes and not the relaxation of torsional strain is rate limiting for the observed changes in fluorescence intensity. This is consistent with estimates from simulations that suggest that relaxation of torsional strain in DNA occurs on $\sim$ μs time scales for $\sim$ kbp DNA segments [300].
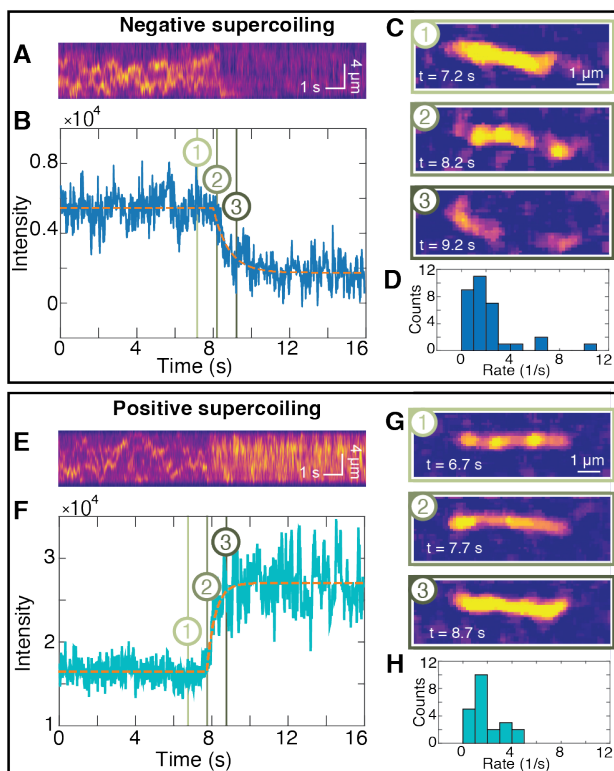
Figure 46: Probing the interplay of dye and supercoil dynamics. A)-D): Negatively supercoiled DNA. A) Kymograph of SYTOX Orange-stained DNA. When the DNA is nicked, the intensity decreases abruptly. B) Integrated fluorescence intensity of the kymograph shown in panel A. The dotted orange line is a fit of the model shown in Equation 70 to the data. C) Fluorescence image snapshots at 7.2 s when the DNA is still negatively supercoiled, at 8.2 s when the nick occurs, and at 9.2 s after the DNA was nicked. Time points are indicated by matching numbers in panel B. D) Experimentally determined rates k for fluorescence decrease from the fits of Equation 70 to time traces from N = 32 independent measurements. The mean ± sem are (2.16 ± 0.38) 1/s. E)-H): Positively supercoiled DNA. E) Kymograph of SYTOX Orange-stained DNA. When the DNA is nicked, the intensity increases abruptly. F) Integrated fluorescence intensity of the kymograph shown in panel E. The dotted orange line is a fit of Equation 70 to the data. G) Fluorescence image snapshots at 6.7 s when the DNA is still positively supercoiled, at 7.7 s when the nick occurs, and at 8.7 s after the DNA was nicked. Time points are indicated by matching numbers in panel F. H) Experimentally determined rates k for the increase in fluorescence after nicking from N = 22 independent measurements. The mean ± sem are (1.92 ± 0.26) 1/s.

The disappearance of the fluorescent spots (Figure 46C and G) allows us to estimate the dynamics of the writhe relaxation upon nicking, i.e., the time scale over which the plectonemic supercoils are resolved. We observe the disappearance of fluorescent spots over at least 3 - 4 frames (Figure 53), suggesting that writhe relaxation occurs over $\geq$ 80 ms in our assay. The observed time scale for plectoneme disappearance is very similar to the lifetime of plectonemes before "hopping" events that have previously been detected by fluorescence imaging [242], suggesting that writhe relaxation occurs via "hopping" relaxation to a nick. Conversely, our measurements suggest that writhe relaxation does not occur predominantly by diffusion of plectonemes along the DNA to the nicking site, which would take on the order of $\tau \approx L^2/D \geq 3$ s, where $L$ is the length over which diffusion occurs ($L \geq 1$ µm) and $D$ the diffusion coefficient, which is $\leq 0.3$ µm2/s [242].

### 6.3.4  *Discussion*

We have developed a quantitative model to describe DNA binding under topological constraints. Intriguingly, a global topological constraint can increase or decrease binding, depending on the concentration and binding regimes. This is an important difference to applied stretching forces, which similarly can modulate binding in an Arrhenius-like exponential dependence [171, 267], but will bias binding in only one direction.

Using our model, we are able to elucidate the complex interplay between topology and ligand affinity. Using the well-characterized and widely used intercalators, SYBR Gold and ethidium bromide, we could show that topology-dependent binding depends on initial topology and intercalator affinity. In particular, we demonstrated that binding of DNA intercalators above their $K_d$ is almost topology independent. With this, we can provide recommendations for optimal use of intercalative dyes to visualize DNA under a topological constraint: To avoid biases due to torque-dependent binding, a dye with a low $K_d$ should be used, ideally at concentrations well above the $K_d$. Specifically, SYBR Gold at a concentration of 1-2 µM satisfies this criterion. Importantly, SYBR Gold at 1-2 µM concentration is also the optimal concentration range to obtain a high signal as well as a linear relation between DNA amount and fluorescence intensity [157]. In general, the choice of intercalator type and concentration range is crucial for reliably topology-unbiased DNA staining and quantification.

Moreover, our model can quantitatively account for observations made with the widely-used intercalator psoralen for UV-induced DNA crosslinking. Importantly, in applications where intercalation is used to detect supercoiling, a dye with a high $K_d$ (i.e.low affinity) and large unwinding angle is desirable. Finally, we extend our model to quantitatively account for observations

in single-molecule fluorescence measurements. This allows us to draw direct conclusions about the binding and dynamics of the DNA supercoiling.

Taken together, our work shows how combining theoretical modeling and multiple complementary experimental techniques can provide a highly quantitative and comprehensive view of DNA-ligand interactions under a global topological constraint. We anticipate our approach to be broadly applicable to other DNA binding agents and allow for reliable and unbiased detection and quantification of different topological states of DNA. In addition, the interplay of DNA binding and topology has important implications for the processing and regulation of genetic information *in vivo*. In the cell, DNA forms topological domains and e. g. advancing polymerases introduce torsional strains of different handedness [251, 252, 301–304]. Together, these factors are expected to modulate binding to DNA, e. g. by nucleosomes and transcription factors, also in a cellular context. Our results provide a baseline to quantitatively investigate these complex processes in the future.

### 6.3.5  *Acknowledgements*

### 6.3.6  *Funding*

### 6.3.7  *Data Availability statement*

All data are included in the article. Custom software that implements the topology dependent binding model written in Matlab is available freely in the repository YODA.

### 6.3.8  *Materials and Methods*

#### 6.3.8.1  *Plasmid DNA preparation*

We used the plasmid pBR322 (NEB) as the DNA substrate for bulk measurements of intercalation. We prepared different topological states of the DNA by cutting (i. e.introducing a double-strand break) or nicking (i. e.a DNA single-strand break) the original supercoiled DNA to obtain linear DNA and open circular DNA, respectively. Reactions were performed in NEBuffer 3.1 (NEB) using the enzymes EcoRV (NEB; incubation temperature 37 °C) to prepare linear DNA and Nt.BspQI (NEB; incubation temperature 50 °C) to create open circular DNA. The reactions were stopped after one hour by heat inactivation at 80 °C for 20 minutes. The products were purified with a PCR clean-up kit (Qiagen). The concentrations were determined using a nanodrop UV/Vis photospectrometer (ThermoFisher Scientific). To every 100 µL reaction volume, we added 20 µL Gel Loading Dye Purple (6x) (NEB, catalogue number B7024S) prior to running the gel. For the plate reader and qPCR cycler experiments, no gel loading dye was added.

#### 6.3.8.2  *DNA dilution series*

For the DNA dilution series, the different topologies were combined to an equimolar mixture and diluted with TAE buffer (40 mM Tris, 20 mM acetic acid, and 1 mM EDTA, pH 8.6) and gel loading dye in form of a serial dilution to obtain 7 different DNA concentrations (Table 8). For the experiments using relaxed DNA, the plasmid pBR322 was relaxed using Wheat Germ Topoisomerase I (Inspiralis). For a total volume of 100 µL, 16.2 µL assay buffer (50 mM Tris HCl, 1 mM EDTA, 1 mM DTT, 20% (v/v) glycerol, 50 mM NaCl, pH 7.9), 82.12 µL RNase-free water, 2.16 µL topoisomerase I, 0.52 µL pBR322 ($c = 1000$ ng/µL) were combined in a reaction tube and incubated for 1 h at 37 °C. For the DNA dilution series, only the linear and the relaxed topologies were combined to an equimolar mixture and diluted with Tris-acetate-EDTA (TAE) buffer and gel loading dye in form of a serial dilution to obtain 7 different DNA concentrations (Table 8).

#### 6.3.8.3  *AFM imaging of DNA plasmids*

AFM imaging of plasmid DNA was performed as described previously [305–307]. In brief, for the AFM imaging, we deposited 20 µL of DNA at different topological states in TE buffer at a final concentration of 1 ng/µL on freshly cleaved poly-L-lysine (Sigma Aldrich, diluted to 0.01% in milliQ water; PLL)-coated muscovite mica. The sample was incubated 30 s before washing with 20 mL MilliQ water and drying with a gentle stream of filtered argon gas. After drying, the AFM images were recorded in tapping mode at room temperature

using a Nanowizard Ultraspeed 2 (JPK, Berlin, Germany) AFM with silicon tips (FASTSCAN-A, drive frequency 1400 kHz, tip radius 5 nm, Bruker, Billerica, Massachusetts, USA). Images were scanned over different fields of view with a scanning speed of 5 Hz. The free amplitude was set to 10 nm. The amplitude setpoint was set to 80% of the free amplitude and adjusted to maintain a good image resolution. AFM image post-processing was performed in the software SPIP (v.6.4, Image Metrology, Hørsholm, Denmark) to flatten and line-wise correct the images (Figure 48).

### 6.3.8.4   *Gel electrophoresis*

For gel electrophoresis we used 1%-broad-range-agarose (Carl Roth) gels and TAE buffer. We used the 1 kb gene ruler (Thermo Scientific; 5 µL) as a size standard. The gels were run for 120 min at 75 V at 4 °C. Subsequently, the gel were removed from the gel box and placed for 20 minutes in 100 mL of 0.5 µM (1:100000 dilution of the stock), 5 µM (1:10000 dilution of the stock), or 50 µLM (1:1000 dilution of the stock) EtBr in TAE buffer, respectively, for staining. Subsequently, the gel was de-stained in TAE buffer for 15 min. The gels were visualized using a Gel Doc XR+ system (Biorad). Since the dye concentration used in staining is reduced by the agarose gel matrix and the de-staining step, we used a staining correction factor of 0.1 as determined previously [157], which we use to correct all gel data.

### 6.3.8.5   *Gel electrophoresis image analysis*

We saved the images from the Gel Doc system in scn format to allow for quantitative fluorescence intensity analysis. The software SPIP (v.6.4, Image Metrology, Hørsholm, Denmark) was used to remove spikes from the image (without changing the intensity of the bands) and to generate average intensity profiles along each lane of the gel. In a next step, we used Origin (OriginLab, Northampton, Massachusetts, USA) to flatten the background of the profiles and to convert the peaks into fractions of supercoiled, open-circular, linear, and/or relaxed DNA respectively, by calculating the area under the lane profiles (Figure 49).

### 6.3.8.6   *Bulk fluorescence experiments*

For the SYBR Gold bulk fluorescence measurements, we used a well plate reader (Tecan Infinite M1000 PRO; well plates: corning black polystyrene 384 well microplate with a flat bottom, Sigma-Aldrich, catalogue number: CLS3821) and a qPCR cycler (CFX96 Touch Real-Time PCR Detection System, BioRad). In the well-plate reader, the DNA mix including various SYBR Gold concentrations was filled in the wells and the fluorescence was read out from the bottom of the wells. The excitation and emission bandwidths were set to 5 nm, the gain

to 100, the flash frequency to 400 Hz, and the integration time to 20 s. We chose the excitation and emission wavelengths - according to the excitation and emission maxima for SYBR Gold provided by Invitrogen - to be 495 nm and 537 nm.

In the fluorescence bulk experiments using a qPCR cycler, the DNA was filled into low-profile PCR tubes (Bio Rad, Nucleic Acids Research, 2021 5, product ID: TLS-0851), closed with flat, optical, ultra-clear caps (Bio Rad, product ID: TCS-0803) since the fluorescence was read out from the top of the tubes (at 24 °C). As read-out channels, channels with absorption and emission wavelengths of 494 and 518 nm, respectively, were chosen because these were the closest match to those of SYBR Gold.

### 6.3.8.7   *Single-molecule fluorescence experiments*

supercoiled DNA were prepared and imaged at the single-molecule level essentially as described previously [271, 273]. Experiments were performed in custom-made flow cells built by connecting a surface-passivated glass slide and a glass coverslip using double-sided tape [271]. The surface of the glass slides was prepared as previously described [308] with slight modifications. In brief, after extensive cleaning, the surface was silanized using APTES (10% v/v) and acetic acid (5% v/v) methanol solution. The surface was passivated with NHS-ester PEG (5,000 Da) and biotinylated NHS-ester PEG (5,000 Da) in relation 40:1. The biotinylated NHS-ester PEG allowed us to tether the DNA molecules to the surface via biotin-streptavidin interactions (Figure 45A).

The DNA used for intercalation with SYTOX Orange was prepared as described in Ref. [309] with the exception of introducing multiple-biotin handles at the DNA ends to allow the torsional constrain on the DNA rotation. To introduce multiple biotins on the DNA handles we performed a PCR on pBluescript SK+ (Stratagene) with GoTaq G2 DNA polymerase (Promega, M7845), in the presence of biotin-16-dUTP (Jena Bioscience, NU-803-BIO16-L) and dTTP (Thermo Fisher Scientific, 10520651) in molar ratio of 1:4, respectively. The PCR was done using primers: accgagatagggttgagtg and cagggtcggaacaggagagc, resulting in a 1,238 bp DNA fragment that contained multiple biotins randomly incorporated due to the presence of biotin-16-dUTP modified nucleotides. The PCR products were cleaned up using a standard purification kit (Promega, A9282) and we digested both the biotin handle and large 42 kb DNA plasmid with SpeI-HF (New England Biolabs, R3133L) for 2 h at 37 °C. The reaction was stopped by subsequent heat-inactivation for 20 min at 80 °C. This resulted in linear 42 kbp DNA and ∼ 600-bp biotin handles. The digested products were mixed, using a 10:1 molar excess of the biotin handle to linear plasmid. We then added T4 DNA ligase (New England Biolabs, M0202L) in the presence of 1 mM ATP overnight at 16 °C and subsequently heat-inactivated for 20 min at 65 °C. The resulting coilable 42 kbp DNA construct was cleaned up by size

exclusion chromatography on an ÄKTA pure system, with a homemade gel filtration column containing approximately 46 mL of Sephacryl S-1000 SF gel filtration media (Cytiva), run with TE + 150 mM NaCl buffer. The sample was run at 0.2 mL min$^{-1}$, and we collected 0.5 mL fractions.

For immobilization of this 42 kbp biotinylated-DNA, we introduced 100 µL of $\sim$ 0.5 pM DNA molecules at a flow rate of 4.2 µL/min in imaging buffer with no oxygen scavenging system components (40 mM Tris-HCl, 2 mM Trolox, 2.5 mM MgCl2, 65 mM KCl). The buffer during the DNA immobilization step contained either a low SYTOX Orange concentration (25 nM; to allow introducing positive supercoiling in a later step, see below), or high concentration of SYTOX Orange (250 nM; to allow introducing negative supercoiling in a later step, see below) during initial immobilization.

Immediately after the introduction of DNA molecules into the flow cell, we further flowed 100 µL of the same buffer without the DNA at the same flow rate to ensure stretching and tethering of the other end of the DNA to the surface (which introduces the topological constraint) as well as to remove unbound DNA molecules. To introduce plectonemic supercoils into the bound DNA molecules that are torsionally constrained, we change the SYTOX Orange concentration by introducing imaging buffer with the same salt concentration but with varying SYTOX Orange concentration and an oxygen scavenging system for imaging (40 mM Tris-HCl, 2 mM Trolox, 2.5 mM MgCl$_2$, 65 mM KCl, 2.5 mM protocatechuic acid (PCA), 50 nM protocatechuate-3,4-dioxygenase (PCD)) [310]. For positive supercoiling we increased the concentration from 25 nM during immobilization to 250 nM SYTOX Orange, while for the negative supercoiling we reduced the concentration from the initial binding at 250 nM to a final concentration of 50 nM for imaging. In both cases we checked for a visible presence of supercoiling on the DNA by moving foci appearing along the DNA molecules (Figure 45, Supplementary Movies S1 and S2). Thus, supercoiling was introduced by differential SYTOX Orange concentrations between the DNA-binding step (where torsional constraint is ensured via multiple biotin molecules) and the imaging step where SYTOX Orange concentration is increased or reduced in order to generate positive or negative supercoils, respectively.

For fluorescence imaging, we used a home-built objective-TIRF microscope. We employed continuous excitation with a 561 nm (15-20 mW) laser in Highly Inclined and Laminated Optical sheet (HiLo) microscopy mode, to image SYTOX Orange-stained DNA as well as to introduce DNA nicking. All images were acquired with an PrimeBSI sCMOS camera at an exposure time of 20-200 ms, depending on the experiment, with a 60× oil immersion, 1.49 NA CFI APO TIRF (Nikon). For DNA visualization, and kymograph generation, we used a custom written python software published in Ref. [311].

6.3.8.8   *Numerical implementation of the binding model under topological constraint*

To model the effects of the global constraint imposed by DNA topology on binding, we developed a model that takes into account changes in linking number due to intercalation and, conversely, torque-dependent binding (see the Section 6.3.3.1 "Model for ligand binding under topological constraint" in Results). The model comprises coupled Equations 63 to 68 that are solved iteratively using a custom routine written in Matlab (Mathworks). Input parameters are the temperature $T$ and for the DNA the number of base pairs $N_{bp}$, the torsional stiffness $C$, the initial linking difference $\Delta Lk_0$, and the DNA concentration cDNA. $N_{bp}$, $\Delta Lk_0$, and cDNA are typically known from how the DNA was prepared and we used a value $C = 100$ nm, unless otherwise noted [116, 290, 291]. For the single-molecule assay, the DNA concentration is poorly defined, but low, much lower than the intercalator concentration used. In this case, we used concentrations in the range of 1 - 100 pM · bp, which are much lower than the intercalator concentration used, but high enough to ensure numerical stability of the calculation. We found that the calculated results are insensitive to the concentration used in this regime. Input parameters for the intercalator are the binding site size $n$, the dissociation constant $K_d$, the length increase per intercalator bound $\Delta z$, the change in DNA helical twist per intercalator bound $\Delta\theta$, and the intercalator concentration $c_{total}$. Values for $n$, $K_d$, $\Delta z$, and $\Delta\theta$ used in this work are provided in Table 7. The outputs of the model are the number of intercalator molecules bound per DNA molecule, the torque in the DNA, and the total fluorescence intensity expected, which contains an overall scaling factor $\alpha$ defined in Equation 69. Our numerical implementation uses the numerical solutions to the McGhee-von Hippel described previously [157, 312] and a successive over-relaxation type approach [313] to speed up convergence.

### 6.3.9    *Supplementary Tables and Figures*

| Equimolar DNA mix | TAE buffer | Gel loading dye | DNA concentration |
|---|---|---|---|
| 20 µL | / | / | 0.9231 µM · bp |
| 15 µL | 5 µL | 1 µL | 0.6585 µM · bp |
| 10 µL | 10 µL | 2 µL | 0.4185 µM · bp |
| 5 µL | 15 µL | 3 µL | 0.2000 µM · bp |
| 2 µL | 20 µL | 4 µL | 0.0708 µM · bp |
| 1 µL | 25 µL | 5 µL | 0.0298 µM · bp |
| 0.5 µL | 25 µL | 5 µL | 0.0151 µM · bp |

Table 8: DNA dilution series for gel electrophoresis assays.
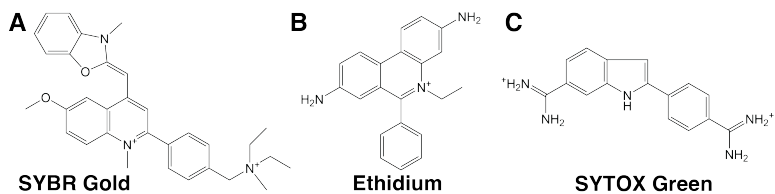
Figure 47: Molecular structure of the three intercalators (A) SYBR Gold, (B) Ethidium, (C) SYTOX Green. The SYBR Gold structure was taken from Ref. [157], the Ethidium structure from Ref. [116]. Since the structure of SYTOX Orange, the dye used for the single-molecule fluorescence assay in this work, is unknown, we show the structure of SYTOX Green (taken from Ref. [314]) here.
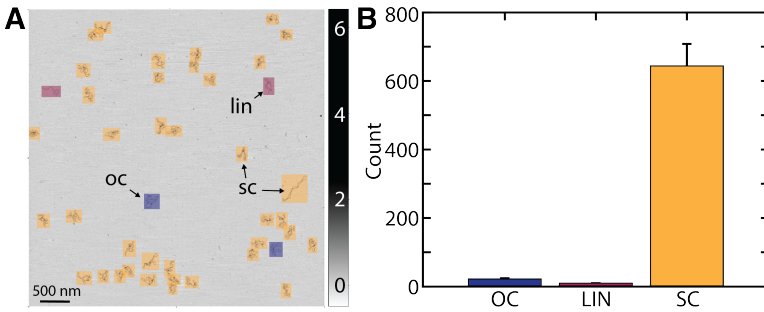
Figure 48: DNA topology analysis and quality control via AFM imaging. A) AFM height image of supercoiled pBR322 DNA at a concentration of 1 ng/µL deposited on PLL mica after drying in air. The different topologies are indicated with different colors, open circular DNA in blue, linear DNA in red, and supercoiled DNA in yellow. Z-ranges are indicated in nm by the scale bar on the right. B) Topology analysis from AFM experiments of pBR322 DNA that was also used as supercoiled DNA for gel experiments. From a total of 676 molecules, 95% are supercoiled, 3% open circular, and 2% linear. Error bars are from counting statistics.
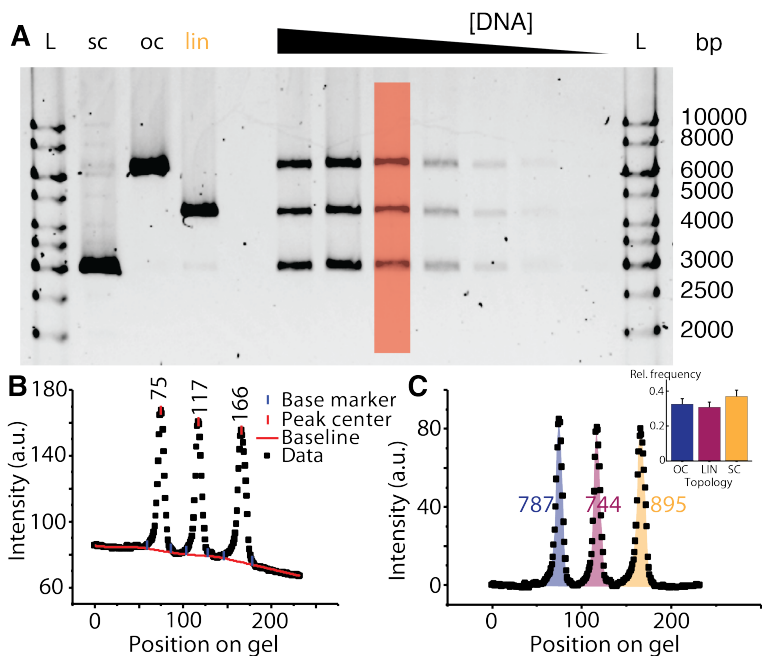
Figure 49: Analysis of gel electrophoresis data. A) Agarose gel stained with SYBR Gold at a final concentration of 0.315 µM. Different DNA topologies are separated on the gel. L: DNA size ladders (1 kb gene ruler, Thermo Scientific, 5 µL). Lanes 2 - 4 are the stock solutions of the supercoiled, linear, and open circular DNA, respectively. Lanes 6 - 12 are equimolar mixtures of the three topologies, at different total DNA concentrations. For quantitative analysis, individual lanes are selected (as highlighted in red) to create intensity profiles. B) Line profile of the area highlighted in red in panel A. Using the software Origin, a baseline is set and the peaks corresponding to the three topologies ("oc", "lin", "sc") are detected automatically. C) Same data as in panel B, only baseline corrected. The area under the peaks (which corresponds to the fluorescence intensity of the individual topologies) is calculated and used to determine the intensity ratios of the three topological states. Inset: integrated and normalized intensities of the individual peaks shown in panel C.
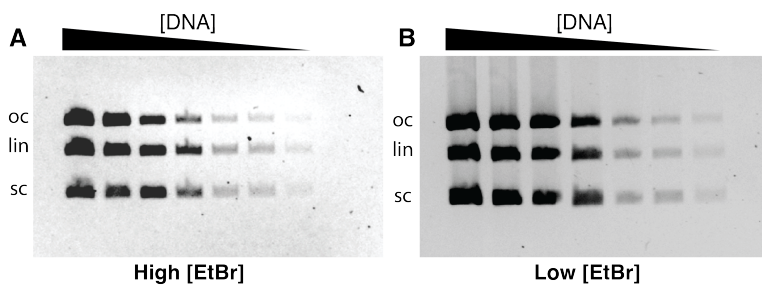
Figure 50: Agarose gel stained with EtBr at a final concentration of 5 µM (A) and 0.05 µM (B), respectively. Different DNA topologies are separated on the gel. Lanes 1-7 are equimolar mixtures of the three topologies, at different total DNA concentrations.
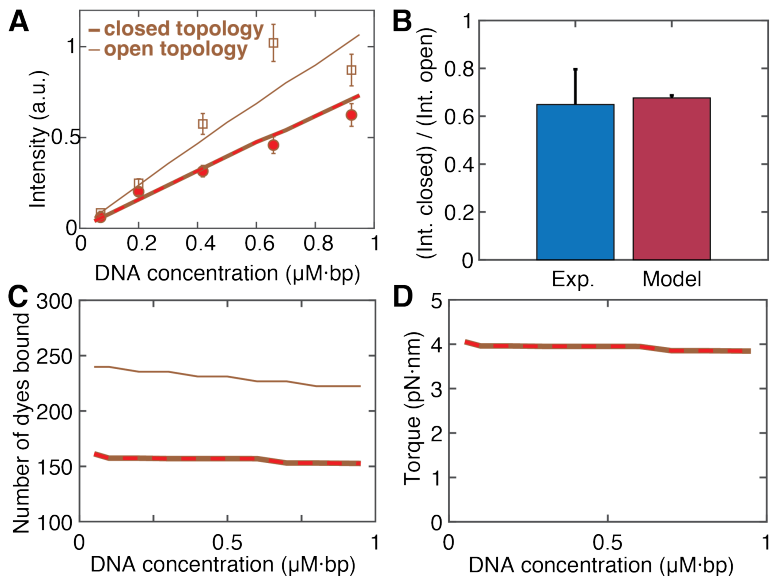
Figure 51: Topology dependent binding of EtBr. A) Experimentally determined fluorescence intensity for topologically closed DNA (circles with red highlight) and linear DNA (squares) as a function of DNA concentration. Lines are predictions of our binding model (same color code as in Figure 42), with the scale factor $\alpha$ as the only fitting parameter (Equation 69). The EtBr concentration is 0.5 µM. B) Relative fluorescence intensity of a topologically closed DNA with $\Delta Lk_0 = 0$ relative to the topologically open DNA. The experimental data are the mean and std over different DNA concentration. C) Predicted number of intercalated molecules $N_{bound}$ as function of DNA concentration for pBR322 DNA (4361 bp) with $\Delta Lk_0 = 0$. Same color code as Figure 42. The number of molecules bound depends only weakly on DNA concentration under the conditions investigated but is clearly reduced for the closed DNA topology compared to linear DNA. D) Predicted torque in the plasmid from our model, same color code as in panel A,C.
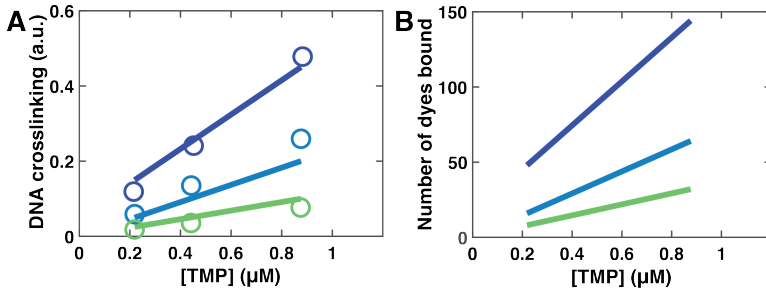
Figure 52: Model prediction for TMP binding to plasmid DNA. A) Number of DNA crosslinks as a function of TMP concentration for DNA plasmids with different initial supercoiling density (from blue to green, top to bottom: $\sigma$ = -0.06, 0, +0.04). Circles are the experimental data from Ref. [275]. Solid lines are the prediction of our model using the parameters in Table 7. B) Number of dyes bound as a function of TMP concentration. Same colour code as in panel A.
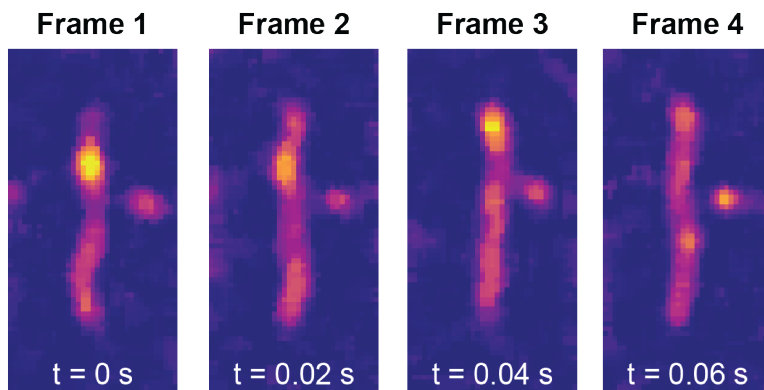
Figure 53: Subsequent fluorescence image snapshots at the transition between negatively supercoiled and nicked DNA. We observe that the fluorescent spots disappear over 4 frames (20 ms frame rate), suggesting that writhe relaxation occurs within approximately 80 ms.

# CONCLUSIONS AND OUTLOOK TO FUTURE WORK

In summary, this work shows how the use of complementary techniques can provide a highly quantitative and comprehensive picture of the interactions between DNA and small molecules. In the first result chapter, I presented a detailed study of the widely used fluorescent dye SYBR Gold. I analyzed its molecular structure, its binding mode to DNA, and its photophysical properties. Using the obtained knowledge about SYBR Gold, I could provide guidelines for optimal use of the fluorescent dye. I anticipate this approach to be broadly applicable to other DNA binding agents. For example, the fluorescent dye SYTOX Orange from the same family of dyes is widely used in various optical microscopy and spectroscopy methods. Nevertheless, its molecular structure and DNA binding mode are still to some extend a topic of discussion. To decipher its molecular structure, an approach similar to that used for SYBR Gold - a combination of NMR spectroscopy and mass spectrometry - may be well suited. In addition, single-molecule MT would allow to study the the binding properties of SYTOX Orange to DNA. The mechanical signature of SYTOX Orange binding to DNA could then be used to extract the unwinding angle of DNA per dye molecule. Another interesting point is fluorescence quenching and internal filter effects which I have shown to be relevant for SYBR Gold and studied using fluorescence lifetime measurements and spectroscopy. Combining these information, it would be possible to give recommendations for optimal use of SYTOX Orange and improve measurements using this dye. In addition, the detailed study of the intercalator SYBR Gold opens the route for various applications. Since we now know the molecular structure, DNA binding mode, and photophysical properties of this widely used DNA stain, it will be the ideal candidate for real-time single-molecule observation of dye-DNA interaction using for example a combined TIRF (total internal reflections fluorescence) microscopy-MT setup. This approach would allow to investigate the molecular mechanisms of intercalation and enable a real-time readout to study the dynamics of DNA intercalation and binding induced fluorescence enhancement in molecular detail.

In the second result chapter, I investigated the binding mode of $Ru(TAP)_3^{2+}$. The presented work makes it possible to reconcile earlier, seemingly contradictory reports on the DNA binding modes of $Ru(TAP)_3^{2+}$. Using single-molecule MT and AFM, I could show that racemic $Ru(TAP)_3^{2+}$ and $Ru(phen)_3^{2+}$ can interact with DNA via (semi-)intercalation that occasionally occurs in a kinked state. These results are consistent with previous results from other ruthenium

complexes [230–234]. In addition, $\text{Ru(TAP)}_3^{2+}$ can mediate DNA loop formation, presumably via a combination of (semi-)intercalation and hydrogen bonding [229]. This multivalent bonding could be an explanation for the differential yield of photoadduct formation on short and long DNA. Recent work has demonstrated targeted photo-induced DNA damage by Ru–TAP complexes *in vivo* [228]. This suggests that Ru–TAP complexes could be used in phototherapeutic applications. Especially for the application of this type of complexes in living cells, the correlation between local DNA concentration and photoadduct formation plays an important role. Therefore, this approach makes a significant contribution to the investigation of these complexes in clinical application. Together with Willem Vanderlinden and Melanie Burkhard from my group, I also started a project to study the binding of ruthenium dyes to nucleosomes. Our results indicate that nucleosomes are stabilized or destabilized depending on the ruthenium concentration. These results could help to better understand supercoiling in chromatin *in vivo* and address the question of how much supercoiling is stored in nucleosomes and how much is stored in the linker parts between them.

In the third and final result chapter of this thesis, I studied small molecule binding to DNA under a global topological constraint. To this end, I combined a quantitative binding model and experimental data from different spectroscopic techniques. The model takes into account ligand-induced conformational changes, the influence of strains on binding equilibria, and the global constraint imposed by a defined linking number due to the defined topology. On the experimental side, I performed experiments with DNA of different topological states and investigated their interactions with the small molecule intercalators ethidium bromide, SYBR Gold, SYTOX Orange, and trimethylpsoralen, which are all commonly used in various assays. The data and the model consistently show that intercalation into DNA is dependent on DNA topology. I anticipate that these results have direct practical applications since gel-based assays for discrimination and detection of topoisomers are widely used to study the properties of circular DNA in interaction with various enzymes that alter DNA topology, including topoisomerases, gyrase, reverse gyrase, and recombinases. Fluorescence staining is increasingly being used as a replacement for radio-labelling due to the hazards associated with the handling, storage and disposal of radioactive material. Based on the findings of this work, it is possible to provide practical guidelines for reliable and accurate detection of different topoisomers. It is essential to consider observed topology dependencies as this is the only way an unbiased quantification of different topoisomers by fluorescence staining is possible. As an extension of this work, it would be intriguing to study genomic DNA supercoiling. In the cell, supercoiling of DNA is an important regulatory factor of various DNA metabolic processes, including replication and transcription. psoralen-type compounds are routinely used to probe DNA supercoiling in cells. Nevertheless, reliable genomic assays for supercoiling

are still lacking but needed to understand the dynamic relationship between transcription and replication. I anticipate, that supercoiling-sensitive DNA intercalators, such as psoralen will be the key to reliable *in vivo* supercoiling assays and unbiased quantification of different DNA topologies *in vivo*. However, other (newly designed) small molecules that are highly DNA torque and topology dependent may also be applicable as quantitative and sensitive probes for *in vitro* and *in vivo* supercoiling assays.

# A

During my PhD thesis, I worked on various projects and applied a broad range of biochemical and biophysical techniques. In this context I have developed, refined, and/or optimized protocols for my laboratory work, experimental preparation and conduction, as well as data analysis which I would like to share in the following.

## A.1 DNA PROTOCOLS

### A.1.1 *Basic PCR*

To perform a PCR, the necessary components - the DNA template, the primers, the DNA polymerase and the nucleotides - are combined in one tube:

- 10 µL  Phusion High-Fidelity PCR Master Mix (NEB, catalogue number: M0531S)
- 1 µL  DNA (c ≈ 100 ng/µL)
- 1 µL  forwards primer (c = 10 ng/µL)
- 1 µL  reverse primer (c = 10 ng/µL)
- 7 µL  milliQ water

The content of the tube is briefly mixed and then place it in a preheated PCR machine. The PCR machine program is described in Table 9. The PCR's success can be checked via gel electrophoresis (explained in Section A.3.1).

| Process | Temperature | Duration | Repetition |
|---------|-------------|----------|------------|
| Preheating | 98°C | ∞ (manual start) | 1x |
| Initialisation | 98°C | 120 sec | 1x |
| Denaturation | 98°C | 10 sec | |
| Annealing | 55°C | 10 sec | }35x |
| Extension | 72°C | 36 sec | |
| Final extension | 72°C | 5 sec | 1x |
| Final hold | 8°C | ∞ (manual stop) | 1x |

Table 9: Steps of the PCR process. The denaturation, annealing, and extension steps are repeated 30x.

### A.1.2  *Megaprimer PCR*

To construct a DNA for MT via megaprimer PCR a three-step protocol is performed.

**1. Generating a linear template**

- Prepare 100-µL reaction mixture on ice
    - 10 µL NEBuffer 4 (NEB)
    - 69 µL milliQ water
    - 1 µL BspH1
    - 20 µL M13mp18 (c = 100 ng/µL)
- Split into 4 PCR tubes (à 25 µL) and place in thermocycler
- Set the thermocycler as follow and start run:
    - Endonuclease reaction: 37 °C for 60 minutes
    - Enzyme deactivation: 65 °C for 20 min
    - Infinite hold: 4 °C
- Check linearization via agarose gel electrophoresis
- Perform DNA clean-up
- Check concentration in nanodrop (should be 5-10 ng/µL)

**2. Making biotin- and DBCO-labeled megaprimers**

- Prepare a $\sim$ 8 mM dNTP mix with the desired amount of biotin-16-dUTP (B-dUTP) or DBCO-dUTP (D-dUTP)
- I typically used 100 mM dATP, dGTP, dCTP, and dTTP and 1 mM B-dUTP and D-dUTP solutions (Table 10)
- Prepare the following mixture on ice (for a final reaction volume of 100 µL):
    - 10 µL KOD polymerase buffer (NEB)
    - 6 µL MgSO$_4$
    - 60 µL milliQ water
    - 3 µL forward primer (c = 10 µM)
    - 3 µL reverse primer (@10 µM)
    - 10 µL dNTP mix with labeled dUTP (see Table 10 for details)
    - 2 µL KOD polymerase (NEB)
    - 6 µL linear M13mp18 (c = 6 ng/µL (final concentration should be 0.36 ng/µL))
- Split into 4 PCR tubes (à 25 µL) and place into thermocycler:

- Preheat lid: 105 °C
- Initial denaturation: 95 °C for 2 min
- Amplification: 35 x (95 °C for 20 s; 60 °C for 10 s; 70 °C for 20 s)
- Final extension: 72 °C for 1 min
- Hold: 10 °C

- Check linearization via agarose gel electrophoresis
- Perform DNA clean-up (e. g., as described in Section A.1.5 or via a clean-up kit (Qiagen))
- Check concentration in nanodrop (should be 100-120 ng/µL)

## 3. Making 6.6 kbp DNA using megaprimers

- Prepare 100-µL reaction mixture for making 6.6 kbp DNA (I recommend scaling this up 6 times to get a final reaction volume of 600 µL):
  - 10 µL KOD polymerase buffer
  - 6 µL $MgSO_4$
  - 62 µL milliQ water (depends on megaprimer and M13mp18 concentration)
  - 8 µL dNTP mix
  - 3 µL Biotin megaprimer (at 0.33 µM = 87 ng/µL, final conc: 0.01 µM)
  - 3 µL DBCO megaprimer (at 0.33 µM = 87 ng/µL, final conc: 0.01 µM)
  - 2 µL KOD polymerase
  - 6 µL linear M13mp18 (at 6 ng/µL)
- Split into 4 PCR tubes à 25 µL (or 6x4 PCR tubes) and place into thermo-cycler:
  - Preheat lid: 105 °C
  - Initial denaturation: 95 °C for 2 min
  - Amplification: 35 x (95 °C for 20 s; 60 °C for 10 s; 70 °C for 2min30 s)
  - Final extension: 72 °C for 1 min
  - Hold: 10 °C
- Check linearization via agarose gel electrophoresis
- I didn't clean the megaprimer DNA, but directly tried it in MT to avoid loosing too much material

| Mixing ratio | d(A/G/C)TP | dTTP | Labeled dUTP | mQ water |
|---|---|---|---|---|
| 50% B-dUTP | 1 µL | 0.5 µL | 50 µL | 0 µL |
| 25% D-dUTP | 1 µL | 0.75 µL | 25 µL | 23 µL |
| 10% D-dUTP | 1 µL | 0.9 µL | 10 µL | 38 µL |

Table 10: Reagent volumes for making dNTP mix with desired amount of labeled dUTPs.

### A.1.3  *Preparation of different DNA topologies*

To prepare different topological states of DNA, the originally supercoiled DNA is cut or nicked to get linear DNA or open circular DNA, respectively. The three prepared DNA samples are: one that contains only supercoiled DNA, one that contains only open circular DNA and one that contains only linear DNA. For a reaction volume of 100 µL, the following ingredients are combined in one tube (in this order):

- 10 µL NEBuffer 3.1 (NEB, catalogue number: B7203S))
- 89.5 µL milliQ water
- 0.4 µL of the appropriate enzyme
  - EcoRV (NEB, catalogue number: R0195S) for linear DNA
  - Nt.BspQI (NEB, catalogue number: R0644S) for open circular DNA
  - Replaced by 0.4 µL milliQ water for supercoiled DNA
- 0.5 µL pBR322 (NEB, catalogue number: N3033S, c = 1000ng/µL)

After stirring the tubes briefly with a pipette tip, they are incubated for 1 h at 50 °C (open circular DNA) or at 37 °C (linear DNA), respectively. The tube without added enzyme (supercoiled DNA) is placed on ice for one hour.

The DNA topologies are diluted in serial dilution each for three different SYBR Gold dilutions: 1:100000 dilution of the stock ($\cong$60 nM, LC), 1:5000 dilution of the stock ($\cong$1.2 µM, MC), and 1:100 dilution of the stock ($\cong$60 µM, HC). The amounts are listed in table 11.

### A.1.4  *DNA relaxation*

To prepare relaxed DNA, the following ingredients are combined in one tube (for a total reaction volume of 100 µL)

- 16.2 µL assay buffer
- 82.12 µL RNase-free water (NEB)
- 2.16 µL Wheat Germ Topoisomerase I

| DNA amount | 1x PBS | SYBR Gold | DNA conc. |
| --- | --- | --- | --- |
| 20 µL | No 1x PBS | 5 µL | 3.5 ng/µL |
| 15 µL | 5 µL | 5 µL | 2.6 ng/µL |
| 10 µL | 10 µL | 5 µL | 1.7 ng/µL |
| 5 µL | 15 µL | 5 µL | 0.86 ng/µL |
| 2 µL | 18 µL | 5 µL | 0.34 ng/µL |
| 1 µL | 19 µL | 5 µL | 0.17 ng/µL |
| 0.5 µL | 19.5 µL | 5 µL | 0.088 ng/µL |

Table 11: SYBR Gold dilution series for gel electrophoresis and fluorescence readout assays. Diluted in serial dilution in 1x PBS; We perform this dilution series for the three different topologies (supercoiled DNA, open circular DNA, and linear DNA) and for the three different SYBR Gold concentrations (LC, MC, and HC).The introduced SYBR Gold concentration is 5x concentrated in order to get the appropriate final concentration.

- 0.52 µL pBR322 (c = 1000ng/µL)

After stirring the tube briefly with a pipette tip, incubate for 1h at 37 °C.

A.1.5  *DNA purification*

The DNA is cleaned via Phenol:Chloroform precipitation. For this, first the required chemicals need to be prepared:

- Phenol:Chloroform:IAA(Isoamyl Alcohol)25:24:1 (saturated with 10 mM Tris, pH8.0, 1mM EDTA, Sigma Aldrich)

- The Tris buffer and phenol:chloroform:IAA (PCI) are stored separately in different dark color glass containers initially; mix them together to make the pH value equal to 8.0

- Once you mix Tris with PCI, the solution will be separated into 2 layers: the upper layer is buffer layer, aqueous phases, and the lower layer is organic layer (PCI)

- Always remember to store the PCI in the locker for organic solvents

- General remark: PCI is toxic and carcinogenic, make sure to be very careful, don't perform the precipitation alone and were a lab coat, safety goggles, and an FFP2 face mask.

After preparing the chemicals, the DNA clean-up can be started:

- Take 3 tubes (with lid) per DNA sample from storage next to cell culture room

- Take 250 µL of the organic layer of the PCI and mix with DNA sample 200-250 µL (add buffer or water to make the sample total volume equal to 200-250 µL)

- Vortex for few seconds

- Centrifuge at room temperature for 5 min at 13000 rpm under flow hood (you should see the two layers separately, the upper layer is buffer layer, and the organic phase is beneath the upper layer)

- Pipette up the upper layer and transfer it to the new eppies (be careful not to take any precipitated material from the interphase)

- Add PCI again and repeat the previous four steps (remove 10 µL less material each step)

- Transfer the upper layer to new tubes.

- Prepare ethanol solution (112 µL 7.5M $NH_4OAc$; 888 µL 100% ethanol; 1 µL glycogen (20 µg/µL)) for precipitation

- Mix and then store in -80°C freezer for at least one hour or over night

- Centrifuge at 14000 rpm at 4°C for 15 minutes

- A white pellet should form at the bottom of the tube

- Remove the supernatant, but don't touch the pellet. (you can leave a little bit supernatant to avoid DNA loss)

- Wash pellet with 500 µL 70% ethanol

- Centrifuge at 14000 rpm at 4°C for 15 minutes

- Remove supernatants and then centrifuge again at 14000 rpm, 4°C, 15 minutes

- Remove all the residual liquid and then let the pellet dry for at least 10min (you can leave the eppies open under the hood, if the color of the pellet becomes transparent, the pellet is dry enough)

- Solve the pellet in 15 µL Tris buffer

A.2.1  *MT flow cell preparation*

MT flow cells (about 6 in parallel) are prepared at least 1 day before starting a new measurement series. They should not be stored longer than one month though.

**1. Preparation**

- cover slides (24 x 60 mm, Carl Roth, Germany) with holes are pre-processed using a laser cutter to introduce two openings with a radius of 1 mm each which serve as liquid inlet and outlet openings by the 'Werkstatt' (top slides)

- Carefully place cover slides with holes in a Teflon cover slide holder and put the holder in suited glas box

- Add a mix of 50% milliQ water and 50% isopropanol (Carl Roth, Germany) so that the slides are fully covered

- Seal the box with parafilm

- Place the box in sonicator for 15 minutes

- Mix 1 µL polystyrene beads (Polysciences, USA) with 5 mL ultra clean ethanol (Carl Roth, Germany; 99.8% pure)

- Vortex briefly

- Sonicate for 15 minutes

- Take Epoxy-silane top cover slides (pre-coated with (3-Glycidoxypropyl) trimethoxysilane (abcr GmbH, Germany) by Tom; bottom slides) and place each in a single 50 mL falcon tube using clean tweezers

- Re-fill the box with the remaining Epoxy-silane cover slides with argon under the flowhood to avoid contamination, and close it with parafilm

**2. Flow cell production**

- Pre-heat the heating plate to a value between 80 and 90°C

- Take bottom cover slides out of their falcon tubes and place down flat on a dust-free tissue

- Cover bottom cover slides with the prepared polystyrene bead solution (about 100 µL)

- Put a lid on top and let them dry for about one hour at room temperature

- Take the box with the top slides from the sonicator and dry the cover slides one by one using a gently stream of nitrogen gas (avoid using sharp tweezers)

- Cut parafilm according to the prepared template and stick it on top of the top slides so that the inlets are left open

- Put the dried bottom slide on top (so that the polystyrene bead coated side faces down)

- Place the two cover slides in between two cleaned glass slides

- Heat for about 30 sec on the heating plate to seal the two slides together, press gently with a pipette tip if needed

- Remove the two outer glass slides and store the flow cells (one by one) in labeled falcon tubes

### 3. Flow cell measurement preparation

- Clean the flow cell holder by sonication for 20 minutes and dry all parts (don't clean screws)

- Introduce the flow cell into the cleaned and dry flow cell holder and carefully but firmly tighten the screws

- Spin down two tubes of 50 µL 100 µg/mL anti-digoxigenin (Roche, Switzerland) in 1x PBS for 5 min at 13000 rpm in table top centrifuge

- Add both anti-digoxigenin tubes to the flow cell; insert a bit less than 100 µL from the upper part of the tube into one inlet (with the pipette tip touching the ground of the inlet), then slowly insert a bit less than 100 µL into the other inlet (with the pipette tip at the border of the inlet)

- Close the inlet and the outlet of the flow cell with parafilm (to prevent the formation of air bubbles in the flow cell due to evaporation)

- Incubated overnight (at least 12 h)

- At the MT setup, add a small droplet of immersion oil to the objective

- Carefully place the flow cell holder on top of the objective and fixate it with the appropriate screws

- Remove the parafilm from the inlet and the outlet and connect the pumping system (be careful to avoid air bubbles)

- Rinse the flow cell by flushing 1 mL of 1x PBS through the system (set speed to about 300 - 500 µL/min)

- Passivate using 1 mL of a commercial passivation mix (BlockAid Blocking Solution, Thermoscientific) for at least 1 h in order to minimize non-specific interactions

- Rinse the flow cell as before with 1 mL of 1x PBS

A.2.2  *DNA constructs and magnetic beads*

For the MT measurements, a 7.9-kbp DNA construct, prepared as described previously [208, 316], was used. Briefly, PCR-generated DNA fragments ($\sim$ 600 base pairs) were labeled with several digoxigenin and biotin groups and subsequently ligated to a target DNA to bind the flow cell surface and magnetic beads, respectively.

I used streptavidin coated MyOne magnetic beads (Life Technologies, USA) with a diameter of 1.0 µm. To attach the DNA construct to the magnetic beads, the following steps are necessary:

- Take magnetic beads from fridge ($+4°$C) and vortex the tube for about 60 sec

- Wash the magnetic beads by performing the following steps:
  - Add 2 µL MyOne beads to a low binding 1.5 mL tube and add 150 µL 1x Phosphate-buffered saline (Sigma-Aldrich, USA; PBS)
  - Vortex the tube for a few seconds
  - Briefly spin down in table top centrifuge
  - Place the tube in a magnetic holder provided for this purpose to move the magnetic beads to the back side of the tube; wait for about 30 sec; remove 145 µL of liquid from the tube and quickly add 145 µL fresh PBS
  - Repeat the previous two steps twice

- Take the 7.9-kpb DNA from the fridge, gently tap the tube and then add 0.5 µL DNA to the beads

- Drop the tube on the bench to mix (from now on, treat the tube carefully to avoid breaking the DNA strands)

- Incubate for 5-10 minutes while gently tapping the tube from time to time

Subsequently, 50 µL of bead-coupled DNA constructs are introduced into the MT flow cell and allowed to bind to the flow cell surface for 2-5 minutes. After that, the flow cell is rinsed with at least 2 mL PBS to flush out unbound beads, and the magnet is mounted to constrain the supercoiling density of the tethers and to apply an upward force on the beads. Set the magnet height to 2 mm.

A.2.3  *MT experimental preparation and quality tests*

Before the measurement is started, the software is initiated and parameters are set. In addition, the beads for the measurement are selected and tested.

## 1. Software initiation

- Open the software parts one by one from left to right as placed on the computer desktop (software tends to crash, so avoid rapid clicking etc.)
- PI micromove (controls piezo): tick 'servo on' for both (height and turning); then press on left arrow: 'start up axes' → 'pos limit' → 'close'; 'start up axes' → 'advanced' → 'ok' → 'ok' → 'close'; close program
- PI nanocapture (connected to piezo): tick 'servo on'; close program
- Bead tracker main program (labview): start by clicking on the arrow in the left upper corner; three windows open: bead tracker main, experiment program, motorUI.vi (here set focal depth piezo to 50)

## 2. Magnet installation and offset determination

- Select file path in the software (usually named by date)
- Bring flow cell surface in focus by moving the stage up or down using the big golden screw underneath the objective
- Select the polystyrene beads in the field of view as reference beads
- Save beadlist and note reference beads in lab book
- Insert the magnet in its holder and tighten using the small golden screw in front
- Switch on the LED (set to about 60 mA)
- Click 'magnet all up' in the software
- Determine the magnet offset:
  - First, go down with magnet in steps of 3 mm, then 0.1 or 0.05 mm (as soon as the surface gets closer)
  - Near the surface of the flow cell: view the flow cell image in the software to see if the magnet is touching the surface (when the magnet touches the surface, the interference rings shift)
  - Go 0.1 mm up from this point and note the value as magnet offset in the lab book
- Click 'magnet all up' and remove the magnet again

## 3. Bead selection and Z-Lookup-Table

- Change piezo position such that moving/tumbling beads are in focus
- Select all moving/tumbling beads and safe the beadlist (not too close to the edges, otherwise program might crush)

- Choose size of the region of interest (ROI) around the beads (about 90 to 110 μm)
- Generate Z-Lookup-Table (Z-LUT):
  - Move magnet to 0.5 mm
  - Change piezo position to get moving/tumbling beads in focus
  - Set piezo about 5 steps higher than this
  - Click 'set current piezo as start z'
  - Click 'generate Z-LUT'
  - 'ok' → 'ok' → 'ok'
  - Save Z-LUT
- Move piezo to centre of Z-LUT (5 steps up)
- Don't change this position during the measurement

### 3. Bead testing

1. Length test
   - Set path and call experiment 'length1'
   - Move magnet to 0.5 mm (F = 5 pN)
   - Click on 'start experiment'
   - Change magnet position from 0.5 mm to 12 mm and then back to 0.5 mm
   - Click on 'abort experiment'
   - Examine traces to see whether the length of the DNA tethers is fine (between 2 and 3 mm is acceptable)
2. Rotation test
   - Set path and call experiment 'rot'
   - Move magnet to 0.5 mm (F = 5 pN)
   - Set magnet velocity to 5 turns per sec
   - Click on 'start experiment'
   - Rotate to -25, then back to 0
   - Change magnet position from 0.5 mm to 4 mm (F = 0.5 pN)
   - Rotate to +25, then back to 0
   - Click on 'abort experiment'
   - Change magnet position from 4 mm to 0.5 mm
   - Rotate back to 0
   - Look at traces to find 'good beads': discard double-tethers (go up and down at high force, negative coiling), discard nicked tethers (don't go down at low force, positive coiling)

Delete unwanted beads and perform a second length test, save the bead list and do not change it from now on. Afterwards, the measurement can be started.

A.2.4 *MT rotation curves*

For MT rotation curves with SYBR Gold, only supercoilable beads were selected. After saving the beadlist, the experiment can be started.

| | Dilution (of the stock) | Concentration (in nM) |
|---|---|---|
| 10 | No SYBR Gold | 0 |
| 9 | 1:1000000 | 6 |
| 8 | 1:500000 | 12 |
| 7 | 1:250000 | 24 |
| 6 | 1:100000 | 60 |
| 5 | 1:50000 | 120 |
| 4 | 1:25000 | 240 |
| 3 | 1:10000 | 600 |
| 2 | 1:5000 | 1200 |
| 1 | 1:1000 | 6000 |

Table 12: SYBR Gold dilution series for MT experiments. Diluted in serial dilution in 1x PBS.

- Set path and name experiment
- Start experiment by introducing 200 µL of 1x PBS in the flow cell (flow rate $\sim$ 300 µL/min; magnet height 0.5 mm (5 pN))
- Record first rotation curves (script 1, see below)
- Introduce increasing concentrations of SYBR Gold (amount: 200 µL) to the flow cell
- At each concentration, record a rotation curve at a constant force of 0.5 pN (magnet height 4 mm)
- The SYBR Gold concentrations and dilutions are listed in Table 12

The labview code for rotation curves at different SYBR Gold is adapted to the shift of the curves to more negative linking numbers. In the following, 2 exemplary scripts for the lowest and the highest SYBR Gold concentration are shown:

**Rotation curve script 10:**
move magrot 24 speed 3.00; idle 6; section;
move magrot 22 speed 3.00; idle 6; section;
move magrot 20 speed 3.00; idle 6; section;
move magrot 18 speed 3.00; idle 6; section;
move magrot 16 speed 3.00; idle 6; section;
move magrot 14 speed 3.00; idle 6; section;
move magrot 12 speed 3.00; idle 6; section;
move magrot 10 speed 3.00; idle 6; section;
move magrot 8 speed 3.00; idle 6; section;
move magrot 6 speed 3.00; idle 6; section;
move magrot 4 speed 3.00; idle 6; section;
move magrot 2 speed 3.00; idle 6; section;
move magrot 0 speed 3.00; idle 6; section;
move magrot -2 speed 3.00; idle 6; section;
move magrot -4 speed 3.00; idle 6; section;
move magrot -6 speed 3.00; idle 6; section;
move magrot -8 speed 3.00; idle 6; section;
move magrot -10 speed 3.00; idle 6; section;
move magrot -12 speed 3.00; idle 6; section;
move magrot -14 speed 3.00; idle 6; section;
move magrot -16 speed 3.00; idle 6; section;
move magrot -18 speed 3.00; idle 6; section;
move magrot -20 speed 3.00; idle 6; section;
move magrot -22 speed 3.00; idle 6; section;
move magrot -24 speed 3.00; idle 6; section;
stop;

**Rotation curve script 1:**
move magrot -180 speed 3.00; idle 6; section;
move magrot -185 speed 3.00; idle 6; section;
move magrot -190 speed 3.00; idle 6; section;
move magrot -195 speed 3.00; idle 6; section;
move magrot -200 speed 3.00; idle 6; section;
move magrot -205 speed 3.00; idle 6; section;
move magrot -210 speed 3.00; idle 6; section;
move magrot -215 speed 3.00; idle 6; section;
move magrot -220 speed 3.00; idle 6; section;
move magrot -225 speed 3.00; idle 6; section;
move magrot -230 speed 3.00; idle 6; section;
move magrot -235 speed 3.00; idle 6; section;
move magrot -240 speed 3.00; idle 6; section;
move magrot -245 speed 3.00; idle 6; section;
move magrot -250 speed 3.00; idle 6; section;

move magrot -255 speed 3.00; idle 6; section;
move magrot -260 speed 3.00; idle 6; section;
move magrot -265 speed 3.00; idle 6; section;
move magrot -270 speed 3.00; idle 6; section;
move magrot -275 speed 3.00; idle 6; section;
move magrot -280 speed 3.00; idle 6; section;
move magrot -285 speed 3.00; idle 6; section;
move magrot -290 speed 3.00; idle 6; section;
move magrot -295 speed 3.00; idle 6; section;
move magrot -300 speed 3.00; idle 6; section;
move magrot -305 speed 3.00; idle 6; section;
move magrot -310 speed 3.00; idle 6; section;
move magrot -315 speed 3.00; idle 6; section;
move magrot -320 speed 3.00; idle 6; section;
move magrot -325 speed 3.00; idle 6; section;
move magrot -330 speed 3.00; idle 6; section;
move magrot -335 speed 3.00; idle 6; section;
move magrot -340 speed 3.00; idle 6; section;
move magrot -345 speed 3.00; idle 6; section;
move magrot -350 speed 3.00; idle 6; section;
move magrot -355 speed 3.00; idle 6; section;
move magrot -360 speed 3.00; idle 6; section;
stop;

A.2.5  *MT force-extension curves*

For MT force-extension curves with SYBR Gold, only nicked beads were selected. After saving the beadlist, the experiment can be started.

- Introduce 200 µL of 1x PBS in the flow cell (flow rate $\sim$ 300 µL/min)

- Move magnet to starting value in calibration script (0.1 mm)

- Set path and name experiment

- Paste script and start experiment

- Introduce 200 µL of the lowest SYBR Gold concentration

- Change name and run experiment as before

- Repeat for all SYBR Gold concentrations in increasing order (Table 12)

The labview code for force-extension curves is identical for the different SYBR Gold concentrations:

**Force-extension curve script:**

```
section; move magpos 0.100 speed 1.00; wait ; section; idle 60;
section; move magpos 0.200 speed 1.00; wait ; section; idle 60;
section; move magpos 0.300 speed 1.00; wait ; section; idle 60;
section; move magpos 0.400 speed 1.00; wait ; section; idle 60;
section; move magpos 0.500 speed 1.00; wait ; section; idle 60;
section; move magpos 0.600 speed 1.00; wait ; section; idle 60;
section; move magpos 0.700 speed 1.00; wait ; section; idle 60;
section; move magpos 0.800 speed 1.00; wait ; section; idle 60;
section; move magpos 0.900 speed 1.00; wait ; section; idle 60;
section; move magpos 1.000 speed 1.00; wait ; section; idle 120;
section; move magpos 1.250 speed 1.00; wait ; section; idle 120;
section; move magpos 1.500 speed 1.00; wait ; section; idle 120;
section; move magpos 1.750 speed 1.00; wait ; section; idle 120;
section; move magpos 2.000 speed 1.00; wait ; section; idle 120;
section; move magpos 2.250 speed 1.00; wait ; section; idle 120;
section; move magpos 2.500 speed 1.00; wait ; section; idle 300;
section; move magpos 2.750 speed 1.00; wait ; section; idle 300;
section; move magpos 3.000 speed 1.00; wait ; section; idle 300;
section; move magpos 3.250 speed 1.00; wait ; section; idle 300;
section; move magpos 3.500 speed 1.00; wait ; section; idle 300;
section; move magpos 3.750 speed 1.00; wait ; section; idle 300;
section; move magpos 4.000 speed 1.00; wait ; section; idle 600;
section; move magpos 4.500 speed 1.00; wait ; section; idle 600;
section; move magpos 5.000 speed 1.00; wait ; section; idle 600;
section; move magpos 5.500 speed 1.00; wait ; section; idle 600;
section; move magpos 6.000 speed 1.00; wait ; section; idle 600;
section; move magpos 7.000 speed 1.00; wait ; section; idle 600;
section; move magpos 2.000 speed 1.00; wait ; section; idle 5;
stop;
```

A.2.6 *MT experiments with covalent DNA attachment*

*Covalent DNA attachment for MT was introduced to the lab by my colleague Yi-Yun Lin (Ref. [138]).*

For MT experiments with covalent DNA attachment, instead of epoxy-silane coated bottom cover slides, amino-silane coated bottom cover slides are used for the flow cell. Other than that, the flow cell production and preparation is identical as described in A.2.1. The DNA-bead tethers are prepared as follows:

• Make 100 mM solution of MS-PEG and azide-PEQ in PBS:
  – 1 4 µL aliquot 3M MS-PEG in DMS (MS-PEG4, Thermo Fisher, blue PCR tube) + 46 µL PBS
  – 1 4 µL aliquot 2.5M azide-PEG in DMS (azide-PEG4-NSH ester, Jena Biosciences, pink PCR tube) + 56 µL PBS

- Mix 50 µL diluted MS-PEG and 50 µL diluted azide-PEG in one tube

- Quickly add MS-PEG-azide-PEQ mix to flow cell

- Incubate for at least 1h at room temperature (close inlet and outlet with parafilm)

- Insert flow cell into the MT setup as described in Section A.2.1

- Flush with 1 mL PBS

- Dilute 0.4 µL DNA in 150 µL PBS

- Close flow cell inlet with parafilm

- Incubate for at least 1 h

- Flush with 1 mL PBS to remove unbound tethers (lowest flush velocity)

- Dilute casein to 1% in PBS: 18 µL casein (casein from cow's milk 5% in water, Sigma Aldrich, catalogue number C4765) + 72 µL PBS

- Add 90 µL diluted casein to flow cell (for passivation)

- Incubate for 1 h

- Flush with 1 mL PBS

- Prepare bead solution from 0.2 µL M270 beads (Life Technologies, USA) and 150 µL PBS

- Clean bead solution as described in Section A.2.2

- Flush bead solution into flow cell and incubate for 20-60 sec (check with pump from time to time to avoid that everything gets stuck)

- Flush with 1 mL PBS to remove unbound beads

- Finalize experimental preparation as described in Section A.2.3

A.3.1  *Basic agarose gel electrophoresis*

The supercoiled DNA, open circular DNA, and linear DNA samples were prepared as described in Section A.1.3, with the only difference that for this measurement, I added 20 µL Gel Loading Dye Purple (6x) (NEB, catalogue number: B7024S, gel loading dye) to every 100 µL reaction volume. For the dilution series I mixed an equimolar amount of each supercoiled DNA, open circular DNA, and linear DNA in one tube (equimolar DNA mixture). The dilution series is conducted from this equimolar mixture in form of a serial dilution (Table 13).

| DNA mix | TAE | Gel loading dye | DNA per band |
|---|---|---|---|
| 20 µL | No TAE 1x | No gel loading dye | 30 ng |
| 15 µL | 5 µL | 1 µL | 21.4 ng |
| 10 µL | 10 µL | 2 µL | 13.6 ng |
| 5 µL | 15 µL | 3 µL | 6.5 ng |
| 2 µL | 20 µL | 4 µL | 2.3 ng |
| 1 µL | 25 µL | 5 µL | 1.0 ng |
| 0.5 µL | 25 µL | 5 µL | 0.5 ng |

Table 13: SYBR Gold dilution series for gel electrophoresis assays. Diluted in serial dilution in 1x PBS.

Next, a 1% agarose gel for electrophoresis is prepared:

- Weigh 0.5 g Broad Range Agarose (Carl Roth, item number: T846.3; agarose) on a weighing paper
- Combine with 50 ml TAE 1x buffer (40 mM Tris, 20 mM Sodium acetate and 1 mM EDTA; TAE) in an Erlenmeyer flask
- Heat the mix in a microwave until just before boiling and mix thoroughly with a magnetic stirrer
- Prepare a gel electrophoresis mould; clean and level it
- Introduce the agarose-TAE mix into the mould
- Insert a cleaned comb in the appropriate position in the mould
- Let dry and solidify for at least 30 minutes
- Fill a gel electrophoresis chamber with TAE
- Introduce the solidified gel and make sure it's completely covered with buffer

- Remove the comb
- In the holes created by the teeth of the comb, carefully inject the entire content of the prepared tubes (Table 13)
- Run gel electrophoresis for 120 min at a constant voltage of 75 V

### A.3.2  *Post-staining with intercalating dyes*

After the gel has run, the staining process is performed:

- Clean two empty pipette tip box
- Fill one box with 100 ml TAE 1x buffer (staining box)
- Add appropriate amount of SYBR Gold to staining box
  - 1:10000 dilution of the stock ($\cong$0.6 µM, LC)
  - 1:4000 dilution of the stock ($\cong$1.5 µM, MC)
  - 1:2000 dilution of the stock ($\cong$3 µM, HC)
- Wrap the box in aluminium foil and set on a shaker
- Incubate with gentle agitation for 20 min at room temperature
- Fill second pipette tip box with 100 ml of TAE 1x buffer (de-staining box)
- Transfer the gel carefully from the staining box to the de-staining box
- Incubate with gentle agitation for 15 min at room temperature
- Visualize the gel using a Gel Doc XR+ System and save the resulting image in scn format

### A.3.3  *Gel electrophoresis image analysis*

The gel electrophoresis images are analyzed using different computer software.

1. Quantitative gel analysis with SPIP (v.6.4, Image Metrology, Hørsholm, Denmark)
   - Open file → inspection box (much background, become main, rot right) → second inspection box (make sure to keep enough background for a background correction later)
   - Modify → quick launch → despiking
   - Modify → plane correction → 2nd order poly global correction
   - 'right click' → properties (x- and y-range 10x) → double resolution (4x)
   - Analyse → average y

- Levelling → zero background offset
- Determine height and FWHM for each peak (go to max → y-value (1 cursor) → half of this with both cursors → x-value)
- Make table with these data

2. Quantitative gel analysis in Origin
    - Open in EXCEL → klick all
    - Copy in Origin workbook
    - Select both columns → 'right klick' → plot → symbols → scatter → graph 1
    - Analysis → peaks and baseline → peak analyser → open dialogue → baseline mode:user defined → enable autofind off, number of points to find: 6 (or 8) → 'find' → interpolation, line → subtract now
    - Copy and save integration result
    - Integrated curve data → select all columns → 'right click' → plot

A.4    SPECTROSCOPIC TECHNIQUE PROTOCOLS

A.4.1    *Fluorescence spectroscopy using a plate reader*

Similar to studying the behavior of different DNA topologies using gel elec-
trophoresis (A.3), I have also used fluorescence spectroscopy in this line of
research, specifically a 96-well plate reader. The different topological states of
DNA were prepared as described in Section A.1.3. The entire amount (25 µL) of
each tube is then transferred into a well of the well plate reader (Tecan Infinite
M1000 PRO, well plate: Corning black polystyrene 384 well microplate with a
flat bottom (Sigma-Aldrich, catalogue number: CLS3821)). The measurement
is designed and recorded using the i-control Microplate Reader Software by
Tecan:

- Switch plate reader off
- Turn the connected computer off and then on again
- Get a new plate (stored in one of the boxes on top of the nanodrop)
- Clean with water and nitrogen if needed
- After computer restart: click 'on' on the plate reader, then start computer
  program control
- Wait while the program does some checks itself
- Specify settings:
    - Plate: Corning 384 Flat black
    - Select the wells in which your samples are loaded
    - Mode: fluorescence bottom reading
    - Excitation and emission bandwidth: 5 nm
    - Gain: 100
    - Flash frequency: 400 Hz
    - Integration time: 20 µs
    - Excitation wavelength: 495 nm
    - Emission wavelength: 537 nm
- Choose either fluorescence intensity scan, excitation scan (set emission
  wavelength) or emission scan (set excitation wavelength)
- Insert plate
- Start scan
- The results are automatically saved in an EXCEL file
- Close software, switch off computer, switch off plate reader

A.4.2  *Fluorescence spectroscopy using a qPCR cycler*

Similar to the fluorescence spectroscopy measurements using a plate reader, fluorescence intensities can also be read out with a qPCR cycler (CFX96 Touch Real-Time PCR Detection System, Bio Rad, courtesy of the lab of Dieter Braun at LMU München). For the fluorescence readout experiments using a qPCR cycler, the prepared DNA-SYBR Gold dilution series are filled into low-profile PCR tubes (Bio Rad, product ID: TLS-0851). These tubes are closed with flat, optical, ultra-clear caps (Bio Rad, product ID: TCS-0803) and placed into the qPCR cycler. The heating pathway is designed using the CFX manager software (Bio Rad), the samples are heated or cooled, respectively, to 24 °C, and 25°C in 0.5 °C steps, in five adjacent cycles. The fluorescence intensity is measured at each step, for the further analysis we use the data corresponding to 24 °C in order to easily compare the values. We choose the channel designed for the fluorescent dye Carboxyfluorescein (FAM) because its absorption and emission wavelengths (494 nm and 518 nm, respectively) are close to those of SYBR Gold (495 nm and 537 nm, respectively):

- File → new protocol
- Melting curve (as described above) → save in Lipfert Lab folder
- Express load
- Select FAM Chanel for SYBR Gold (closest to SYBR Gold)
- Run → save again
- Program then automatically runs for 28 minutes
- Export results in EXCEL: melt curve data (melt peak, RFU (relative fluorescence intensity))

# BIBLIOGRAPHY

[1] J. Zhang, F. Li, and D. Yang. „DNA: From Carrier of Genetic Information to Polymeric Materials." In: *Transactions of Tianjin University* 25.4 (2019), pp. 301–311. ISSN: 1995-8196. DOI: 10.1007/s12209-019-00188-w (cit. on p. 1).

[2] J. Burkhardt Richard W. „Lamarck, Evolution, and the Inheritance of Acquired Characters." In: *Genetics* 194.4 (2013), pp. 793–805. ISSN: 1943-2631. DOI: 10.1534/genetics.113.151852 (cit. on pp. 1, 2).

[3] J.-B. de Lamarck. *Flore francoise ou descriptions succinctes de toutes les plantes qui croissent naturellement en France, disposees selon une nouvelle methode d'analyse, et precedees par un expose des principes elementaires de la botanique.* Vol. 6. 1815 (cit. on p. 1).

[4] C. Darwin. „On the origin of species by means of natural selection, or the preservation of favoured races in the struggle for life." In: *London: John Murray* (1859) (cit. on pp. 1, 2).

[5] C. Darwin. *On the origin of species, 1859.* Routledge, 2004. ISBN: 0203509102 (cit. on p. 1).

[6] F Miescher. „Letter I; to Wilhelm His." In: *Tübingen, February 26th* (1869) (cit. on p. 2).

[7] R. Dahm. „Friedrich Miescher and the discovery of DNA." In: *Developmental Biology* 278.2 (2005), pp. 274–288. ISSN: 0012-1606. DOI: https://doi.org/10.1016/j.ydbio.2004.11.028 (cit. on pp. 2–4).

[8] R. Dahm. „Discovering DNA: Friedrich Miescher and the early years of nucleic acid research." In: *Human Genetics* 122.6 (2008), pp. 565–581. ISSN: 1432-1203. DOI: 10.1007/s00439-007-0433-0 (cit. on pp. 2, 3).

[9] A. Kossel. „Ueber das Nuclein der Hefe." In: (1879). ISSN: 1437-4315 (cit. on p. 2).

[10] A. Kossel. „Ueber die chemische Zusammensetzung der Zelle." In: *Du Bois-Reymond's Archiv/Arch Anat Physiol Physiol Abt* 278 (1891), pp. 181–186 (cit. on p. 2).

[11] W. Johannsen. „The genotype conception of heredity." In: *The American Naturalist* 45.531 (1911), pp. 129–159. ISSN: 0003-0147 (cit. on p. 3).

[12]  N. Roll-Hansen. „The holist tradition in twentieth century genetics. Wilhelm Johannsen's genotype concept." In: *The Journal of Physiology* 592.11 (2014), pp. 2431–2438. ISSN: 0022-3751. DOI: 10.1113/jphysiol.2014.272120 (cit. on p. 3).

[13]  T. H. Morgan, A. H. Sturtevant, H. J. Muller, and C. B. Bridges. *The mechanism of Mendelian heredity*. H. Holt, 1923 (cit. on p. 3).

[14]  *An introduction to genetic analysis*. WH Freeman and Company., 1976. ISBN: 0716705745 (cit. on p. 3).

[15]  The Nobel Foundation. *The Nobel Prize in Physiology or Medicine 1933*. (accessed March 14, 2023). URL: https://www.nobelprize.org/prizes/medicine/1933/summary/ (cit. on p. 3).

[16]  B. McClintock. „A Cytological and Genetical Study of Triploid Maize." In: *Genetics* 14.2 (1929), pp. 180–222. ISSN: 0016-6731 (Print) 0016-6731. DOI: 10.1093/genetics/14.2.180 (cit. on p. 3).

[17]  B. McClintock. „The Stability of Broken Ends of Chromosomes in Zea Mays." In: *Genetics* 26.2 (1941), pp. 234–82. ISSN: 0016-6731 (Print) 0016-6731. DOI: 10.1093/genetics/26.2.234 (cit. on p. 3).

[18]  B. McClintock. „The origin and behavior of mutable loci in maize." In: *Proceedings of the National Academy of Sciences* 36.6 (1950), pp. 344–355. DOI: doi:10.1073/pnas.36.6.344 (cit. on p. 3).

[19]  The Nobel Foundation. *The Nobel Prize in Physiology or Medicine 1983*. (accessed March 14, 2023). URL: https://www.nobelprize.org/prizes/medicine/1983/summary/ (cit. on p. 3).

[20]  O. T. Avery, C. M. MacLeod, and M. McCarty. „Studies on the chemical nature of the substance inducing transformation of pneumococcal types: Induction of Transformation by a Desoxyribonucleic Acid Fraction Isolated from Pneumococcus Type III." In: *The Journal of Experimental Medicine* 79.2 (1944), pp. 137–158. ISSN: 1540-9538 (cit. on p. 4).

[21]  A. Hershey and M Chase. „Independent functions of viral protein and nucleic acid in growth of bacteriophage." In: *Journal of General Physiology* 36 (1952), pp. 39–56. ISSN: 1540-7748 (cit. on p. 4).

[22]  R. E. Franklin and R. G. Gosling. „Evidence for 2-Chain Helix in Crystalline Structure of Sodium Deoxyribonucleate." In: *Nature* 172.4369 (1953), pp. 156–157. ISSN: 1476-4687. DOI: 10.1038/172156a0 (cit. on p. 4).

[23]  R. E. Franklin and R. G. Gosling. „Molecular Configuration in Sodium Thymonucleate." In: *Nature* 171.4356 (1953), pp. 740–741. ISSN: 1476-4687. DOI: 10.1038/171740a0 (cit. on p. 4).

[24]  J. D. Watson and F. H. C. Crick. „Molecular Structure of Nucleic Acids: A Structure for Deoxyribose Nucleic Acid." In: *Nature* 171.4356 (1953), pp. 737–738. ISSN: 1476-4687. DOI: 10.1038/171737a0 (cit. on p. 4).

[25]  M. Cobb and N. Comfort. „What Rosalind Franklin truly contributed to the discovery of DNA's structure." In: *Nature* 616.7958 (2023), pp. 657–660. ISSN: 0028-0836 (cit. on p. 4).

[26]  F. Crick. „How to live with a golden helix." In: *From Gene to Protein: Information Transfer in Normal and Abnormal Cells.* Ed. by T. R. Russell, K. Brew, H. Faber, and J. Schultz. Academic Press, 1979, pp. 1–13. ISBN: 978-0-12-604450-8. DOI: 10.1016/B978-0-12-604450-8.50006-7 (cit. on p. 4).

[27]  R. W. Holley, J. Apgar, G. A. Everett, J. T. Madison, M. Marquisee, S. H. Merrill, J. R. Penswick, and A. Zamir. „Structure of a ribonucleic acid." In: *Science* 147.3664 (1965), pp. 1462–1465. ISSN: 0036-8075 (cit. on p. 5).

[28]  H. G. Khorana, H Büuchi, H Ghosh, N Gupta, T. Jacob, H Kössel, R Morgan, S. Narang, E Ohtsuka, and R. Wells. „Polynucleotide synthesis and the genetic code." In: *Cold Spring Harbor symposia on quantitative biology.* Vol. 31. Cold Spring Harbor Laboratory Press, pp. 39–49. ISBN: 0091-7451 (cit. on p. 5).

[29]  M. W. Nirenberg and J. H. Matthaei. „The dependence of cell-free protein synthesis in E. coli upon naturally occurring or synthetic polyribonucleotides." In: *Proceedings of the National Academy of Sciences* 47.10 (1961), pp. 1588–1602. DOI: doi:10.1073/pnas.47.10.1588 (cit. on p. 5).

[30]  The Nobel Foundation. *The Nobel Prize in Physiology or Medicine 1968.* (accessed May 5, 2023). URL: https://www.nobelprize.org/prizes/medicine/1968/summary/ (cit. on p. 5).

[31]  L. T. C. França, E. Carrilho, and T. B. L. Kist. „A review of DNA sequencing techniques." In: *Quarterly Reviews of Biophysics* 35.2 (2002), pp. 169–200. ISSN: 0033-5835. DOI: 10.1017/S0033583502003797 (cit. on p. 5).

[32]  M. Zwolak and M. Di Ventra. „Colloquium: Physical approaches to DNA sequencing and detection." In: *Reviews of Modern Physics* 80.1 (2008), pp. 141–165. DOI: 10.1103/RevModPhys.80.141 (cit. on p. 5).

[33]  J. M. Heather and B. Chain. „The sequence of sequencers: The history of sequencing DNA." In: *Genomics* 107.1 (2016), pp. 1–8. ISSN: 0888-7543. DOI: https://doi.org/10.1016/j.ygeno.2015.11.003 (cit. on pp. 5, 7).

[34]   F. Sanger and A. R. Coulson. „A rapid method for determining sequences in DNA by primed synthesis with DNA polymerase." In: *Journal of Molecular Biology* 94.3 (1975), pp. 441–448. ISSN: 0022-2836. DOI: https://doi.org/10.1016/0022-2836(75)90213-2 (cit. on p. 5).

[35]   F. Sanger, S. Nicklen, and A. R. Coulson. „DNA sequencing with chain-terminating inhibitors." In: *Proceedings of the National Academy of Sciences* 74.12 (1977), pp. 5463–5467. DOI: doi:10.1073/pnas.74.12.5463 (cit. on p. 6).

[36]   The Nobel Foundation. *The Nobel Prize in Chemistry 1958*. 2023 (accessed July 10, 2023). URL: https://www.nobelprize.org/prizes/chemistry/1958/summary/ (cit. on p. 6).

[37]   The Nobel Foundation. *The Nobel Prize in Chemistry 1980*. 2023 (accessed July 10, 2023). URL: https://www.nobelprize.org/prizes/chemistry/1980/summary/ (cit. on p. 6).

[38]   J. D. Watson. „The Human Genome Project: Past, Present, and Future." In: *Science* 248.4951 (1990), pp. 44–49. DOI: doi:10.1126/science.2181665 (cit. on p. 6).

[39]   R. A. Gibbs. „The Human Genome Project changed everything." In: *Nature Reviews Genetics* 21.10 (2020), pp. 575–576. ISSN: 1471-0064. DOI: 10.1038/s41576-020-0275-3 (cit. on p. 6).

[40]   B. Guo and Y. Bi. „Cloning PCR products." In: *PCR cloning protocols* (2002), pp. 111–119 (cit. on p. 7).

[41]   J. M. S. Barlett and S. D. *A short history of the Polymerase Chain Reaction*. Ed. by J. M. S. Barlett and S. D. Vol. 226. PCR protocols, 2nd edition. Humana Press Inc., 2003, pp. 2–6 (cit. on p. 7).

[42]   B. Alberts, A. Johnson, J. Lewis, M. Raff, K. Roberts, and P. Walter. *Molecular Biology of the Cell, 5th edition, Chapter 4*. New York, USA and Abingdon, UK: Garland Science, Taylor and Francis Group, 2008. Chap. DNA Replication, Repair, and Recombination (cit. on pp. 7, 11, 38).

[43]   D. Proudnikov and A. Mirzabekov. „Chemical Methods of DNA and RNA Fluorescent Labeling." In: *Nucleic Acids Research* 24.22 (1996), pp. 4535–4542. ISSN: 0305-1048. DOI: 10.1093/nar/24.22.4535 (cit. on p. 7).

[44]   B. W. Ying, D. Fourmy, and S. Yoshizawa. „Substitution of the use of radioactivity by fluorescence for biochemical studies of RNA." In: *Rna* 13.11 (2007), pp. 2042–50. ISSN: 1355-8382 (Print) 1355-8382. DOI: 10.1261/rna.637907 (cit. on p. 7).

[45]  R. Phillips, J. Kondev, J. Theriot, and H. Garcia. *Physical biology of the cell, Chapter 1*. Garland Science, 2012. ISBN: 0429168837 (cit. on pp. 11, 38).

[46]  National Human Genome Research Institute (NIH). *DEOXYRIBONUCLEIC ACID (DNA)*. May 16, 2023 (accessed May 19, 2023). URL: https://www.genome.gov/genetics-glossary/Deoxyribonucleic-Acid (cit. on p. 11).

[47]  G. Litwack. „Chapter 10 - Nucleic Acids and Molecular Genetics." In: *Human Biochemistry*. Ed. by G. Litwack. Boston: Academic Press, 2018, pp. 257–317. ISBN: 978-0-12-383864-3. DOI: 10.1016/B978-0-12-383864-3.00010-7 (cit. on pp. 12, 13, 16, 49).

[48]  K. Hoogsteen. „The structure of crystals containing a hydrogen-bonded complex of 1-methylthymine and 9-methyladenine." In: *Acta Crystallographica* 12.10 (1959), pp. 822–823. ISSN: 0365-110X. DOI: doi:10.1107/S0365110X59002389 (cit. on p. 13).

[49]  D. E. Gilbert, G. A. van der Marel, J. H. van Boom, and J Feigon. „Unstable Hoogsteen base pairs adjacent to echinomycin binding sites within a DNA duplex." In: *Proceedings of the National Academy of Sciences* 86.9 (1989), pp. 3006–3010. DOI: doi:10.1073/pnas.86.9.3006 (cit. on p. 13).

[50]  P. Yakovchuk, E. Protozanova, and M. D. Frank-Kamenetskii. „Base-stacking and base-pairing contributions into thermal stability of the DNA double helix." In: *Nucleic Acids Res* 34.2 (2006), pp. 564–74. ISSN: 0305-1048 (Print) 0305-1048. DOI: 10.1093/nar/gkj454 (cit. on p. 13).

[51]  M. H. Wilkins. „Molecular Configuration of Nucleic Acids: From extensive diffraction data and molecular model building a more detailed picture is emerging." In: *Science* 140.3570 (1963), pp. 941–950. ISSN: 0036-8075 (cit. on p. 13).

[52]  J. D. Griffith. „DNA Structure: Evidence from Electron Microscopy." In: *Science* 201.4355 (1978), pp. 525–527. DOI: doi:10.1126/science.663672 (cit. on p. 13).

[53]  T. Zettl, R. S. Mathew, S. Seifert, S. Doniach, P. A. B. Harbury, and J. Lipfert. „Absolute Intramolecular Distance Measurements with Angstrom-Resolution Using Anomalous Small-Angle X-ray Scattering." In: *Nano Letters* 16.9 (2016), pp. 5353–5357. ISSN: 1530-6984. DOI: 10.1021/acs.nanolett.6b01160 (cit. on p. 13).

[54]  A. Vologodskii. *Biophysics of DNA*. Cambridge University Press, 2015. ISBN: 9781316239889 (cit. on pp. 13, 24, 26, 31–33, 38, 39, 51).

[55]  National Center for Biotechnology Information. *Genetics Review*. 1999
      (accessed February 15, 2023). URL: https://www.ncbi.nlm.nih.gov/
      Class/MLACourse/Original8Hour/Genetics/rna2.html (cit. on p. 14).

[56]  F. H. Crick. „The genetic code - yesterday, today, and tomorrow." In:
      *Cold Spring Harbor symposia on quantitative biology*. Vol. 31. Cold
      Spring Harbor Laboratory Press, pp. 3–9. ISBN: 0091-7451 (cit. on
      p. 16).

[57]  F. H. Crick. „On protein synthesis." In: *Symp Soc Exp Biol* 12 (1958),
      pp. 138–63. ISSN: 0081-1386 (Print) 0081-1386 (cit. on p. 16).

[58]  S. B. Smith, L. Finzi, and C. Bustamante. „Direct Mechanical
      Measurements of the Elasticity of Single DNA Molecules by Using
      Magnetic Beads." In: *Science* 258.5085 (1992), pp. 1122–1126. DOI:
      doi:10.1126/science.1439819 (cit. on pp. 17, 32, 47).

[59]  C. Bustamante, J. F. Marko, E. D. Siggia, and S Smith. „Entropic
      elasticity of lambda-phage DNA." In: *Science* 265.5178 (1994),
      pp. 1599–1600. ISSN: 0036-8075 (cit. on pp. 17, 18, 31, 47, 62).

[60]  S. B. Smith, Y. Cui, and C. Bustamante. „Overstretching B-DNA: The
      Elastic Response of Individual Double-Stranded and Single-Stranded
      DNA Molecules." In: *Science* 271.5250 (1996), pp. 795–799. DOI:
      doi:10.1126/science.271.5250.795 (cit. on pp. 17, 18, 47).

[61]  T. R. Strick, J.-F. Allemand, D. Bensimon, A. Bensimon, and
      V. Croquette. „The Elasticity of a Single Supercoiled DNA Molecule."
      In: *Science* 271.5257 (1996), pp. 1835–1837. DOI:
      doi:10.1126/science.271.5257.1835 (cit. on pp. 17, 47, 48, 110,
      111).

[62]  J. P. Peters, S. P. Yelgaonkar, S. G. Srivatsan, Y. Tor, and
      r. James Maher L. „Mechanical properties of DNA-like polymers." In:
      *Nucleic Acids Res* 41.22 (2013), pp. 10593–604. ISSN: 0305-1048 (Print)
      0305-1048. DOI: 10.1093/nar/gkt808 (cit. on p. 17).

[63]  S. R. Gallagher. „Quantitation of DNA and RNA with Absorption and
      Fluorescence Spectroscopy." In: *Current Protocols in Human Genetics*
      00.1 (1994), A.3D.1–A.3D.8. ISSN: 1934-8266. DOI:
      10.1002/0471142905.hga03ds00 (cit. on p. 19).

[64]  M. D. Frank-Kamenetskii. „Biophysics of the DNA molecule." In:
      *Physics Reports* 288.1-6 (1997), pp. 13–60. ISSN: 0370-1573 (cit. on
      pp. 19, 26, 31, 34, 35, 49–51).

[65] J. B. Schimelman, D. M. Dryden, L. Poudel, K. E. Krawiec, Y. Ma, R. Podgornik, V. A. Parsegian, L. K. Denoyer, W.-Y. Ching, N. F. Steinmetz, et al. „Optical properties and electronic transitions of DNA oligonucleotides as a function of composition and stacking sequence." In: *Physical Chemistry Chemical Physics* 17.6 (2015), pp. 4589–4599. ISSN: 1463-9076. DOI: 10.1039/C4CP03395G (cit. on p. 19).

[66] J. Lipfert, S. Doniach, R. Das, and D. Herschlag. „Understanding nucleic acid-ion interactions." In: *Annu Rev Biochem* 83 (2014), pp. 813–41. ISSN: 0066-4154 (Print) 0066-4154. DOI: 10.1146/annurev-biochem-060409-092720 (cit. on pp. 19–21, 75).

[67] G. S. Manning. „Limiting Laws and Counterion Condensation in Polyelectrolyte Solutions II. Self-Diffusion of the Small Ions." In: *The Journal of Chemical Physics* 51.3 (1969), pp. 934–938. ISSN: 0021-9606. DOI: 10.1063/1.1672158 (cit. on p. 20).

[68] G. S. Manning. „Limiting laws and counterion condensation in polyelectrolyte solutions: IV. The approach to the limit and the extraordinary stability of the charge fraction." In: *Biophysical Chemistry* 7.2 (1977), pp. 95–102. ISSN: 0301-4622. DOI: 10.1016/0301-4622(77)80002-1 (cit. on p. 20).

[69] G. S. Manning. „The molecular theory of polyelectrolyte solutions with applications to the electrostatic properties of polynucleotides." In: *Quarterly Reviews of Biophysics* 11.2 (1978), pp. 179–246. ISSN: 0033-5835. DOI: 10.1017/S0033583500002031 (cit. on p. 20).

[70] T. Vuletic, S. D. Babic, D. Grgicin, D. Aumiler, J. Rädler, F. Livolant, and S. Tomic. „Manning free counterion fraction for a rodlike polyion: Aqueous solutions of short DNA fragments in presence of very low added salt." In: *Physical Review E* 83.4 (2011), p. 041803. DOI: 10.1103/PhysRevE.83.041803 (cit. on p. 20).

[71] M. Gouy. „Sur la constitution de la charge electrique a la surface d'un electrolyte." In: *J. Phys. Theor. Appl.* 9.1 (1910), pp. 457–468 (cit. on p. 20).

[72] D. L. Chapman. „LI. A contribution to the theory of electrocapillarity." In: *The London, Edinburgh, and Dublin philosophical magazine and journal of science* 25.148 (1913), pp. 475–481. ISSN: 1941-5982 (cit. on p. 20).

[73] F. Fogolari, A. Brigo, and H. Molinari. „The Poisson-Boltzmann equation for biomolecular electrostatics: a tool for structural biology." In: *Journal of Molecular Recognition* 15.6 (2002), pp. 377–392. ISSN: 0952-3499. DOI: 10.1002/jmr.577 (cit. on p. 21).

[74]    P. Debye and E. Hückel. „Zur Theorie der Elektrolyte. I. Gefrierpunktserniedrigung und verwandte Erscheinungen." In: *Physikalische Zeitschrift* 24.9 (1923), pp. 185–206 (cit. on p. 21).

[75]    The Nobel Foundation. *The Nobel Prize in Chemistry 1936.* 1936 (accessed February 19, 2023). URL: https://www.nobelprize.org/prizes/chemistry/1936/debye/biographical/ (cit. on p. 21).

[76]    T. Markovich, D. Andelman, and R. Podgornik. „Charged Membranes: Poisson-Boltzmann Theory, The DLVO Paradigm, and Beyond." In: *Handbook of lipid membranes.* CRC Press, 2021, pp. 99–128. ISBN: 0429194072 (cit. on p. 21).

[77]    T. Schlick. „Modeling superhelical DNA: recent analytical and dynamic approaches." In: *Current Opinion in Structural Biology* 5.2 (1995), pp. 245–262. ISSN: 0959-440X. DOI: 10.1016/0959-440X(95)80083-2 (cit. on p. 23).

[78]    W. Kuhn. „Über die Gestalt fadenförmiger Moleküle in Lösungen." In: *Kolloid-Zeitschrift* 68.1 (1934), pp. 2–15. ISSN: 1435-1536. DOI: 10.1007/BF01451681 (cit. on p. 24).

[79]    M. Mazars. „Statistical physics of the freely jointed chain." In: *Physical Review E* 53.6 (1996), p. 6297 (cit. on p. 25).

[80]    O. Kratky and G. Porod. „Röntgenuntersuchung gelöster fadenmoleküle." In: *Recueil des Travaux Chimiques des Pays-Bas* 68.12 (1949), pp. 1106–1122. ISSN: 0165-0513 (cit. on p. 25).

[81]    P. J. Flory. *Principles of polymer chemistry.* Cornell university press, 1953. ISBN: 0801401348 (cit. on pp. 27, 32).

[82]    P. J. Flory and M. Volkenstein. „Statistical mechanics of chain molecules." In: *Biopolymers* 8.5 (1969), pp. 699–700. ISSN: 0006-3525. DOI: 10.1002/bip.1969.360080514 (cit. on p. 27).

[83]    P. A. Wiggins, T. van der Heijden, F. Moreno-Herrero, A. Spakowitz, R. Phillips, J. Widom, C. Dekker, and P. C. Nelson. „High flexibility of DNA on short length scales probed by atomic force microscopy." In: *Nature Nanotechnology* 1.2 (2006), pp. 137–141. ISSN: 1748-3395. DOI: 10.1038/nnano.2006.63 (cit. on pp. 27, 112, 118).

[84]    J. F. Marko and E. D. Siggia. „Stretching DNA." In: *Macromolecules* 28.26 (1995), pp. 8759–8770. ISSN: 0024-9297. DOI: 10.1021/ma00130a008 (cit. on p. 28).

[85]    K. R. Chaurasiya, T. Paramanathan, M. J. McCauley, and M. C. Williams. „Biophysical characterization of DNA binding from single molecule force measurements." In: *Physics of Life Reviews* 7.3 (2010), pp. 299–341. ISSN: 1571-0645. DOI: 10.1016/j.plrev.2010.06.001 (cit. on pp. 31, 37, 40).

[86]    J. F. Marko. „Biophysics of protein-DNA interactions and chromosome organization." In: *Physica A: Statistical Mechanics and its Applications* 418 (2015), pp. 126–153. ISSN: 0378-4371. DOI: 10.1016/j.physa.2014.07.045 (cit. on pp. 31, 34, 35).

[87]    R. Weil and J. Vinograd. „The cyclic helix and cyclic coil forms of polyoma viral DNA." In: *Proceedings of the National Academy of Sciences* 50.4 (1963), pp. 730–738. DOI: doi:10.1073/pnas.50.4.730 (cit. on p. 34).

[88]    J. Vinograd and J. Lebowitz. „Physical and topological properties of circular DNA." In: *J. Gen. Physiol.* 49.6 (1966), pp. 103–125 (cit. on p. 34).

[89]    J. F. Marko and E. D. Siggia. „Statistical mechanics of supercoiled DNA." In: *Phys Rev E Stat Phys Plasmas Fluids Relat Interdiscip Topics* 52.3 (1995), pp. 2912–2938. ISSN: 1063-651X (Print) 1063-651X (Linking) (cit. on p. 34).

[90]    F. B. Fuller. „The Writhing Number of a Space Curve." In: *Proceedings of the National Academy of Sciences* 68.4 (1971), pp. 815–819. DOI: doi:10.1073/pnas.68.4.815 (cit. on p. 34).

[91]    A. V. Vologodskii, S. Levene, K. V. Klenin, M. Frank-Kamenetskii, and N. R. Cozzarelli. „Conformational and thermodynamic properties of supercoiled DNA." In: *Journal of Molecular Niology* 227 (1992), pp. 1224–1243 (cit. on p. 34).

[92]    K. V. Klenin, A. V. Vologodskii, V. V. Anshelevich, A. M. Dykhne, and M. D. Frank-Kamenetskii. „Computer simulation of DNA supercoiling." In: *Journal of Molecular Biology* 217.3 (1991), pp. 413–419. ISSN: 0022-2836. DOI: 10.1016/0022-2836(91)90745-R (cit. on p. 35).

[93]    A. Bates and A. Maxwell. *DNA Topology.* Oxford University Press, 2005. ISBN: 9780198567097 (cit. on p. 35).

[94]    T. C. Boles, J. H. White, and N. R. Cozzarelli. „Structure of plectonemically supercoiled DNA." In: *J. Mol. Biol.* 213.4 (1990), pp. 931–951 (cit. on pp. 35, 134).

[95]    J. H. White. „Self-linking and Gauss-integral in higher dimensions." In: *American Journal of Mathematics* 91.3 (1969), p. 693. ISSN: 0002-9327. DOI: 10.2307/2373348 (cit. on pp. 36, 133).

[96]    „Physics of Nucleic Acids." In: *Fundamentals of Polymer Physics and Molecular Biophysics.* Ed. by H. B. Bohidar. Cambridge: Cambridge University Press, 2015, pp. 272–302. ISBN: 9781107415959. DOI: DOI:10.1017/CBO9781107415959.016 (cit. on p. 37).

[97]   J. Markovits, Y. Pommier, M. R. Mattern, C. Esnault, B. P. Roques, J.-B. Le Pecq, and K. W. Kohn. „Effects of the Bifunctional Antitumor Intercalator Ditercalinium on DNA in Mouse Leukemia L1210 Cells and DNA Topoisomerase II." In: *Cancer Research* 46.11 (1986), pp. 5821–5826. ISSN: 0008-5472 (cit. on p. 37).

[98]   R. Palchaudhuri and P. J. Hergenrother. „DNA as a target for anticancer compounds: methods to determine the mode of binding and the mechanism of action." In: *Curr Opin Biotechnol* 18.6 (2007), pp. 497–503. ISSN: 0958-1669 (Print) 0958-1669. DOI: 10.1016/j.copbio.2007.09.006 (cit. on p. 37).

[99]   B. A. D. Neto and A. A. M. Lapis. „Recent Developments in the Chemistry of Deoxyribonucleic Acid (DNA) Intercalators: Principles, Design, Synthesis, Applications and Trends." In: *Molecules* 14.5 (2009), pp. 1725–1746. ISSN: 1420-3049 (cit. on pp. 37, 40).

[100]  M. R. Gill and J. A. Thomas. „Ruthenium(ii) polypyridyl complexes and DNA-from structural probes to cellular imaging and therapeutics." In: *Chemical Society Reviews* 41.8 (2012), pp. 3179–3192. ISSN: 0306-0012. DOI: 10.1039/C2CS15299A (cit. on p. 37).

[101]  K. Cheung-Ong, G. Giaever, and C. Nislow. „DNA-Damaging Agents in Cancer Chemotherapy: Serendipity and Chemical Biology." In: *Chemistry and Biology* 20.5 (2013), pp. 648–659. ISSN: 1074-5521. DOI: 10.1016/j.chembiol.2013.04.007 (cit. on p. 37).

[102]  E. W. Taylor. „The mechanism of colchicine inhibition of mitosis: I. Kinetics of Inhibition and the Binding of H3-Colchicine." In: *Journal of Cell Biology* 25.1 (1965), pp. 145–160. ISSN: 0021-9525. DOI: 10.1083/jcb.25.1.145 (cit. on p. 37).

[103]  A. A. Almaqwashi, T. Paramanathan, I. Rouzina, and M. C. Williams. „Mechanisms of small molecule-DNA interactions probed by single-molecule force spectroscopy." In: *Nucleic Acids Research* 44.9 (2016), pp. 3971–3988. ISSN: 0305-1048. DOI: 10.1093/nar/gkw237 (cit. on pp. 37, 40).

[104]  A. S. Zasedatelev, G. V. Gurskii, and M. V. Vol'kenshtein. „Theory of one-dimensional adsorption. I. Adsorption of small molecules on a homopolymer." In: *Molecular biology* 5.2 (1971), pp. 194–198. ISSN: 0026-8933 (cit. on p. 38).

[105]  J. D. McGhee and P. H. von Hippel. „Theoretical aspects of DNA-protein interactions: Co-operative and non-co-operative binding of large ligands to a one-dimensional homogeneous lattice." In: *Journal of Molecular Biology* 86.2 (1974), pp. 469–489. ISSN: 0022-2836. DOI: 10.1016/0022-2836(74)90031-X (cit. on pp. 39, 63, 85, 110, 131).

[106]  L. S. Lerman. „Structural considerations in the interaction of DNA and acridines." In: *J Mol Biol* 3 (1961), pp. 18–30. ISSN: 0022-2836 (Print) 0022-2836. DOI: 10.1016/s0022-2836(61)80004-1 (cit. on pp. 40, 64, 86, 129).

[107]  V. Luzzati, F. Masson, and L. S. Lerman. „Interaction of DNA and proflavine: A small-angle X-ray scattering study." In: *Journal of Molecular Biology* 3.5 (1961), pp. 634–639. ISSN: 0022-2836. DOI: 10.1016/S0022-2836(61)80026-0 (cit. on p. 40).

[108]  H. M. Sobell and S. C. Jain. „Stereochemistry of actinomycin binding to DNA. II. Detailed molecular model of actinomycin-DNA complex and its implications." In: *J Mol Biol* 68.1 (1972), pp. 21–34. ISSN: 0022-2836 (Print) 0022-2836. DOI: 10.1016/0022-2836(72)90259-8 (cit. on p. 40).

[109]  C. C. Tsai, S. C. Jain, and H. M. Sobell. „Drug-nucleic acid interaction: X-ray crystallographic determination of an ethidium-dinucleoside monophosphate crystalline complex, ethidium: 5-iodouridylyl(3'-5')adenosine." In: *Philos Trans R Soc Lond B Biol Sci* 272.915 (1975), pp. 137–46. ISSN: 0962-8436 (Print) 0962-8436. DOI: 10.1098/rstb.1975.0076 (cit. on p. 40).

[110]  R. Krautbauer, L. H. Pope, T. E. Schrader, S. Allen, and H. E. Gaub. „Discriminating small molecule DNA binding modes by single molecule force spectroscopy." In: *FEBS Lett* 510.3 (2002), pp. 154–8. ISSN: 0014-5793 (Print) 0014-5793. DOI: 10.1016/s0014-5793(01)03257-4 (cit. on pp. 40, 59, 123).

[111]  R. Eckel, R. Ros, A. Ros, S. D. Wilking, N. Sewald, and D. Anselmetti. „Identification of Binding Mechanisms in Single Molecule-DNA Complexes." In: *Biophysical Journal* 85.3 (2003), pp. 1968–1973. ISSN: 0006-3495. DOI: 10.1016/S0006-3495(03)74624-4 (cit. on pp. 40, 59).

[112]  J. B. Chaires. „A thermodynamic signature for drug-DNA binding mode." In: *Archives of Biochemistry and Biophysics* 453.1 (2006), pp. 26–31. ISSN: 0003-9861. DOI: 10.1016/j.abb.2006.03.027 (cit. on p. 40).

[113]  M. Waring. „Variation of the supercoils in closed circular DNA by binding of antibiotics and drugs: Evidence for molecular models involving intercalation." In: *Journal of Molecular Biology* 54.2 (1970), pp. 247–279. ISSN: 0022-2836. DOI: 10.1016/0022-2836(70)90429-8 (cit. on p. 40).

[114]  H. M. Berman, W. K. Olson, D. L. Beveridge, J. Westbrook,
       A. Gelbin, T. Demeny, S. H. Hsieh, A. R. Srinivasan, and B. Schneider.
       „The nucleic acid database. A comprehensive relational database of
       three-dimensional structures of nucleic acids." In: *Biophys J* 63.3
       (1992), pp. 751–9. ISSN: 0006-3495 (Print) 0006-3495. DOI:
       10.1016/s0006-3495(92)81649-1 (cit. on p. 40).

[115]  B. Coimbatore Narayanan, J. Westbrook, S. Ghosh, A. I. Petrov,
       B. Sweeney, C. L. Zirbel, N. B. Leontis, and H. M. Berman. „The
       Nucleic Acid Database: new features and capabilities." In: *Nucleic
       Acids Research* 42.D1 (2013), pp. D114–D122. ISSN: 0305-1048. DOI:
       10.1093/nar/gkt980 (cit. on p. 40).

[116]  J. Lipfert, S. Klijnhout, and N. H. Dekker. „Torsional sensing of
       small-molecule binding using magnetic tweezers." In: *Nucleic acids
       research* 38.20 (2010), pp. 7122–7132. ISSN: 1362-4962 (cit. on pp. 40,
       59, 62, 64, 67, 80, 86, 109, 111, 117, 120, 123–125, 129–131, 133, 134,
       138, 141, 151, 154).

[117]  K. M. Langner, P. Kedzierski, W. A. Sokalski, and J. Leszczynski.
       „Physical Nature of Ethidium and Proflavine Interactions with Nucleic
       Acid Bases in the Intercalation Plane." In: *The Journal of Physical
       Chemistry B* 110.19 (2006), pp. 9720–9727. ISSN: 1520-6106. DOI:
       10.1021/jp056836b (cit. on pp. 40, 59, 129).

[118]  M. D. Disney. „Targeting RNA with Small Molecules To Capture
       Opportunities at the Intersection of Chemistry, Biology, and
       Medicine." In: *Journal of the American Chemical Society* 141.17
       (2019), pp. 6776–6790. ISSN: 0002-7863. DOI: 10.1021/jacs.8b13419
       (cit. on p. 41).

[119]  S. M. Meyer, C. C. Williams, Y. Akahori, T. Tanaka, H. Aikawa,
       Y. Tong, J. L. Childs-Disney, and M. D. Disney. „Small molecule
       recognition of disease-relevant RNA structures." In: *Chemical Society
       Reviews* 49.19 (2020), pp. 7167–7199. ISSN: 0306-0012. DOI:
       10.1039/D0CS00560F (cit. on p. 41).

[120]  A. Di Marco, M. Gaetani, P. Orezzi, B. M. Scarpinato, R. Silvestrini,
       M. Soldati, T. Dasdia, and L. Valentini. „'Daunomycin', a New
       Antibiotic of the Rhodomycin Group." In: *Nature* 201.4920 (1964),
       pp. 706–707. ISSN: 1476-4687. DOI: 10.1038/201706a0 (cit. on p. 41).

[121]  P. Chandra, D. Gericke, F. Zunino, and B. C. G. Kornhuber. „The
       relationship of chemical structure to cytostatic activity of some
       daunomycin derivatives." In: *Pharmacological Research
       Communications* 4.3 (1972), pp. 269–272. ISSN: 0031-6989. DOI:
       https://doi.org/10.1016/0031-6989(72)90014-8 (cit. on p. 41).

[122]  D. A. Gewirtz. „A critical evaluation of the mechanisms of action proposed for the antitumor effects of the anthracycline antibiotics adriamycin and daunorubicin." In: *Biochemical Pharmacology* 57.7 (1999), pp. 727–741. ISSN: 0006-2952. DOI: https://doi.org/10.1016/S0006-2952(98)00307-4 (cit. on p. 41).

[123]  U. Ray, S. K. Raul, V. K. Gopinatha, D. Ghosh, K. S. Rangappa, K. Mantelingu, and S. C. Raghavan. „Identification and characterization of novel SCR7-based small-molecule inhibitor of DNA end-joining, SCR130 and its relevance in cancer therapeutics." In: *Molecular Carcinogenesis* 59.6 (2020), pp. 618–628. ISSN: 0899-1987. DOI: https://doi.org/10.1002/mc.23186 (cit. on p. 41).

[124]  M. Arya, I. S. Shergill, M. Williamson, L. Gommersall, N. Arya, and H. R. H. Patel. „Basic principles of real-time quantitative PCR." In: *Expert Review of Molecular Diagnostics* 5.2 (2005), pp. 209–219. ISSN: 1473-7159. DOI: 10.1586/14737159.5.2.209 (cit. on pp. 41, 42).

[125]  S. A. Bustin. „Real-time, fluorescence-based quantitative PCR: a snapshot of current procedures and preferences." In: *Expert Review of Molecular Diagnostics* 5.4 (2005), pp. 493–498. ISSN: 1473-7159. DOI: 10.1586/14737159.5.4.493 (cit. on p. 41).

[126]  A. Garrido-Maestu, S. Azinheiro, F. Roumani, J. Carvalho, and M. Prado. „Application of Short Pre-enrichment, and Double Chemistry Real-Time PCR, Combining Fluorescent Probes and an Intercalating Dye, for Same-Day Detection and Confirmation of Salmonella spp. and Escherichia coli O157 in Ground Beef and Chicken Samples." In: *Frontiers in Microbiology* 11 (2020). ISSN: 1664-302X. DOI: 10.3389/fmicb.2020.591041 (cit. on p. 42).

[127]  R. Conroy. „Force Spectroscopy with Optical and Magnetic Tweezers." In: *Handbook of Molecular Force Spectroscopy*. Ed. by A. Noy. Boston, MA: Springer US, 2008, pp. 23–96. ISBN: 978-0-387-49989-5. DOI: 10.1007/978-0-387-49989-5_2 (cit. on pp. 44, 45, 47).

[128]  F. H. C. Crick and A. F. W. Hughes. „The physical properties of cytoplasm: A study by means of the magnetic particle method Part I. Experimental." In: *Experimental Cell Research* 1.1 (1950), pp. 37–80. ISSN: 0014-4827. DOI: 10.1016/0014-4827(50)90048-6 (cit. on p. 44).

[129]  The Nobel Foundation. *The Nobel Prize in Physics 2018*. 2018 (accessed February 21, 2023). URL: https://www.nobelprize.org/prizes/physics/2018/summary/ (cit. on p. 44).

[130]   A. Ashkin, J. M. Dziedzic, J. E. Bjorkholm, and S. Chu. „Observation of a single-beam gradient force optical trap for dielectric particles." In: *Opt Lett* 11.5 (1986), p. 288. ISSN: 0146-9592 (Print) 0146-9592 (Linking). DOI: `8652[pii]` (cit. on p. 44).

[131]   D. Dulin, T. J. Cui, J. Cnossen, M. Docter, J. Lipfert, and N. Dekker. „High Spatiotemporal-Resolution Magnetic Tweezers: Calibration and Applications for DNA Dynamics." In: *Biophysical Journal* 109.10 (2015), pp. 2113–2125. ISSN: 0006-3495. DOI: `10.1016/j.bpj.2015.10.018` (cit. on pp. 45, 47, 48).

[132]   J. P. Cnossen, D. Dulin, and N. H. Dekker. „An optimized software framework for real-time, high-throughput tracking of spherical beads." In: *Review of Scientific Instruments* 85.10 (2014), p. 103712. DOI: `10.1063/1.4898178` (cit. on pp. 45, 47, 81, 118).

[133]   A. Huhle, D. Klaue, H. Brutzer, P. Daldrop, S. Joo, O. Otto, U. F. Keyser, and R. Seidel. „Camera-based three-dimensional real-time particle tracking at kHz rates and Angström accuracy." In: *Nature Communications* 6.1 (2015), p. 5885. ISSN: 2041-1723. DOI: `10.1038/ncomms6885` (cit. on pp. 45, 47).

[134]   F. Kriegel, W. Vanderlinden, T. Nicolaus, A. Kardinal, and J. Lipfert. „Measuring Single-Molecule Twist and Torque in Multiplexed Magnetic Tweezers." In: *Nanoscale Imaging: Methods and Protocols*. Ed. by Y. L. Lyubchenko. New York, NY: Springer New York, 2018, pp. 75–98. ISBN: 978-1-4939-8591-3. DOI: `10.1007/978-1-4939-8591-3_6` (cit. on pp. 46, 47, 118).

[135]   F. Kriegel, N. Ermann, and J. Lipfert. „Probing the mechanical properties, conformational changes, and interactions of nucleic acids with magnetic tweezers." In: *Journal of Structural Biology* 197.1 (2017), pp. 26–36. ISSN: 1047-8477. DOI: `10.1016/j.jsb.2016.06.022` (cit. on pp. 46–48, 81, 110, 134).

[136]   F. Kriegel, N. Ermann, R. Forbes, D. Dulin, N. H. Dekker, and J. Lipfert. „Probing the salt dependence of the torsional stiffness of DNA by multiplexed magnetic torque tweezers." In: *Nucleic Acids Research* 45.10 (2017), pp. 5920–5929. ISSN: 0305-1048. DOI: `10.1093/nar/gkx280` (cit. on pp. 46–48, 134).

[137]   F. Kriegel, C. Matek, T. Drsata, K. Kulenkampff, S. Tschirpke, M. Zacharias, F. Lankas, and J. Lipfert. „The temperature dependence of the helical twist of DNA." In: *Nucleic Acids Res* 46.15 (2018), pp. 7998–8009. ISSN: 1362-4962 (Electronic) 0305-1048 (Linking). DOI: `10.1093/nar/gky599` (cit. on pp. 46, 120).

[138] Y.-Y. Lin, T. Brouns, <u>P. J. Kolbeck</u>, W. Vanderlinden, and J. Lipfert. „High-yield ligation-free assembly of DNA constructs with nucleosome positioning sequence repeats for single-molecule manipulation assays." In: *Journal of Biological Chemistry* 299.7 (2023). ISSN: 0021-9258. DOI: 10.1016/j.jbc.2023.104874 (cit. on pp. 47, 50, 180).

[139] A. J. W. te Velthuis, J. W. J. Kerssemakers, J. Lipfert, and N. H. Dekker. „Quantitative Guidelines for Force Calibration through Spectral Analysis of Magnetic Tweezers Data." In: *Biophysical Journal* 99.4 (2010), pp. 1292–1302. ISSN: 0006-3495. DOI: 10.1016/j.bpj.2010.06.008 (cit. on pp. 47, 48, 82, 119).

[140] D. Dulin, J. Lipfert, M. C. Moolman, and N. H. Dekker. „Studying genomic processes at the single-molecule level: introducing the tools and applications." In: *Nature Reviews Genetics* 14.1 (2013), pp. 9–22. ISSN: 1471-0064. DOI: 10.1038/nrg3316 (cit. on pp. 47, 48).

[141] B. M. Lansdorp, S. J. Tabrizi, A. Dittmore, and O. A. Saleh. „A high-speed magnetic tweezer beyond 10,000 frames per second." In: *Rev Sci Instrum* 84.4 (2013), p. 044301. ISSN: 1089-7623 (Electronic) 0034-6748 (Linking). DOI: 10.1063/1.4802678 (cit. on p. 47).

[142] C.-H. Chiou, Y.-Y. Huang, M.-H. Chiang, H.-H. Lee, and G.-B. Lee. „New magnetic tweezers for investigation of the mechanical properties of single DNA molecules." In: *Nanotechnology* 17.5 (2006), p. 1217. ISSN: 0957-4484. DOI: 10.1088/0957-4484/17/5/009 (cit. on p. 47).

[143] B. M. Lansdorp and O. A. Saleh. „Power spectrum and Allan variance methods for calibrating single-molecule video-tracking instruments." In: *Rev Sci Instrum* 83.2 (2012), p. 025115. ISSN: 1089-7623 (Electronic) 0034-6748 (Linking). DOI: 10.1063/1.3687431 (cit. on pp. 48, 82, 119).

[144] J. E. Thies. „Molecular approaches to studying the soil biota." In: *Soil Microbiology, Ecology and Biochemistry*. Elsevier, 2015, pp. 151–185 (cit. on p. 49).

[145] A. Drabik, A. Bodzon-Kulakowska, and J. Silberring. „7 - Gel Electrophoresis." In: *Proteomic Profiling and Analytical Chemistry (Second Edition)*. Ed. by P. Ciborowski and J. Silberring. Boston: Elsevier, 2016, pp. 115–143. ISBN: 978-0-444-63688-1. DOI: 10.1016/B978-0-444-63688-1.00007-0 (cit. on p. 50).

[146] T. Biver. „Use of UV-Vis Spectrometry to Gain Information on the Mode of Binding of Small Molecules to DNAs and RNAs." In: *Applied Spectroscopy Reviews* 47.4 (2012), pp. 272–325. ISSN: 0570-4928. DOI: 10.1080/05704928.2011.641044 (cit. on p. 51).

[147] C. R. Cantor, M. M. Warshaw, and H SHAPIRO. „Oligonucleotide interactions. 3. Circular dichroism studies of the conformation of deoxyoligonucleotides." In: *Biopolymers* 9.9 (1970), pp. 1059–1077 (cit. on p. 52).

[148] M. J. Cavaluzzi and P. N. Borer. „Revised UV extinction coefficients for nucleoside-5'-monophosphates and unpaired DNA and RNA." In: *Nucleic Acids Research* 32.1 (2004), e13–13 (cit. on p. 52).

[149] B. S. P. Reddy, S. M. Sondhi, and J. W. Lown. „Synthetic DNA minor groove-binding drugs." In: *Pharmacology & Therapeutics* 84.1 (1999), pp. 1–111. ISSN: 0163-7258. DOI: https://doi.org/10.1016/S0163-7258(99)00021-2 (cit. on p. 53).

[150] L. F. P. De Castro and M. Zacharias. „DAPI binding to the DNA minor groove: a continuum solvent analysis." In: *Journal of Molecular Recognition* 15.4 (2002), pp. 209–220. ISSN: 0952-3499. DOI: https://doi.org/10.1002/jmr.581 (cit. on p. 53).

[151] A. Biancardi, T. Biver, F. Secco, and B. Mennucci. „An investigation of the photophysical properties of minor groove bound and intercalated DAPI through quantum-mechanical and spectroscopic tools." In: *Physical Chemistry Chemical Physics* 15.13 (2013), pp. 4596–4603. ISSN: 1463-9076. DOI: 10.1039/C3CP44058C (cit. on p. 53).

[152] L. J. Kricka. „Stains, labels and detection strategies for nucleic acids assays." In: *Annals of Clinical Biochemistry* 39.2 (2002), pp. 114–129. ISSN: 0004-5632 (cit. on pp. 54, 55).

[153] H. Zipper, H. Brunner, J. Bernhagen, and F. Vitzthum. „Investigations on DNA intercalation and surface binding by SYBR Green I, its structure determination and methodological implications." In: *Nucleic Acids Research* 32.12 (2004), e103–e103. ISSN: 0305-1048. DOI: 10.1093/nar/gnh101 (cit. on pp. 54, 61, 62, 79).

[154] L. R. Williams. „Staining nucleic acids and proteins in electrophoresis gels." In: *Biotechnic and Histochemistry* 76.3 (2001), pp. 127–132. ISSN: 1052-0295. DOI: 10.1080/bih.76.3.127.132 (cit. on p. 55).

[155] B. A. Armitage. „Cyanine Dye-Nucleic Acid Interactions." In: *Heterocyclic Polymethine Dyes: Synthesis, Properties and Applications*. Ed. by L. Strekowski. Berlin, Heidelberg: Springer Berlin Heidelberg, 2008, pp. 11–29. ISBN: 978-3-540-79064-8. DOI: 10.1007/7081_2007_109 (cit. on pp. 55, 56).

[156] A. Mishra, R. K. Behera, P. K. Behera, B. K. Mishra, and G. B. Behera. „Cyanines during the 1990s: A Review." In: *Chemical Reviews* 100.6 (2000), pp. 1973–2012. ISSN: 0009-2665. DOI: 10.1021/cr990402t (cit. on p. 56).

[157]   P. J. Kolbeck, W. Vanderlinden, G. Gemmecker, C. Gebhardt,
        M. Lehmann, A. Lak, T. Nicolaus, T. Cordes, and J. Lipfert.
        „Molecular structure, DNA binding mode, photophysical properties
        and recommendations for use of SYBR Gold." In: *Nucleic Acids
        Research* 49.9 (2021), pp. 5143–5158. ISSN: 0305-1048. DOI:
        `10.1093/nar/gkab265` (cit. on pp. 57, 124, 129–131, 133, 134, 137–139,
        141, 145, 148, 151, 154).

[158]   R. S. Tuma, M. P. Beaudet, X. Jin, L. J. Jones, C.-Y. Cheung, S. Yue,
        and V. L. Singer. „Characterization of SYBR Gold Nucleic Acid Gel
        Stain: A Dye Optimized for Use with 300-nm Ultraviolet
        Transilluminators." In: *Analytical Biochemistry* 268.2 (1999),
        pp. 278–288. ISSN: 0003-2697. DOI: `10.1006/abio.1998.3067` (cit. on
        pp. 59, 68, 70, 86, 130, 137).

[159]   G. Cosa, K.-S. Focsaneanu, J. R. N. McLean, J. P. McNamee, and
        J. C. Scaiano. „Photophysical Properties of Fluorescent DNA-dyes
        Bound to Single- and Double-stranded DNA in Aqueous Buffered
        Solution." In: *Photochemistry and Photobiology* 73.6 (2001),
        pp. 585–599. ISSN: 0031-8655. DOI:
        `10.1562/0031-8655(2001)0730585PPOFDD2.0.CO2` (cit. on pp. 59, 68,
        70, 71, 74, 86, 130, 137).

[160]   A. S. Biebricher, I. Heller, R. F. H. Roijmans, T. P. Hoekstra,
        E. J. G. Peterman, and G. J. L. Wuite. „The impact of DNA
        intercalators on DNA and DNA-processing enzymes elucidated
        through force-dependent binding kinetics." In: *Nature Communications*
        6.1 (2015), p. 7304. ISSN: 2041-1723. DOI: `10.1038/ncomms8304` (cit. on
        pp. 59, 62, 64, 86, 130, 131, 133, 141, 143).

[161]   J. L. McKillip and M. Drake. „Real-Time Nucleic Acid-Based
        Detection Methods for Pathogenic Bacteria in Food." In: *Journal of
        Food Protection* 67.4 (2004), pp. 823–832. ISSN: 0362-028X. DOI:
        `10.4315/0362-028x-67.4.823` (cit. on p. 59).

[162]   C. Uslan and B. Sebnem Sesalan. „The synthesis, photochemical and
        biological properties of new silicon phthalocyanines." In: *Inorganica
        Chimica Acta* 394 (2013), pp. 353–362. ISSN: 0020-1693. DOI:
        `10.1016/j.ica.2012.08.004` (cit. on p. 59).

[163]   P. Kühler, E.-M. Roller, R. Schreiber, T. Liedl, T. Lohmüller, and
        J. Feldmann. „Plasmonic DNA-Origami Nanoantennas for
        Surface-Enhanced Raman Spectroscopy." In: *Nano Letters* 14.5 (2014),
        pp. 2914–2919. ISSN: 1530-6984. DOI: `10.1021/nl5009635` (cit. on
        p. 59).

[164] J. G. Wang. „The degree of unwinding of the DNA helix by ethidium: I. Titration of twisted PM2 DNA molecules in alkaline cesium chloride density gradients." In: *Journal of Molecular Biology* 89.4 (1974), pp. 783–801. ISSN: 0022-2836. DOI: 10.1016/0022-2836(74)90053-9 (cit. on pp. 59, 129–131).

[165] P. Cluzel, A. Lebrun, C. Heller, R. Lavery, J.-L. Viovy, D. Chatenay, and F. Caron. „DNA: An Extensible Molecule." In: *Science* 271.5250 (1996), pp. 792–794. DOI: doi:10.1126/science.271.5250.792 (cit. on pp. 59, 62).

[166] M. L. Bennink, O. D. Schärer, R. Kanaar, K. Sakata-Sogawa, J. M. Schins, J. S. Kanger, B. G. de Grooth, and J. Greve. „Single-molecule manipulation of double-stranded DNA using optical tweezers: Interaction studies of DNA with RecA and YOYO-1." In: *Cytometry* 36.3 (1999), pp. 200–208. ISSN: 0196-4763 (cit. on p. 59).

[167] I. Tessmer, C. G. Baumann, G. M. Skinner, J. E. Molloy, J. G. Hoggett, S. J. B. Tendler, and S. Allen. „Mode of drug binding to DNA determined by optical tweezers force spectroscopy." In: *Journal of Modern Optics* 50.10 (2003), pp. 1627–1636. ISSN: 0950-0340. DOI: 10.1080/09500340308235236 (cit. on p. 59).

[168] A. Sischka, K. Toensing, R. Eckel, S. D. Wilking, N. Sewald, R. Ros, and D. Anselmetti. „Molecular Mechanisms and Kinetics between DNA and DNA Binding Ligands." In: *Biophysical Journal* 88.1 (2005), pp. 404–411. ISSN: 0006-3495. DOI: 10.1529/biophysj.103.036293 (cit. on pp. 59, 109, 130).

[169] A. Mihailovic, I. Vladescu, M. McCauley, E. Ly, M. C. Williams, E. M. Spain, and M. E. Nunez. „Exploring the Interaction of Ruthenium(II) Polypyridyl Complexes with DNA Using Single-Molecule Techniques." In: *Langmuir* 22.10 (2006), pp. 4699–4709. ISSN: 0743-7463. DOI: 10.1021/la053242r (cit. on p. 59).

[170] I. D. Vladescu, M. J. McCauley, I. Rouzina, and M. C. Williams. „Mapping the phase diagram of single DNA molecule force-induced melting in the presence of ethidium." In: *Physical review letters* 95.15 (2005), p. 158102 (cit. on p. 59).

[171] I. D. Vladescu, M. J. McCauley, M. E. Nunez, I. Rouzina, and M. C. Williams. „Quantifying force-dependent and zero-force DNA intercalation by single-molecule stretching." In: *Nature methods* 4.6 (2007), pp. 517–522 (cit. on pp. 59, 62, 64, 86, 109, 110, 129–131, 145).

[172]   T. Paramanathan, F. Westerlund, M. J. McCauley, I. Rouzina,
        P. Lincoln, and M. C. Williams. „Mechanically manipulating the DNA
        threading intercalation rate." In: *Journal of the American Chemical
        Society* 130.12 (2008), pp. 3752–3753. DOI: 10.1021/ja711303p (cit. on
        p. 59).

[173]   T.-S. Yang, Y. Cui, C.-M. Wu, J.-M. Lo, C.-S. Chiang, W.-Y. Shu,
        W.-J. Chung, C.-S. Yu, K.-N. Chiang, and I. C. Hsu. „Determining the
        Zero-Force Binding Energetics of an Intercalated DNA Complex by a
        Single-Molecule Approach." In: *ChemPhysChem* 10.16 (2009),
        pp. 2791–2794. DOI: 10.1002/cphc.200900435 (cit. on p. 59).

[174]   D. H. Paik and T. T. Perkins. „Dynamics and Multiple Stable Binding
        Modes of DNA Intercalators Revealed by Single-Molecule Force
        Spectroscopy." In: *Angewandte Chemie International Edition* 51.8
        (2012), pp. 1811–1815. ISSN: 1433-7851. DOI: 10.1002/anie.201105540
        (cit. on p. 59).

[175]   K. Schakenraad, A. S. Biebricher, M. Sebregts, B. ten Bensel,
        E. J. G. Peterman, G. J. L. Wuite, I. Heller, C. Storm, and
        P. van der Schoot. „Hyperstretching DNA." In: *Nature
        Communications* 8.1 (2017), p. 2197. ISSN: 2041-1723. DOI:
        10.1038/s41467-017-02396-1 (cit. on pp. 59, 62).

[176]   M. Manosas, J. Camunas-Soler, V. Croquette, and F. Ritort. „Single
        molecule high-throughput footprinting of small and large DNA
        ligands." In: *Nature Communications* 8.1 (2017), p. 304. ISSN:
        2041-1723. DOI: 10.1038/s41467-017-00379-w (cit. on pp. 59, 109).

[177]   A. G. Clark, M. N. Naufer, F. Westerlund, P. Lincoln, I. Rouzina,
        T. Paramanathan, and M. C. Williams. „Reshaping the Energy
        Landscape Transforms the Mechanism and Binding Kinetics of DNA
        Threading Intercalation." In: *Biochemistry* 57.5 (2018), pp. 614–619.
        ISSN: 0006-2960. DOI: 10.1021/acs.biochem.7b01036 (cit. on p. 59).

[178]   D. Salerno, D. Brogioli, V. Cassina, D. Turchi, G. L. Beretta,
        D. Seruggia, R. Ziano, F. Zunino, and F. Mantegazza. „Magnetic
        tweezers measurements of the nanomechanical properties of DNA in
        the presence of drugs." In: *Nucleic Acids Research* 38.20 (2010),
        pp. 7089–7099. ISSN: 0305-1048. DOI: 10.1093/nar/gkq597 (cit. on
        pp. 59, 129, 130).

[179]   K. Günther, M. Mertig, and R. Seidel. „Mechanical and structural
        properties of YOYO-1 complexed DNA." In: *Nucleic Acids Research*
        38.19 (2010), pp. 6526–6532. ISSN: 0305-1048. DOI:
        10.1093/nar/gkq434 (cit. on pp. 59, 64, 109).

[180]  Y. Wang, A. Sischka, V. Walhorn, K. Tönsing, and D. Anselmetti.
       „Nanomechanics of Fluorescent DNA Dyes on DNA Investigated by
       Magnetic Tweezers." In: *Biophysical Journal* 111.8 (2016),
       pp. 1604–1611. ISSN: 0006-3495. DOI: 10.1016/j.bpj.2016.08.042
       (cit. on pp. 59, 67).

[181]  G. A. King, A. S. Biebricher, I. Heller, E. J. G. Peterman, and
       G. J. L. Wuite. „Quantifying Local Molecular Tension Using
       Intercalated DNA Fluorescence." In: *Nano Letters* 18.4 (2018),
       pp. 2274–2281. ISSN: 1530-6984. DOI: 10.1021/acs.nanolett.7b04842
       (cit. on pp. 62, 130).

[182]  C. Bouchiat, M. D. Wang, J. F. Allemand, T. Strick, S. M. Block, and
       V. Croquette. „Estimating the Persistence Length of a Worm-Like
       Chain Molecule from Force-Extension Measurements." In: *Biophysical
       Journal* 76.1 (1999), pp. 409–413. ISSN: 0006-3495. DOI:
       10.1016/S0006-3495(99)77207-3 (cit. on pp. 62, 82, 110, 119).

[183]  W. T. Vetterling, W. T. Vetterling, W. H. Press, W. H. Press,
       S. A. Teukolsky, B. P. Flannery, and B. P. Flannery. *Numerical
       recipes: example book C.* Cambridge University Press, 1992. ISBN:
       0521437202 (cit. on p. 64).

[184]  H. M. Berman and P. R. Young. „The interaction of intercalating
       drugs with nucleic acids." In: *Annual Review of Biophysics and
       Bioengineering* 10.1 (1981), pp. 87–114. DOI:
       10.1146/annurev.bb.10.060181.000511 (cit. on p. 64).

[185]  Y. Wang, H. Schellenberg, V. Walhorn, K. Toensing, and
       D. Anselmetti. „Binding mechanism of PicoGreen to DNA
       characterized by magnetic tweezers and fluorescence spectroscopy." In:
       *European Biophysics Journal* 46.6 (2017), pp. 561–566. ISSN: 1432-1017.
       DOI: 10.1007/s00249-017-1204-z (cit. on pp. 64, 67, 92).

[186]  W. Vanderlinden, P. J. Kolbeck, W. Frederickx, S. F. Konrad,
       T. Nicolaus, C. Lampe, A. S. Urban, C. Moucheron, and J. Lipfert.
       „Ru(TAP)32+ uses multivalent binding to accelerate and constrain
       photo-adduct formation on DNA." In: *Chem. Commun.* 55 (2019),
       pp. 8764–8767. DOI: 10.1039/C9CC02838B (cit. on pp. 64, 107, 141).

[187]  S. R. Quake, H. Babcock, and S. Chu. „The dynamics of partially
       extended single molecules of DNA." In: *Nature* 388.6638 (1997),
       pp. 151–154. ISSN: 1476-4687. DOI: 10.1038/40588 (cit. on p. 64).

[188]  J. A. Bordelon, K. J. Feierabend, S. A. Siddiqui, L. L. Wright, and
       J. T. Petty. „Viscometry and Atomic Force Microscopy Studies of the
       Interactions of a Dimeric Cyanine Dye with DNA." In: *The Journal of
       Physical Chemistry B* 106.18 (2002), pp. 4838–4843. ISSN: 1520-6106.
       DOI: 10.1021/jp014680j (cit. on p. 64).

[189]  J. Dikic and R. Seidel. „Anticooperative Binding Governs the Mechanics of Ethidium-Complexed DNA." In: *Biophysical Journal* 116.8 (2019), pp. 1394–1405. ISSN: 0006-3495. DOI: 10.1016/j.bpj.2019.03.005 (cit. on pp. 67, 68, 130).

[190]  T. R. Strick, M. N. Dessinges, G. Charvin, N. H. Dekker, J. F. Allemand, D. Bensimon, and V. Croquette. „Stretching of macromolecules and proteins." In: *Reports on Progress in Physics* 66.1 (2003), p. 1. ISSN: 0034-4885. DOI: 10.1088/0034-4885/66/1/201 (cit. on p. 67).

[191]  I. D. Vilfan, J Lipfert, D. Koster, S. Lemay, and N. Dekker. „Magnetic tweezers for single-molecule experiments." In: *Handbook of single-molecule biophysics* (2009), pp. 371–395 (cit. on p. 67).

[192]  A. Celedon, D. Wirtz, and S. Sun. „Torsional Mechanics of DNA Are Regulated by Small-Molecule Intercalation." In: *The Journal of Physical Chemistry B* 114.50 (2010), pp. 16929–16935. ISSN: 1520-6106. DOI: 10.1021/jp107541q (cit. on pp. 67, 130, 131).

[193]  G. L. Silva, V. Ediz, D. Yaron, and B. A. Armitage. „Experimental and Computational Investigation of Unsymmetrical Cyanine Dyes: Understanding Torsionally Responsive Fluorogenic Dyes." In: *Journal of the American Chemical Society* 129.17 (2007), pp. 5710–5718. ISSN: 0002-7863. DOI: 10.1021/ja070025z (cit. on p. 70).

[194]  J. Nygren, N. Svanvik, and M. Kubista. „The interactions between the fluorescent dye thiazole orange and DNA." In: *Biopolymers* 46.1 (1998), pp. 39–51. ISSN: 0006-3525. DOI: 10.1002/(SICI)1097-0282(199807)46:1<39::AID-BIP4>3.0.CO;2-Z (cit. on p. 70).

[195]  J. Mohanty, N. Thakur, S. Dutta Choudhury, N. Barooah, H. Pal, and A. C. Bhasikuttan. „Recognition-Mediated Light-Up of Thiazole Orange with Cucurbit[8]uril: Exchange and Release by Chemical Stimuli." In: *The Journal of Physical Chemistry B* 116.1 (2012), pp. 130–135. ISSN: 1520-6106. DOI: 10.1021/jp210432t (cit. on p. 70).

[196]  T. Cordes, T. Schadendorf, B. Priewisch, K. Rück-Braun, and W. Zinth. „The Hammett Relationship and Reactions in the Excited Electronic State: Hemithioindigo Z/E-Photoisomerization." In: *The Journal of Physical Chemistry A* 112.4 (2008), pp. 581–588. ISSN: 1089-5639. DOI: 10.1021/jp077472l (cit. on p. 71).

[197]  T. Cordes, T. Schadendorf, K. Rück-Braun, and W. Zinth. „Chemical control of Hemithioindigo-photoisomerization - Substituent-effects on different molecular parts." In: *Chemical Physics Letters* 455.4 (2008), pp. 197–201. ISSN: 0009-2614. DOI: 10.1016/j.cplett.2008.02.096 (cit. on p. 71).

[198]  F. F. Graupner, T. T. Herzog, F. Rott, S. Oesterling,
R. de Vivie-Riedle, T. Cordes, and W. Zinth. „Photoisomerization of
hemithioindigo compounds: Combining solvent- and substituent-
effects into an advanced reaction model." In: *Chemical Physics* 515
(2018), pp. 614–621. ISSN: 0301-0104. DOI:
10.1016/j.chemphys.2018.07.043 (cit. on p. 71).

[199]  W. Rettig. „TICT states and beyond: Reaction dimensionality and
application to photosynthesis." In: *Proceedings of the Indian Academy
of Sciences - Chemical Sciences* 104.2 (1992), pp. 89–104. ISSN:
0973-7103. DOI: 10.1007/BF02863355 (cit. on p. 71).

[200]  P. Czerney, G. Graness, E. Birckner, F. Vollmer, and W. Rettig.
„Molecular engineering of cyanine-type fluorescent and laser dyes." In:
*Journal of Photochemistry and Photobiology A: Chemistry* 89.1 (1995),
pp. 31–36. ISSN: 1010-6030. DOI: 10.1016/1010-6030(94)04018-W
(cit. on p. 71).

[201]  K. Uno, T. Sasaki, N. Sugimoto, H. Ito, T. Nishihara, S. Hagihara,
T. Higashiyama, N. Sasaki, Y. Sato, and K. Itami. „Key Structural
Elements of Unsymmetrical Cyanine Dyes for Highly Sensitive
Fluorescence Turn-On DNA Probes." In: *Chemistry - An Asian
Journal* 12.2 (2017), pp. 233–238. ISSN: 1861-4728. DOI:
10.1002/asia.201601430 (cit. on pp. 71, 79).

[202]  C. Petermayer and H. Dube. „Indigoid Photoswitches: Visible Light
Responsive Molecular Tools." In: *Accounts of Chemical Research* 51.5
(2018), pp. 1153–1163. ISSN: 0001-4842. DOI:
10.1021/acs.accounts.7b00638 (cit. on p. 71).

[203]  J. R. Albani. *Principles and applications of fluorescence spectroscopy.*
John Wiley & Sons, 2008. ISBN: 0470691336 (cit. on pp. 71, 73, 75, 76,
85).

[204]  A. L. Benvin, Y. Creeger, G. W. Fisher, B. Ballou, A. S. Waggoner,
and B. A. Armitage. „Fluorescent DNA Nanotags: Supramolecular
Fluorescent Labels Based on Intercalating Dye Arrays Assembled on
Nanostructured DNA Templates." In: *Journal of the American
Chemical Society* 129.7 (2007), pp. 2025–2034. ISSN: 0002-7863. DOI:
10.1021/ja066354t (cit. on p. 73).

[205]  F. Mao, W.-Y. Leung, and X. Xin. „Characterization of EvaGreen and
the implication of its physicochemical properties for qPCR
applications." In: *BMC Biotechnology* 7.1 (2007), p. 76. ISSN:
1472-6750. DOI: 10.1186/1472-6750-7-76 (cit. on p. 79).

[206] W. E. Evenson, L. M. Boden, K. A. Muzikar, and D. J. O'Leary. „1H and 13C NMR Assignments for the Cyanine Dyes SYBR Safe and Thiazole Orange." In: *The Journal of Organic Chemistry* 77.23 (2012), pp. 10967–10971. ISSN: 0022-3263. DOI: 10.1021/jo3021659 (cit. on pp. 80, 89–91).

[207] A. M. Castillo, L. Patiny, and J. Wist. „Fast and accurate algorithm for the simulation of NMR spectra of large spin systems." In: *Journal of Magnetic Resonance* 209.2 (2011), pp. 123–130. ISSN: 1090-7807. DOI: 10.1016/j.jmr.2010.12.008 (cit. on p. 80).

[208] J. Lipfert, D. A. Koster, I. D. Vilfan, S. Hage, and N. H. Dekker. „Single-molecule magnetic tweezers studies of type IB topoisomerases." In: *Methods Mol Biol* 582 (2009), pp. 71–89. ISSN: 1064-3745. DOI: 10.1007/978-1-60761-340-4_7 (cit. on pp. 81, 118, 174).

[209] M. M. van Oene, L. E. Dickinson, F. Pedaci, M. Köber, D. Dulin, J. Lipfert, and N. H. Dekker. „Biological Magnetometry: Torque on Superparamagnetic Beads in Magnetic Fields." In: *Physical Review Letters* 114.21 (2015), p. 218301. DOI: 10.1103/PhysRevLett.114.218301 (cit. on p. 82).

[210] C. Gebhardt, M. Lehmann, M. M. Reif, M. Zacharias, G. Gemmecker, and T. Cordes. „Molecular and Spectroscopic Characterization of Green and Red Cyanine Fluorophores from the Alexa Fluor and AF Series." In: *ChemPhysChem* 22.15 (2021), pp. 1566–1583. ISSN: 1439-4235. DOI: 10.1002/cphc.202000935 (cit. on p. 84).

[211] I. Kostova. „Ruthenium complexes as anticancer agents." In: *Curr Med Chem* 13.9 (2006), pp. 1085–107. ISSN: 0929-8673 (Print) 0929-8673. DOI: 10.2174/092986706776360941 (cit. on p. 103).

[212] C. S. Allardyce and P. J. Dyson. „Ruthenium in Medicine: Current Clinical Uses and Future Prospects." In: *Platinum Metals Review* 45.2 (2001), pp. 62–69 (cit. on p. 103).

[213] V. Balzani and A. Juris. „Photochemistry and photophysics of Ru(II)polypyridine complexes in the Bologna group. From early studies to recent developments." In: *Coordination Chemistry Reviews* 211.1 (2001), pp. 97–115. ISSN: 0010-8545. DOI: 10.1016/S0010-8545(00)00274-5 (cit. on p. 104).

[214] J.-P. Lecomte, A. K.-D. Mesmaeker, J. M. Kelly, A. B. Tossi, and H. Görner. „Photo-induced electron transfer from nucleotides to ruthenium-tris-1,4,5,8-tetraazaphenanthrene: model for photosensitized DNA oxidation." In: *Photochemistry and Photobiology* 55.5 (1992), pp. 681–689. ISSN: 0031-8655. DOI: 10.1111/j.1751-1097.1992.tb08511.x (cit. on pp. 104, 105, 109).

[215]   R. J. Watts. „Ruthenium polypyridyls: A case study." In: *Journal of Chemical Education* 60.10 (1983), p. 834. ISSN: 0021-9584. DOI: 10.1021/ed060p834 (cit. on p. 104).

[216]   O. S. Wenger. „Is Iron the New Ruthenium?" In: *Chemistry - A European Journal* 25.24 (2019), pp. 6043–6052. ISSN: 0947-6539. DOI: 10.1002/chem.201806148 (cit. on p. 104).

[217]   „Einführung: Spektroskopische Methoden in der organischen Chemie." In: ed. by S. Bienz, L. Bigler, and T. Fox. 9. Auflage. Georg Thieme Verlag, 2016. ISBN: 9783135761091. DOI: 10.1055/b-004-129729 (cit. on pp. 104, 139).

[218]   L. Mohapatra and K. Parida. „A review of solar and visible light active oxo-bridged materials for energy and environment." In: *Catalysis Science and Technology* 7.11 (2017), pp. 2153–2164. ISSN: 2044-4753. DOI: 10.1039/C7CY00116A (cit. on p. 104).

[219]   E. Alessio, G. Mestroni, A. Bergamo, and G. Sava. „Ruthenium anticancer drugs." In: *Metal Ions in Biological Systems* (2004), pp. 323–351. ISSN: 0429215991 (cit. on p. 105).

[220]   E. Alessio, G. Mestroni, A. Bergamo, and G. Sava. „Ruthenium Antimetastatic Agents." In: *Current Topics in Medicinal Chemistry* 4.15 (2004), pp. 1525–1535. DOI: 10.2174/1568026043387421 (cit. on p. 105).

[221]   F. E. Poynton, S. A. Bright, S. Blasco, D. C. Williams, J. M. Kelly, and T. Gunnlaugsson. „The development of ruthenium(ii) polypyridyl complexes and conjugates for in vitro cellular and in vivo applications." In: *Chemical Society Reviews* 46.24 (2017), pp. 7706–7756. ISSN: 0306-0012. DOI: 10.1039/C7CS00680B (cit. on pp. 105, 109).

[222]   F. Heinemann, J. Karges, and G. Gasser. „Critical Overview of the Use of Ru(II) Polypyridyl Complexes as Photosensitizers in One-Photon and Two-Photon Photodynamic Therapy." In: *Accounts of Chemical Research* 50.11 (2017), pp. 2727–2736. ISSN: 0001-4842. DOI: 10.1021/acs.accounts.7b00180 (cit. on p. 109).

[223]   A. E. Friedman, J. C. Chambron, J. P. Sauvage, N. J. Turro, and J. K. Barton. „A molecular light switch for DNA: Ru (bpy) 2 (dppz) 2+." In: *Journal of the American Chemical Society* 112.12 (1990), pp. 4960–4962. ISSN: 0002-7863 (cit. on p. 109).

[224]   C. Moucheron, A. Kirsch-De Mesmaeker, and S. Choua. „Photophysics of Ru(phen)2(PHEHAT)2+: A Novel "Light Switch" for DNA and Photo-oxidant for Mononucleotides." In: *Inorganic Chemistry* 36.4 (1997), pp. 584–592. ISSN: 0020-1669. DOI: 10.1021/ic9609315 (cit. on p. 109).

[225]   A. N. Boynton, L. Marcelis, and J. K. Barton.
        „[Ru(Me4phen)2dppz]2+, a Light Switch for DNA Mismatches." In:
        *Journal of the American Chemical Society* 138.15 (2016),
        pp. 5020–5023. ISSN: 0002-7863. DOI: 10.1021/jacs.6b02022 (cit. on
        p. 109).

[226]   Q. Deraedt, L. Marcelis, F. Loiseau, and B. Elias. „Towards
        mismatched DNA photoprobes and photoreagents: "elbow-shaped"
        Ru(ii) complexes." In: *Inorganic Chemistry Frontiers* 4.1 (2017),
        pp. 91–103. DOI: 10.1039/C6QI00223D (cit. on p. 109).

[227]   L. Jacquet, R. J. H. Davies, A. Kirsch-De Mesmaeker, and J. M. Kelly.
        „Photoaddition of Ru(tap)2(bpy)2+ to DNA: A New Mode of Covalent
        Attachment of Metal Complexes to Duplex DNA." In: *Journal of the
        American Chemical Society* 119.49 (1997), pp. 11763–11768. ISSN:
        0002-7863. DOI: 10.1021/ja971163z (cit. on p. 109).

[228]   C. S. Burke, A. Byrne, and T. E. Keyes. „Targeting Photoinduced
        DNA Destruction by Ru(II) Tetraazaphenanthrene in Live Cells by
        Signal Peptide." In: *Journal of the American Chemical Society* 140.22
        (2018), pp. 6945–6955. ISSN: 0002-7863. DOI: 10.1021/jacs.8b02711
        (cit. on pp. 109, 162).

[229]   W. Vanderlinden, M. Blunt, C. C. David, C. Moucheron,
        A. Kirsch-De Mesmaeker, and S. De Feyter. „Mesoscale DNA
        structural changes on binding and photoreaction with
        Ru[(TAP)2PHEHAT]2+." In: *J Am Chem Soc* 134.24 (2012),
        pp. 10214–21. ISSN: 1520-5126 (Electronic) 0002-7863 (Linking). DOI:
        10.1021/ja303091q (cit. on pp. 109, 114, 116, 162).

[230]   J. K. Barton, A. Danishefsky, and J. Goldberg.
        „Tris(phenanthroline)ruthenium(II): stereoselectivity in binding to
        DNA." In: *Journal of the American Chemical Society* 106.7 (1984),
        pp. 2172–2176. ISSN: 0002-7863. DOI: 10.1021/ja00319a043 (cit. on
        pp. 109, 116, 162).

[231]   S. Satyanarayana, J. C. Dabrowiak, and J. B. Chaires. „Neither
        .DELTA.- nor .LAMBDA.-tris(phenanthroline)ruthenium(II) binds to
        DNA by classical intercalation." In: *Biochemistry* 31.39 (1992),
        pp. 9319–9324. ISSN: 0006-2960. DOI: 10.1021/bi00154a001 (cit. on
        pp. 109, 116, 162).

[232]   P. Lincoln and B. Norden. „DNA Binding Geometries of
        Ruthenium(II) Complexes with 1,10-Phenanthroline and
        2,2'-Bipyridine Ligands Studied with Linear Dichroism Spectroscopy.
        Borderline Cases of Intercalation." In: *The Journal of Physical
        Chemistry B* 102.47 (1998), pp. 9583–9594. ISSN: 1520-6106. DOI:
        10.1021/jp9824914 (cit. on pp. 109, 110, 116, 162).

[233]  K. Gisselfält, P. Lincoln, B. Norden, and M. Jonsson. „Interactions of
       Tris(phenanthroline)ruthenium(II) Enantiomers with DNA: Effects on
       Helix Flexibility Studied by the Electrophoretic Behavior of Reptating
       DNA in Agarose Gel." In: *The Journal of Physical Chemistry B* 104.15
       (2000), pp. 3651–3659. ISSN: 1520-6106. DOI: 10.1021/jp993369n
       (cit. on pp. 109, 116, 162).

[234]  J. P. Hall, K. O'Sullivan, A. Naseer, J. A. Smith, J. M. Kelly, and
       C. J. Cardin. „Structure determination of an intercalating ruthenium
       dipyridophenazine complex which kinks DNA by semiintercalation of a
       tetraazaphenanthrene ligand." In: *Proceedings of the National
       Academy of Sciences* 108.43 (2011), pp. 17610–17614. DOI:
       10.1073/pnas.1108685108 (cit. on pp. 109, 111, 116, 162).

[235]  T. Brouns, H. De Keersmaecker, S. F. Konrad, N. Kodera, T. Ando,
       J. Lipfert, S. De Feyter, and W. Vanderlinden. „Free Energy
       Landscape and Dynamics of Supercoiled DNA by High-Speed Atomic
       Force Microscopy." In: *ACS Nano* 12.12 (2018), pp. 11907–11916. ISSN:
       1936-0851. DOI: 10.1021/acsnano.8b06994 (cit. on pp. 110, 112, 134).

[236]  Y. O. Popov and A. V. Tkachenko. „Effects of kinks on DNA
       elasticity." In: *Physical Review E* 71.5 (2005), p. 051905. DOI:
       10.1103/PhysRevE.71.051905 (cit. on p. 111).

[237]  J. M. Kelly, A. B. Tossi, D. J. McConnell, and C. OhUigin. „A study
       of the interactions of some polypyridylruthenium (II) complexes with
       DNA using fluorescence spectroscopy, topoisomerisation and thermal
       denaturation." In: *Nucleic acids research* 13.17 (1985), pp. 6017–6034.
       ISSN: 0305-1048 1362-4962 (cit. on p. 112).

[238]  A. B. Tossi and J. M. Kelly. „A study of some
       polypyridylruthenium(II) complexes as DNA binders and
       photocleavage reagents." In: *Photochemistry and Photobiology* 49.5
       (1989), pp. 545–556. ISSN: 0031-8655. DOI:
       10.1111/j.1751-1097.1989.tb08423.x (cit. on p. 112).

[239]  M. M. Feeney, J. M. Kelly, A. B. Tossi, A. K.-d. Mesmaeker, and
       J.-P. Lecomte. „Photoaddition of
       ruthenium(II)-tris-1,4,5,8-tetraazaphenanthrene to DNA and
       mononucleotides." In: *Journal of Photochemistry and Photobiology B:
       Biology* 23.1 (1994), pp. 69–78. ISSN: 1011-1344. DOI:
       10.1016/1011-1344(93)06985-C (cit. on p. 116).

[240]  M. N. Ackermann and L. V. Interrante. „Ruthenium(II) complexes of
       modified 1,10-phenanthrolines. 1. Synthesis and properties of
       complexes containing dipyridophenazines and a
       dicyanomethylene-substituted 1,10-phenanthroline." In: *Inorganic
       Chemistry* 23.24 (1984), pp. 3904–3911. ISSN: 0020-1669. DOI:
       10.1021/ic00192a014 (cit. on p. 117).

[241]   P. U. Walker, W. Vanderlinden, and J. Lipfert. „Dynamics and energy landscape of DNA plectoneme nucleation." In: *Physical Review E* 98.4 (2018), p. 042412. DOI: 10.1103/PhysRevE.98.042412 (cit. on p. 118).

[242]   M. T. van Loenhout, J. W. Kerssemakers, I. De Vlaminck, and C. Dekker. „Non-bias-limited tracking of spherical particles, enabling nanometer resolution at low magnification." In: *Biophys J* 102.10 (2012), pp. 2362–71. ISSN: 1542-0086 (Electronic) 0006-3495 (Linking). DOI: 10.1016/j.bpj.2012.03.073 (cit. on pp. 118, 145).

[243]   H. Zhang and J. F. Marko. „Maxwell relations for single-DNA experiments: Monitoring protein binding and double-helix torque with force-extension measurements." In: *Physical Review E* 77.3 (2008), p. 031916. DOI: 10.1103/PhysRevE.77.031916 (cit. on p. 123).

[244]   P. Pandya, M. M. Islam, G. S. Kumar, B. Jayaram, and S. Kumar. „DNA minor groove binding of small molecules: Experimental and computational evidence." In: *Journal of Chemical Sciences* 122.2 (2010), pp. 247–257. ISSN: 0973-7103. DOI: 10.1007/s12039-010-0029-4 (cit. on p. 123).

[245]   H. Gattuso, T. Duchanois, V. Besancenot, X. Assfeld, P. Becuwe, P. Gros, S. Grandemange, and A. Monari. „Iron Complexes Interacting with DNA. Insights from Molecular Modeling and Cellular Biology." In: *Frontiers in Chemistry* 3 (2015). DOI: 10.3389/fchem.2015.00067 (cit. on pp. 123, 124).

[246]   A. Sanchez-Gonzalez, T. G. Castro, M. Melle-Franco, and A. Gil. „From groove binding to intercalation: unravelling the weak interactions and other factors modulating the modes of interaction between methylated phenanthroline-based drugs and duplex DNA." In: *Physical Chemistry Chemical Physics* 23.47 (2021), pp. 26680–26695. ISSN: 1463-9076. DOI: 10.1039/D1CP04529F (cit. on p. 123).

[247]   S. Priyadarshy, S. M. Risser, and D. N. Beratan. „DNA Is Not a Molecular Wire: Protein-like Electron-Transfer Predicted for an Extended pi-Electron System." In: *The Journal of Physical Chemistry* 100.44 (1996), pp. 17678–17682. ISSN: 0022-3654. DOI: 10.1021/jp961731h (cit. on p. 123).

[248]   C. Medhi, J. B. O. Mitchell, S. L. Price, and A. B. Tabor. „Electrostatic factors in DNA intercalation." In: *Biopolymers* 52.2 (1999), pp. 84–93. ISSN: 0006-3525. DOI: https://doi.org/10.1002/1097-0282(1999)52:2<84::AID-BIP2>3.0.CO;2-S (cit. on pp. 123, 124).

[249]   B. C. Baguley, L. P. G. Wakelin, J. D. Jacintho, and P. Kovacic. „Mechanisms of Action of DNA Intercalating Acridine-based Drugs: How Important are Contributions from Electron Transfer and Oxidative Stress?" In: *Current Medicinal Chemistry* 10.24 (2003), pp. 2643–2649. DOI: 10.2174/0929867033456332 (cit. on p. 123).

[250]   H. L. Le Chatelier. „A general statement of the laws of chemical equilibrium." In: *Comptes rendus* 99 (1884), pp. 786–789 (cit. on pp. 124, 125).

[251]   D. A. Koster, A. Crut, S. Shuman, M. A. Bjornsti, and N. H. Dekker. „Cellular strategies for regulating DNA supercoiling: a single-molecule perspective." In: *Cell* 142.4 (2010), pp. 519–30. ISSN: 1097-4172 (Electronic) 0092-8674 (Linking). DOI: S0092-8674(10)00896-2[pii]10.1016/j.cell.2010.08.001 (cit. on pp. 129, 146).

[252]   L. F. Liu and J. C. Wang. „Supercoiling of the DNA template during transcription." In: *Proc Natl Acad Sci U S A* 84.20 (1987), pp. 7024–7. ISSN: 0027-8424 (Print) (cit. on pp. 129, 132, 146).

[253]   J. Ubbink and T. Odijk. „Electrostatic-undulatory theory of plectonemically supercoiled DNA." In: *Biophys J* 76.5 (1999), pp. 2502–19. ISSN: 0006-3495 (Print) 0006-3495 (Linking). DOI: 10.1016/S0006-3495(99)77405-9 (cit. on p. 129).

[254]   A. V. Vologodskii and N. R. Cozzarelli. „Conformational and thermodynamic properties of supercoiled DNA." In: *Annual Review of Biophysics and Biomolecular Structure* 23 (1994), pp. 609–643 (cit. on p. 129).

[255]   S. Corless and N. Gilbert. „Effects of DNA supercoiling on chromatin architecture." In: *Biophysical Reviews* 8.3 (2016), pp. 245–258. ISSN: 1867-2469. DOI: 10.1007/s12551-016-0210-1 (cit. on p. 129).

[256]   C. Gebhardt, M. Lehmann, M. M. Reif, M. Zacharias, and T. Cordes. „Molecular and spectroscopic characterization of green and red cyanine fluorophores from the Alexa Fluor and AF series." In: *bioRxiv* (2020), p. 2020.11.13.381152. DOI: 10.1101/2020.11.13.381152 (cit. on p. 129).

[257]   N. Gilbert and J. Allan. „Supercoiling in DNA and chromatin." In: *Current Opinion in Genetics & Development* 25 (2014), pp. 15–21. ISSN: 0959-437X. DOI: https://doi.org/10.1016/j.gde.2013.10.013 (cit. on p. 129).

[258]   F. Kouzine, J. Liu, S. Sanford, H. J. Chung, and D. Levens. „The dynamic response of upstream DNA to transcription-generated torsional stress." In: *Nat Struct Mol Biol* 11.11 (2004), pp. 1092–100. ISSN: 1545-9993 (Print) 1545-9985 (Linking) (cit. on p. 129).

[259]    F. Kouzine, S. Sanford, Z. Elisha-Feil, and D. Levens. „The functional response of upstream DNA to dynamic supercoiling in vivo." In: *Nat Struct Mol Biol* 15.2 (2008), pp. 146–54. ISSN: 1545-9985 (Electronic) 1545-9985 (Linking) (cit. on p. 129).

[260]    B. Baguley. „DNA intercalating anti-tumour agents." In: *Anti-cancer drug design* 6.1 (1991), pp. 1–35. ISSN: 0266-9536 (cit. on p. 129).

[261]    E. C. Long and J. K. Barton. „On demonstrating DNA intercalation." In: *Accounts of Chemical Research* 23.9 (1990), pp. 271–273. ISSN: 0001-4842 (cit. on pp. 129, 131).

[262]    F. C. Chou, J. Lipfert, and R. Das. „Blind predictions of DNA and RNA tweezers experiments with force and torque." In: *PLoS Comput Biol* 10.8 (2014), e1003756. ISSN: 1553-7358 (Electronic) 1553-734X (Linking). DOI: 10.1371/journal.pcbi.1003756 (cit. on p. 129).

[263]    W. K. Olson, A. A. Gorin, X. J. Lu, L. M. Hock, and V. B. Zhurkin. „DNA sequence-dependent deformability deduced from protein-DNA crystal complexes." In: *Proc Natl Acad Sci U S A* 95.19 (1998), pp. 11163–8. ISSN: 0027-8424 (Print) 0027-8424 (Linking) (cit. on p. 129).

[264]    Y. Seol and K. C. Neuman. „The Dynamic Interplay Between DNA Topoisomerases and DNA Topology." In: *Biophys Rev* 8.3 (2016), pp. 221–231. ISSN: 1867-2450 (Print) 1867-2450. DOI: 10.1007/s12551-016-0206-x (cit. on p. 129).

[265]    E. Skoruppa, S. K. Nomidis, J. F. Marko, and E. Carlon. „Bend-Induced Twist Waves and the Structure of Nucleosomal DNA." In: *Physical Review Letters* 121.8 (2018), p. 088101. DOI: 10.1103/PhysRevLett.121.088101 (cit. on p. 129).

[266]    W. Vanderlinden, J. Lipfert, J. Demeulemeester, Z. Debyser, and S. De Feyter. „Structure, mechanics, and binding mode heterogeneity of LEDGF/p75-DNA nucleoprotein complexes revealed by scanning force microscopy." In: *Nanoscale* 6.9 (2014), pp. 4611–4619. ISSN: 2040-3364. DOI: 10.1039/C4NR00022F (cit. on p. 129).

[267]    G. I. Bell. „Models for the specific adhesion of cells to cells." In: *Science* 200.4342 (1978), pp. 618–27. ISSN: 0036-8075 (Print) 0036-8075 (Linking). DOI: 10.1126/science.347575 (cit. on pp. 129, 145).

[268]    E. Evans and K. Ritchie. „Dynamic strength of molecular adhesion bonds." In: *Biophys J* 72.4 (1997), pp. 1541–55. ISSN: 0006-3495 (Print) 0006-3495 (Linking). DOI: 10.1016/S0006-3495(97)78802-7 (cit. on p. 129).

[269]  M. Hayashi and Y. Harada. „Direct observation of the reversible unwinding of a single DNA molecule caused by the intercalation of ethidium bromide." In: *Nucleic Acids Res* 35.19 (2007), e125. ISSN: 1362-4962 (Electronic) 0305-1048 (Linking). DOI: gkm529[pii]10.1093/nar/gkm529 (cit. on p. 130).

[270]  P. R. Selvin, D. N. Cook, N. G. Pon, W. R. Bauer, M. P. Klein, and J. E. Hearst. „Torsional rigidity of positively and negatively supercoiled DNA." In: *Science* 255.5040 (1992), pp. 82–5. ISSN: 0036-8075 (Print) 0036-8075 (Linking) (cit. on pp. 130, 134).

[271]  M. Ganji, S. H. Kim, J. van der Torre, E. Abbondanzieri, and C. Dekker. „Intercalation-Based Single-Molecule Fluorescence Assay To Study DNA Supercoil Dynamics." In: *Nano Letters* 16.7 (2016), pp. 4699–4707. ISSN: 1530-6984. DOI: 10.1021/acs.nanolett.6b02213 (cit. on pp. 130, 139, 149).

[272]  M. Ganji, I. A. Shaltiel, S. Bisht, E. Kim, A. Kalichava, C. H. Haering, and C. Dekker. „Real-time imaging of DNA loop extrusion by condensin." In: *Science* 360.6384 (2018), pp. 102–105. DOI: doi:10.1126/science.aar7831 (cit. on p. 130).

[273]  S. H. Kim, M. Ganji, E. Kim, J. van der Torre, E. Abbondanzieri, and C. Dekker. „DNA sequence encodes the position of DNA supercoils." In: *eLife* 7 (2018), e36557. ISSN: 2050-084X. DOI: 10.7554/eLife.36557 (cit. on pp. 130, 139, 149).

[274]  W. Lapolla, B. A. Yentzer, J. Bagel, C. R. Halvorson, and S. R. Feldman. „A review of phototherapy protocols for psoriasis treatment." In: *Journal of the American Academy of Dermatology* 64.5 (2011), pp. 936–949. ISSN: 0190-9622. DOI: https://doi.org/10.1016/j.jaad.2009.12.054 (cit. on pp. 130, 139).

[275]  I. Bermúdez, J. García-Martínez, J. E. Pérez-Ortín, and J. Roca. „A method for genome-wide analysis of DNA helical tension by means of psoralen–DNA photobinding." In: *Nucleic Acids Research* 38.19 (2010), e182–e182. ISSN: 0305-1048. DOI: 10.1093/nar/gkq687 (cit. on pp. 130, 139, 140, 159).

[276]  T. Cech and M. L. Pardue. „Cross-linking of DNA with trimethylpsoralen is a probe for chromatin structure." In: *Cell* 11.3 (1977), pp. 631–640. ISSN: 0092-8674. DOI: https://doi.org/10.1016/0092-8674(77)90080-0 (cit. on pp. 130, 139).

[277]   G. D. Cimino, H. B. Gamper, S. T. Isaacs, and J. E. Hearst.
        „Psoralens as photoactive probes of nucleic acid structure and function:
        organic chemistry, photochemistry, and biochemistry." In: *Annual
        Review of Biochemistry* 54.1 (1985), pp. 1151–1193. DOI:
        `10.1146/annurev.bi.54.070185.005443` (cit. on pp. 130, 139).

[278]   C. Naughton, N. Avlonitis, S. Corless, J. G. Prendergast, I. K. Mati,
        P. P. Eijk, S. L. Cockroft, M. Bradley, B. Ylstra, and N. Gilbert.
        „Transcription forms and remodels supercoiling domains unfolding
        large-scale chromatin structures." In: *Nature Structural & Molecular
        Biology* 20.3 (2013), pp. 387–395. ISSN: 1545-9985. DOI:
        `10.1038/nsmb.2509` (cit. on pp. 130, 139).

[279]   R. R. Sinden, J. O. Carlson, and D. E. Pettijohn. „Torsional tension in
        the DNA double helix measured with trimethylpsoralen in living E.
        coli cells: Analogous measurements in insect and human cells." In: *Cell*
        21.3 (1980), pp. 773–783. ISSN: 0092-8674. DOI:
        `https://doi.org/10.1016/0092-8674(80)90440-7` (cit. on pp. 130,
        139, 140).

[280]   A. Maxwell, N. P. Burton, and N. O'Hagan. „High-throughput assays
        for DNA gyrase and other topoisomerases." In: *Nucleic Acids Research*
        34.15 (2006), e104–e104. ISSN: 0305-1048. DOI: `10.1093/nar/gkl504`
        (cit. on pp. 130, 137).

[281]   M. R. Webb and S. E. Ebeler. „A gel electrophoresis assay for the
        simultaneous determination of topoisomerase I inhibition and DNA
        intercalation." In: *Analytical Biochemistry* 321.1 (2003), pp. 22–30.
        ISSN: 0003-2697. DOI:
        `https://doi.org/10.1016/S0003-2697(03)00459-7` (cit. on p. 130).

[282]   Y. Yamashita, N. Fujii, C. Murakata, T. Ashizawa, M. Okabe, and
        H. Nakano. „Induction of mammalian DNA topoisomerase I mediated
        DNA cleavage by antitumor indolocarbazole derivatives." In:
        *Biochemistry* 31.48 (1992), pp. 12069–12075. ISSN: 0006-2960 (cit. on
        p. 130).

[283]   L. Lercher, M. A. McDonough, A. H. El-Sagheer, A. Thalhammer,
        S. Kriaucionis, T. Brown, and C. J. Schofield. „Structural insights into
        how 5-hydroxymethylation influences transcription factor binding." In:
        *Chemical Communications* 50.15 (2014), pp. 1794–1796. ISSN:
        1359-7345. DOI: `10.1039/C3CC48151D` (cit. on p. 132).

[284]   W. R. Bauer. „Structure and reactions of closed duplex DNA." In:
        *Annual review of biophysics and bioengineering* 7.1 (1978),
        pp. 287–313. ISSN: 0084-6589 (cit. on p. 131).

[285]  J. C. Wang. „Variation of the average rotation angle of the DNA helix and the superhelical turns of covalently closed cyclic Lambda DNA." In: *Journal of Molecular Biology* 43.1 (1969), pp. 25–39. ISSN: 0022-2836. DOI: http://dx.doi.org/10.1016/0022-2836(69)90076-X (cit. on p. 131).

[286]  P. Anderson and W. Bauer. „Supercoiling in closed circular DNA: dependence upon ion type and concentration." In: *Biochemistry* 17.4 (1978), pp. 594–601. ISSN: 0006-2960 (Print) 0006-2960 (Linking). DOI: 10.1021/bi00597a006 (cit. on p. 131).

[287]  J. Diekmann, I. Theves, K. A. Thom, and P. Gilch. „Tracing the Photoaddition of Pharmaceutical Psoralens to DNA." In: *Molecules* 25.22 (2020), p. 5242. ISSN: 1420-3049 (cit. on p. 133).

[288]  G. Wiesehahn and J. E. Hearst. „DNA unwinding induced by photoaddition of psoralen derivatives and determination of dark-binding equilibrium constants by gel electrophoresis." In: *Proc Natl Acad Sci U S A* 75.6 (1978), pp. 2703–7. ISSN: 0027-8424 (Print) 0027-8424. DOI: 10.1073/pnas.75.6.2703 (cit. on p. 133).

[289]  J. D. Moroz and P. Nelson. „Torsional directed walks, entropic elasticity, and DNA twist stiffness." In: *Proc Natl Acad Sci U S A* 94.26 (1997), pp. 14418–22 (cit. on p. 134).

[290]  Z. Bryant, M. D. Stone, J. Gore, S. B. Smith, N. R. Cozzarelli, and C. Bustamante. „Structural transitions and elasticity from torque measurements on DNA." In: *Nature* 424.6946 (2003), pp. 338–41. ISSN: 1476-4687 (Electronic). DOI: 10.1038/nature01810nature01810[pii] (cit. on pp. 134, 151).

[291]  F. Mosconi, J. F. Allemand, D. Bensimon, and V. Croquette. „Measurement of the torque on a single stretched and twisted DNA using magnetic tweezers." In: *Phys Rev Lett* 102.7 (2009), p. 078301. ISSN: 0031-9007 (Print) 0031-9007 (Linking) (cit. on pp. 134, 151).

[292]  B. S. Fujimoto and J. M. Schurr. „Dependence of the torsional rigidity of DNA on base composition." In: *Nature* 344.6262 (1990), pp. 175–7. ISSN: 0028-0836 (Print) 0028-0836 (Linking). DOI: 10.1038/344175a0 (cit. on p. 134).

[293]  P. J. Heath, J. B. Clendenning, B. S. Fujimoto, and J. M. Schurr. „Effect of bending strain on the torsion elastic constant of DNA." In: *J Mol Biol* 260.5 (1996), pp. 718–30. ISSN: 0022-2836 (Print) 0022-2836 (Linking). DOI: S0022283696904325[pii] (cit. on p. 134).

[294] M. J. Molloy, V. S. Hall, S. I. Bailey, K. J. Griffin, J. Faulkner, and M. Uden. „Effective and robust plasmid topology analysis and the subsequent characterization of the plasmid isoforms thereby observed." In: *Nucleic Acids Research* 32.16 (2004), e129–e129. ISSN: 0305-1048. DOI: 10.1093/nar/gnh124 (cit. on p. 137).

[295] W. Vanderlinden, T. Brouns, P. U. Walker, P. J. Kolbeck, L. F. Milles, W. Ott, P. C. Nickels, Z. Debyser, and J. Lipfert. „The free energy landscape of retroviral integration." In: *Nature Communications* 10.1 (2019), p. 4738. ISSN: 2041-1723. DOI: 10.1038/s41467-019-12649-w (cit. on p. 137).

[296] M. Wang, J.-K. Liu, T. Gao, L.-L. Xu, X.-X. Zhang, J.-H. Nie, Y. Li, and H.-X. Chen. „A platform method for plasmid isoforms analysis by capillary gel electrophoresis." In: *Electrophoresis* 43.11 (2022), pp. 1174–1182. ISSN: 0173-0835. DOI: https://doi.org/10.1002/elps.202100343 (cit. on p. 137).

[297] N. Paillous and P. Vicendo. „Mechanisms of photosensitized DNA cleavage." In: *Journal of Photochemistry and Photobiology B: Biology* 20.2 (1993), pp. 203–209. ISSN: 1011-1344. DOI: https://doi.org/10.1016/1011-1344(93)80152-Y (cit. on p. 141).

[298] M. A. Tycon, C. F. Dial, K. Faison, W. Melvin, and C. J. Fecko. „Quantification of dye-mediated photodamage during single-molecule DNA imaging." In: *Analytical Biochemistry* 426.1 (2012), pp. 13–21. ISSN: 0003-2697. DOI: https://doi.org/10.1016/j.ab.2012.03.021 (cit. on p. 141).

[299] W. Liu, H. Zhong, R. Wang, and N. C. Seeman. „Crystalline Two-Dimensional DNA-Origami Arrays." In: *Angewandte Chemie International Edition* 50.1 (2011), pp. 264–267. ISSN: 1433-7851. DOI: 10.1002/anie.201005911 (cit. on p. 142).

[300] Y. A. G. Fosado, D. Michieletto, C. A. Brackley, and D. Marenduzzo. „Nonequilibrium dynamics and action at a distance in transcriptionally driven DNA supercoiling." In: *Proceedings of the National Academy of Sciences* 118.10 (2021), e1905215118. DOI: doi:10.1073/pnas.1905215118 (cit. on p. 143).

[301] L. Finzi and D. Dunlap. „Supercoiling biases the formation of loops involved in gene regulation." In: *Biophys Rev* 8.Suppl 1 (2016), pp. 65–74. ISSN: 1867-2450 (Print) 1867-2450 (Linking). DOI: 10.1007/s12551-016-0211-0 (cit. on p. 146).

[302]   J. Lipfert, M. M. van Oene, M. Lee, F. Pedaci, and N. H. Dekker.
        „Torque spectroscopy for the study of rotary motion in biological
        systems." In: *Chem Rev* 115.3 (2015), pp. 1449–74. ISSN: 1520-6890
        (Electronic) 0009-2665 (Linking). DOI: 10.1021/cr500119k (cit. on
        p. 146).

[303]   N. Naumova, M. Imakaev, G. Fudenberg, Y. Zhan, B. R. Lajoie,
        L. A. Mirny, and J. Dekker. „Organization of the mitotic chromosome."
        In: *Science* 342.6161 (2013), pp. 948–53. ISSN: 1095-9203 (Electronic)
        0036-8075 (Linking). DOI: 10.1126/science.1236083 (cit. on p. 146).

[304]   L. Postow, C. D. Hardy, J. Arsuaga, and N. R. Cozzarelli.
        „Topological domain structure of the Escherichia coli chromosome." In:
        *Genes Dev* 18.14 (2004), pp. 1766–79. ISSN: 0890-9369 (Print)
        0890-9369 (Linking). DOI: 10.1101/gad.1207504 (cit. on p. 146).

[305]   M. Bussiek, N. Mücke, and J. Langowski. „Polylysine-coated mica can
        be used to observe systematic changes in the supercoiled DNA
        conformation by scanning force microscopy in solution." In: *Nucleic
        Acids Research* 31.22 (2003), e137–e137. ISSN: 0305-1048. DOI:
        10.1093/nar/gng137 (cit. on p. 147).

[306]   P. J. Kolbeck, M. Dass, I. V. Martynenko, R. J. A. van Dijk-Moes,
        K. J. H. Brouwer, A. van Blaaderen, W. Vanderlinden, T. Liedl, and
        J. Lipfert. „DNA Origami Fiducial for Accurate 3D Atomic Force
        Microscopy Imaging." In: *Nano Letters* 23.4 (2023). PMID: 36745573,
        pp. 1236–1243. DOI: 10.1021/acs.nanolett.2c04299 (cit. on p. 147).

[307]   S. F. Konrad, W. Vanderlinden, W. Frederickx, T. Brouns,
        B. H. Menze, S. De Feyter, and J. Lipfert. „High-throughput AFM
        analysis reveals unwrapping pathways of H3 and CENP-A
        nucleosomes." In: *Nanoscale* 13.10 (2021), pp. 5435–5447. ISSN:
        2040-3364. DOI: 10.1039/D0NR08564B (cit. on p. 147).

[308]   S. D. Chandradoss, A. C. Haagsma, Y. K. Lee, J.-H. Hwang,
        J.-M. Nam, and C. Joo. „Surface Passivation for Single-molecule
        Protein Studies." In: *JoVE* 86 (2014), e50549. ISSN: 1940-087X. DOI:
        doi:10.3791/50549 (cit. on p. 149).

[309]   M. Tisma, M. Panoukidou, H. Antar, Y.-M. Soh, R. Barth,
        B. Pradhan, A. Barth, J. van der Torre, D. Michieletto, S. Gruber,
        et al. „ParB proteins can bypass DNA-bound roadblocks via
        dimer-dimer recruitment." In: *Science Advances* 8.26 (2022), eabn3299.
        DOI: doi:10.1126/sciadv.abn3299 (cit. on p. 149).

[310]   C. E. Aitken, R. A. Marshall, and J. D. Puglisi. „An Oxygen
        Scavenging System for Improvement of Dye Stability in
        Single-Molecule Fluorescence Experiments." In: *Biophysical Journal*
        94.5 (2008), pp. 1826–1835. ISSN: 0006-3495. DOI:
        https://doi.org/10.1529/biophysj.107.117689 (cit. on p. 150).

[311]   B. Pradhan, T. Kanno, M. Umeda Igarashi, M. S. Loke, M. D. Baaske,
        J. S. K. Wong, K. Jeppsson, C. Björkegren, and E. Kim. „The Smc5/6
        complex is a DNA loop-extruding motor." In: *Nature* 616.7958 (2023),
        pp. 843–848. ISSN: 1476-4687. DOI: 10.1038/s41586-023-05963-3
        (cit. on p. 150).

[312]   M. Ali, J. Lipfert, S. Seifert, D. Herschlag, and S. Doniach. „The
        ligand-free state of the TPP riboswitch: a partially folded RNA
        structure." In: *J Mol Biol* 396.1 (2010), pp. 153–65. ISSN: 1089-8638
        (Electronic) 0022-2836 (Linking). DOI:
        S0022-2836(09)01407-7[pii]10.1016/j.jmb.2009.11.030 (cit. on
        p. 151).

[313]   G. H. Golub and C. F. Van Loan. *Matrix computations*. JHU press,
        2013. ISBN: 1421408597 (cit. on p. 151).

[314]   D. A. Wright and N. A. Welschmeyer. „Establishing benchmarks in
        compliance assessment for the ballast water management convention
        by port state control." In: *Journal of Marine Engineering &
        Technology* 14.1 (2015), pp. 9–18. ISSN: 2046-4177. DOI:
        10.1080/20464177.2015.1022380 (cit. on p. 154).

[315]   D. H. Paik, V. A. Roskens, and T. T. Perkins. „Torsionally constrained
        DNA for single-molecule assays: an efficient, ligation-free method." In:
        *Nucleic Acids Research* 41.19 (2013), e179–e179. ISSN: 0305-1048. DOI:
        10.1093/nar/gkt699 (cit. on p. 166).

[316]   J. Lipfert, J. W. Kerssemakers, T. Jager, and N. H. Dekker. „Magnetic
        torque tweezers: measuring torsional stiffness in DNA and RecA-DNA
        filaments." In: *Nat Methods* 7.12 (2010), pp. 977–80. ISSN: 1548-7105
        (Electronic) 1548-7091 (Linking). DOI: 10.1038/nmeth.1520 (cit. on
        p. 174).

## DECLARATION | VERKLARING

I hereby declare, to have written the present thesis independently and to have used none but the sources and means declared in the thesis.

Hierbij verklaar ik dit proefschrift onafhankelijk te hebben geschreven en alleen de bronnen en middelen te hebben gebruikt die in het proefschrift worden vermeld.

*München, 12.07.2023*

Pauline Julika Kolbeck